

2016

Spatial and temporal dynamics of receptor for advanced glycation endproducts, integrins, and actin cytoskeleton as probed with fluorescence-based imaging techniques

Aleem Syed
Iowa State University

Follow this and additional works at: <https://lib.dr.iastate.edu/etd>

 Part of the [Analytical Chemistry Commons](#), [Biophysics Commons](#), and the [Cell Biology Commons](#)

Recommended Citation

Syed, Aleem, "Spatial and temporal dynamics of receptor for advanced glycation endproducts, integrins, and actin cytoskeleton as probed with fluorescence-based imaging techniques" (2016). *Graduate Theses and Dissertations*. 16026.
<https://lib.dr.iastate.edu/etd/16026>

This Dissertation is brought to you for free and open access by the Iowa State University Capstones, Theses and Dissertations at Iowa State University Digital Repository. It has been accepted for inclusion in Graduate Theses and Dissertations by an authorized administrator of Iowa State University Digital Repository. For more information, please contact digirep@iastate.edu.

**Spatial and temporal dynamics of receptor for advanced glycation endproducts,
integrins, and actin cytoskeleton as probed with fluorescence-based imaging techniques**

by

Aleem Syed

A dissertation submitted to the graduate faculty
in partial fulfillment of the requirements for the degree of

DOCTOR OF PHILOSOPHY

Major: Analytical Chemistry

Program of Study Committee:
Emily A. Smith, Major Professor
Robert S. Houk
Jacob W. Petrich
Arthur H. Winter
Edward Yu

Iowa State University

Ames, Iowa

2016

Copyright © Aleem Syed, 2016. All rights reserved.

Dedicated to my father Syed Gouse

TABLE OF CONTENTS

	Page
ACKNOWLEDGMENTS	v
ABSTRACT.....	vi
DISSERTATION OVERVIEW.....	viii
CHAPTER 1 GENERAL INTRODUCTION.....	1
CHAPTER 2 LATERAL DIFFUSION AND SIGNALING OF RECEPTOR FOR ADVANCED GLYCATION ENDPRODUCTS: A RECEPTOR INVOLVED IN CHRONIC INFLAMMATION.....	22
2.1. Abstract.....	22
2.2. Introduction.....	23
2.3. Materials and Methods.....	25
2.4. Results and Discussion	29
2.5. Conclusions.....	34
2.6. References.....	35
2.7. Figures and Tables	39
2.8. Supplementary Information	48
CHAPTER 3 LIGAND BINDING AFFINITY AND CHANGES IN THE LATERAL DIFFUSION OF RECEPTOR FOR ADVANCED GLYCATION ENDPRODUCTS	56
3.1. Abstract.....	56
3.2. Introduction.....	56
3.3. Materials and Methods.....	58
3.4. Results and Discussion	62
3.5. Conclusions.....	67
3.6. References.....	69
3.7. Figures and Tables	71
3.8. Supplementary Information	81
CHAPTER 4 THE ROLE OF A CONSERVED MEMBRANE PROXIMAL CYSTEINE IN ALTERING αPS2βPS INTEGRIN DIFFUSION	95
4.1. Abstract.....	95
4.2. Introduction.....	96
4.3. Materials and Methods.....	97
4.4. Results and Discussion	100
4.5. Conclusions.....	103

4.6. References.....	105
4.7. Figures and Tables	107
4.8. Supplementary Information	116
CHAPTER 5 THE NUMBER OF ACCUMULATED PHOTONS AND THE QUALITY OF STIMULATED EMISSION DEPLETION LIFETIME IMAGES.....	117
5.1. Abstract.....	117
5.2. Introduction.....	118
5.3. Materials and Methods.....	120
5.4. Results and Discussion	122
5.5. Conclusions.....	127
5.6. References.....	129
5.7. Figures and Tables	131
CHAPTER 6 GENERAL CONCLUSIONS AND FUTURE WORK	137
APPENDIX A SINGLE PARTICLE TRACKING WITH STEROL MODULATION REVEALS THE CHOLESTEROL-MEDIATED DIFFUSION PROPERTIES OF INTEGRIN RECEPTORS.....	140
APPENDIX B SELF-IMMOLATIVE PHTHALATE ESTERS SENSITIVE TO HYDROGEN PEROXIDE AND LIGHT	168
APPENDIX C BODIPY-DERIVED PHOTOREMOVABLE PROTECTING GROUPS UNMASKED WITH GREEN LIGHT.....	187
APPENDIX D BODIPY-DERIVED PHOTOCAGES CLEAVED WITH RED LIGHT.....	213

ACKNOWLEDGMENTS

The journey presented here wouldn't have been successful without the help from the people through their direct and indirect involvement in paving a path little smoother. First, I would like to thank my supervisor, Emily, for accepting me into her group as a graduate student and for her constant guidance in pointing me in the correct direction. She provided me the support when I needed it the most. I doubt I will have a second thought in my mind when I say I owe my degree to her. She always encouraged independence in research and appreciated new ideas.

Additionally, I would like to thank my POS committee members for their guidance throughout the course of the degree. I also want to thank my collaborators Dr. Winter and Dr. Petrich for providing the opportunity to work on very exciting research problems. I was lucky to work with Pratik P. Goswami, an excellent colleague and a good friend. Special thanks to Joel Nott of protein facility and Bill Halterman of machine shop who went out of their way to help me with my research problems. I thank all Smith group members past and present, especially, Dipak, Mike, Neha, Jon, Deyny, Danny, Chu and Charles for making my stay in the group fun and enjoyable. It was a great pleasure working beside all these kind people.

Finally, I would like to thank my fellow travelers Avipsa, Naresh, Jani, Abhijith, Raghu and Nitin for sharing their wonderful journeys with me. Especially, Avipsa, Abhijith, Raghu, Naresh for providing the care when I needed it the most. Finally, my family, my parents were always an immense source of inspiration and my siblings were the limitless source of love and affection. It is for them what I was and what I am to become...

ABSTRACT

Systematic spatial and temporal fluctuations are a fundamental part of any biological process. For example, lateral diffusion of membrane proteins is one of the key mechanisms in their cellular function. Lateral diffusion governs how membrane proteins interact with intracellular, transmembrane, and extracellular components to achieve their function. Herein, fluorescence-based techniques are used to elucidate the dynamics of receptor for advanced glycation end-products (RAGE) and integrin membrane proteins.

RAGE is a transmembrane protein that is being used as a biomarker for various diseases. RAGE dependent signaling in numerous pathological conditions is well studied. However, RAGE lateral diffusion in the cell membrane is poorly understood. For this purpose, effect of cholesterol, cytoskeleton dynamics, and presence of ligand on RAGE lateral diffusion is investigated. RAGE diffusion in the cell membrane is probed with fluorescence recovery after photobleaching (FRAP) and single particle tracking (SPT). The ensemble diffusion measurement of RAGE with FRAP indicated that RAGE diffuses freely in the cell membrane with a large mobile fraction. Also, a decrease in the mobile fraction is observed when the actin cytoskeleton dynamics are altered with cytoskeletal drugs cytochalasin-D and Jasplakinolide. Further, RAGE signaling is observed to be dependent on an intact actin cytoskeleton in cells. On the other hand, confined diffusion of RAGE is measured when the lateral diffusion is probed one protein at a time with SPT. Methylglyoxal modified-bovine serum albumin (MGO-BSA) is used as a RAGE ligand to study how the presence of ligand affects RAGE lateral diffusion. RAGE's affinity for ligand increases linearly with the net negative surface charge on the MGO-BSA. Although incubation of MGO-BSA with different percent primary amine modification changes the diffusion

properties of RAGE, no correlation is measured in the magnitude of the change in the diffusion properties with the ligand binding affinity and the net negative surface charge. Ligand induced changes are not present when cholesterol is depleted from the cell membrane, indicating that cholesterol plays a role in ligand induced changes on RAGE lateral diffusion. The work advances our understanding of factors that affect RAGE lateral diffusion and signaling and also the connection between RAGE lateral diffusion and signaling.

The effect of a highly conserved membrane proximal cysteine (Cys¹³⁶⁸) residue on the diffusion properties of integrins in *Drosophila* S2 cells is elucidated using FRAP and SPT. Mutating Cys¹³⁶⁸ to Val¹³⁶⁸ altered the lateral diffusion properties of this receptor. Both FRAP and SPT indicate larger mobile population for the Val¹³⁶⁸ integrins compared to wild-type integrins. Tandem mass spectrometry results and protein sequence analysis show that Cys¹³⁶⁸ is a potential palmitoylation or redox post-translational modification site.

Finally, a method for imaging protein distribution and for probing local environment around fluorophore in cells at sub-diffraction spatial resolution is discussed. Stimulated emission depletion coupled with fluorescence lifetime microscopy (STED-FLIM) is used to image the actin cytoskeleton with 40-nm spatial resolution at ambient conditions. The quality of the fluorescence lifetime data is evaluated by time binning the photon data to increase the number of photons in the peak channel of the fluorescence decay curve. STED-FLIM can be used to image the distribution of protein in the cell membrane or STED-FLIM can be coupled with complementary techniques such as fluorescence correlation spectroscopy to obtain the diffusion properties of membrane proteins.

DISSERTATION OVERVIEW

This dissertation is organized in 6 chapters and 4 appendixes. A brief introduction to diffusion in the cell membrane and the fluorescence techniques that are discussed in the subsequent chapters is given in Chapter 1. The work presented in Chapter 2 describes the link between RAGE lateral diffusion and actin cytoskeleton dynamics that is probed with fluorescence recovery after photobleaching. Chapter 3 describes the ligand induced changes in RAGE lateral diffusion measured at the single receptor level using single particle tracking. The effects of highly conserved membrane proximal cysteine on the lateral diffusion of integrin membrane protein are presented in Chapter 4. The implementation of stimulated emission depletion microscopy to perform fluorescence lifetime imaging of Alexa Flour 594 phalloidin bound to the actin cytoskeleton is presented in Chapter 5. General conclusions and possible future directions for the work presented in the previous chapters are summarized in Chapter 6. In Appendix A, the role of cholesterol on lateral diffusion of a integrin membrane proteins is presented. Finally, photocages that are cleaved with far-UV to far-red wavelength light in the cellular environment are presented in Appendix B, C and D.

CHAPTER I

GENERAL INTRODUCTION

A portion of the text from this chapter is to be incorporated in the review “Chemical Imaging in the Cell Membrane” that is in preparation for Annual Review of Analytical Chemistry, 2017 issue

Aleem Syed and Emily A. Smith

Cell Membrane and Membrane Protein Diffusion

Our perception of the cell membrane structure has evolved over time. In the model proposed by Singer and Nicolson in 1972, the cell membrane is assumed to be a two dimensional uniform fluid where membrane proteins diffuse freely (Brownian diffusion) [1]. However, later experiments to simulate the diffusion of membrane proteins in artificial membranes could not describe the motion observed in the cell membrane [2-5]. In fact, the observed diffusion coefficients for membrane protein in the cell membrane are ten to hundred-fold slower than predicted by Singer and Nicolson's model. In revised diffusion models, new types of interactions, such as lipid-lipid, lipid-protein and protein-protein are considered that influence the Brownian diffusion of membrane proteins [5-11]. In 2014, Nicholson updated his original membrane model by adding the newly discovered interactions that govern membrane protein diffusion in the cell membrane [12].

The self-assembly of the lipid bilayer is mainly driven by hydrophobic and van der Waals forces that stabilize the cell membrane [13]. The cell membrane consists of about a hundred types of lipids that are distributed in the outer and inner leaflet [14, 15]. There is an asymmetry that exists between the outer and inner leaflet [16] that leads to formation of membrane domains in the outer leaflet called lipid rafts. These lipid rafts provide a signaling platform for many membrane proteins [17, 18]. Also, specific lipids such as cholesterol and sphingomyelins are concentrated in these lipid rafts. Cholesterol and other lipids recruit specific membrane proteins into these domains for the assembly of signaling complexes by adjusting the local thickness of the bilayer [19-21]. These rafts are believed to be dynamic in nature with

variable sizes ranging from 10-200 nm, and with typical half-lives in the range of 10-20 ms [5, 22, 23]. Lipid rafts limit Brownian diffusion of membrane proteins.

Another type of interaction that limits the Brownian diffusion of membrane proteins is protein-protein interactions in the cell membrane. For example, the well-studied class of membrane proteins, integrins, can be triggered to form protein oligomers by interactions with extracellular matrix or ligand [24-26]. Integrins are an important family of transmembrane proteins that communicate signals across the membrane for survival, growth, proliferation and differentiation of cells [27]. Integrins are composed of non-covalently associated α and β subunits. Upon ligand binding there is a conformational change in the integrins [28]. This conformational change triggers the formation of a signaling complex in the cell membrane. Then the signal is transferred to the intracellular cytoskeleton by membrane associated signaling molecules. This protein-protein interaction leads to the formation of large focal adhesion complexes in the cell membrane [29, 30].

The third added complexity to Singer and Nicholson's membrane model is the membrane associated cytoskeleton. Kusumi et al. have proposed a picket and fence model for the cell membrane, where the cytoskeleton forms corrals in the inner leaflet of the cell membrane [5, 19]. Integral membrane proteins diffuse freely in domains within these fences. Sometimes the protein escapes out of these corrals resulting into a hop-diffusion of membrane proteins. In a study using keratinocytes as a model cell membrane, Kusumi et al. have measured the approximate size of these domains. The typical size of these domains is about 40- to 300 nm and the residence time for membrane proteins in these domains is about 3-30 s [31]. In some cases, membrane proteins are directly or indirectly attached to the membrane associated cytoskeleton resulting in a directed motion of membrane protein.

Jacobson et al. have classified the motion of membrane proteins into four types. They are i) free diffusion with no interactions, ii) constrained diffusion in lipid rafts, iii) hop-diffusion due to cytoskeletal fences and iv) directed motion due to interactions with the cytoskeleton [10]. A cell membrane with some of the factors that influence the lateral mobility of membrane proteins is depicted

in Figure 1.1. As reported by Yeagle, cell membranes are extremely crowded and there may be only few molecules of lipids present between integral membrane proteins [32]. Figure 1.1, as with most figures of membrane structure, for simplicity does not show the true membrane crowding.

Receptor for Advanced Glycation Endproducts (RAGE)

RAGE is a transmembrane protein with a large extracellular domain, a single transmembrane and a short cytoplasmic tail as depicted in Figure 1.2. It belongs to the immunoglobulin (Ig) super family. The extracellular domain of RAGE can be sub-classified as containing a variable (V) and two constant (C1 and C2) Ig type domains. RAGE is a multi-ligand receptor; several RAGE ligands have been identified including advanced glycation endproducts (AGE), S100/Calgranulins family proteins and amyloid beta peptides [33-35]. RAGE and RAGE's ligand are used as a biomarker in several pathological diseases such as chronic inflammation, diabetic complications, neuro degenerative disorders and cancer [35-38]. Upon engagement with its ligands, RAGE is reported to activate various signaling cascades that are used as markers for the activity of RAGE in the pathological conditions [39-42]. Structural analysis of extracellular domains of RAGE indicates that RAGE mainly binds to its ligand through electrostatic interaction between V and C1 domains [43]. The ligand binding domains of RAGE are mainly positively charged as shown in Figure 1.3 [44]. Although ligands for RAGE are structurally diverse, all ligands possess large negative binding domains as shown in Figure 1.3 [44]. Although RAGE signaling has been studied extensively, knowledge pertaining to the molecular diffusion of RAGE is generally unknown.

Fluorescence-Based Imaging Techniques

Despite the limited spatial resolution, optical techniques are still the primary analysis tool for imaging biological samples. Ease of implementation, the minimally invasive nature and selectivity make light-based techniques unparalleled in routine biological research compared to techniques that are capable of

providing atomic spatial resolution (X-ray crystallography, atomic force microscopy, cryo-electron microscopy, transmission electron microscopy and scanning electron microscopy) [45, 46]. Fluorescence microscopy is one such optical technique where the sample is either labeled with a fluorophore molecule or endogenous fluorescence from a specific biological structure is measured. A specific wavelength of light is used to excite the fluorophore to the excited electronic state. Then the excited fluorophore decays back to the ground electronic state by emitting a photon at a longer wavelength that can be detected as a fluorescence signal. A Jablonski diagram for fluorescence is depicted in Figure 1.4. The typical residence time for fluorophore in the excited state is between sub-nanoseconds to few microseconds, this residence time is known as fluorescence lifetime of the fluorophore. The average fluorescence lifetime can be calculated by measuring the time it takes to $1/e$ of the excited population to decay back to the ground electronic state.

There are mainly three types of fluorescence-based techniques to measure the lateral mobility of membrane proteins in the cell membrane. They are i) fluorescence recovery after photobleaching (FRAP), ii) single particle tracking (SPT) and iii) fluorescence correlation spectroscopy (FCS). FRAP and SPT are discussed in this dissertation to measure the lateral diffusion of receptor for advanced glycation endproducts (RAGE) and integrin membrane proteins.

Fluorescence Recovery after Photobleaching (FRAP)

FRAP can be used to measure the ensemble diffusion properties of membrane proteins. In general, a fluorescent protein is genetically fused to the membrane protein of interest. The plasmid containing the sequence for protein of interest fused with a fluorescent protein is transfected in the organism or cell. The targeted protein is expressed with an endogenous fluorescent tag. A high intensity laser pulse is used to bleach a region of few microns width on the cell membrane. Then the fluorescence recovery from the bleached spot is recorded over time as shown in Figure 1.5. The fluorescence recovery from the unbleached region on the membrane is used to normalize the fluorescence recovery curve.

Normalization is essential in order to account for the photobleaching during the recovery period. The

fluorescence recovery over time is fit to the equation $F(t) = \frac{F_0 + F_\infty \left(\frac{t}{\tau}\right)^\alpha}{1 + \left(\frac{t}{\tau}\right)^\alpha}$ derived by Feder et al. [47].

Where $F(t)$ is the fluorescence recovery over time, F_0 is the fluorescence intensity immediately after photobleaching, F_∞ is the maximum fluorescence recovery, τ is the time for 50% fluorescence recovery and α is the time exponent. The mobile fraction can be calculated with the equation $MF (\%) =$

$\left(\frac{F_\infty - F_0}{1 - F_0}\right) \times 100$. The diffusion coefficient is calculated from $D = \frac{\omega^2}{4\tau^\alpha t^{\alpha-1}}$; where ω is the radius of the photobleached spot. The time exponent describes the nature of the diffusion. An α value of 1 represents Brownian diffusion, whereas α less than 1 represents confined diffusion. Generally a range of α between 0.9 to 1.1 is assumed to be Brownian. It is worth noting that the estimated diffusion parameters from FRAP are the ensemble average of few thousand proteins in the cell membrane.

Single Particle Tracking (SPT)

On the other hand, SPT experiments measure the diffusion properties of a single membrane protein at a time [48, 49]. Since the diffusion of protein in the cell membrane is not synchronized across similar membrane proteins, it is essential to measure the protein diffusion one protein at a time in order to account for the diffusion heterogeneity. In a SPT experiment, the fluorescence signal is commonly generated from a single fluorophore bound to the target protein, hence it is necessary that the fluorophore be photostable and bright. As shown in Table 1.1, quantum dots are a good choice as labels for SPT experiments for fast acquisition times and long observation times [50]. Several methods can be used to conjugate the quantum dots to a ligand or antibody that will specifically bind to the receptor. Ligand or antibody can be conjugated by covalent or electrostatic interaction to the quantum dot surface; some of the conjugation strategies are shown in Figure 1.6 [51]. In some cases where a specific ligand is not available for a membrane protein, then external tags (*e.g.* His-tag) are introduced in the

extracellular domains of target membrane protein. An antibody to the tag or a complexing moiety (*e.g.* Ni-NTA for His-tag) is then coated on to the quantum dot surface. The specific binding of quantum dots to the interested protein is a key step in SPT experiments.

Once the specific labeling is achieved, tracking of a single membrane protein on the cell membrane is performed using fast cameras with high sensitivity. A series of images of quantum dot-labeled target protein are acquired over time. An ImageJ plugin developed by Sablarzini et al. is used to extract the trajectories reported in this dissertation for single membrane protein [52]. The extraction of the trajectory begins with localization of the quantum dot in each frame. The localization uncertainty in the SPT experiment can be as good as a few nanometers and depends on the signal-to-noise ratio. The intrinsic blinking of quantum dots is used to identify single quantum dots from aggregates that do not blink. Then the extracted trajectories are further analyzed by the method described by Simons et al. [53]. The trajectory is analyzed over a specific timeframe and the probability (ψ) of a protein diffusing by Brownian motion in the selected timeframe is given by $\log(\psi) = 0.2048 - 2.5117 \times \frac{Dt}{R^2}$ where D ($\mu\text{m}^2/\text{s}$) is the diffusion coefficient, t (s) is the time and R (μm) is the radius of the given region. The computed probability is then converted to a confinement index (L) by a relation $L = \begin{cases} -\log(\psi) - 1 & \psi \leq 0.1 \\ 0 & \psi > 0.1 \end{cases}$. The confinement index plot along the trajectory is used to identify the confined domains in the given trajectory. This method has been implemented in a MATLAB-platform as a graphical user interface where extracted trajectories can be input for the analysis [54].

In order to assign meaning to the confinement index, simulation of Brownian trajectories must be analyzed to establish a threshold. Brownian trajectories are simulated over the range of observed experimental diffusion coefficients and time resolution using MATLAB. The critical confinement value (L_c) and critical confinement time (t_c) are identified for the simulated trajectories. These critical parameters are used to differentiate Brownian and confined diffusion in the experimental data. The regions in the experimental trajectory where the confinement index rises above L_c for longer than t_c are

identified as confined domains. The confined domains are further analyzed for domain size and the duration of confinement. Additionally, for each trajectory, a global diffusion coefficient is also calculated.

Stimulated Emission Depletion Fluorescence Lifetime Imaging (STED-FLIM)

The major drawback of light-based microscopy is the diffraction limit stemming from the wave nature of the light. The light generated from a point-like object cannot be imaged as a point, rather it forms a three dimensional intensity distribution called a point spread function (PSF). A schematic of PSF is shown in Figure 1.7. If two objects are closer than the diffraction limit of the optical system, they cannot be resolved as described by Ernst Abbe. The diffraction limit in the lateral dimensions (or the full-width at half-maximum (FWHM) of the PSF) for an optical system can be approximated by $\approx 0.61\lambda/NA$, where λ is the wavelength of the light and NA is the numerical aperture of the focusing objective. The diffraction limit is 2-3 times larger in the axial dimension [55]. For example, 550-nm wavelength light and optics with a NA of 1.40 result in a PSF with a lateral FWHM of about 200 nm and 500 nm in the axial direction. In recent years, various far-field techniques have been developed to surpass the diffraction limit in fluorescence microscopy. A few examples are stimulated emission depletion (STED) microscopy, stochastic optical reconstruction microscopy, photoactivable and localization microscopy and structured illumination microscopy [56-59]. The potential of these techniques has been appreciated with the Nobel Prize in chemistry for the year 2014 awarded to Eric Betzig, Stefan W. Hell and William E. Moerner for the development of “*super-resolved fluorescence microscopy*”.

STED-based fluorescence microscopy is described in this dissertation for imaging the actin cytoskeleton in the fixed cells. The Jablonski diagram representing relevant STED transitions is given in Figure 1.8. In STED experiment, an excitation pulse is used for exciting a molecule to an electronic excited state from the ground state. Immediately, a depletion pulse shaped in a donut (with zero intensity in the center) is used to deactivate the fluorophore from the lowest vibrational state of the

electronic excited state to some higher vibrational state of the ground electronic state. The wavelength of the depletion beam is a critical parameter in order to avoid re-excitation of the fluorophore with the depletion beam. Since the shape of the depletion beam is a donut with a zero intensity center, molecules at the center of the donut have an opportunity to spontaneously fluoresce, resulting in a narrow effective PSF. The diffraction limit relevant for STED is given by $\approx \lambda / (2NA \times (1 + \frac{I_m}{I_s})^{\frac{1}{2}})$, where I_m is the intensity of the depletion beam and I_s is the saturation intensity (and the other symbols are defined above) [60]. The size of the null at the donut center can be tuned with the intensity of the depletion beam [60]. In theory, molecular-level spatial resolution can be achieved with an intense depletion beam and an extremely photostable fluorophore. For example, the nitrogen vacancy center in diamond are imaged with a spatial resolution of 10 nanometers using STED [61]. As shown in Figure 1.9, sub-diffraction spatial resolution in STED provides a means to probe the heterogeneity present in domains smaller than the diffraction limit, which are otherwise impossible to probe in dense systems using traditional fluorescence microscopy.

The home-built STED apparatus used to generate data presented in this dissertation is shown in Figure 1.10. The complete description of this setup is given by Lesoine et al. [62]. Briefly, a super-continuum laser is split into an excitation beam and a depletion beam using a polarizing beam splitter. An optical delay is used in the depletion beam path to offset the depletion beam arrival on to the sample by ~ 100 ps. The donut profile of the depletion beam is generated using a vortex phase plate. Half-wave plates and quarter-wave plates are used in the beam paths as required to adjust the polarization of the excitation and depletion beams. Spatially expanded depletion and excitation beams are recombined using a dichroic mirror and directed to the sample through a microscope immersion oil objective with a second dichroic mirror. The fluorescence signal is collected by the same objective and guided to a photo-multiplier tube (PMT) detector. To construct a sub-diffraction image the sample is raster scanned over the excitation and depletion beams. The PMT detector is connected to single-photon counter card

that can record the photon arrival times at each pixel. The photon distribution over time can be fit to an exponential decay to extract the fluorescence lifetime of the fluorophore. In addition to intensity images, fluorescence lifetime images can be obtained at sub-diffraction spatial resolution. The fluorescence lifetime is sensitive to changes in the local environment and the structure of the proteins that is labeled with a fluorescent probe. Hence STED coupled with fluorescence lifetime imaging can be used to probe the spatial heterogeneity at sub-diffraction resolution.

References

- [1] S.J. Singer, G.L. Nicolson, The fluid mosaic model of the structure of cell membranes, *Science*, 175 (1972) 720-731.
- [2] J.M. Sanderson, Resolving the kinetics of lipid, protein and peptide diffusion in membranes, *Mol. Membr. Biol.*, 29 (2012) 118-143.
- [3] K. Jacobson, A. Ishihara, R. Inman, Lateral Diffusion of Proteins in Membranes, *Annu. Rev. Physiol.*, 49 (1987) 163-175.
- [4] A. Kusumi, T.K. Fujiwara, R. Chadda, M. Xie, T.A. Tsunoyama, Z. Kalay, R.S. Kasai, K.G.N. Suzuki, Dynamic Organizing Principles of the Plasma Membrane that Regulate Signal Transduction: Commemorating the Fortieth Anniversary of Singer and Nicolson's Fluid-Mosaic Model, *Annu. Rev. Cell Biol.*, 28 (2012) 215-250.
- [5] A. Kusumi, I. Koyama-Honda, K. Suzuki, Molecular Dynamics and Interactions for Creation of Stimulation-Induced Stabilized Rafts from Small Unstable Steady-State Rafts, *Traffic*, 5 (2004) 213-230.
- [6] G.L. Nicolson, Transmembrane control of the receptors on normal and tumor cells, *Biochim. Biophys. Acta (BBA) - Reviews on Biomembranes*, 457 (1976) 57-108.
- [7] A. Kusumi, C. Nakada, K. Ritchie, K. Murase, K. Suzuki, H. Murakoshi, R.S. Kasai, J. Kondo, T. Fujiwara, Paradigm Shift of the Plasma Membrane Concept from the Two-Dimensional Continuum Fluid to the Partitioned Fluid: High-Speed Single-Molecule Tracking of Membrane Molecules, *Annu. Rev. Biophys. Biomol. Struct.*, 34 (2005) 351-378.
- [8] E.J. Luna, A.L. Hitt, Cytoskeleton--plasma membrane interactions, *Science*, 258 (1992) 955-964.
- [9] A. Watts, Membrane structure and dynamics, *Curr. Opin. Cell Biol.*, 1 (1989) 691-700.
- [10] K. Jacobson, E.D. Sheets, R. Simson, Revisiting the fluid mosaic model of membranes, *Science*, 268 (1995) 1441-1442.
- [11] M. Edidin, S.C. Kuo, M.P. Sheetz, Lateral movements of membrane glycoproteins restricted by dynamic cytoplasmic barriers, *Science*, 254 (1991) 1379-1382.
- [12] G.L. Nicolson, The Fluid-Mosaic Model of Membrane Structure: still relevant to understanding the structure, function and dynamics of biological membranes after more than 40 years, *Biochim. Biophys. Acta*, 1838 (2014) 1451-1466.
- [13] S.J. Singer, The Molecular Organization of Membranes, *Annu. Rev. Biochem*, 43 (1974) 805-833.
- [14] P.R. Cullis, B. De Kruijff, Lipid polymorphism and the functional roles of lipids in biological membranes, *Biochim. Biophys. Acta (BBA) - Reviews on Biomembranes*, 559 (1979) 399-420.
- [15] L.A. Bagatolli, J.H. Ipsen, A.C. Simonsen, O.G. Mouritsen, An outlook on organization of lipids in membranes: Searching for a realistic connection with the organization of biological membranes, *Prog. Lipid Res.*, 49 (2010) 378-389.
- [16] M.S. Bretscher, Membrane structure: some general principles, *Science*, 181 (1973) 622-629.
- [17] D.A. Brown, E. London, Functions of lipid rafts in biological membranes, *Annu. Rev. Cell Biol.*, 14 (1998) 111-136.
- [18] A.G. Lee, How lipids affect the activities of integral membrane proteins, *Biochim. Biophys. Acta*, 1666 (2004) 62-87.
- [19] A. Kusumi, K.G.N. Suzuki, R.S. Kasai, K. Ritchie, T.K. Fujiwara, Hierarchical mesoscale domain organization of the plasma membrane, *Trends Biochem. Sci.*, 36 (2011) 604-615.
- [20] T. Gil, M.C. Sabra, J.H. Ipsen, O.G. Mouritsen, Wetting and capillary condensation as means of protein organization in membranes, *Biophys. J.*, 73 (1997) 1728-1741.
- [21] M.S. Bretscher, S. Munro, Cholesterol and the Golgi apparatus, *Science*, 261 (1993) 1280-1281.

- [22] C. Eggeling, C. Ringemann, R. Medda, G. Schwarzmann, K. Sandhoff, S. Polyakova, V.N. Belov, B. Hein, C. von Middendorff, A. Schönle, S.W. Hell, Direct observation of the nanoscale dynamics of membrane lipids in a living cell, *Nature*, 457 (2008) 1159-1162.
- [23] P.J. Quinn, A lipid matrix model of membrane raft structure, *Prog. Lipid Res.*, 49 (2010) 390-406.
- [24] I.D. Campbell, M.J. Humphries, Integrin structure, activation, and interactions, *Cold Spring Harb. Perspect. Biol.*, 3 (2011).
- [25] B. Geiger, A. Bershadsky, Assembly and mechanosensory function of focal contacts, *Curr. Opin. Cell Biol.*, 13 (2001) 584-592.
- [26] B. Geiger, A. Bershadsky, R. Pankov, K.M. Yamada, Transmembrane crosstalk between the extracellular matrix--cytoskeleton crosstalk, *Nat. Rev. Mol. Cell Biol.*, 2 (2001) 793-805.
- [27] W. Cho, Building signaling complexes at the membrane, *Sci. STKE*, 2006 (2006) pe7.
- [28] F.G. Giancotti, E. Ruoslahti, Integrin signaling, *Science*, 285 (1999) 1028-1032.
- [29] B. Geiger, A. Bershadsky, R. Pankov, K.M. Yamada, *Nat. Rev. Mol. Cell Biol.*, 2 (2001) 793-805.
- [30] B. Geiger, A. Bershadsky, Assembly and mechanosensory function of focal contacts, *Curr. Opin. Cell Biol.*, 13 (2001) 584-592.
- [31] A. Kusumi, Y. Sako, M. Yamamoto, Confined lateral diffusion of membrane receptors as studied by single particle tracking (nanovid microscopy). Effects of calcium-induced differentiation in cultured epithelial cells, *Biophys. J.*, 65 (1993) 2021-2040.
- [32] P.L. Yeagle, Lipid regulation of cell membrane structure and function, *FASEB J.*, 3 (1989) 1833-1842.
- [33] E. Leclerc, G. Fritz, S.W. Vetter, C.W. Heizmann, Binding of S100 proteins to RAGE: an update, *Biochim. Biophys. Acta*, 1793 (2009) 993-1007.
- [34] A.M. Schmidt, M. Vianna, M. Gerlach, J. Brett, J. Ryan, J. Kao, C. Esposito, H. Hegarty, W. Hurley, M. Clauss, et al., Isolation and characterization of two binding proteins for advanced glycosylation end products from bovine lung which are present on the endothelial cell surface, *J. Biol. Chem.*, 267 (1992) 14987-14997.
- [35] S.D. Yan, A. Bierhaus, P.P. Nawroth, D.M. Stern, RAGE and Alzheimer's disease: a progression factor for amyloid-beta-induced cellular perturbation?, *J. Alzheimers Dis.*, 16 (2009) 833-843.
- [36] A. Bierhaus, P.P. Nawroth, Multiple levels of regulation determine the role of the receptor for AGE (RAGE) as common soil in inflammation, immune responses and diabetes mellitus and its complications, *Diabetologia*, 52 (2009) 2251-2263.
- [37] C.D. Logsdon, M.K. Fuentes, E.H. Huang, T. Arumugam, RAGE and RAGE ligands in cancer, *Curr. Mol. Med.*, 7 (2007) 777-789.
- [38] M.A. Hofmann, S. Drury, C. Fu, W. Qu, A. Taguchi, Y. Lu, C. Avila, N. Kambham, A. Bierhaus, P. Nawroth, M.F. Neurath, T. Slattey, D. Beach, J. McClary, M. Nagashima, J. Morser, D. Stern, A.M. Schmidt, RAGE mediates a novel proinflammatory axis: a central cell surface receptor for S100/calgranulin polypeptides, *Cell*, 97 (1999) 889-901.
- [39] S. Ghavami, I. Rashedi, B.M. Dattilo, M. Eshraghi, W.J. Chazin, M. Hashemi, S. Wesselborg, C. Kerkhoff, M. Los, S100A8/A9 at low concentration promotes tumor cell growth via RAGE ligation and MAP kinase-dependent pathway, *J. Leukoc. Biol.*, 83 (2008) 1484-1492.
- [40] A. Hermani, B. De Servi, S. Medunjanin, P.A. Tessier, D. Mayer, S100A8 and S100A9 activate MAP kinase and NF-kappaB signaling pathways and trigger translocation of RAGE in human prostate cancer cells, *Exp. Cell Res.*, 312 (2006) 184-197.
- [41] H.J. Huttunen, J. Kuja-Panula, H. Rauvala, Receptor for advanced glycation end products (RAGE) signaling induces CREB-dependent chromogranin expression during neuronal differentiation, *J. Biol. Chem.*, 277 (2002) 38635-38646.
- [42] H.M. Lander, J.M. Tauras, J.S. Ogiste, O. Hori, R.A. Moss, A.M. Schmidt, Activation of the receptor for advanced glycation end products triggers a p21(ras)-dependent mitogen-activated protein kinase pathway regulated by oxidant stress, *J. Biol. Chem.*, 272 (1997) 17810-17814.

- [43] M. Koch, S. Chitayat, B.M. Dattilo, A. Schiefner, J. Diez, W.J. Chazin, G. Fritz, Structural basis for ligand recognition and activation of RAGE, *Structure*, 18 (2010) 1342-1352.
- [44] G. Fritz, RAGE: a single receptor fits multiple ligands, *Trends Biochem. Sci.*, 36 (2011) 625-632.
- [45] J.W. Lichtman, J.A. Conchello, Fluorescence microscopy, *Nat. Methods*, 2 (2005) 910-919.
- [46] B.N. Giepmans, S.R. Adams, M.H. Ellisman, R.Y. Tsien, The fluorescent toolbox for assessing protein location and function, *Science*, 312 (2006) 217-224.
- [47] T.J. Feder, I. Brust-Mascher, J.P. Slattery, B. Baird, W.W. Webb, Constrained diffusion or immobile fraction on cell surfaces: a new interpretation, *Biophys. J.*, 70 (1996) 2767-2773.
- [48] M.J. Saxton, Single-particle tracking: the distribution of diffusion coefficients, *Biophys. J.*, 72 (1997) 1744-1753.
- [49] R.N. Ghosh, W.W. Webb, Automated detection and tracking of individual and clustered cell surface low density lipoprotein receptor molecules, *Biophys. J.*, 66 (1994) 1301-1318.
- [50] M. Dahan, P. Alivisatos, J.W. Parak, Quantum Dots: Inorganic Fluorescent Probes for Single-Molecule Tracking Experiments in Live Cells, in: C. Bräuchle, D.C. Lamb, J. Michaelis (Eds.) *Single Particle Tracking and Single Molecule Energy Transfer*, WILEY-VCH Verlag GmbH & Co. KGaA, Weinheim, 2010, pp. 67-92.
- [51] Y. Xing, Q. Chaudry, C. Shen, K.Y. Kong, H.E. Zhau, L.W. Chung, J.A. Petros, R.M. O'Regan, M.V. Yezhelyev, J.W. Simons, M.D. Wang, S. Nie, Bioconjugated quantum dots for multiplexed and quantitative immunohistochemistry, *Nat. Protoc.*, 2 (2007) 1152-1165.
- [52] I.F. Sbalzarini, P. Koumoutsakos, Feature point tracking and trajectory analysis for video imaging in cell biology, *J. Struct. Biol.*, 151 (2005) 182-195.
- [53] R. Simson, E.D. Sheets, K. Jacobson, Detection of temporary lateral confinement of membrane proteins using single-particle tracking analysis, *Biophys. J.*, 69 (1995) 989-993.
- [54] S.A. Menchon, M.G. Martin, C.G. Dotti, APM_GUI: analyzing particle movement on the cell membrane and determining confinement, *BMC Biophys.*, 5 (2012) 4.
- [55] B. Huang, M. Bates, X. Zhuang, Super-Resolution Fluorescence Microscopy, *Annu. Rev. Biochem.*, 78 (2009) 993-1016.
- [56] S.W. Hell, J. Wichmann, Breaking the diffraction resolution limit by stimulated emission: stimulated-emission-depletion fluorescence microscopy, *Opt. Lett.*, 19 (1994) 780-782.
- [57] T.A. Klar, S.W. Hell, Subdiffraction resolution in far-field fluorescence microscopy, *Opt. Lett.*, 24 (1999) 954-956.
- [58] M.J. Rust, M. Bates, X. Zhuang, Sub-diffraction-limit imaging by stochastic optical reconstruction microscopy (STORM), *Nat. Methods*, 3 (2006) 793-796.
- [59] E. Betzig, G.H. Patterson, R. Sougrat, O.W. Lindwasser, S. Olenych, J.S. Bonifacino, M.W. Davidson, J. Lippincott-Schwartz, H.F. Hess, Imaging intracellular fluorescent proteins at nanometer resolution, *Science*, 313 (2006) 1642-1645.
- [60] G. Vicidomini, G. Moneron, K.Y. Han, V. Westphal, H. Ta, M. Reuss, J. Engelhardt, C. Eggeling, S.W. Hell, Sharper low-power STED nanoscopy by time gating, *Nat. Methods*, 8 (2011) 571-573.
- [61] S. Arroyo-Camejo, M.P. Adam, M. Besbes, J.P. Hugonin, V. Jacques, J.J. Greffet, J.F. Roch, S.W. Hell, F. Treussart, Stimulated emission depletion microscopy resolves individual nitrogen vacancy centers in diamond nanocrystals, *ACS Nano*, 7 (2013) 10912-10919.
- [62] M.D. Lesoine, S. Bose, J.W. Petrich, E.A. Smith, Supercontinuum stimulated emission depletion fluorescence lifetime imaging, *J. Phys. Chem B.*, 116 (2012) 7821-7826.

Figures and Tables

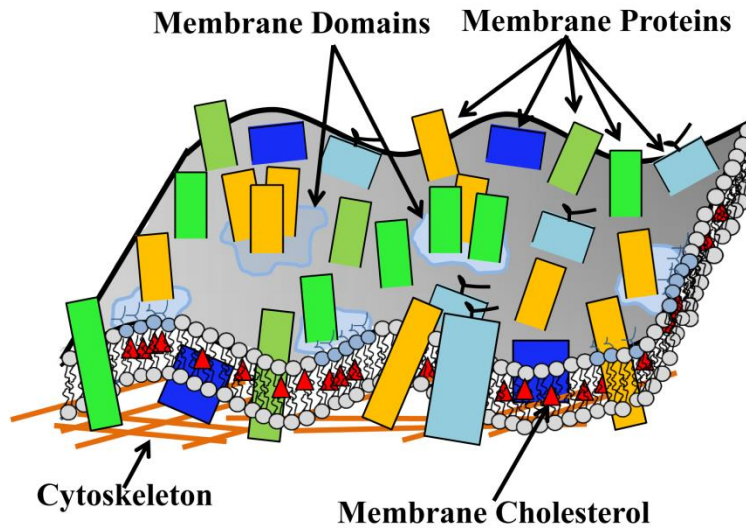


Figure 1.1. Organization of the cell membrane and associated components.

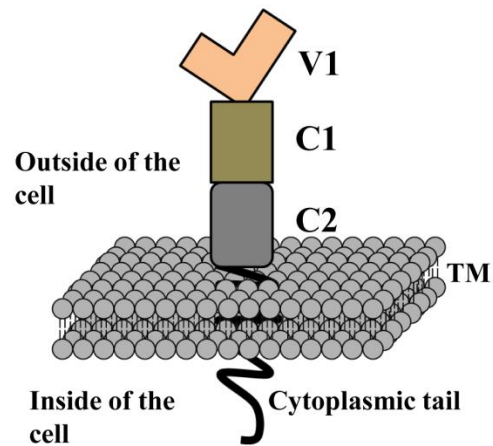


Figure 1.2. Domain structure of receptor for advanced glycation endproducts (RAGE) in the cell membrane. V, C1 and C2 are the extracellular domains of RAGE. TM: transmembrane

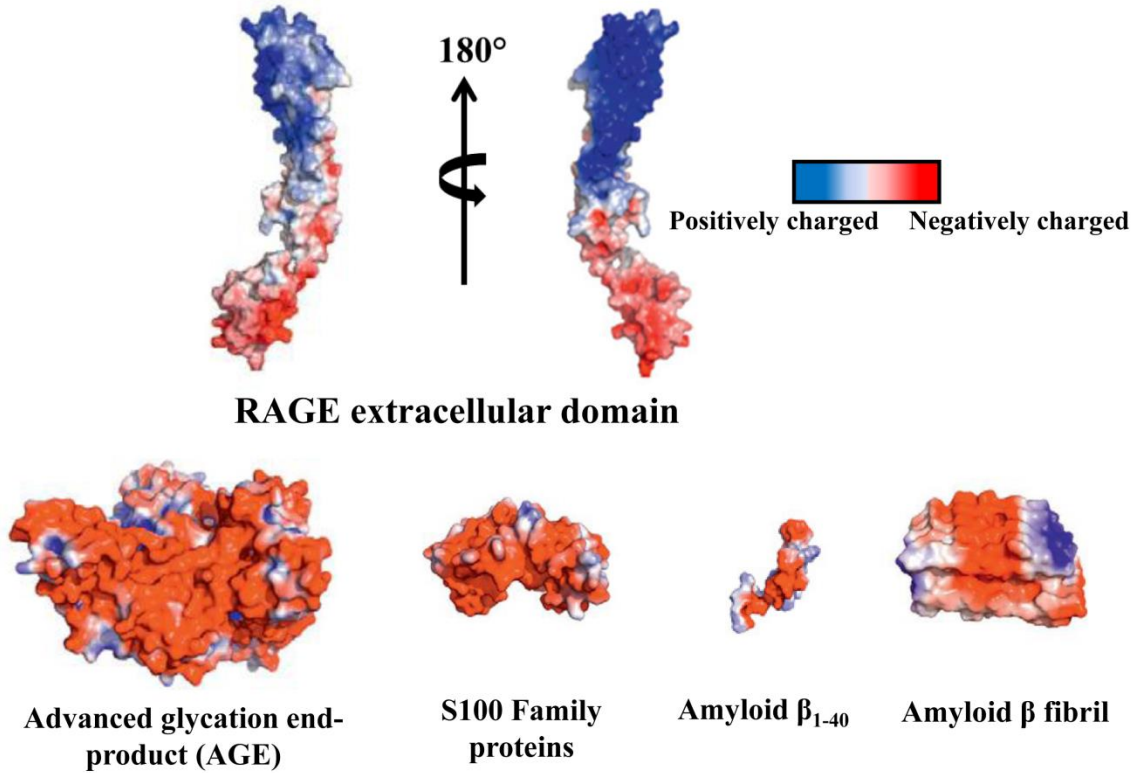
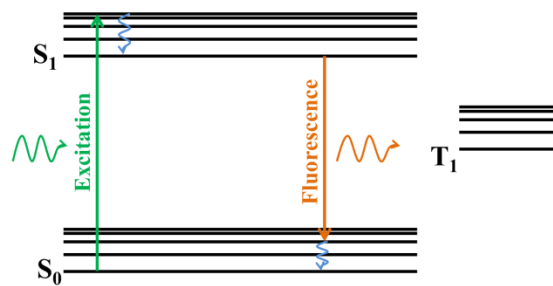


Figure 1.3. Charge density map of the extracellular domain of RAGE and RAGE ligands. The figure is reproduced from reference [41].



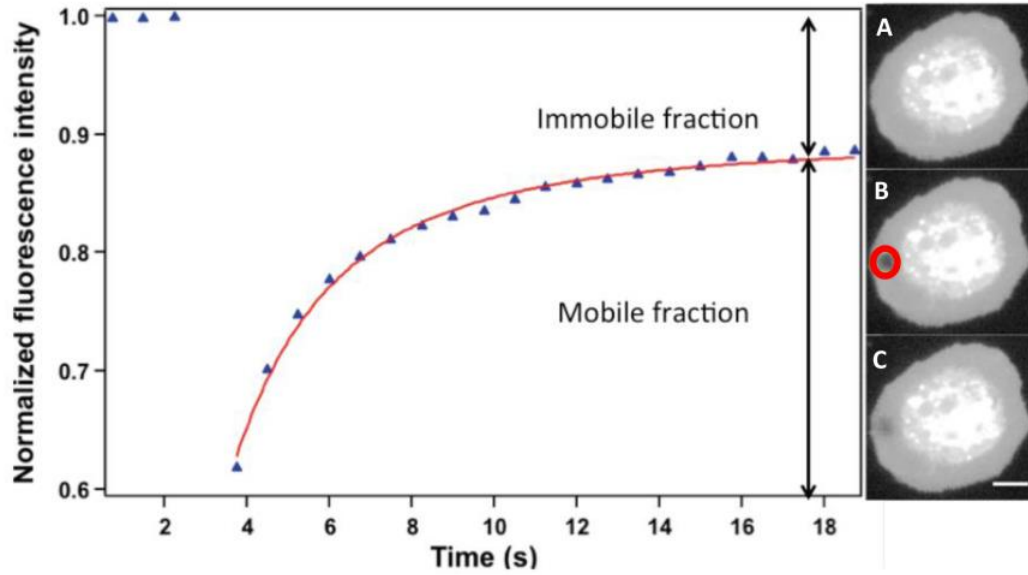


Figure 1.5. Selected images of a cell (right panel) during a FRAP experiment at A) prebleach, B) bleach and C) postbleach events. Scale bar is $5\mu\text{m}$. The resulting fluorescence recovery curve for the fluorescence intensity measured from the bleached region (red circle) is shown in the left panel.

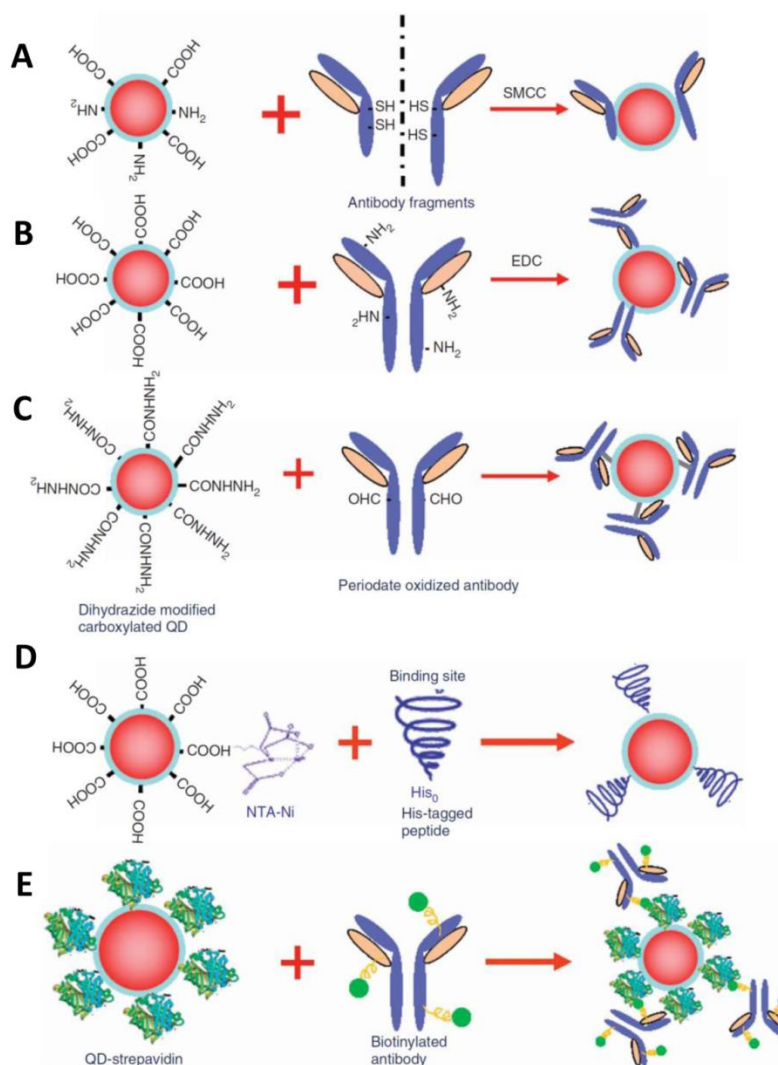


Figure 1.6. Methods for QD-antibody or ligand bioconjugation. (A) The disulphide bonds in antibody are reduced for conjugation with QDs through sulfhydryl-amine coupling, (B) carboxylic acid (-COOH)-coated QDs are covalently attached to primary amine (-NH₂) groups on intact antibody using EDC as a catalyst, (C) covalent site-directed conjugation of antibody to hydrazide-modified QDs, (D) histidine-tagged ligands are conjugated to Ni-NTA modified QDs, (E) biotinylated antibody is non-covalently conjugated to streptavidin-coated QDs. The figure is reproduced from reference [48].

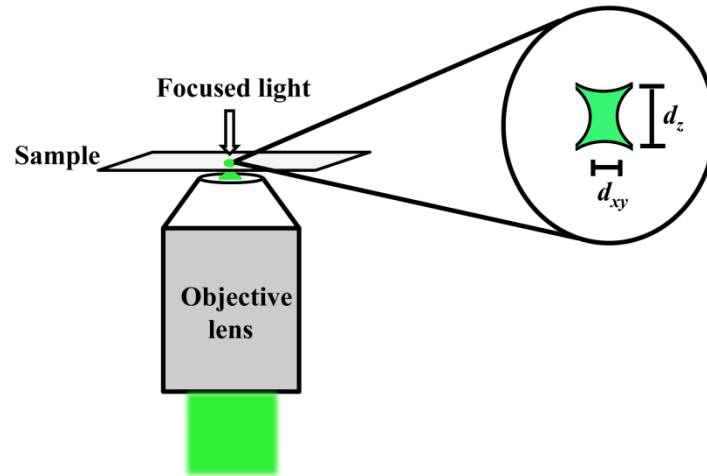


Figure 1.7. Light is focused into a three dimensional point spread function (PSF) through an objective lens on to the sample. The lateral and axial full-width at half-maximums of the PSF are represented with d_{xy} and d_z , respectively.

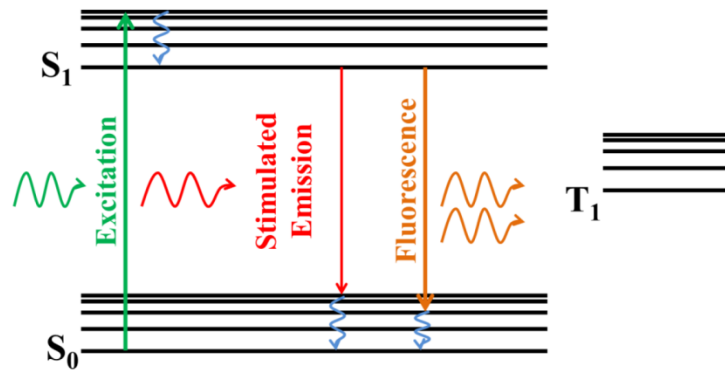


Figure 1.8. Electronic transitions in a typical STED measurement.

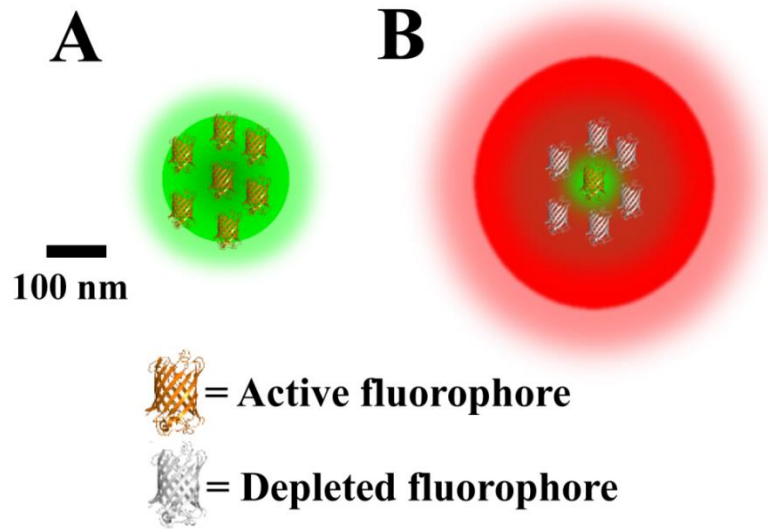
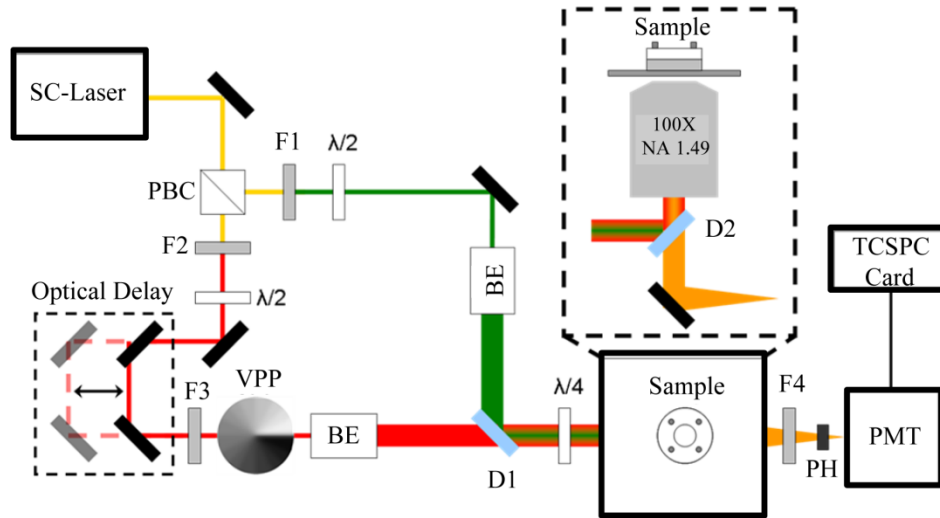


Figure 1.9. Illumination profiles in A) in diffraction limited confocal microscopy, and B) in STED imaging. Fluorophore molecules are not drawn to scale.

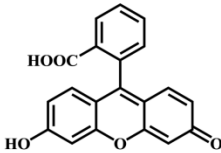
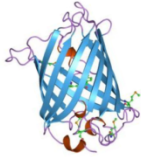
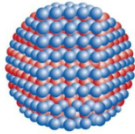


PBC: polarizing beam cube
F1: excitation filter
F2/F3: STED filters
 $\lambda/2$: half wave plate
 $\lambda/4$: quarter wave plate
VPP: vortex phase plate

BE: beam expander
D: dichroic mirror
F4: emission filter
PH: pinhole
PMT: photomultiplier tube
TCSPC: time correlated single photon counting

Figure 1.10. Schematic of a home-built stimulated emission depletion microscope. The figure is reproduced from reference [59].

Table 1.1. Comparison of different fluorescent labels (the table is adapted and modified from reference [47]).

Fluorescent labels	Size (nm)	Photostability (s)	Excitation coefficient ($\times 10^4 \text{ M}^{-1} \text{ cm}^{-1}$)	Structure
Organic fluorophores	~1	1-10	1-20	
Fluorescent proteins	2-4	<1	1-5	
Quantum dots	10-30 (hydrodynamic diameter)	>1000	10-1000	

CHAPTER 2**LATERAL DIFFUSION AND SIGNALING OF RECEPTOR FOR ADVANCED GLYCATION
ENDPRODUCTS (RAGE): A RECEPTOR INVOLVED IN CHRONIC INFLAMMATION**

A paper submitted for publication as a research article

Aleem Syed, Qiaochu Zhu and Emily A. Smith

2.1. Abstract

Membrane diffusion is one of the key mechanisms in the cellular function of receptor proteins. Receptor for advanced glycation end-products (RAGE) signaling has been extensively studied in the context of several pathological conditions, however, very little is known about RAGE diffusion. To fill this gap, RAGE lateral diffusion is probed in native, cholesterol depleted and cytoskeleton altered cellular conditions as well as in the presence of RAGE ligand. In native GM07373 cellular conditions, RAGE mainly follows Brownian diffusion with a large (90%) mobile fraction and an average diffusion coefficient of $0.3 \pm 0.2 \mu\text{m}^2/\text{s}$. Alteration of the actin cytoskeleton dynamics with the small molecules cytochalasin-D (CD) or Jasplakinolide lowered the RAGE mobile fraction by 10% without affecting the RAGE diffusion coefficient or mode of diffusion. There is also a 50% decrease in phosphorylation of extracellular signal-regulated kinase (p-ERK) when the actin cytoskeleton is disrupted by CD in RAGE expressing GM07373 cells. Disrupting the actin cytoskeleton in GM07373 cells that do not express detectable amounts of RAGE results in no change in p-ERK. This suggests there is a connection between RAGE diffusion, RAGE-dependent signaling, and a dynamic actin cytoskeleton. In contrast, there is no statistically significant change in the RAGE mobile fraction, diffusion coefficient or signaling measured with cholesterol depletion from the cells or in the presence of a RAGE ligand. This work serves to further our understanding of the factors influencing RAGE lateral diffusion and the connection between RAGE mobility and signaling.

2.2. Introduction

Lateral diffusion of membrane proteins is often interrelated with their cellular signaling and functions in the cell membrane [1-3]. The receptor for advanced glycation endproducts (RAGE) is a transmembrane protein that belongs to the immunoglobulin (Ig) superfamily. Many RAGE ligands have been identified, including advanced glycation endproducts (AGEs), S100 proteins, high mobility group box 1 (HMGB1), and amyloid- β fibrils [4-8]. RAGE and its signaling are associated with many disease states, including cancer, retinal disease, cardiovascular disease, Alzheimer's disease, respiratory disorders, chronic inflammation and diabetic complications [9-15]. RAGE is reported to activate various signaling cascades, including mitogen-activated protein kinases (MAPKs), Rac/Cdc42 and Janus kinases (JAK)/signal transducers and activator of transcriptions (STATs) and NF- κ B [16-21]. Through these signaling pathways, RAGE influences cell survival, motility and the inflammatory response. Even though RAGE signaling has been studied extensively in different disease states, very little is reported regarding RAGE diffusion in the cell membrane. The goal of the current study is to investigate the lateral diffusion and cellular signaling of RAGE in the endothelial cell membrane and to study the effects of external stimuli such as cholesterol depletion and alterations to the actin cytoskeleton on diffusion.

Cholesterol and the actin cytoskeleton play an important role in the organization of the cell membrane. Functional domains in the cell membrane, known as lipid rafts or lipid nanodomains, contain about 3 to 5-fold excess cholesterol compared to neighboring regions of bilayer [22-25]. These functional domains act as platforms for localization and signaling of many membrane proteins. Altering membrane cholesterol levels has been reported to affect the organization and signaling of a number of receptors [22, 26-30]. The actin cytoskeleton serves as a structural element that can affect the functionality of membrane proteins, including their oligomerization and transmembrane signal transfer [31].

Both cholesterol and the actin cytoskeleton have been reported to play a key role in RAGE functions. For example Reddy et al. showed cholesterol depletion inhibited the S100-induced effects involving RAGE in vascular smooth muscle cells and that intact caveolae are necessary for RAGE signaling [32]. RAGE has also been reported to be part of functional cholesterol-enriched domains in neural endothelial cells [33, 34]. Xiong et al. showed that the actin cytoskeleton played a pivotal role in RAGE-mediated plasma membrane plasticity in a human umbilical vein endothelial cell line [35]. They found that RAGE overexpression reorganizes filamentous actin (F-actin) by increasing β -catenin levels, resulting in inhibition of membrane sealing. Although it is evident that cholesterol and the actin cytoskeleton affect some RAGE functions, possible roles in affecting RAGE lateral diffusion remain unknown.

In this study, we have genetically fused monomeric red fluorescent protein (mRFP) to the C-terminal of RAGE and measured its lateral diffusion using fluorescence recovery after photobleaching (FRAP) in endothelial cells. In FRAP, a small area on the cell membrane is photobleached with a tightly focused laser beam and the fluorescence recovery from diffusion of neighboring fluorescent molecules into the photobleached spot is recorded over time. Several models have been constructed to extract diffusion parameters such as the immobile population, diffusion coefficient and time-dependency of the diffusion [36, 37]. RAGE diffusion at native, cholesterol depleted and altered actin cytoskeleton conditions as well as in the presence of a reported RAGE ligand have been studied. Methyl- β -cyclodextrin (M β CD) was used to deplete cholesterol from the endothelial cells. The actin cytoskeleton was altered using cytoskeletal drugs cytochalasin-D (CD) and Jasplakinolide (Jsp). Finally, cellular signaling was measured by quantifying the phosphorylation in extracellular-signal-regulated kinase (p-ERK) in endothelial cells at native and altered cellular conditions.

2.3. Materials Methods

Cell culture

All experiments were performed using bovine artery GM07373 endothelial cells (Coriell Institute Biorepositories, Camden, NJ). GM07373 cells were grown in complete growth medium consisting of Dulbecco's modified eagle medium (DMEM) (Sigma-Aldrich, St. Louis, MO), 10% fetal bovine serum (FBS) (Irvine Scientific, Santa Ana, CA) and 12.5 mM Streptomycin and 36.5 mM Penicillin (Fisher Scientific, Pittsburgh, PA) in a water-jacketed CO₂ incubator (Thermo Scientific, Waltham, MA). Cells were sub-cultured using 0.25% (w/v) trypsin-EDTA (Life Technology, Carlsbad, CA) solution every two days. All transfected GM07373 cells were established to express respective recombinant proteins stably before any microscopy or molecular biology experiments were performed. Plasmid and transfection details are in the supplementary information.

Western blotting

GM07373 cells expressing RAGE (GM07373-RAGE) or RAGE-mRFP (GM07373-RAGE-mRFP) were cultured to 100% confluence and rinsed with ice cold phosphate buffered saline (PBS). Cells were lysed with RIPA buffer (150 mM sodium chloride, 1.0% NP-40 detergent, 0.5% sodium deoxycholate, 0.1% SDS, 50 mM Tris, pH 8.0) with Halt™ protease inhibitor cocktail (1×, Thermo Scientific, Rockford, IL). After the initial lysis treatment, cells were passed through a 21 gauge needle to ensure complete cell lysis. The protein mixture was first separated on the NuPAGE® Novex® 4-12% Bis-Tris protein gel (Life Technology, Eugene, OR) and then electro blotted onto Immun-Blot® LF PVDF membrane (Bio-Rad, Hercules, CA) as described previously [38, 39]. The PVDF membrane was probed following the manufacturer's protocol (Bio-Rad). Antibodies used for probing were: anti-RAGE rabbit (H-300, Santa Cruz Biotechnology), anti-RFP rabbit (Life Technology), anti-Vinculin goat (sc-7649, Santa Cruz Biotechnology), anti-Actin rabbit (sc-1616-R, Santa Cruz Biotechnology), anti-p-ERK rabbit (Tyr 204, sc-101761, Santa Cruz Biotechnology). Fluorescence from the labeled secondary

antibody was measured on a Typhoon FLA 9500 variable mode laser scanner (GE Healthcare, Waukesha, WI). The vinculin protein band was used as a loading control in all Western blot experiments. Protein sequences were analyzed by mass spectrometry as reported in the supplemental information.

FRAP sample preparation

Sterile glass bottom culture dishes were made by attaching a cover glass (22mm × 22mm, No. 1.5, Corning Inc., Corning, NY) to the bottom of a polystyrene petri dish (35mm × 10mm, Fisher Scientific) containing a pre-drilled 3/4 inch diameter hole as described previously [40]. GM07373-RAGE or GM07373-RAGE-mRFP cells were sub-cultured onto the culture dishes two days before the experiment. Cells were either used without further treatment or treated with M β CD (Sigma-Aldrich, 5mM, in serum free DMEM for 30 minutes) to deplete the cholesterol or with CD (Sigma-Aldrich, 10 μ M, in serum free DMEM for 60 minutes) or with Jsp (Santa Cruz Biotechnology, 3 μ M, in serum free DMEM for 30 minutes) to alter the actin cytoskeleton before the FRAP experiments [29, 41, 42]. For measurements of the diffusion of a lipid mimic, GM07373 and GM07373-RAGE cells were stained with lipophilic dye DiI (Invitrogen, Eugene, OR, 1mM, in serum free DMEM for 30 minutes) before the FRAP experiments.

FRAP microscopy

All FRAP experiments were performed on a Nikon Eclipse TE2000U inverted microscope (Nikon, Melville, NY) which was equipped with an oil-immersion objective (100 \times , Apo TIRF, 1.49 numerical aperture). The microscope was housed in a home built 0.9 \times 0.6 \times 0.5 m³ Plexiglas box containing a heat source to maintain a 36 \pm 2 $^{\circ}$ C temperature at the sample throughout the experiment. Fluorescence was excited with a mercury lamp (X-cite 120 PC, EXFO Photonic Solutions Inc., Mississauga, Ontario, Canada) operating at 25% of the power and an excitation filter (HQ545/30x, Chroma Technology Corp.,

Bellows Falls, VT). The resulting fluorescence emission was collected through an emission filter (HQ620/60x, Chroma Technology Corp.). For photobleaching a region of the cell membrane, a 488-nm laser was directed to the sample with a dichroic mirror (Q495lp, Chroma Technology Corp.). The laser power and photobleaching spot diameter at the sample were 10 mW and 4.8 μm , respectively. A LabView program (National Instruments, Austin, TX) was developed to control a shutter (Thorlabs, Jessup, MD) in the laser path. The photobleaching time was 2 msec. Fluorescence images were recorded using a PhotonMAX 512B EMCCD camera (Princeton Instruments, Trenton, NJ) and Winview (Photometric, Tucson, AZ) image acquisition software. Ten pre-photobleach and 100 post-photobleach images were collected with a time resolution of 410 ms per image. Data collection was completed within 1 h after adding imaging medium (pH=7.2, 155 mM NaCl, 5 mM KCl, 2 mM CaCl₂, 1 mM MgCl₂, 2 mM NaH₂PO₄, 10 mM HEPES and 10 mM Glucose) to the cells.

FRAP data analysis

The fluorescence images collected pre-photobleach and post-photobleach were analyzed with ImageJ (version 1.48, National Institutes of Health) software. The fluorescence intensity from three regions of interest (ROIs) was extracted for each image in the series of 110 images. The ROIs were classified as the photobleached region (an area on the plasma membrane illuminated by the laser spot), the non-photobleached region (an area on the plasma membrane away from the photobleached region), and the background (an area where there was no cell present in the field of view). Fluorescence recovery curves were constructed with a three-step process: (i) the background intensity was subtracted from fluorescence intensities in the photobleached ROI, the resulting curves were normalized with the fluorescence intensities from (ii) the non-photobleached ROI and (iii) the average pre-photobleached intensity from the subsequently photobleached region to account for the lamp intensity fluctuations as well as photobleaching during the image acquisition period as described by Phair *et al.* [43].

Fluorescence recovery curves were analyzed and the results were averaged over 9 to 13 cells for each data set. Mobile fractions (MF) were calculated using equation 1.

$$MF = \frac{F_{\infty} - F_0}{F^0 - F_0} \times 100 \quad (1)$$

Where F_0 is the intensity immediately after photobleaching, F^0 is the pre-photobleaching intensity and F_{∞} is the final intensity (i.e., in image 110), where all fluorescence intensities refer to the values from the fluorescence recovery curves. Each fluorescence recovery curve was further fit to equation 2 using IGOR Pro V 6.32A (WaveMetrics Inc., Lake Oswego, OR) to measure the time dependency of the fluorescence recovery as well as diffusion coefficients [36].

$$F(t) = \frac{F_0 + F_{\infty} \left(\frac{t}{\tau}\right)^{\alpha}}{1 + \left(\frac{t}{\tau}\right)^{\alpha}} \quad (2)$$

Where $F(t)$ is the fluorescence intensity at time t , α is the time exponent and τ is time for 50% fluorescence recovery. Diffusion coefficients were calculated using equation 3.

$$D(t) = \frac{\omega^2}{4\tau\alpha t^{(\alpha-1)}} \quad (3)$$

Where $D(t)$ is the diffusion coefficient at time t and ω is the radius of the photobleaching spot. The statistical significance of all reported data sets was measured using the student's-t test.

Actin cytoskeleton staining

Cells were sub-cultured onto glass-bottom petri dishes and allowed to spread in the incubator for two days before the experiment. Cells were treated as described above with 5 mM M β CD, 10 μ M CD, or 3 μ M Jsp before the actin cytoskeleton was stained for fluorescence imaging. The staining protocol was described previously [44]. Briefly, cells were fixed with 4% (w/v) paraformaldehyde in PBS for 10 minutes. Triton X-100 (0.1% (v/v) in PBS) was used for cell membrane permeabilization. Blocking was performed using bovine serum albumin (1% (w/v) in PBS) for 5 minutes. Cells were further incubated

with Atto 647N conjugated phalloidin (Sigma-Aldrich) to stain the F-actin overnight at 4 °C. Stained cells were rinsed with imaging medium before imaging using the Nikon Eclipse TE2000U inverted microscope described above. The actin cytoskeleton was further quantified to measure the alignment in the actin fibers. Anisotropy was calculated using an ImageJ plugin, FibrilTool, as described previously [45]. Calculated anisotropy values were in the range from 1 to 0, a value of 1 represents perfect alignment in the fibers and value of 0 represents no (i.e., random) alignment in the fibers.

Bovine serum albumin (BSA)-AGE preparation and quantification

BSA-AGE was made by incubating 50 mg/mL BSA (Sigma-Aldrich) and 100 mM methylglyoxal (Sigma-Aldrich) in PBS at 37 °C for 5 days. Glycation of amine functional groups on amino acid residues in BSA with methylglyoxal was quantified by measuring the free amine content using ortho-phthaldialdehyde assay as previously described [46].

2.4. Results and Discussion

Characterization of RAGE and RAGE fused to mRFP (RAGE-mRFP) expression

The primary goal of this study is to probe the lateral diffusion of RAGE in the GM07373 cell membrane to characterize the role of the actin cytoskeletal and membrane organization in altering RAGE diffusion. To achieve this goal, plasmids were transfected into GM07373 cells to stably express full-length RAGE or RAGE-mRFP. RAGE or RAGE-mRFP expression was confirmed by Western blot analysis of cell lysates as shown in Figure 2.1. A protein band corresponding to RAGE at ~55 kDa was observed in the GM07373-RAGE cell lysate (lane B, Figure 2.1) but not in the GM07373 cell lysate (lane A, Figure 2.1). Surprisingly, the GM07373-RAGE-mRFP cell lysate (lane C, Figure 2.1) showed three bands in the 60 to 80 kDa molecular weight range after probing the membrane with the RAGE primary antibody. The RAGE-mRFP protein is expected to show a single band at ~80 kDa. Mass spectrometry analysis was positive for RAGE peptides for bands 1 to 4. One possible explanation for the observed multiple bands

in lane C may be the result of proteolytic cleavage of the fused fluorescent protein during translation, maturation or analysis. Similar findings were reported previously for another red fluorescent protein variant which showed molecular weights corresponding to an intact and two fragmented sequences [47].

In order to identify the reason for three RAGE-positive bands in the Western blot of the GM07373-RAGE-mRFP cell lysate, which may influence the fluorescence measurements, the PVDF membrane was probed with a polyclonal antibody to mRFP. Only a single band was observed (band 5, Figure 2.1) near the molecular weight of band 4. The lack of a band near the molecular weight of band 2 or 3 when the membrane is probed with the mRFP antibody suggests these bands lack the binding epitopes and do not contain the full mRFP sequence. It was confirmed by fluorescence imaging of the PVDF membrane that these bands do not produce a fluorescent species, and do not contribute to the fluorescence microscopy results reported below.

Phosphorylation in extracellular-signal-regulated kinase (p-ERK) is used as a marker for downstream RAGE signaling [48, 49]. There was a low but detectable p-ERK expression in GM07373 cells, and a two-fold increase with RAGE expression in GM07373 cells (Figure 2.2). RAGE-mRFP expression generates the same level of p-ERK expression as RAGE lacking the fluorescent protein fusion (Figure S2.1). This demonstrates that the exogenous expression of RAGE or RAGE-mRFP does generate ERK signaling in GM07373 cells.

RAGE-mRFP exhibits Brownian diffusion in the native GM07373 cell membrane with a high mobile fraction

FRAP experiments on GM07373 cells expressing RAGE-mRFP were performed and the average recovery curve from 10 cells is shown in supporting information (Figure S2.2). Each replicate curve was individually fit to the time-dependent diffusion model with an immobile fraction (i.e., all parameters α , F_0 , F_∞ and τ in equation 2 were allowed to vary) as described by Feder et al. [36]. The time exponent (α) from the fit parameters provides information on the nature of the mode of diffusion. An α value that

equals 1 indicates time-independent Brownian diffusion, whereas a value less than 1 indicates time-dependent diffusion. The average α value measured for RAGE-mRFP is 1.0 ± 0.2 indicating that RAGE exhibits Brownian diffusion in the GM07373 cell membrane (Table 2.1). The average mobile fraction was 90% and the average diffusion coefficient was $0.3 \pm 0.2 \mu\text{m}^2/\text{s}$ for RAGE-mRFP at native cellular conditions. Similar to the RAGE diffusion properties reported here, other membrane proteins such as histocompatibility complex class II, Acetylcholine receptor, and vesicle-associated membrane protein have also been found to exhibit Brownian diffusion with a large mobile fraction [50-54]. While the average diffusion of RAGE-mRFP is Brownian, it may be possible that there are rare populations of RAGE-mRFP with confined diffusion characteristics that are not detectable with the ensemble FRAP method.

Alterations to the F-actin cytoskeleton decrease the RAGE-mRFP mobile fraction but cholesterol depletion and ligand incubation have a minimal effect on the RAGE-mRFP diffusion properties measured by FRAP

To study the possible effect of the actin cytoskeleton on RAGE lateral diffusion, the actin cytoskeleton was altered with two drugs, CD and Jsp. CD depolymerizes the filamentous actin cytoskeleton and prevents re-polymerization by tightly binding to actin monomers [55]. Jsp tightly binds with filamentous actin and inhibits de-polymerization [56]. Atto 647N conjugated phalloidin was used to measure the effect of CD and Jsp on the actin cytoskeleton in GM07373-RAGE cells as shown in Figure 2.3. In the native GM07373 cells, the actin cytoskeleton staining generated partially aligned fibers with a well-defined cell boundary as shown in Figure 2.3a. After the CD treatment, the actin structure was significantly altered and no clear cell boundary was observed (Figure 2.3c). Jsp binds to the actin cytoskeleton in competition with the Atto 647N conjugated phalloidin [57]. Hence, actin cytoskeleton staining was diminished with Atto647N conjugated phalloidin staining for Jsp treated cells (Fig. 2.3d),

which suggests that the Jsp treatment was successful. There was no change in the actin expression as measured from Western blot analysis of the cell lysate treated with CD or Jsp (Figure 2.4 and S2.3).

RAGE-mRFP diffusion parameters were measured for CD or Jsp treated cells. The RAGE-mRFP mobile fraction was decreased by 10% when the actin cytoskeleton was altered with either CD or Jsp (Table 2.1). However, the diffusion coefficient and mode of diffusion were not significantly different when the actin cytoskeleton was altered with CD or Jsp. Even though the mechanism of altering the actin polymerization is different for CD and Jsp treatments, similar effects were observed on the diffusion behavior of RAGE-mRFP in the cell membrane with both treatments. This suggests that a dynamic actin structure is necessary for increasing the mobile fraction of RAGE. No change to the lipid mobile fraction probed with the DiI lipid mimetic was measured after CD or Jsp treatment (Table 2.2), indicating the decreased RAGE mobile fraction after these treatments is not the result of a more mobile lipid fraction. Similarly, there is a statistically significant 38% and 50% decrease in the lipid diffusion coefficient after CD and Jsp treatment (Table 2.2 and Figure S2.4), respectively, while there is no change to the RAGE diffusion coefficient measured after these treatments.

To understand if the decreased RAGE mobile fraction associated with CD and Jsp treatments is also associated with altered RAGE downstream signaling, phosphorylation in ERK (p-ERK) is measured in both GM07373 and GM07373-RAGE cells. p-ERK was decreased by 52% when the actin cytoskeleton was disrupted with CD in GM07373-RAGE cells (Figure 2.5). There was no statistically significant change in p-ERK observed in GM07373-RAGE cells with Jsp treatment or in GM07373 cells lacking detectable RAGE expression after CD or Jsp treatment (Figure S2.5). These observations indicate that actin disruption with CD plays a role in RAGE mobility and this correlates with reduced RAGE downstream signaling. It appears inconsistent that Jsp decreases the RAGE mobile fraction similar to CD, but Jsp does not alter downstream RAGE signaling measured by p-ERK. It is possible, however, that there are distinct mechanisms by which the RAGE mobile fraction is decreased with CD

and Jsp treatments, and the actin depolymerization associated with CD treatment is necessary for reduced p-ERK levels since Jsp treatment prevents depolymerization.

To investigate the effect of cholesterol on the lateral diffusion of RAGE-mRFP, cholesterol was depleted using M β CD. The total free cholesterol was depleted by 45% and no statistically significant change in the endogenous cholesterol ester was observed when cells were incubated with 5 mM M β CD as measured by Amplex[®] Red cholesterol quantification assay (Figure 2.6). There was a 38% decrease in the lipid diffusion coefficient with cholesterol depletion (Table 2.2 and Figure S2.4), however, the diffusion parameters remained unchanged for RAGE-mRFP (Table 2.1). There is also no change in p-ERK measured after cholesterol depletion from the GM07373 or GM07373-RAGE cells (Figure 2.6 and S2.6). Although no change in the actin expression was observed with cholesterol depletion, interestingly, a significant 40% decrease in the actin fiber alignment (anisotropy) with cholesterol depletion was observed in the GM07373 and GM07373-RAGE cell lines as shown in Figure 2.3b and Table 2.3. These observations indicate that cholesterol depletion affects the actin cytoskeleton organization. It has been previously reported that a change in membrane cholesterol not only affects the cell membrane structure but also has a global effect, including reorganization of the actin structure [58]. The cholesterol-depletion-induced changes to the actin cytoskeleton organization are not associated with changes in RAGE diffusion.

Finally, a possible role for ligand binding in altering RAGE diffusion was measured. A ligand for RAGE is termed the advanced glycation endproducts (AGE), which can be synthetically produced by bovine serum albumin (BSA) incubation with methylglyoxal (BSA-AGE). p-ERK increased by 38% and 25% after 5 mg/mL BSA-AGE incubation with GM07373 and GM07373-RAGE cells, respectively (Figure 2.2). While the increase in p-ERK in GM07373 cells after BSA-AGE incubation may be the result of low levels of endogenous RAGE that were not detected by Western blot (lane A, Figure 2.1), it is likely that other signaling pathways that do not involve RAGE are the primary reason for increased p-ERK in this case. AGE ligands are reported to interact with other cell surface receptors besides RAGE

[59]. Consistent with the lack of a definitive RAGE-induced increase in p-ERK signaling after BSA-AGE incubation, there is also no change in the RAGE diffusion properties after incubation with the BSA-AGE ligand (data not shown). Given the chemical and biological complexity of RAGE ligands, further work to elucidate possible effects of ligand binding on RAGE diffusion is warranted.

2.5. Conclusions

RAGE-mRFP diffuses freely in the cell membrane with a large mobile fraction at native GM07373 cellular conditions. The polymerization and depolymerization dynamics of the actin cytoskeleton play a role in increasing the RAGE mobile fraction, although only the depolymerizing CD treatment showed a RAGE-dependent change in p-ERK signaling. Even though there is a significant change in the actin cytoskeleton structure, cholesterol depletion has no effect on RAGE lateral diffusion measured by FRAP or signaling measured by p-ERK. Preliminary data support the notion that ligand binding also has no effect on the ensemble RAGE diffusion parameters measured by FRAP. The combined data point to an important role for actin dynamics in the diffusing population of RAGE.

Acknowledgements

This work was supported by the National Science Foundation (CHE-1412084). The authors thank Joel Nott of the protein facility at Iowa State University for help with mass spectrometry, and Dipak Mainali and Chamari Wijesoorya for their assistance with cell culture.

2.6. References

- [1] D. Axelrod, Lateral motion of membrane proteins and biological function, *J. Membr. Biol.*, 75 (1983) 1-10.
- [2] P. Ronchi, S. Colombo, M. Francolini, N. Borgese, Transmembrane domain-dependent partitioning of membrane proteins within the endoplasmic reticulum, *J. Cell Biol.*, 181 (2008) 105-118.
- [3] S. Ganguly, T.J. Pucadyil, A. Chattopadhyay, Actin cytoskeleton-dependent dynamics of the human serotonin1A receptor correlates with receptor signaling, *Biophys. J.*, 95 (2008) 451-463.
- [4] A. Taguchi, D.C. Blood, G. del Toro, A. Canet, D.C. Lee, W. Qu, N. Tanji, Y. Lu, E. Lalla, C. Fu, M.A. Hofmann, T. Kislinger, M. Ingram, A. Lu, H. Tanaka, O. Hori, S. Ogawa, D.M. Stern, A.M. Schmidt, Blockade of RAGE-amphoterin signalling suppresses tumour growth and metastases, *Nature*, 405 (2000) 354-360.
- [5] A.M. Schmidt, M. Vianna, M. Gerlach, J. Brett, J. Ryan, J. Kao, C. Esposito, H. Hegarty, W. Hurley, M. Clauss, et al., Isolation and characterization of two binding proteins for advanced glycosylation end products from bovine lung which are present on the endothelial cell surface, *J. Biol. Chem.*, 267 (1992) 14987-14997.
- [6] E. Leclerc, G. Fritz, S.W. Vetter, C.W. Heizmann, Binding of S100 proteins to RAGE: an update, *Biochim. Biophys. Acta*, 1793 (2009) 993-1007.
- [7] S.D. Yan, X. Chen, J. Fu, M. Chen, H. Zhu, A. Roher, T. Slattery, L. Zhao, M. Nagashima, J. Morser, A. Migheli, P. Nawroth, D. Stern, A.M. Schmidt, RAGE and amyloid-beta peptide neurotoxicity in Alzheimer's disease, *Nature*, 382 (1996) 685-691.
- [8] M. Koch, S. Chitayat, B.M. Dattilo, A. Schiefner, J. Diez, W.J. Chazin, G. Fritz, Structural basis for ligand recognition and activation of RAGE, *Structure*, 18 (2010) 1342-1352.
- [9] C.D. Logsdon, M.K. Fuentes, E.H. Huang, T. Arumugam, RAGE and RAGE ligands in cancer, *Curr. Mol. Med.*, 7 (2007) 777-789.
- [10] G.R. Barile, A.M. Schmidt, RAGE and its ligands in retinal disease, *Curr. Mol. Med.*, 7 (2007) 758-765.
- [11] G. Basta, Receptor for advanced glycation endproducts and atherosclerosis: From basic mechanisms to clinical implications, *Atherosclerosis*, 196 (2008) 9-21.
- [12] S.D. Yan, A. Bierhaus, P.P. Nawroth, D.M. Stern, RAGE and Alzheimer's disease: a progression factor for amyloid-beta-induced cellular perturbation?, *J. Alzheimers Dis.*, 16 (2009) 833-843.
- [13] R. Briot, J.A. Frank, T. Uchida, J.W. Lee, C.S. Calfee, M.A. Matthay, Elevated levels of the receptor for advanced glycation end products, a marker of alveolar epithelial type I cell injury, predict impaired alveolar fluid clearance in isolated perfused human lungs, *Chest*, 135 (2009) 269-275.
- [14] M.A. Hofmann, S. Drury, C. Fu, W. Qu, A. Taguchi, Y. Lu, C. Avila, N. Kambham, A. Bierhaus, P. Nawroth, M.F. Neurath, T. Slattery, D. Beach, J. McClary, M. Nagashima, J. Morser, D. Stern, A.M. Schmidt, RAGE mediates a novel proinflammatory axis: a central cell surface receptor for S100/calgranulin polypeptides, *Cell*, 97 (1999) 889-901.
- [15] A. Bierhaus, P.P. Nawroth, Multiple levels of regulation determine the role of the receptor for AGE (RAGE) as common soil in inflammation, immune responses and diabetes mellitus and its complications, *Diabetologia*, 52 (2009) 2251-2263.
- [16] H.M. Lander, J.M. Tauras, J.S. Ogiste, O. Hori, R.A. Moss, A.M. Schmidt, Activation of the receptor for advanced glycation end products triggers a p21(ras)-dependent mitogen-activated protein kinase pathway regulated by oxidant stress, *J. Biol. Chem.*, 272 (1997) 17810-17814.
- [17] H.J. Huttunen, C. Fages, H. Rauvala, Receptor for advanced glycation end products (RAGE)-mediated neurite outgrowth and activation of NF-kappaB require the cytoplasmic domain of the receptor but different downstream signaling pathways, *J. Biol. Chem.*, 274 (1999) 19919-19924.

- [18] A. Hermani, B. De Servi, S. Medunjanin, P.A. Tessier, D. Mayer, S100A8 and S100A9 activate MAP kinase and NF-kappaB signaling pathways and trigger translocation of RAGE in human prostate cancer cells, *Exp. Cell. Res.*, 312 (2006) 184-197.
- [19] C.H. Yeh, L. Sturgis, J. Haidacher, X.N. Zhang, S.J. Sherwood, R.J. Bjerkce, O. Juhasz, M.T. Crow, R.G. Tilton, L. Denner, Requirement for p38 and p44/p42 mitogen-activated protein kinases in RAGE-mediated nuclear factor-kappaB transcriptional activation and cytokine secretion, *Diabetes*, 50 (2001) 1495-1504.
- [20] L. Wang, S. Li, F.B. Jungalwala, Receptor for advanced glycation end products (RAGE) mediates neuronal differentiation and neurite outgrowth, *J. Neurosci. Res.*, 86 (2008) 1254-1266.
- [21] S. Ghavami, I. Rashedi, B.M. Dattilo, M. Eshraghi, W.J. Chazin, M. Hashemi, S. Wesselborg, C. Kerkhoff, M. Los, S100A8/A9 at low concentration promotes tumor cell growth via RAGE ligation and MAP kinase-dependent pathway, *J. Leukoc. Biol.*, 83 (2008) 1484-1492.
- [22] L.J. Pike, Lipid rafts: bringing order to chaos, *J. Lipid Res.*, 44 (2003) 655-667.
- [23] D. Lingwood, K. Simons, Lipid rafts as a membrane-organizing principle, *Science*, 327 (2010) 46-50.
- [24] K. Simons, M.J. Gerl, Revitalizing membrane rafts: new tools and insights, *Nat. Rev. Mol. Cell Biol.*, 11 (2010) 688-699.
- [25] J. Ando, M. Kinoshita, J. Cui, H. Yamakoshi, K. Dodo, K. Fujita, M. Murata, M. Sodeoka, Sphingomyelin distribution in lipid rafts of artificial monolayer membranes visualized by Raman microscopy, *Proc. Natl. Acad. Sci. U.S.A.*, 112 (2015) 4558-4563.
- [26] E.M. Adkins, D.J. Samuvel, J.U. Fog, J. Eriksen, L.D. Jayanthi, C.B. Vaegter, S. Ramamoorthy, U. Gether, Membrane mobility and microdomain association of the dopamine transporter studied with fluorescence correlation spectroscopy and fluorescence recovery after photobleaching, *Biochemistry*, 46 (2007) 10484-10497.
- [27] N. Bag, S. Huang, T. Wohland, Plasma Membrane Organization of Epidermal Growth Factor Receptor in Resting and Ligand-Bound States, *Biophys. J.*, 109 (2015) 1925-1936.
- [28] D.A. Brown, E. London, Functions of lipid rafts in biological membranes, *Annu. Rev. Cell Biol.*, 14 (1998) 111-136.
- [29] N. Arora, A. Syed, S. Sander, E.A. Smith, Single particle tracking with sterol modulation reveals the cholesterol-mediated diffusion properties of integrin receptors, *Phys. Biol.*, 11 (2014) 066001.
- [30] T.J. Pucadyil, A. Chattopadhyay, Role of cholesterol in the function and organization of G-protein coupled receptors, *Prog. Lipid Res.*, 45 (2006) 295-333.
- [31] A. Kusumi, K.G. Suzuki, R.S. Kasai, K. Ritchie, T.K. Fujiwara, Hierarchical mesoscale domain organization of the plasma membrane, *Trends Biochem. Sci.*, 36 (2011) 604-615.
- [32] M.A. Reddy, S.L. Li, S. Sahar, Y.S. Kim, Z.G. Xu, L. Lanting, R. Natarajan, Key role of Src kinase in S100B-induced activation of the receptor for advanced glycation end products in vascular smooth muscle cells, *J. Biol. Chem.*, 281 (2006) 13685-13693.
- [33] M.P. Lisanti, P.E. Scherer, J. Vidugiriene, Z. Tang, A. Hermanowski-Vosatka, Y.H. Tu, R.F. Cook, M. Sargiacomo, Characterization of caveolin-rich membrane domains isolated from an endothelial-rich source: implications for human disease, *J. Cell Biol.*, 126 (1994) 111-126.
- [34] O. Sbai, T.S. Devi, M.A. Melone, F. Feron, M. Khrestchatsky, L.P. Singh, L. Perrone, RAGE-TXNIP axis is required for S100B-promoted Schwann cell migration, fibronectin expression and cytokine secretion, *J. Cell Sci.*, 123 (2010) 4332-4339.
- [35] F. Xiong, S. Leonov, A.C. Howard, S. Xiong, B. Zhang, L. Mei, P. McNeil, S. Simon, W.C. Xiong, Receptor for advanced glycation end products (RAGE) prevents endothelial cell membrane resealing and regulates F-actin remodeling in a beta-catenin-dependent manner, *J. Biol. Chem.*, 286 (2011) 35061-35070.
- [36] T.J. Feder, I. Brust-Mascher, J.P. Slattey, B. Baird, W.W. Webb, Constrained diffusion or immobile fraction on cell surfaces: a new interpretation, *Biophys. J.*, 70 (1996) 2767-2773.

- [37] E.J. van Zoelen, L.G. Tertoolen, S.W. de Laat, Simple computer method for evaluation of lateral diffusion coefficients from fluorescence photobleaching recovery kinetics, *Biophys. J.*, 42 (1983) 103-108.
- [38] H. Towbin, T. Staehelin, J. Gordon, Electrophoretic transfer of proteins from polyacrylamide gels to nitrocellulose sheets: procedure and some applications, *Proc. Natl. Acad. Sci. U.S.A.*, 76 (1979) 4350-4354.
- [39] P.T. Matsudaira, Strategies for obtaining partial amino acid sequence data. In a practical guide to protein and peptide purification for microsequencing, in, Academic Press, New York, 1989, pp. 29-30.
- [40] D.W. Buster, J. Nye, J.E. Klebba, G.C. Rogers, Preparation of *Drosophila* S2 cells for light microscopy, *J. Vis. Exp.*, (2010).
- [41] U.E. Schwab, C.M. Ribeiro, H. Neubauer, R.C. Boucher, Role of actin filament network in *Burkholderia multivorans* invasion in well-differentiated human airway epithelia, *Infect. Immun.*, 71 (2003) 6607-6609.
- [42] M.K. Shaw, L.G. Tilney, Induction of an acrosomal process in *Toxoplasma gondii*: visualization of actin filaments in a protozoan parasite, *Proc. Natl. Acad. Sci. U.S.A.*, 96 (1999) 9095-9099.
- [43] R.D. Phair, S.A. Gorski, T. Misteli, Measurement of dynamic protein binding to chromatin in vivo, using photobleaching microscopy, *Meth. Enzymol.*, 375 (2004) 393-414.
- [44] A. Syed, M.D. Lesoine, U. Bhattacharjee, J.W. Petrich, E.A. Smith, The number of accumulated photons and the quality of stimulated emission depletion lifetime images, *Photochem. Photobiol.*, 90 (2014) 767-772.
- [45] A. Boudaoud, A. Burian, D. Borowska-Wykret, M. Uyttewaal, R. Wrzalik, D. Kwiatkowska, O. Hamant, FibrilTool, an ImageJ plug-in to quantify fibrillar structures in raw microscopy images, *Nat. Protoc.*, 9 (2014) 457-463.
- [46] J.V. Valencia, S.C. Weldon, D. Quinn, G.H. Kiers, J. DeGroot, J.M. TeKoppele, T.E. Hughes, Advanced glycation end product ligands for the receptor for advanced glycation end products: biochemical characterization and formation kinetics, *Anal. Biochem.*, 324 (2004) 68-78.
- [47] L.A. Gross, G.S. Baird, R.C. Hoffman, K.K. Baldrige, R.Y. Tsien, The structure of the chromophore within DsRed, a red fluorescent protein from coral, *Proc. Natl. Acad. Sci. U.S.A.*, 97 (2000) 11990-11995.
- [48] H.J. Huttunen, J. Kuja-Panula, H. Rauvala, Receptor for advanced glycation end products (RAGE) signaling induces CREB-dependent chromogranin expression during neuronal differentiation, *J. Biol. Chem.*, 277 (2002) 38635-38646.
- [49] H. Zong, A. Madden, M. Ward, M.H. Mooney, C.T. Elliott, A.W. Stitt, Homodimerization is essential for the receptor for advanced glycation end products (RAGE)-mediated signal transduction, *J. Biol. Chem.*, 285 (2010) 23137-23146.
- [50] D. Mainali, A. Syed, N. Arora, E.A. Smith, Role of insulin receptor and insulin signaling on alphaPS2CbetaPS integrins' lateral diffusion, *Eur. Biophys. J.*, 43 (2014) 603-611.
- [51] S. Sander, N. Arora, E.A. Smith, Elucidating the role of select cytoplasmic proteins in altering diffusion of integrin receptors, *Anal. Bioanal. Chem.*, 403 (2012) 2327-2337.
- [52] F.J. Barrantes, Cell-surface translational dynamics of nicotinic acetylcholine receptors, *Front. Synaptic Neurosci.*, 6 (2014) 25.
- [53] D.M. Owen, D. Williamson, C. Rentero, K. Gaus, Quantitative microscopy: protein dynamics and membrane organization, *Traffic*, 10 (2009) 962-971.
- [54] J.A. Dix, A.S. Verkman, Crowding effects on diffusion in solutions and cells, *Annu. Rev. Biophys.*, 37 (2008) 247-263.
- [55] J.F. Casella, M.D. Flanagan, S. Lin, Cytochalasin D inhibits actin polymerization and induces depolymerization of actin filaments formed during platelet shape change, *Nature*, 293 (1981) 302-305.
- [56] I. Spector, F. Braet, N.R. Shochet, M.R. Bubb, New anti-actin drugs in the study of the organization and function of the actin cytoskeleton, *Microsc. Res. Tech.*, 47 (1999) 18-37.

- [57] M.R. Bubb, I. Spector, B.B. Beyer, K.M. Fosen, Effects of jasplakinolide on the kinetics of actin polymerization. An explanation for certain in vivo observations, *J. Biol. Chem.*, 275 (2000) 5163-5170.
- [58] J. Kwik, S. Boyle, D. Fooksman, L. Margolis, M.P. Sheetz, M. Edidin, Membrane cholesterol, lateral mobility, and the phosphatidylinositol 4,5-bisphosphate-dependent organization of cell actin, *Proc. Natl. Acad. Sci. U.S.A.*, 100 (2003) 13964-13969.
- [59] A. Goldin, J.A. Beckman, A.M. Schmidt, M.A. Creager, Advanced glycation end products: sparking the development of diabetic vascular injury, *Circulation*, 114 (2006) 597-605.

2.7. Figures and Tables

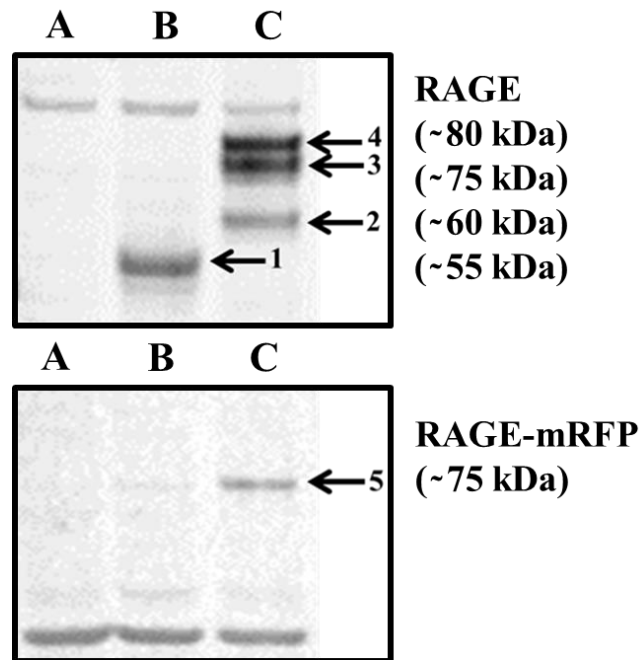


Figure 2.1. Western blot analysis of (A) GM07373 cell lysate, (B) GM07373-RAGE cell lysate, and (C) GM07373-RAGE-mRFP cell lysate. (Top) fluorescence image of the PVDF membrane probed with RAGE antibody; (bottom) fluorescence image of the PVDF membrane probed with RFP antibody. Unlabeled bands (three upper bands in the top image and three lower bands in the bottom image) are present in all lanes and likely represent non-specific interactions of antibodies.

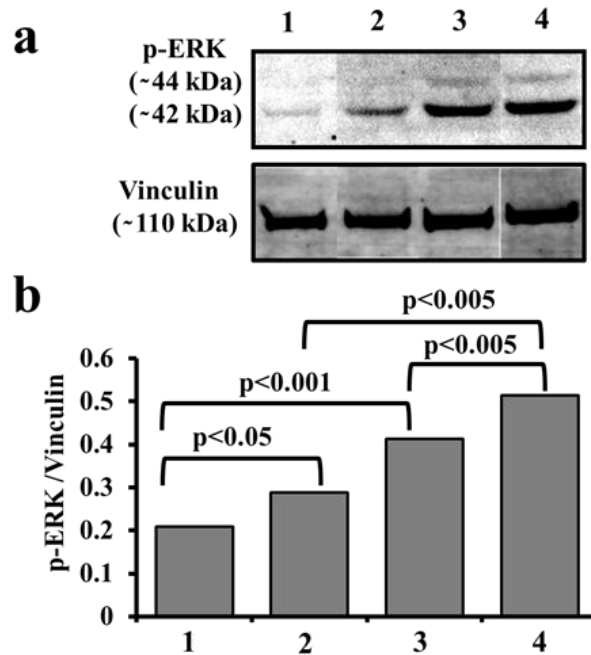


Figure 2.2. Western blot analysis of phosphorylation in ERK in the GM07373 cell lysate with (1) no treatment, or (2) 5 mg/mL BSA-AGE treatment, and in the GM07373-RAGE cell lysate with (3) no treatment or (4) 5 mg/mL BSA-AGE treatment. (a) Fluorescence image of the PVDF membrane probed with phospho-ERK (p-ERK) antibody or vinculin antibody. (b) Average ($n = 2$) fluorescence intensities of the 42 kDa band of p-ERK divided by the vinculin band intensities.

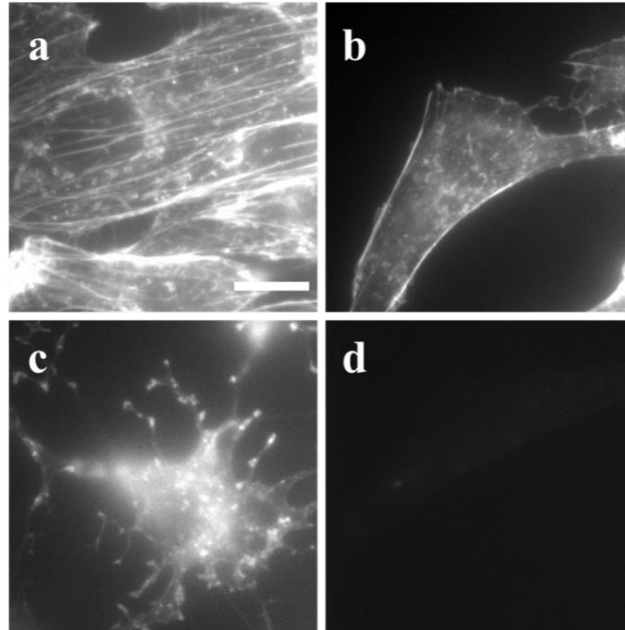


Figure 2.3. Fluorescence images of GM07373-RAGE cells with the actin cytoskeleton stained with Atto 647 conjugated phalloidin. (a) No treatment, (b) 5 mM M β CD treatment, (c) 10 μ M CD treatment, or (d) 3 μ M Jsp treatment. Top two images are intensity scaled from 1700 to 7000 intensity units, whereas bottom two images are intensity scaled from 1500 to 3000 intensity units. Scale bar is 20 μ m and is the same for all images.

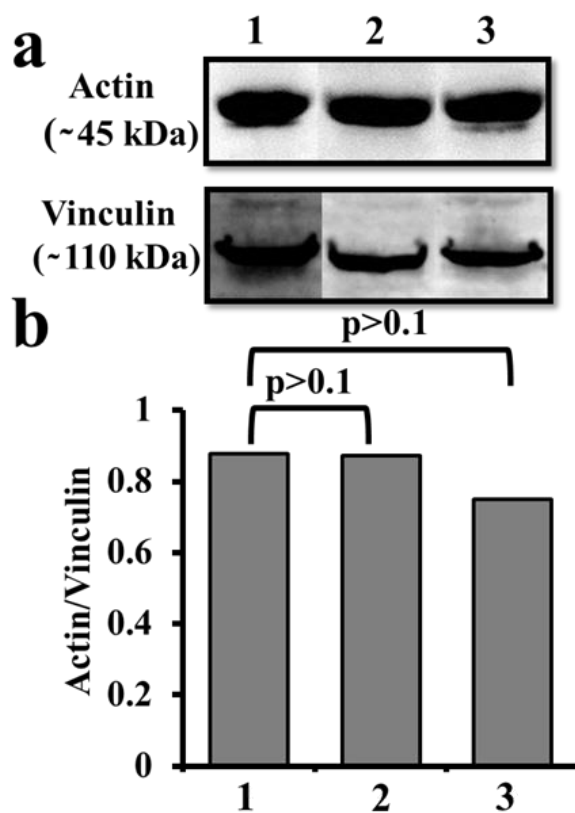


Figure 2.4. Western blot analysis of actin expression in the GM0737-RAGE cell lysate with (1) no treatment, (2) 10 μ M CD treatment, or (3) 3 μ M Jsp treatment. (a) Fluorescence image of the PVDF membrane probed with actin or vinculin antibody. (b) Average ($n = 2$) fluorescence intensities of the actin band divided by the vinculin band intensities.

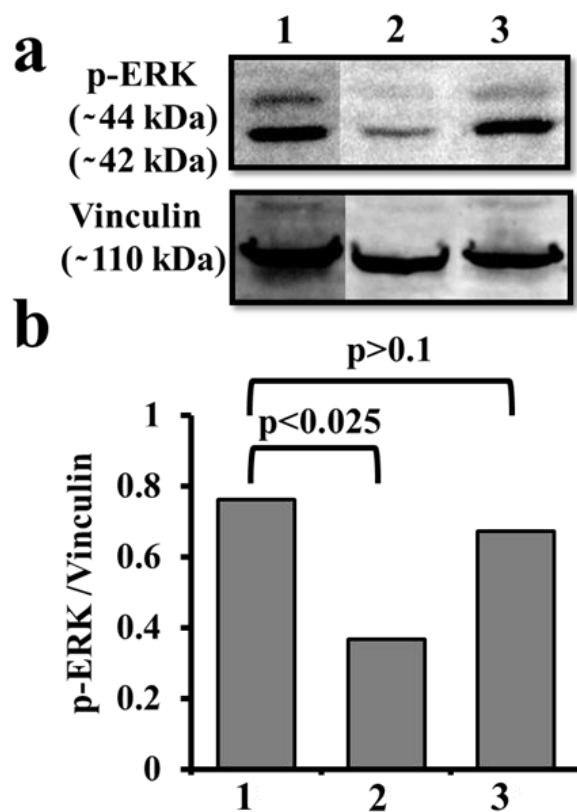


Figure 2.5. Western blot analysis of phosphorylation in ERK in the GM07373-RAGE cell lysate with (1) no treatment, (2) 10 μ M CD treatment, or (3) 3 μ M Jsp treatment. (a) Fluorescence image of the PVDF membrane probed with p-ERK or vinculin antibody. (b) Average ($n = 2$) fluorescence intensities of the 42 kDa p-ERK band divided by the vinculin band intensities

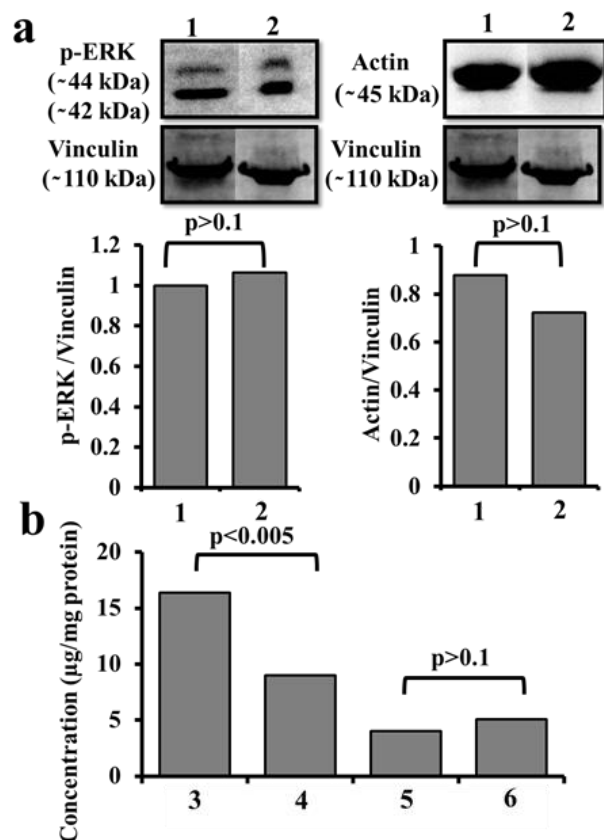


Figure 2.6. Effect of M β CD treatment on GM07373-RAGE cells. (a) Western blot analysis of phosphorylation in ERK and actin expression with (1) no treatment or (2) 5 mM M β CD treated. (b) Average ($n = 2$) vinculin-normalized fluorescence intensities of the 42 kDa band of p-ERK or actin. (b) Cholesterol quantification with Amplex[®] Red assay. Average ($n = 2$) free cholesterol (3 and 4) and cholesterol ester (5 and 6) concentration as measured from GM07373-RAGE cell lysate at native cellular conditions (3 and 5) and 5 mM M β CD treated (4 and 6).

Table 2.1. Average RAGE-mRFP diffusion parameters in the GM07373-RAGE-mRFP cell membrane obtained from FRAP. Entries with a p-value below 0.05 are shown in bold.

Treatment	α	D_{1s} ($\mu\text{m}^2/\text{s}$)	Mobile fraction (%)	Number of cells
No treatment	1.0	0.3	90	10
M β CD treatment	1.1 (p>0.1)	0.2 (p>0.1)	80 (p>0.05)	11
CD treatment	1.1 (p>0.1)	0.2 (p>0.1)	80 (p<0.025)	13
Jsp treatment	0.9 (p>0.1)	0.3 (p>0.1)	80 (p<0.025)	9

α is the time-exponent that describes time dependency of the diffusion

D_{1s} is the diffusion coefficient measured at 1s

Table 2.2. Average lipid mimetic (DiI) diffusion parameters in the GM07373-RAGE cell membrane obtained from FRAP. Entries with a p-value below 0.05 are shown in bold.

Treatment	α	D_{1s} ($\mu\text{m}^2/\text{s}$)	Mobile fraction (%)	Number of cells
No treatment	0.8	1.6	80	13
M β CD treatment	0.8 (p>0.1)	1.0 (p<0.025)	84 (p>0.1)	9
CD treatment	0.9 (p>0.1)	1.0 (p<0.01)	84 (p>0.1)	9
Jsp Treatment	0.72 (p>0.1)	0.8 (p<0.001)	82 (p>0.1)	9

α is the time-exponent that describes time dependency of the diffusion

D_{1s} is the diffusion coefficient measured at 1s

Table 2.3. Average anisotropy in F-actin fibers as analyzed by FibrilTool.

Cells Treatment	Average Anisotropy*	Number of Cells
GM07373 cells No treatment	0.13	21
GM07373 cells MβCD treatment	0.08 (p<0.001)	41
GM07373-RAGE cells No treatment	0.12	32
GM07373-RAGE cells MβCD treatment	0.07 (p<0.001)	36

*The standard deviation in anisotropy values obtained from 21 to 41 cells.

2.8. Supporting information for chapter 2

Plasmids and transfection

Full-length human RAGE coding pcDNA3 vector (pcDNA3.RAGE) was a generous gift from Prof. Ann Marie Schmidt (New York School of Medicine, [60]). pcDNA3.mRFP plasmid was purchased from Addgene (#13032, Cambridge, MA). All oligonucleotides were obtained from Integrated DNA Technologies (Coralville, IA). To generate mRFP fused RAGE (pcDNA3.RAGE-mRFP), the RAGE sequence of pcDNA3.RAGE was amplified by polymerase chain reaction (PCR) using 5'-CCGGAATTCATGGCAGCCGGAACAGCAGTT-3' and 5'-CCGCTCGAGAGGCCCTCCAGTACTACTCTC-3' primers. The amplified RAGE region was sub-cloned into EcoRI/XhoI restriction sites of the pcDNA3.mRFP vector. The DNA sequence coding for human influenza hemagglutinin (HA) tag (YPYDVPDYA) was inserted in the N-terminal of RAGE and RAGE-mRFP plasmids using the following oligonucleotides 5'-TACCCGTACGACGTGCCGGACTACGCCATCACAGCCCCGGATTGGC-3' and 5'-GGCG-TAGTCCGGCAGTCGTAGTTTTGAGCACCTACTACTGCCC-3' to generate pcDNA3.HA-RAGE or pcDNA3.HA-RAGE-mRFP plasmids. The recombinant plasmids were first transformed into DH5 α *E. Coli* cells and transformed cells were selected on Luria broth agar (US biological, Salem, MA) plates containing 50 μ g/mL Carbenicillin (Sigma-Aldrich, St. Louis, MO). GM07373 cells were transfected with purified recombinant plasmids obtained from DH5 α cells using Lipofectamine 2000 using the manufacturer's instructions (Life Technology). Transfected GM07373 cells were selected using Geneticine sulfate (Santa Cruz Biotechnology, Inc., Santa Cruz, CA) in the complete growth medium.

Immunoprecipitation and LC-MS/MS analysis of RAGE and RAGE-mRFP

RAGE and RAGE-mRFP were purified using an N-terminal HA tag. Cell lysates from HA-RAGE or HA-RAGE-mRFP expressing GM07373 cells were incubated overnight at 4 °C with HA antibody

conjugated agarose beads (Thermo Scientific). Agarose beads were washed with phosphate buffered saline (PBS) five times to remove the non-specifically bound components from the crude cell lysate. Bound HA-RAGE or HA-RAGE-mRFP was eluted by incubating the beads at 70 °C for 10 minutes with sodium dodecyl sulfate sample buffer (5% SDS, 5% Glycerol, 125 mM Tris-HCl (pH=6.8) and 0.01% bromophenol blue) with a reducing agent (5 mM dithiothreitol). After centrifuging the beads (14,000 rpm, 3 minutes), supernatant from the elution step was directly added to a pre-cast protein gel for separation by electrophoresis. Coomassie stained protein bands corresponding to HA-RAGE or HA-RAGE-mRFP were excised from the gel and were digested with trypsin on an automated ProGest (Digilab, Marlborough, MA) protein digestion station. Digested fragments were loaded onto the Q-Exactive tandem mass spectrometer (Thermo Scientific) for LC-MS/MS analysis. The measured peptide fragments were searched with both SEQUEST and Mascot to identify sequence matches.

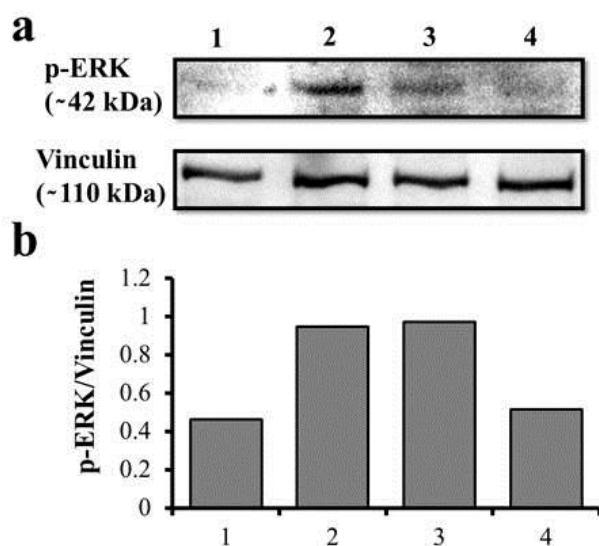


Figure S2.1. Western blot analysis for phosphorylation in ERK and vinculin expression in (1) GM07373 cell lysate (2) GM07373-RAGE cell lysate (3) GM07373-RAGE-mRFP cell lysate and (4) GM07373-RAGE-mRFP cell lysate treated with 10 μ M CD. (a) Fluorescence image of the PVDF membrane probed with p-ERK or vinculin antibody. (b) Fluorescence intensities of the 42 kDa p-ERK band divided by the vinculin band intensities.

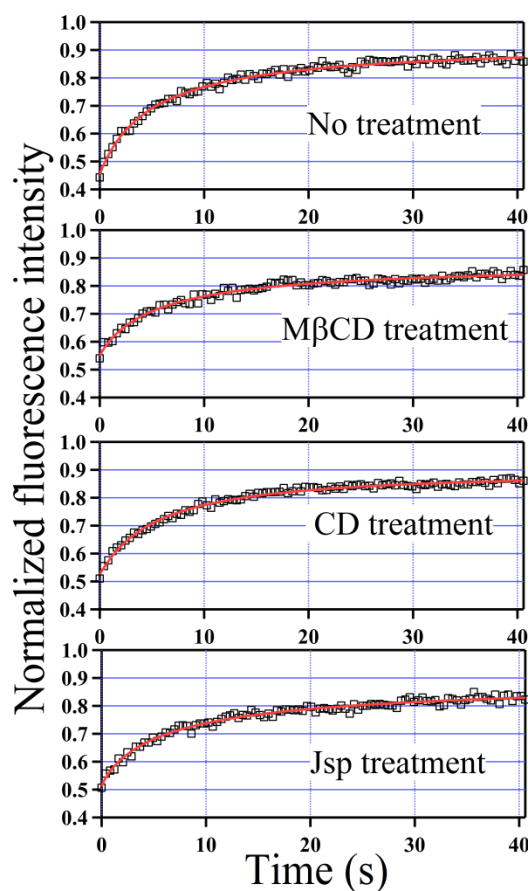


Figure S2.2. Average ($n = 9$ to 13) fluorescence recovery after photobleaching curves from RAGE-mRFP diffusion measurements from GM07373-RAGE-mRFP cells. The diffusion properties obtained from the fit to the data (red line) are reported in Table 1. There is a statistically significant 10% decrease in the RAGE-mRFP mobile fraction after Cd and Jsp treatment. The mobile fraction (MF) is calculated with the equation $MF = \frac{F_{\infty} - F_0}{F^0 - F_0} \times 100$ and depends on both the 0 second and 40 second (∞) data points.

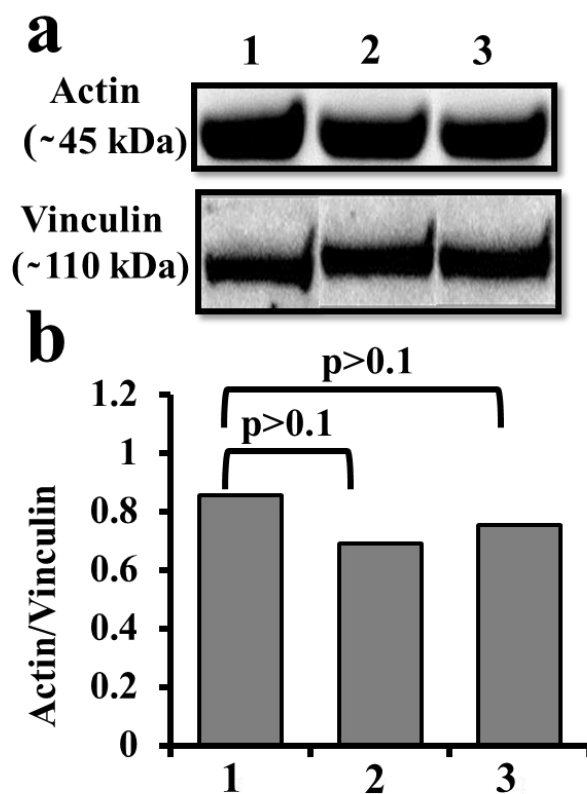


Figure S2.3. Western blot analysis of actin expression in the GM07373 cell lysate (lacking detectable levels of RAGE) with (1) no treatment, (2) 10 μ M CD treatment, or (3) 3 μ M Jsp treatment. (a) Fluorescence image of the PVDF membrane probed with actin or vinculin (loading control) antibody. (b) Average ($n = 2$) fluorescence intensities of the actin band divided by the vinculin band intensities.

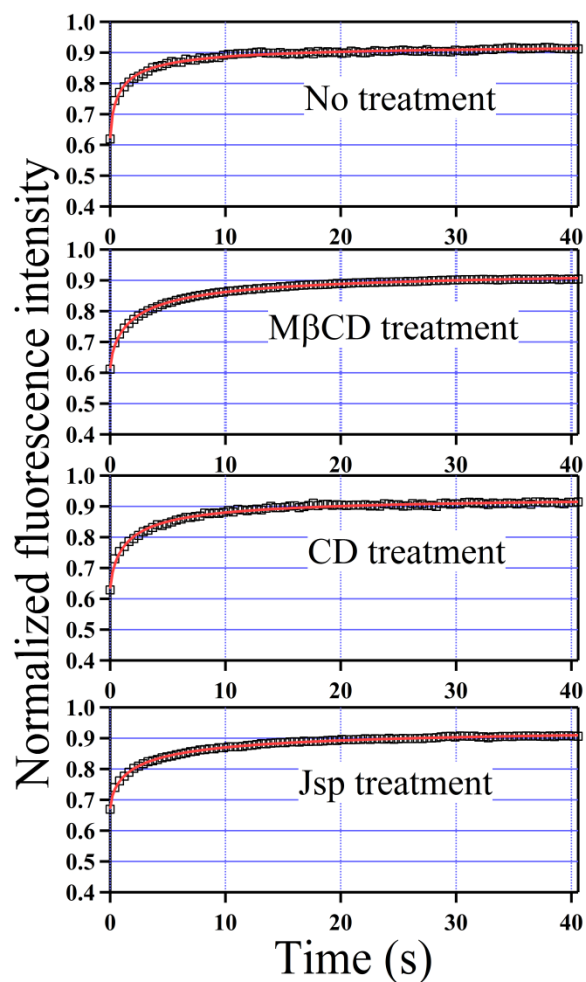


Figure S2.4. Average ($n = 9$ to 13) fluorescence recovery after photobleaching curves for a lipid mimetic (DiI) from GM07373-RAGE cells. The diffusion properties obtained from the fit to the data (red line) are reported in Table 4.2.

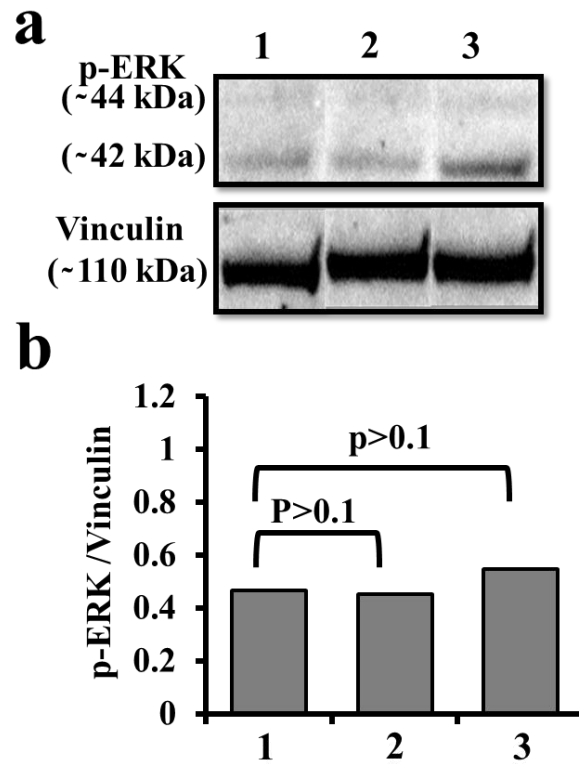


Figure S2.5. Western blot analysis for phosphorylation in ERK in the GM07373 cell lysate (lacking detectable levels of RAGE) with (1) no treatment, (2) 10 μ M CD treatment, or (3) 3 μ M Jsp treatment. The GM07373 cells probed have a low level of endogenous p-ERK in the absence of RAGE expression. (a) Fluorescence image of the PVDF membrane probed with p-ERK antibody or vinculin (loading control) antibody. (b) Average ($n = 2$) fluorescence intensities of the 42 kDa p-ERK band divided by the vinculin band intensities.

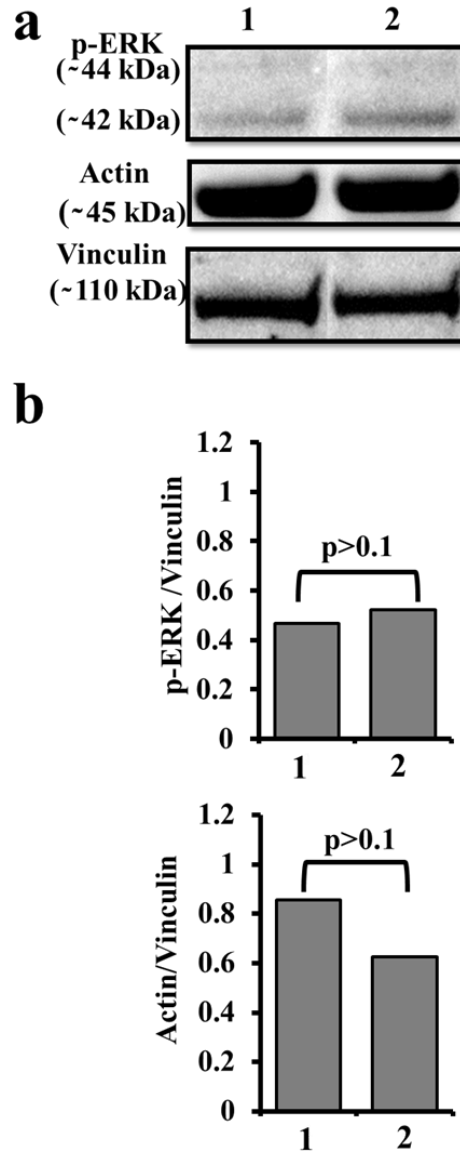


Figure S2.6. Western blot analysis for phosphorylation in ERK and actin expression in the GM07373 cell lysate (lacking detectable levels of RAGE) with (1) no treatment or (2) 5 mM M β CD treatment. (a) Fluorescence image of the PVDF membrane probed with p-ERK, vinculin, or actin antibody. The GM07373 cells probed have a low level of endogenous p-ERK in the absence of RAGE expression. (b) Average ($n = 2$) fluorescence intensities of the 42 kDa p-ERK band or actin band divided by the vinculin band intensities.

CHAPTER 3**LIGAND BINDING AFFINITY AND CHANGES IN THE LATERAL DIFFUSION OF RECEPTOR FOR ADVANCED GLYCATION ENDPRODUCTS (RAGE)**

A paper submitted for publication as a research article

Aleem Syed¹, Qiaochu Zhu¹ and Emily A. Smith

3.1. Abstract

The effect of ligand on the lateral diffusion of receptor for advanced glycation endproducts (RAGE), a receptor involved in numerous pathological conditions, remains unknown. Single particle tracking experiments that use quantum dots specifically bound to hemagglutinin (HA)-tagged RAGE (HA-RAGE) are reported to elucidate the effect of ligand binding on HA-RAGE diffusion in GM07373 cell membranes. The ligand used in these studies is methylglyoxal modified-bovine serum albumin (MGO-BSA) containing advanced glycation end product modifications. The binding affinity between soluble RAGE and MGO-BSA increases by 1.8 to 9.7-fold as the percent primary amine modification increases from 24 to 74% and with increasing negative charge on the MGO-BSA. Ligand incubation affects the HA-RAGE diffusion coefficient, the radius of confined domains of diffusion, and duration in confined domains of diffusion. There is, however, no correlation between MGO-BSA ligand binding affinity and the extent of the changes in HA-RAGE lateral diffusion. The ligand induced changes to HA-RAGE lateral diffusion do not occur when cholesterol is depleted from the cell membrane, indicating the mechanism for ligand-induced changes to HA-RAGE diffusion is cholesterol dependent. The results presented here serve as a first step in unraveling how ligand binding influences RAGE lateral diffusion.

3.2. Introduction

The receptor for advanced glycation endproducts (RAGE) is a transmembrane receptor that is involved in several pathological disorders [1-3]. It is a multi-ligand receptor with a diverse array of chemically

distinct ligands [4]. Although ligand induced RAGE signaling has been studied extensively in various pathological states, knowledge of the molecular diffusion of RAGE in the cell membrane is generally unknown. The lateral diffusion of membrane proteins plays a role in how receptors interface with other membrane proteins, extracellular ligands, and intracellular proteins, and more generally, how receptors function. The goal of the work reported herein is to understand the effect of ligand incubation on the lateral diffusion and signaling of RAGE in GM07373 bovine artery endothelial cell membranes.

RAGE belongs to the immunoglobulin superfamily, and consists of one variable (V) and two constant (C1 and C2) domains in the extracellular region, a single transmembrane domain and a short cytoplasmic tail. RAGE interacts with several ligands including advanced glycation endproducts (AGE), members of the S100/calgranulins family of proteins and amyloid-beta peptides [5-7]. AGE are the product of non-enzymatic protein cross linking through surface amino acid residues such as lysine, arginine and cysteine. The resulting AGE-modified proteins have a net increase in negative surface charge [8]. Although RAGE ligands are structurally different, all ligands are reported to contain negatively charged domains that are important for binding. Structural analysis of the RAGE extracellular domain with X-ray crystallography and nuclear magnetic resonance spectroscopy corroborates the notion that negatively charged ligands interact with positively charged V and C1-type RAGE ectodomains [9, 10].

We have recently reported properties of RAGE lateral diffusion as measured by fluorescence recovery photobleaching (FRAP) [11]. The lateral diffusion of RAGE and RAGE-dependent signaling were found to be connected to the dynamics of the actin cytoskeleton. In a FRAP experiment, the measured diffusion parameters represent an ensemble average of numerous RAGE. However, receptor lateral diffusion is generally not synchronized across each receptor, and the heterogeneity of all possible diffusion behaviors is not measured by FRAP. For this purpose, it is necessary to probe the diffusion one receptor at a time. One such approach is single particle tracking (SPT), where the receptor is exogenously labeled with a fluorophore and the diffusion of labeled receptor is extracted by following

the trajectory of the label [12]. It is imperative that the signal from the fluorophore be bright and photostable to facilitate fast acquisition times over long durations. Inorganic quantum dots (QDs) satisfy the requirements, and the size of the QD is of similar magnitude to many receptors. Labeling specificity to the desired receptor is achieved by modifying the QD surface with a ligand or another similar strategy [13].

Given the importance of electrostatic interactions in RAGE binding to ligand, increasing the negative charge of the ligand may influence binding and the functional consequences of binding to RAGE; this may include influencing the lateral diffusion of RAGE. To test this hypothesis, methylglyoxal modified-bovine serum albumin (MGO-BSA, a model AGE) with different extents of primary amine modification are prepared. The extent of modification is characterized by measuring free primary amine content and zeta potentials. Ligand binding between MGO-BSA and soluble RAGE (sRAGE, containing the RAGE extracellular domains V, C1 and C2) is measured *in vitro* using surface plasmon resonance (SPR). The effect of ligand on the lateral diffusion of HA-RAGE is measured with single particle tracking (SPT). The role of cholesterol in ligand-induced changes to HA-RAGE lateral diffusion is measured by depleting cellular cholesterol concentrations with methyl- β -cyclodextrin. Finally, HA-RAGE downstream signaling is studied by Western blot to identify possible correlations in HA-RAGE lateral diffusion, signaling, and ligand binding properties.

3.3. Materials and Methods

Cell culture, protein expression and Western blotting

All microscopy and molecular biology experiments were performed using bovine artery GM07373 endothelial cells (Coriell Institute Biorepositories, Camden, NJ) maintained according to the procedure described previously [11]. GM07373 cells were transfected with purified recombinant plasmid using Lipofectamine 2000 and the manufacturer's instructions (Life Technology). Transfected GM07373 cells were selected using Geneticin sulfate (Santa Cruz Biotechnology, Inc., Santa Cruz, CA). The transfected

cells were established to express HA-RAGE protein stably before microscopy or molecular biology experiments. Details of the HA-RAGE expression plasmid, soluble RAGE expression and purification and Western blotting experiments are provided in the supplementary material.

Preparation and characterization of methylglyoxal (MGO) modified-bovine serum albumin (BSA)

BSA was modified with different concentration of MGO to generate various MGO-BSA. 10 mM, 40 mM, 60 mM, 80 mM and 100 mM MGO was incubated with 50 mg/mL BSA in 0.1 M phosphate buffered saline (PBS) pH 7.4 at 37 °C for five days. On the fifth day, unreacted MGO was removed by dialysis in 0.1 M PBS. The *ortho*-phthaldialdehyde assay was performed to evaluate the extent of modification *via* quantifying the free primary amine content of BSA [14]. The fluorescence intensity was measured with a microplate reader (Synergy 2 Multi-Mode Reader, BioTek) at excitation and emission wavelengths of 340 nm and 435 nm, respectively. The resulting fluorescence intensities were translated into a percent modification using the signal measured from unmodified BSA (without MGO incubation) as a control.

Zeta potential measurement

The zeta potential and protein mobility of the prepared MGO modified-BSA were obtained using a Zetasizer Nano ZS (Malvern Instruments, Ltd) with laser Doppler velocimetry. MGO-BSA and BSA control were diluted five times in PBS solution at pH=7.4. Three replicates were measured for each sample at 25 °C and 200 continuous runs.

Surface plasmon resonance (SPR)

The binding affinity between MGO-BSA and sRAGE was measured using a home-built SPR instrument. The MGO-BSA was immobilized by physisorption on a 50-nm thick gold film. 100 nM sRAGE in HEPES buffer (pH=7.5) was pumped into a flow cell at the flow rate of 0.8 ml/min for one

minute, and then the SPR response was monitored for 20 min. After the 20 min association step, the HEPES buffer was flowed for 1 min at the flow rate of 0.8 ml/min, and then the response during dissociation step was monitored for an additional 20 min. The kinetics parameters for the MGO-BSA sRAGE's interaction were obtained from the resulting sensorgrams as previously reported using the equations provided in the supplementary material [15].

Quantum dot conjugation and sample preparation for single particle tracking (SPT)

Quantum dots (QDs) conjugated with streptavidin were used as a fluorescent probe in SPT experiments. 5 μ L of streptavidin coated QDs in 1 μ M borate buffer were added to 21 μ L of HA-epitope tag antibody conjugated with biotin in 74 μ L of PBS buffer (pH=7.4) and incubated for 2 hours at room temperature. The resulting anti-HA labeled QDs (AHA-QDs) were stored in the refrigerator until use.

Cells were sub cultured onto 8-well Nunc™ Lab-Tek™ chambered glass slide for 24 hours. On the next day, spread cells were incubated with 3% (W/V) BSA in DMEM (BSA-DMEM) medium overnight before imaging experiments to minimize the nonspecific binding. Cells were either used without further treatment or treated with specific MGO-BSA (5 mg/mL in BSA-DMEM) for 1 h. In the case of sequential cholesterol depletion, cells were further treated with M β CD (5 mM in BSA-DMEM) before labeling with AHA-QDs. For SPT experiments, AHA-QDs were sonicated for 2 h to avoid aggregation of the QDs. The AHA-QDs were diluted to 100 pM in the imaging medium containing 0.1% (W/V) BSA. Cells were incubated with the AHA-QDs for 15 minutes at 37 °C in the incubator. Cells were then rinsed with imaging medium five times before mounting the sample onto the microscope.

The SPT experiments were performed using a Nikon Eclipse TE2000U microscope (Melville, NY, USA) operating in wide-field, epi-fluorescence mode with a 100 \times objective and mercury lamp illumination. Filter sets for excitation (425/45 nm) and emission (605/20 nm) were obtained from Omega Optical (XF304-1, Brattleboro, VT, USA). The microscope was housed inside a physiological

chamber. All imaging experiments were performed at 36 ± 2 °C. Fluorescence images were collected using a PhotonMAX 512 EMCCD camera (Princeton Instrument, Trenton, NJ, USA) with a 40 ms camera exposure time and a full-chip (512×512 pixels) field of view for a total of 40 s.

QD binding specificity, localization, and tracking

The AHA-QD binding specificity was measured using two cell lines: GM07373 cells that do not express HA-RAGE and GM07373 cells that express HA-RAGE. Nonspecific binding was reported as the average number of AHA-QDs in cells lacking HA-RAGE divided by the average number in cells expressing HA-RAGE. The ImageJ particle tracker 2D/3D plug-in implementing the algorithm developed by Sbalzarini and Koumoutsakos was used for detecting QDs, and calculating localization and tracking [16, 17]. The intrinsic blinking property of the QDs was used to identify single particles and the extracted single particle trajectories that were at least 8 s in duration (i.e., in between blinking events) were further analyzed.

SPT data analysis

Extracted single particle trajectories were analyzed using APM_GUI (Analyzing Particle Movement with Graphical User Interface), which is a MATLAB-implemented application based on an established algorithm reported by Simson and co-workers [18, 19]. Diffusion coefficients measured for AHA-QDs on GM07373 cells were used as a threshold to select mobile trajectories to account for the non-specific binding. All mobile trajectories were classified either as confined or as non-confined (Brownian) trajectories based on the probability of particle motion being Brownian in a given region. The probability level or the confinement index (L) was calculated for each trajectory to highlight the regions of confined behavior as described previously [19]. The simulated Brownian trajectories for a range of diffusion coefficients were used to estimate the critical confinement index (L_c) and critical confinement time (t_c). These two parameters were used as a threshold to separate Brownian motion from confined

motion. In general, the greater the value of L , the greater the tendency for a trajectory to exhibit confined motion. For a given trajectory, a confined diffusion region is defined by the regions where L increases above a critical threshold L_c for a duration of time longer than a critical time t_c . Based on the simulation data for Brownian trajectories, the trajectories with $L > 3.16$ for a duration $t_c > 1.95$ s had a 99.93 % likelihood to be in confined motion. For a trajectory classified as confined, the size of the confinement region, the duration of the confinement time, and the diffusion coefficients inside the confined zones and outside the confined regions were further analyzed. The plot of mean square displacement (MSD) vs time was used to calculate the characteristic diffusion coefficient of a given region [18].

3.4. Results and Discussion

Characterization of MGO-BSA ligand and its interactions with RAGE

Five MGO-BSA samples were prepared by incubating BSA with 10 to 100 mM MGO. Two of the possible amino acid modifications that occur after MGO incubation are shown in Figure S3.1. The extent of primary amine modification as measured by the *ortho*-phthaldialdehyde assay increases linearly ($R^2 = 0.98$) when increasing concentrations of MGO are used for the *in vitro* modification of BSA (Figure 3.1A). The percent primary amine modification ranges from 24 to 74% compared to control BSA that is not incubated with MGO. BSA that has not been incubated with MGO has a net positive surface charge, but all MGO-BSA samples have a net negative surface charge that increases as the MGO concentration used for the modification of BSA increases (Figure 3.1B).

RAGE ligands mainly bind to the extracellular V and C1 domains [9, 10], so a soluble variant for RAGE (sRAGE) is commonly used as an antigen for binding affinity studies. Surface plasmon resonance measurements of the dissociation constant (K_d) between each MGO-BSA sample and sRAGE are shown in Figure S3.2. The K_d values obtained from the SPR curves are shown in Figure 3.1C. With increasing percent primary amine modification, the affinity of MGO-BSA for sRAGE increases (i.e., the

solution concentration of MGO-BSA required to occupy half of the available binding sites on sRAGE decreases). Combining the results of the affinity and MGO-BSA surface charge measurements, the affinity between sRAGE and MGO-BSA is linearly dependent ($R^2 = 0.94$) on the net MGO-BSA negative surface charge, which is consistent with an interaction to a positively charged binding pocket on the V-domain of sRAGE.

Extracellular HA epitope tag enables the specific labeling of QDs to RAGE

Single particle tracking experiments require the specific binding between a nanoparticle and a receptor. In these studies the nanoparticles are fluorescent quantum dots (QDs). A ligand can be directly coated on the surface of the QDs [20, 21], however, up to 88% nonspecific binding is observed when ligand (AGE or S100 A8/A9)-coated QDs are incubated with cells that do not express RAGE (data not shown). A possible reason for the observed nonspecific binding may be due to the affinity of RAGE ligands for other membrane proteins [8]. As an alternative labeling route, the 9 amino acid (YPYDVPDYA) hemagglutinin (HA) tag was added to the RAGE extracellular domain at a position three amino acids away from the N-terminal of the signal peptide. The cellular signaling of HA-RAGE is similar to that of RAGE lacking the HA tag as measured by phosphorylation in ERK (p-ERK). There is a two-fold increase in p-ERK signaling in GM07373 cells expressing HA-RAGE compared to GM07373 cells that do not express detectable amounts of RAGE (Figure S3.3). This increase is consistent with the two-fold increase in p-ERK signaling in GM07373 cells expressing RAGE lacking the HA tag, as reported previously [11]. Lowest energy structures determined using the I-TASSER software suite [22-24] predict that the HA tag remains accessible to the antibody as shown in Figure S3.4.

Anti-HA-coated QDs (AHA-QDs) are generated by incubating streptavidin-coated QDs with biotin-labeled anti-HA to specifically label HA-RAGE. The specific binding of AHA-QDs for HA-RAGE is measured using cells that are incubated with 100 pM AHA-QDs as shown in Figure S3.5. The number of AHA-QDs per cell is counted for at least 34 cells expressing HA-RAGE or lacking HA-

RAGE. There is 4.8% nonspecific AHA-QD binding, indicating that a majority of the AHA-QDs observed in the HA-RAGE expressing cells are specifically bound to HA-RAGE. A goal of this work is to measure the diffusion properties of HA-RAGE as measured by the trajectories of AHA-QDs. The nonspecifically bound AHA-QDs on the cell membrane are immobile and do not diffuse. To prevent biasing the HA-RAGE diffusion measurements, the immobile AHA-QDs are excluded from the analysis since immobile trajectories could arise from either nonspecific binding or immobile HA-RAGE. Excluding the immobile AHA-QDs from the analysis does prohibit measuring the fraction of immobile HA-RAGE.

Diffusion properties for the Brownian trajectories of HA-RAGE in the presence and absence of MGO-BSA ligand

Fluorescence microscopy is used to collect at least 400 trajectories of AHA-QDs from at least 10 cells to measure the diffusion of HA-RAGE in the presence or absence of MGO-BSA. Trajectories are classified as exhibiting either Brownian or confined diffusion. If the trajectory has a minimum of one confined domain (where the confinement index (L) is higher than the critical confinement value for longer than the critical time as described in the experimental section) then the trajectory is classified as confined. In the absence of ligand, 31% of HA-RAGE exhibit Brownian diffusion and 69% exhibit confined diffusion, indicating a majority of HA-RAGE measured by SPT exhibit confined diffusion at least once in ~ 20 seconds (i.e., the average length of a trajectory as shown in Table 3.1). When the cells are incubated with MGO-BSA, a 3 to 7% increase in the Brownian population is measured when the MGO-BSA percent primary amine modification is at least 41%.

The average diffusion coefficient for the Brownian trajectories of HA-RAGE in the absence of ligand is $0.085 \mu\text{m}^2/\text{s}$. The histogram of diffusion coefficients (Figure 3.2) shows a bimodal population with maximum diffusion coefficients of 0.0006 and $0.065 \mu\text{m}^2/\text{s}$. When the cells are exposed to 24% MGO-BSA, the average diffusion coefficient drops to $0.039 \mu\text{m}^2/\text{s}$ (Table 3.1). The distribution of

diffusion coefficients remains bimodal but with a higher percentage of the slower population (Figure 3.2). Between 24% MGO-BSA and 62% MGO-BSA treatment, there is an increase in the average diffusion coefficient and a decrease in the population of HA-RAGE in the slower diffusion coefficient range. Interestingly, compared to the 62% MGO-BSA treatments, the average diffusion coefficient decreases after 74% MGO-BSA treatment, and there is a recurrence of the bimodal diffusion coefficient distribution. There is no direct correlation between the average HA-RAGE diffusion coefficient and MGO-BSA percent primary amine modification, net surface charge, or binding affinity. It is possible the binding affinity measured by SPR between sRAGE and MGO-BSA does not represent the affinity of MGO-BSA toward the full length RAGE in the cell, it is also possible that ligand binding to another receptor (as stated above AGE binds to other receptors) may indirectly impact RAGE diffusion.

Diffusion properties for the fraction of HA-RAGE with at least one confined domain in the presence and absence of MGO-BSA ligand

Two regions are identified for each trajectory classified as exhibiting a confined domain based on the measured confinement index (L). First, the regions where L is higher than the critical confinement value for longer than the critical time. Second, since the time HA-RAGE is in confined domains (Table 3.2) is less than the average trajectory time, parts of the trajectory represent diffusion outside confined domains. Outside of the confined domains, Brownian diffusion properties are expected. Table 3.2 and Figure 3.3 confirm that the diffusion coefficients measured outside the confined domains of diffusion are within expected experimental uncertainties to the values measured for the trajectories exhibiting pure Brownian diffusion (Table 3.1 and Figure 3.2), including a maximum average diffusion coefficient ($0.085 \mu\text{m}^2/\text{s}$) measured after treatment with 62% MGO-BSA. When HA-RAGE is in a confined domain and in the absence of ligand, the average diffusion coefficient is 7-fold slower compared to HA-RAGE exhibiting Brownian diffusion. For HA-RAGE in confined domains in the presence of MGO-BSA, the same trends are measured in the average diffusion coefficient and the histogram of diffusion

coefficients as measured for HA-RAGE exhibiting Brownian diffusion, although the magnitude of the average diffusion coefficient is 4 to 6-fold slower within the confined domains (Table 3.2 and Figure 3.4).

The average confinement radius and time in confined domains measured for HA-RAGE in the absence of ligand were 0.199 μm and 3.89 seconds, respectively (Table 3.2). The confinement radius decreases after treatment with 24% MGO-BSA, and the confinement radius is the largest after 74% MGO-BSA treatment (Figure 3.5, Table 3.2). Overall the confinement radius shows the same trend as the average diffusion coefficient with increasing MGO-BSA percent primary amine modification. The time HA-RAGE remains in confined domains remains approximately 4 seconds after cellular incubation with MGO-BSA. While the size of the domains of confined diffusion varies with MGO-BSA incubation, the time HA-RAGE spends within these domains is relatively independent of ligand incubation.

p-ERK signaling and HA-RAGE expression are independent of the percent primary amine modification on MGO-BSA

Phosphorylation in ERK (p-ERK) and Akt (p-Akt) have been used to measure RAGE signaling [11, 25]. After incubation with MGO-BSA, there is a 2 to 2.4-fold increase in p-ERK signaling compared to p-ERK measured in the absence of MGO-BSA (Figure 3.6A and 3.6B). There is no statistically significant difference in p-ERK signaling for cells incubated with varying MGO-BSA percent primary amine modification. A similar trend was measured for cells lacking HA-RAGE expression (Figure S3.3). It is possible that a non-RAGE-dependent mechanism is responsible for some or all of the increase in p-ERK signaling after incubation with MGO-BSA. In contrast to the increasing p-ERK levels after MGO-BSA incubation, no statistically significant difference in p-Akt signaling is measured in cells expressing or lacking HA-RAGE (Figure S3.6). There is a 15 to 28% decrease in HA-RAGE expression after incubating cells with MGO-BSA (Figure 3.6C and 3.6D). As with p-ERK signaling, the reduced HA-

RAGE expression is statistically the same regardless of the percent primary amine modification on MGO-BSA. Previously, RAGE expression was shown to be down regulated in monocytes upon incubation with AGE prepared by glyceraldehyde modification [26]. The glyceraldehyde-prepared AGE reported in this previous study best matches the AGE used in the studies reported herein. In some experimental conditions, RAGE expression has been shown to be upregulated by incubation with ligand [27, 28].

Insight into the nature of the confined domains of diffusion: Cholesterol depletion eliminates the ligand-induced changes to HA-RAGE diffusion

Previously RAGE has been reported to be part of cholesterol rich membrane domains [29, 30]. However, cholesterol depletion did not affect the lateral diffusion properties of RAGE as observed with FRAP [11]. The effect of cholesterol depletion on ligand-induced changes in HA-RAGE lateral diffusion is explored by depleting cholesterol from untreated and 62% MGO-BSA-treated cells. Considering all diffusion properties for Brownian and confined diffusion, the changes in HA-RAGE diffusion that are measured after 62% MGO-BSA treatment are not measured when cholesterol is extracted from the membrane (Table 3.3, 3.4 and Figure S3.7, S3.8, S3.9 and S3.10). After treatment with 62% MGO-BSA and cholesterol extraction, the HA-RAGE diffusion parameters are similar to the values measured after cholesterol extraction without ligand incubation. The ligand-induced changes in HA-RAGE diffusion are cholesterol dependent, and are not measured when cholesterol concentrations and/or cholesterol-dependent structures in the membrane are altered.

3.5. Conclusions

MGO-BSA binding affinity to sRAGE was observed to be dependent on the percent primary amine modification and the net negative surface charge on the ligand. MGO-BSA incubation affected HA-RAGE lateral diffusion, however, there was no direct correlation measured between ligand binding

affinity, net negative surface charge on the ligand and HA-RAGE diffusion coefficient, radius of confinement or duration of confinement. Cholesterol depletion was found to ameliorate the ligand induced changes on HA-RAGE lateral diffusion, indicating a direct or indirect role for cholesterol in MGO-BSA-induced changes to HA-RAGE diffusion. Other factors such as ligand valency and receptor clustering, as well as, other membrane changes that may result from the MGO-BSA ligand are possible avenues for further study.

Author contribution

¹These authors have contributed equally

Acknowledgements

This work was supported by the National Science Foundation (CHE- 1412084). Authors thank Dr. Ann Marie Schmidt (NYU School of Medicine) for providing full length human RAGE plasmid and Dr. Walter Chazin (Vanderbilt University) for providing S100 A8/A9 ligand that was tested for preliminary SPT studies and the sRAGE expression system.

3.6. References

- [1] G.R. Barile, A.M. Schmidt, RAGE and its ligands in retinal disease, *Curr. Mol. Med.*, 7 (2007) 758-765.
- [2] C.D. Logsdon, M.K. Fuentes, E.H. Huang, T. Arumugam, RAGE and RAGE ligands in cancer, *Curr. Mol. Med.*, 7 (2007) 777-789.
- [3] S.D. Yan, X. Chen, J. Fu, M. Chen, H. Zhu, A. Roher, T. Slattery, L. Zhao, M. Nagashima, J. Morser, A. Migheli, P. Nawroth, D. Stern, A.M. Schmidt, RAGE and amyloid-beta peptide neurotoxicity in Alzheimer's disease, *Nature*, 382 (1996) 685-691.
- [4] G. Fritz, RAGE: a single receptor fits multiple ligands, *Trends Biochem Sci*, 36 (2011) 625-632.
- [5] S.D. Yan, A. Bierhaus, P.P. Nawroth, D.M. Stern, RAGE and Alzheimer's disease: a progression factor for amyloid-beta-induced cellular perturbation?, *J. Alzheimers Dis.*, 16 (2009) 833-843.
- [6] A.M. Schmidt, M. Vianna, M. Gerlach, J. Brett, J. Ryan, J. Kao, C. Esposito, H. Hegarty, W. Hurley, M. Clauss, et al., Isolation and characterization of two binding proteins for advanced glycosylation end products from bovine lung which are present on the endothelial cell surface, *J. Biol. Chem.*, 267 (1992) 14987-14997.
- [7] E. Leclerc, G. Fritz, S.W. Vetter, C.W. Heizmann, Binding of S100 proteins to RAGE: an update, *Biochim. Biophys. Acta*, 1793 (2009) 993-1007.
- [8] A. Goldin, J.A. Beckman, A.M. Schmidt, M.A. Creager, Advanced glycation end products: sparking the development of diabetic vascular injury, *Circulation*, 114 (2006) 597-605.
- [9] H. Park, F.G. Adsit, J.C. Boyington, The 1.5 Å crystal structure of human receptor for advanced glycation endproducts (RAGE) ectodomains reveals unique features determining ligand binding, *J. Biol. Chem.*, 285 (2010) 40762-40770.
- [10] M. Koch, S. Chitayat, B.M. Dattilo, A. Schiefner, J. Diez, W.J. Chazin, G. Fritz, Structural basis for ligand recognition and activation of RAGE, *Structure*, 18 (2010) 1342-1352.
- [11] A. Syed, Q. Zhu, E. Smith, Lateral Diffusion and Signaling of Receptor for Advanced Glycation End-products (RAGE): A Receptor Involved in Chronic Inflammation, *Eur. Biophys. J.*, Submitted (2016).
- [12] M.J. Saxton, Single-particle tracking: the distribution of diffusion coefficients, *Biophys. J.*, 72 (1997) 1744-1753.
- [13] H. Bannai, S. Levi, C. Schweizer, M. Dahan, A. Triller, Imaging the lateral diffusion of membrane molecules with quantum dots, *Nat. Protoc.*, 1 (2006) 2628-2634.
- [14] J.V. Valencia, S.C. Weldon, D. Quinn, G.H. Kiers, J. DeGroot, J.M. TeKoppele, T.E. Hughes, Advanced glycation end product ligands for the receptor for advanced glycation end products: biochemical characterization and formation kinetics, *Anal. Biochem.*, 324 (2004) 68-78.
- [15] D.J. O'Shannessy, M. Brigham-Burke, K.K. Soneson, P. Hensley, I. Brooks, Determination of rate and equilibrium binding constants for macromolecular interactions using surface plasmon resonance: use of nonlinear least squares analysis methods, *Anal. Biochem.*, 212 (1993) 457-468.
- [16] I.F. Sbalzarini, P. Koumoutsakos, Feature point tracking and trajectory analysis for video imaging in cell biology, *J. Struct. Biol.*, 151 (2005) 182-195.
- [17] D. Mainali, E.A. Smith, Select cytoplasmic and membrane proteins increase the percentage of immobile integrins but do not affect the average diffusion coefficient of mobile integrins, *Anal. Bioanal. Chem.*, 405 (2013) 8561-8568.
- [18] S.A. Menchon, M.G. Martin, C.G. Dotti, APM_GUI: analyzing particle movement on the cell membrane and determining confinement, *BMC Biophys.*, 5 (2012) 4.
- [19] R. Simson, E.D. Sheets, K. Jacobson, Detection of temporary lateral confinement of membrane proteins using single-particle tracking analysis, *Biophys. J.*, 69 (1995) 989-993.

- [20] X. Michalet, F.F. Pinaud, L.A. Bentolila, J.M. Tsay, S. Doose, J.J. Li, G. Sundaresan, A.M. Wu, S.S. Gambhir, S. Weiss, Quantum dots for live cells, in vivo imaging, and diagnostics, *Science*, 307 (2005) 538-544.
- [21] D. Mainali, E.A. Smith, The effect of ligand affinity on integrins' lateral diffusion in cultured cells, *Eur. Biophys. J.*, 42 (2013) 281-290.
- [22] J. Yang, R. Yan, A. Roy, D. Xu, J. Poisson, Y. Zhang, The I-TASSER Suite: protein structure and function prediction, *Nat. Methods*, 12 (2015) 7-8.
- [23] A. Roy, A. Kucukural, Y. Zhang, I-TASSER: a unified platform for automated protein structure and function prediction, *Nat. Protoc.*, 5 (2010) 725-738.
- [24] Y. Zhang, I-TASSER server for protein 3D structure prediction, *BMC Bioinformatics*, 9 (2008) 40.
- [25] H. Zong, A. Madden, M. Ward, M.H. Mooney, C.T. Elliott, A.W. Stitt, Homodimerization Is Essential for the Receptor for Advanced Glycation End Products (RAGE)-mediated Signal Transduction, *J. Biol. Chem.*, 285 (2010) 23137-23146.
- [26] J. Miura, Y. Uchigata, Y. Yamamoto, M. Takeuchi, S. Sakurai, T. Watanabe, H. Yonekura, S.-i. Yamagishi, Z. Makita, A. Sato, Y. Omori, H. Yamamoto, Y. Iwamoto, AGE down-regulation of monocyte RAGE expression and its association with diabetic complications in type 1 diabetes, *J. Dia. Com.*, 18 (2004) 53-59.
- [27] L. Yu, Y. Zhao, S. Xu, F. Ding, C. Jin, G. Fu, S. Weng, Advanced Glycation End Product (AGE)-AGE Receptor (RAGE) System Upregulated Connexin43 Expression in Rat Cardiomyocytes via PKC and Erk MAPK Pathways, *Int. J. Mol. Sci.*, 14 (2013) 2242-2257.
- [28] N. Tanaka, H. Yonekura, S.i. Yamagishi, H. Fujimori, Y. Yamamoto, H. Yamamoto, The Receptor for Advanced Glycation End Products Is Induced by the Glycation Products Themselves and Tumor Necrosis Factor- through Nuclear Factor- B, and by 17 -Estradiol through Sp-1 in Human Vascular Endothelial Cells, *J. Biol. Chem.*, 275 (2000) 25781-25790.
- [29] O. Sbai, T.S. Devi, M.A. Melone, F. Feron, M. Khrestchatisky, L.P. Singh, L. Perrone, RAGE-TXNIP axis is required for S100B-promoted Schwann cell migration, fibronectin expression and cytokine secretion, *J. Cell Sci.*, 123 (2010) 4332-4339.
- [30] M.P. Lisanti, P.E. Scherer, J. Vidugiriene, Z. Tang, A. Hermanowski-Vosatka, Y.H. Tu, R.F. Cook, M. Sargiacomo, Characterization of caveolin-rich membrane domains isolated from an endothelial-rich source: implications for human disease, *J. Cell Biol.*, 126 (1994) 111-126.

3.7. Figures and Tables

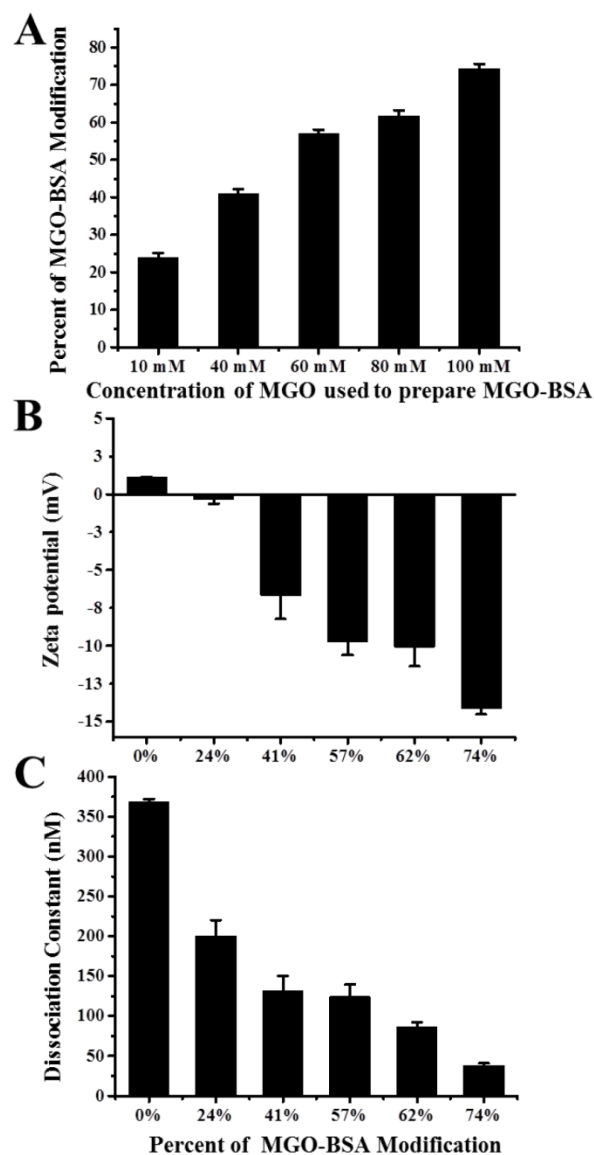


Figure 3.1. Characterization of methylglyoxal modified-bovine serum albumin (MGO-BSA). (A) Percent modification of free primary amines in BSA as measured by an *ortho*-phthaldialdehyde assay after modification with the indicated concentration of MGO; (B) Measured Zeta potential for MGO-BSA with the indicated percent primary amine modification; (C) Dissociation constant as measured by SPR for MGO-BSA with the indicated percent primary amine modification and sRAGE.

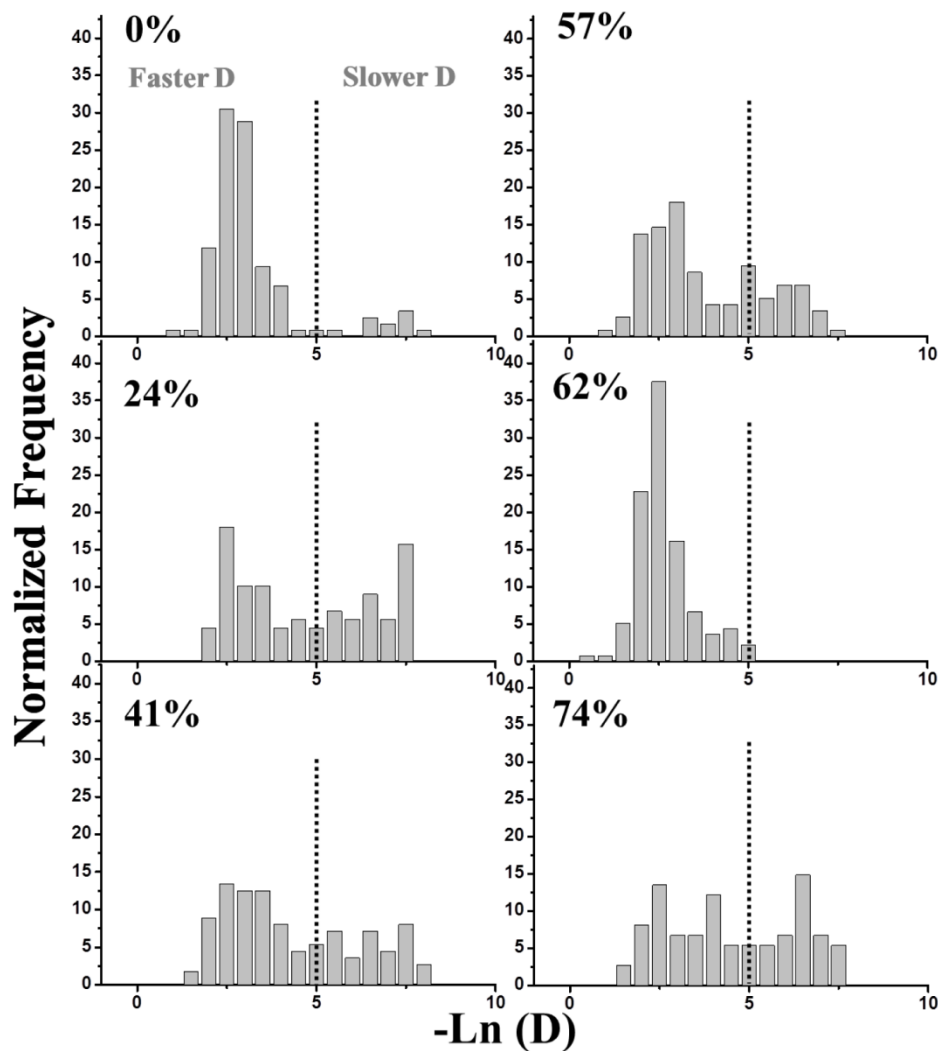


Figure 3.2. Histograms of diffusion coefficients for the **Brownian trajectories** of HA-RAGE in the GM07373 cell membrane treated with MGO-BSA having the indicated percent primary amine modification. The diffusion coefficient is plotted as the negative natural logarithm; slower diffusion coefficients appear on the right side of the graph. The dotted line is shown for clarity in comparing the changes in the distribution.

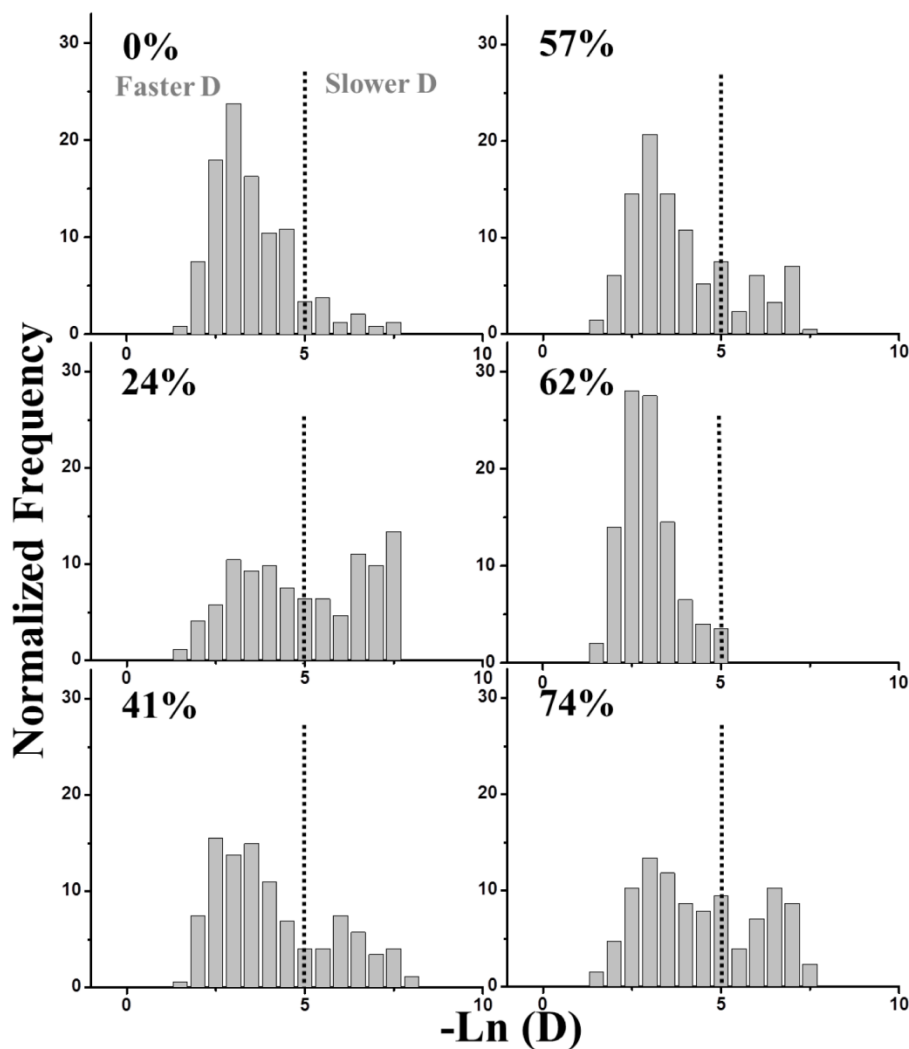


Figure 3.3. Histograms of diffusion coefficients for the **confined trajectories (outside domains of confined diffusion)** of HA-RAGE in the GM07373 cell membrane treated with MGO-BSA having the indicated percent primary amine modification. The diffusion coefficient is plotted as the negative natural logarithm. The dotted line is shown for clarity in comparing the changes in the distribution.

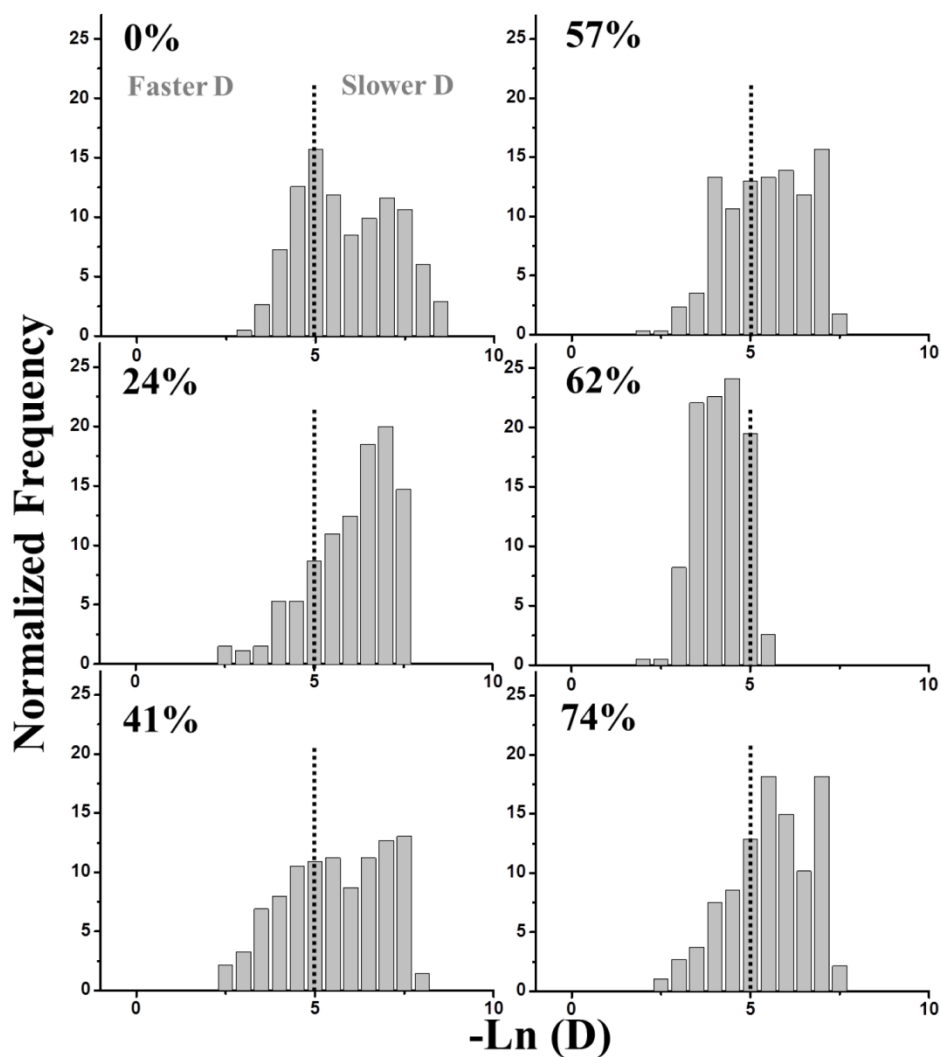


Figure 3.4. Histograms of diffusion coefficients for the **confined trajectories (inside domains of confined diffusion)** trajectories of HA-RAGE in GM07373 cell membrane treated with MGO-BSA having the indicated percent primary amine modification. The diffusion coefficient is plotted as the negative natural logarithm. The dotted line is shown for clarity in comparing the changes in the distribution.

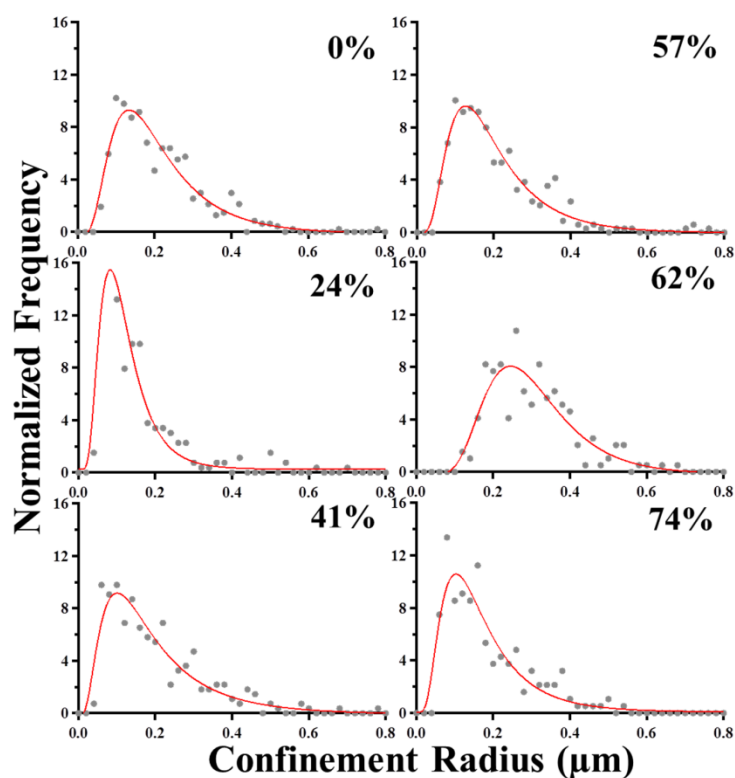


Figure 3.5. Distribution of confinement radius for the **confined trajectories (inside domains of confined diffusion)** of HA-RAGE in the GM07373 cell membrane treated with MGO-BSA having the indicated percent primary amine modification. The corresponding fits (red solid line) are obtained by fitting the distribution to a log-normal function.

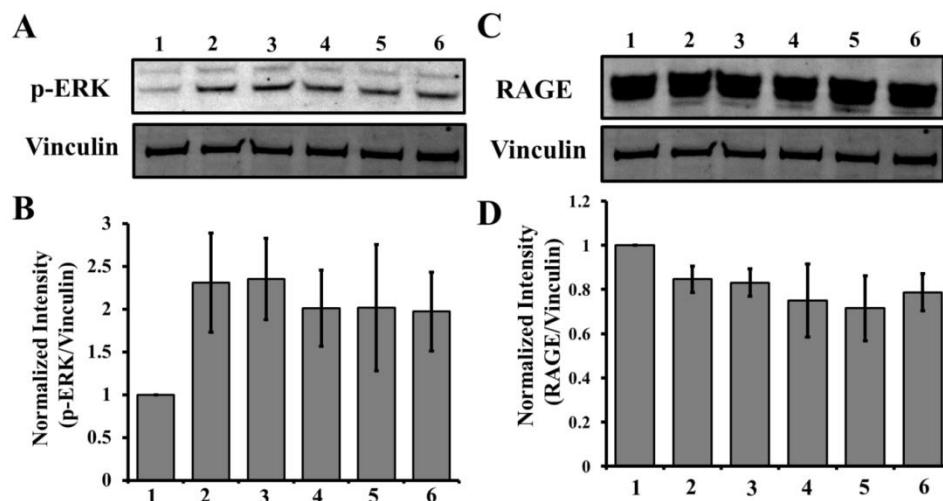


Figure 3.6. Western blot analysis of phosphorylation in ERK (p-ERK) and HA-RAGE expression in the GM07373 cell lysate with: (Lane 1) no treatment, or 5 mg/mL MGO-BSA treatment with the following percent primary amine modification: (Lane 2) 24%, (Lane 3) 41%, (Lane 4) 57%, (Lane 5) 62%, or (Lane 6) 74%. Fluorescence images of the PVDF membrane probed with: (A) p-ERK antibody or vinculin antibody, and (C) RAGE antibody or vinculin antibody. Average ($n = 5$) fluorescence intensities of the: (B) 42 kDa band of p-ERK divided by the vinculin band and (D) RAGE band divided by the vinculin band.

Table 3.1. Average diffusion parameters for the **Brownian trajectories** of HA-RAGE in the GM07373 cell membrane treated with MGO-BSA with the indicated percent primary amine modification.

	% of Brownian trajectories	D ($\mu\text{m}^2/\text{s}$)	Average length of the trajectory (s)
No treatment	31%	0.085	20 \pm 10
24% MGO-BSA treatment	31%	0.039 (p < 0.01)	19 \pm 9
41% MGO-BSA treatment	36%	0.052 (p < 0.01)	19 \pm 9
57% MGO-BSA treatment	34%	0.069 (p < 0.01)	20 \pm 10
62% MGO-BSA treatment	39%	0.115 (p < 0.01)	20 \pm 9
74% MGO-BSA treatment	36%	0.050 (p < 0.01)	30 \pm 10

Diffusion coefficients with a p-value below 0.05 are highlighted in bold to show statistically significant differences compared to the cells that were not treated. The percentage of Brownian trajectories is obtained from counting, so no uncertainty is provided.

Table 3.2. Average diffusion parameters for the **confined trajectories** of HA-RAGE in the GM07373 cell membrane treated with MGO-BSA with the indicated percent primary amine modification.

	D ($\mu\text{m}^2/\text{s}$) (Outside confined domains)	D($\mu\text{m}^2/\text{s}$) (Inside confined domains)	Radius (μm)	Confinement time (s)	Average length of the trajectory (s)
No treatment	0.060	0.012	0.199	3.89	32 \pm 9
24% MGO-BSA treatment	0.031 (p < 0.01)	0.007 (p < 0.01)	0.138 (p < 0.01)	4.09 (p < 0.01)	31 \pm 9
41% MGO-BSA treatment	0.050 (p < 0.01)	0.013 (p=0.09)	0.192 (p < 0.01)	3.90 (p=0.07)	30 \pm 10
57% MGO-BSA treatment	0.053 (p < 0.01)	0.011 (p=0.09)	0.195 (p=0.06)	3.99 (p=0.2)	30 \pm 10
62% MGO-BSA treatment	0.085 (p < 0.01)	0.026 (p < 0.01)	0.294 (p < 0.01)	3.46 (p=0.19)	31 \pm 9
74% MGO-BSA treatment	0.042 (p < 0.01)	0.010 (p=0.01)	0.178 (p=0.02)	3.97 (p < 0.01)	20 \pm 10

Entries with a p-value below 0.05 are highlighted in bold to show statistically significant differences compared to the cells that were not treated.

Table 3.3. Average diffusion parameters for the **Brownian trajectories** for HA-RAGE in the GM07373 cell membrane for the indicated cellular treatments.

	% of Brownian trajectories	D($\mu\text{m}^2/\text{s}$)	Average length of the trajectory (s)
No treatment	31%	0.085	20 \pm 10
62% MGO-BSA ligand	36%	0.115 (p < 0.01)	20 \pm 9
5 mM MβCD to extract cholesterol	33%	0.036 (p < 0.01)	19 \pm 9
62% MGO-BSA and 5mM MβCD	34%	0.041 (p < 0.01)	18 \pm 9

Diffusion coefficients with a p-value below 0.05 are highlighted in bold to show statistically significant differences compared to the cells that were not treated. The percentage of Brownian trajectories is obtained from counting, so no uncertainty is provided.

Table 3.4. Average diffusion parameters for the **confined trajectories** for HA-RAGE in the GM07373 cell membrane for the indicated cellular treatments.

	D ($\mu\text{m}^2/\text{s}$) (Outside confined domains)	D($\mu\text{m}^2/\text{s}$) (Inside confined domains)	Radius (μm)	Confinement time (s)	Average length of the trajectory (s)
No treatment	0.06	0.012	0.199	3.89	32 \pm 9
62% MGO-BSA ligand	0.085 (p < 0.01)	0.026 (p < 0.01)	0.294 (p < 0.01)	3.46 (p=0.19)	31 \pm 9
5 mM MβCD to extract cholesterol	0.035 (p < 0.01)	0.003 (p < 0.01)	0.160 (p < 0.01)	3.94 (p=0.55)	30 \pm 10
62% MGO-BSA and 5mM MβCD	0.038 (p < 0.01)	0.008 (p < 0.01)	0.164 (p < 0.01)	3.92 (p=0.33)	30 \pm 10

Entries with a p-value below 0.05 are highlighted in bold to show statistically significant differences compared to the cells that were not treated.

3.8. Supporting Information for Chapter 3

HA-RAGE plasmid, expression and purification

Full-length human RAGE coding pcDNA3 vector (pcDNA3.RAGE) was a generous gift from Prof. Ann Marie Schmidt (New York School of Medicine) [1]. All oligonucleotides for generating recombinant proteins were obtained from Integrated DNA Technologies (Coralville, IA). The DNA sequence coding for human influenza hemagglutinin (HA) tag (YPYDVPDYA) was inserted in the N-terminal of RAGE plasmid using the following oligonucleotides 5'-TACCCGTACGACGTGCCGGACTACGCCATCA CAGCCCGGATTGGC-3' and 5'-GGCGTAGTCCGGCACGTCGTAGTTTTGAGCACCTACTACT GCCC-3' to generate pcDNA3.HA-RAGE plasmid as reported previously [2]. The recombinant plasmid was first transformed into DH5 α *E. Coli* cells for expression and purification and transformed cells were selected on Luria broth agar (US biological, Salem, MA) plates containing 50 μ g/mL Carbenicillin (Sigma-Aldrich, St. Louis, MO).

Expression and purification of soluble RAGE

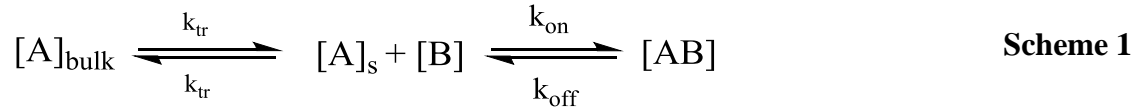
Soluble RAGE (sRAGE) is an endogenous splice variant of full length RAGE lacking the transmembrane and intracellular domains. His-tagged sRAGE transformed *E. Coli* strain *Origami*TM *B* (*DE3*) was a generous gift from Dr. Walter Chazin (Vanderbilt University). The cells were grown at 37 °C until the optical density at 600 nm was approximately 0.8 AU. Then sRAGE's expression was induced with 0.5 mM isopropyl β -D-1-thiogalactopyranoside. After 6 hours at room temperature, cells were harvested and the resulting cell pellet was resuspended in buffer A (20mM Tris-HCL, 300 mM NaCl, 20 mM imidazole at pH 8.0) with 5 mg/mL lysozyme. His-tagged sRAGE from the cell lysate was purified with nickel nitrilotriacetic acid (Ni-NTA) agarose beads (Qiagen) using the manufacturer's instructions. The Ni-NTA column was washed with buffer A, and elution fractions were collected in buffer B (20 mM Tris-HCL, 300 mM NaCl, 150 mM imidazole at pH 8.0). The fractions containing

sRAGE were dialyzed with HEPES buffer (15 mM HEPES, 150 mM NaCl at pH 7.5) for 24 hours. Finally, the sRAGE's concentration was quantified with the bicinchoninic acid assay.

Kinetic equations for interaction between MGO-BSA and sRAGE in SPR experiment

Taking into account the mass transfer in the flow channel, the interaction can be described by scheme 1.

The sensorgrams (Figure S2) were fitted by equations 1-3.



$$\frac{d[AB]}{dt} = k_{on}[A]_s[B] - k_{off}[AB] \quad \text{Equation 1}$$

$$\frac{d[A]_s}{dt} = k_{tr}[A]_{bulk} - k_{tr}[A]_s - k_{on}[A]_s[B] + k_{off}[AB] \quad \text{Equation 2}$$

$$\frac{d[A]_{bulk}}{dt} = -(k_{tr}[A]_{bulk} - k_{tr}[A]_s) \quad \text{Equation 3}$$

Where $[A]_{bulk}$ is the solution concentration of sRAGE flowed into the flow cell. $[A]_s$ is the concentration of sRAGE due to the mass transfer near to the surface. $[B]$ is the concentration of MGO-BSA. k_{tr} is the mass transfer rate constant. k_{on} and k_{off} are the association and dissociation rate constant, respectively.

The dissociation constant is defined as $K_d = k_{off}/k_{on}$.

Western blot analysis

GM07373 or HA-RAGE expressing GM07373 cells were sub-cultured in 25 cm² culture flasks for 24 hours. On the following day, cells were incubated in 3% BSA in DMEM media overnight. Cells were either used without further treatment or treated with specific 5 mg/mL MGO modified-BSA (MGO-BSA) in DMEM with 3% (w/v) BSA for 1 hour. For sequential cholesterol depletion, cells were further incubated with 5 mM M β CD in in DMEM with 3% (w/v) BSA for 30 minutes. Cells were rinsed with phosphate buffered saline (PBS) prior to cell lysis. Cell lysis was performed with 300 μ L of cold RIPA buffer (150 mM sodium chloride, 1.0% NP-40 detergent, 0.5% sodium deoxycholate, 0.1% SDS, 50

mM Tris, pH 8.0) with Halt™ protease inhibitor cocktail (1×, Thermo Scientific, Rockford, IL). After the initial lysis treatment, cells were passed through a 21 gauge needle to ensure complete cell lysis. The protein mixture (20 µL of the sample, 7 µL of gel loading buffer and 3 µL of sample reducing agent) was first separated on a NuPAGE® Novex® 4-12% Bis-Tris protein gel (Life Technology, Eugene, OR) and then electro blotted onto Immun-Blot® LF PVDF membrane (Bio-Rad, Hercules, CA) as described previously [3, 4]. The primary antibodies used for probing the PVDF membrane were: anti-RAGE rabbit (H-300, Santa Cruz Biotechnology), anti-vinculin goat (sc-7649, Santa Cruz Biotechnology), anti-p-ERK rabbit (Tyr 204, sc-101761, Santa Cruz Biotechnology), anti-p-Akt rabbit (Ser 473, sc-101761, Santa Cruz Biotechnology). Fluorescence from the labeled secondary antibody was measured on a Typhoon FLA 9500 variable mode laser scanner (GE Healthcare, Waukesha, WI). The vinculin protein band was used as a loading control in all Western blot experiments. The resulting fluorescence band intensities were quantified with ImageJ.

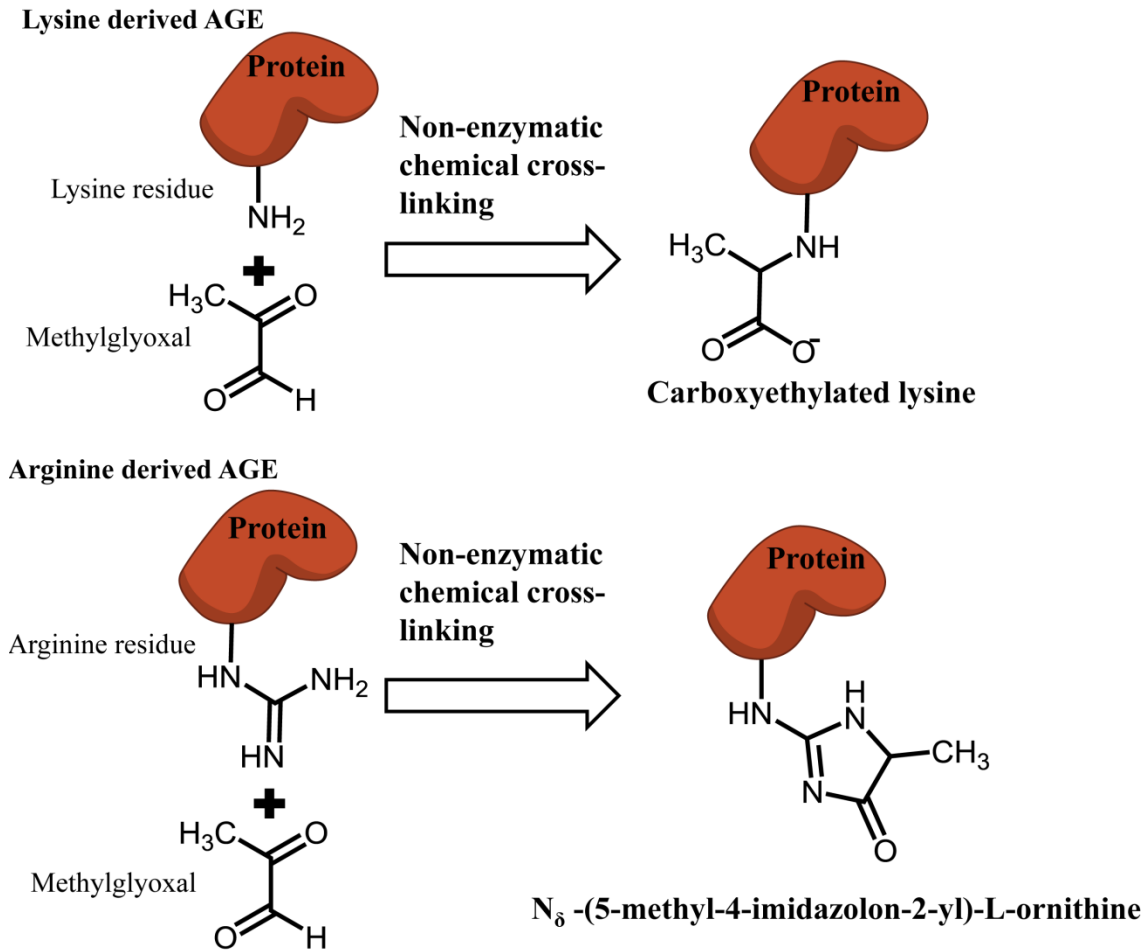


Figure S3.1. Two of the chemical modifications on lysine and arginine residues after incubation with methylglyoxal. A more complete list of protein modifications that can occur after incubation with methylglyoxal can be found in a review by Vistoli et al [5].

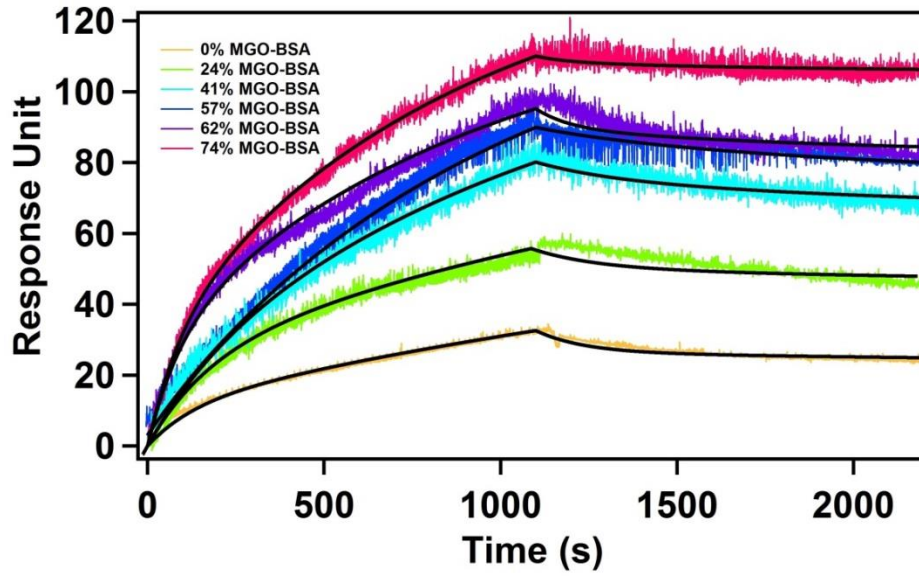


Figure S3.2. Measured surface plasmon resonance (SPR) response over time for binding between MGO-BSA with the indicated percent primary amine modification and sRAGE. The corresponding fits to equations 1 to 3 are shown as solid black lines.

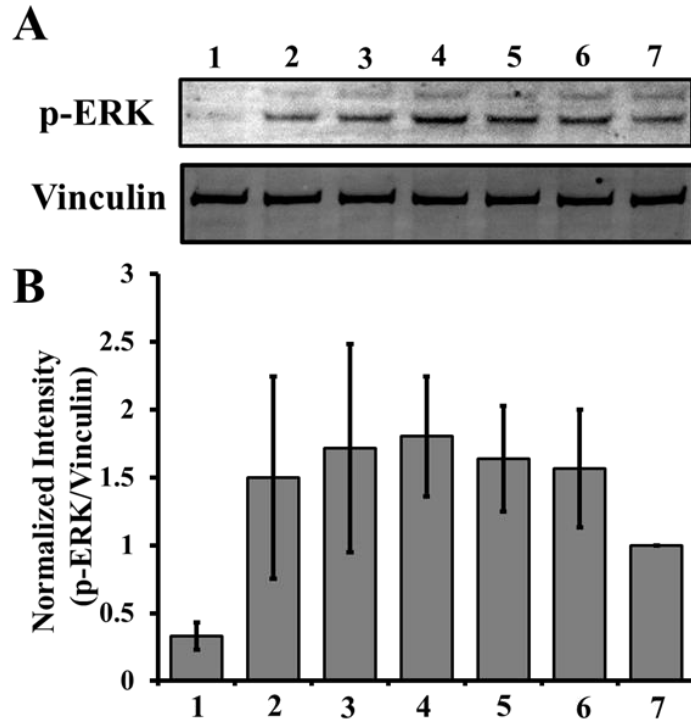


Figure S3.3. Western blot analysis of the **GM07373 cell lysate (no detectable RAGE expression)** with: (Lane 1) no treatment, or 5 mg/mL MGO-BSA treatment with the following percent primary amine modification: (Lane 2) 24%, (Lane 3) 41%, (Lane 4) 57%, (Lane 5) 62%, or (Lane 6) 74%. (Lane 7) No treatment **HA-RAGE expressing GM07373 cell lysate** shows higher p-ERK intensities compared to cells that do not express RAGE (Lane 1). (A) Fluorescence images of the PVDF membrane probed with p-ERK antibody or vinculin antibody. (B) Average ($n = 5$) normalized fluorescence intensities of the 42 kDa band of p-ERK divided by the vinculin band.

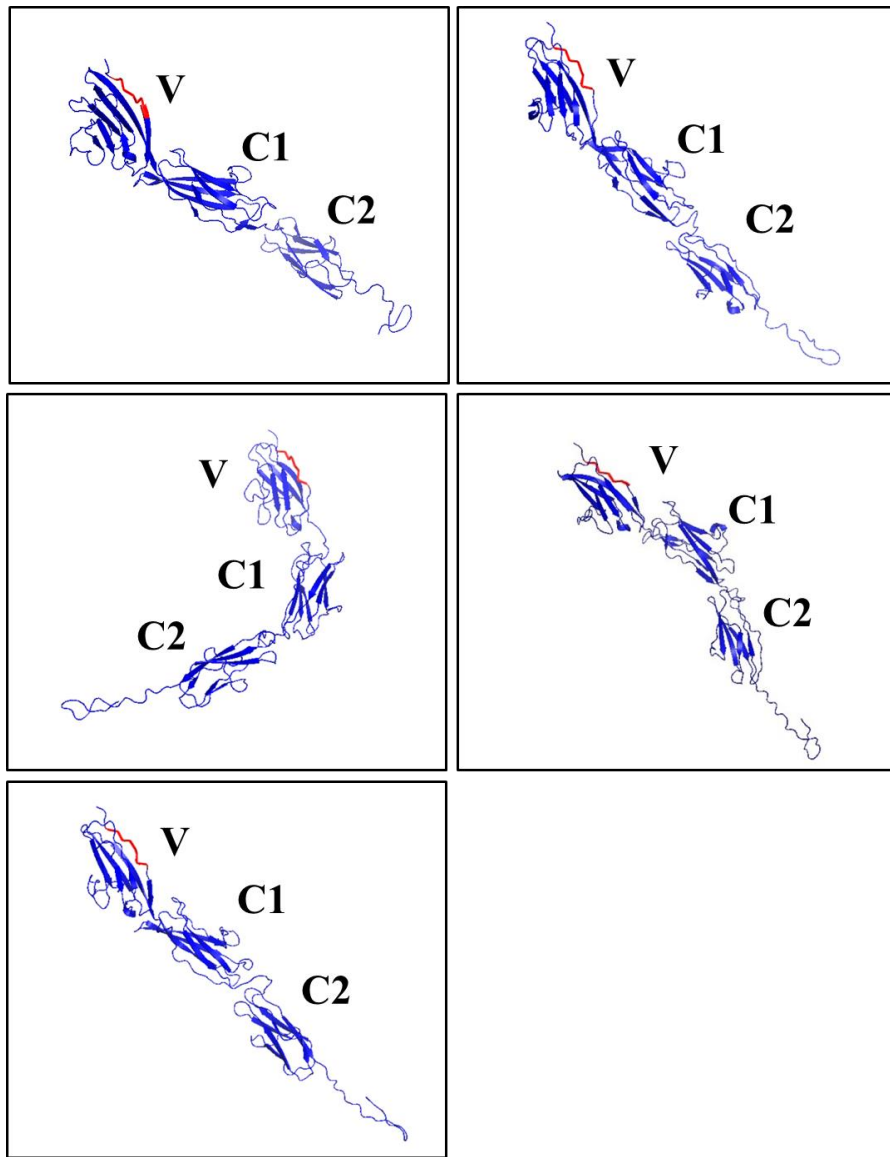


Figure S3.4. I-TASSER suite (<http://zhanglab.ccmb.med.umich.edu/I-TASSER/about.html>) top 5 predicted models for the extracellular domains (V, C1 and C2) of RAGE containing the HA tag (shown in red). Models are reoriented with PyMOL protein structure visualization software for clarity.

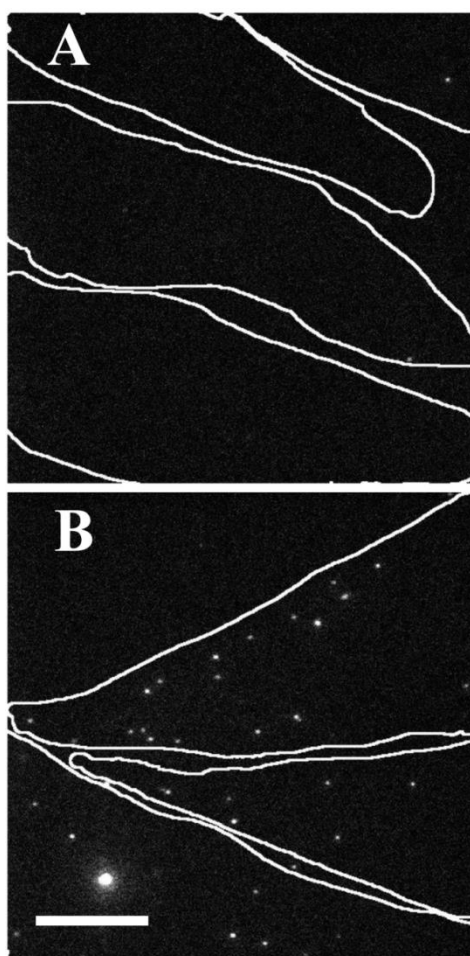


Figure S3.5. Representative fluorescence images after incubation of 100 pM AHA-QDs (in 0.1 % w/v BSA-imaging medium for 15 minutes at 37 °C) with: (A) **GM07373** and (B) **HA-RAGE expressing GM07373** cells. The cell boundaries are outlined in white. The scale bar in the lower left corner of the image B is the same for both images: 20 μm .

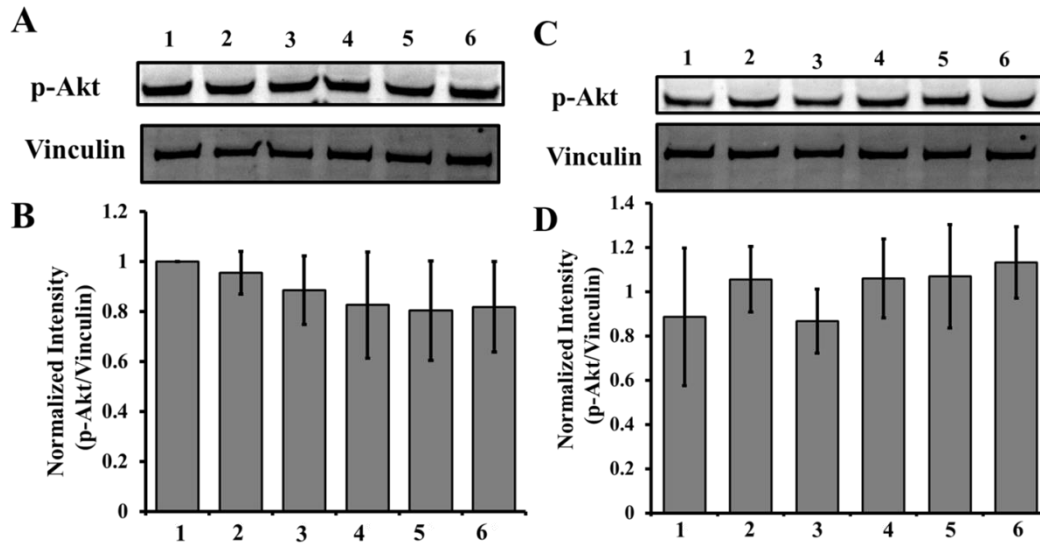


Figure S3.6. Western blot analysis of the (A, B) **HA-RAGE expressing GM07373** or (C, D) **GM07373** cell lysate with: (Lane 1) no treatment, or 5 mg/mL MGO-BSA treatment with the following percent primary amine modification: (Lane 2) 24%, (Lane 3) 41%, (Lane 4) 57%, (Lane 5) 62%, or (Lane 6) 74%. (A, C) Fluorescence images of the PVDF membrane probed with p-Akt antibody or vinculin antibody. (B, D) Average ($n = 5$) normalized fluorescence intensities of the 42 kDa band of p-Akt divided by the vinculin band.

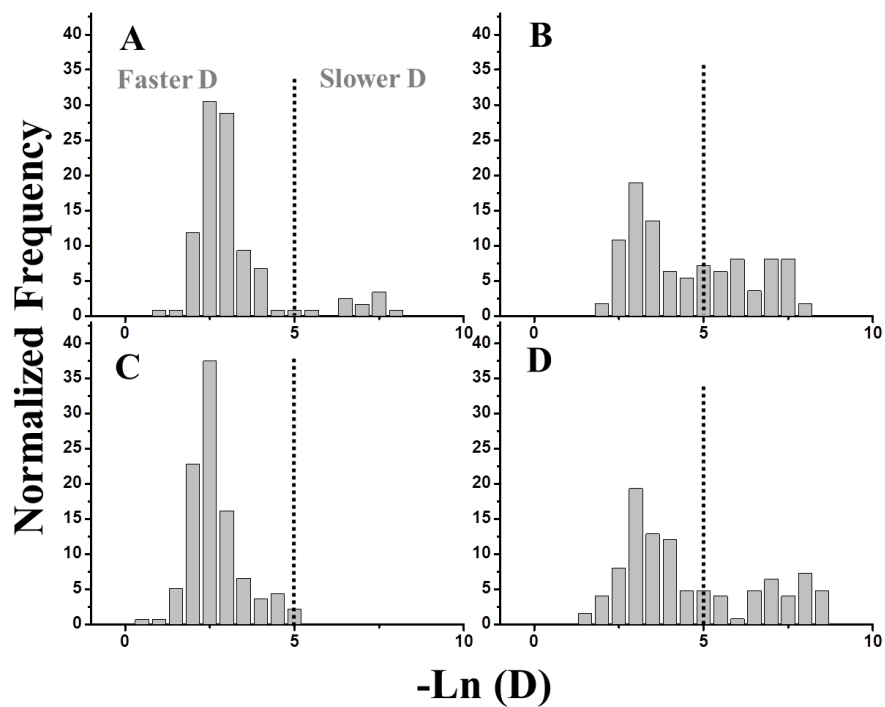


Figure S3.7. Histograms of diffusion coefficients for the **Brownian trajectories** of HA-RAGE in the GM07373 cell membrane treated with: (A) No treatment; (B) 5 mM M β CD to extract cholesterol from the membrane; (C) 62% MGO-BSA and (D) 62% MGO-BSA and 5 mM M β CD. The diffusion coefficient is plotted as the negative natural logarithm; slower diffusion coefficients appear on the right side of the graph. The dotted line is shown for clarity in comparing the changes in the distribution.

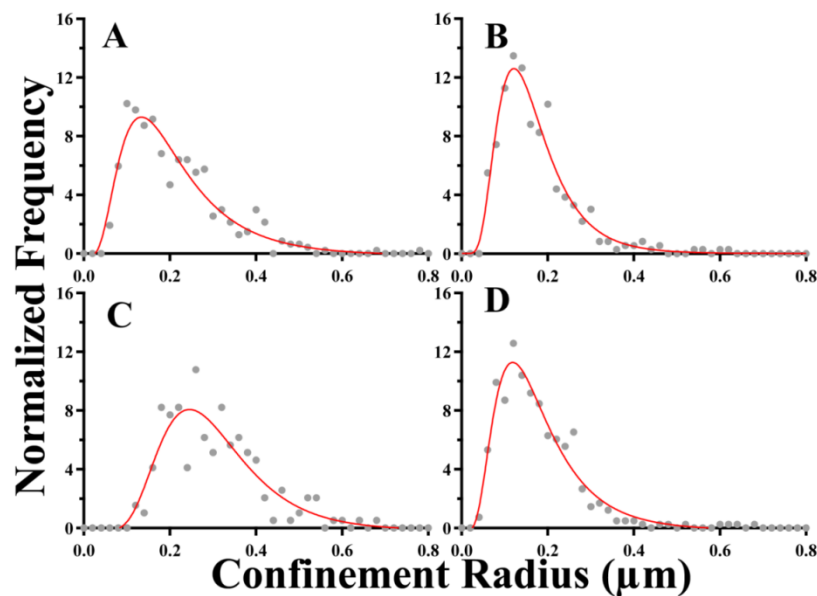


Figure S3.8. Distribution of confinement radius for the **confined trajectories (inside domains of confined diffusion)** of HA-RAGE in the GM07373 cell membrane treated with: (A) No treatment; (B) 5 mM M β CD to extract cholesterol from the membrane; (C) 62% MGO-BSA and (D) 62% MGO-BSA and 5 mM M β CD. The corresponding fits (red solid line) are obtained by fitting the distribution to a log-normal function.

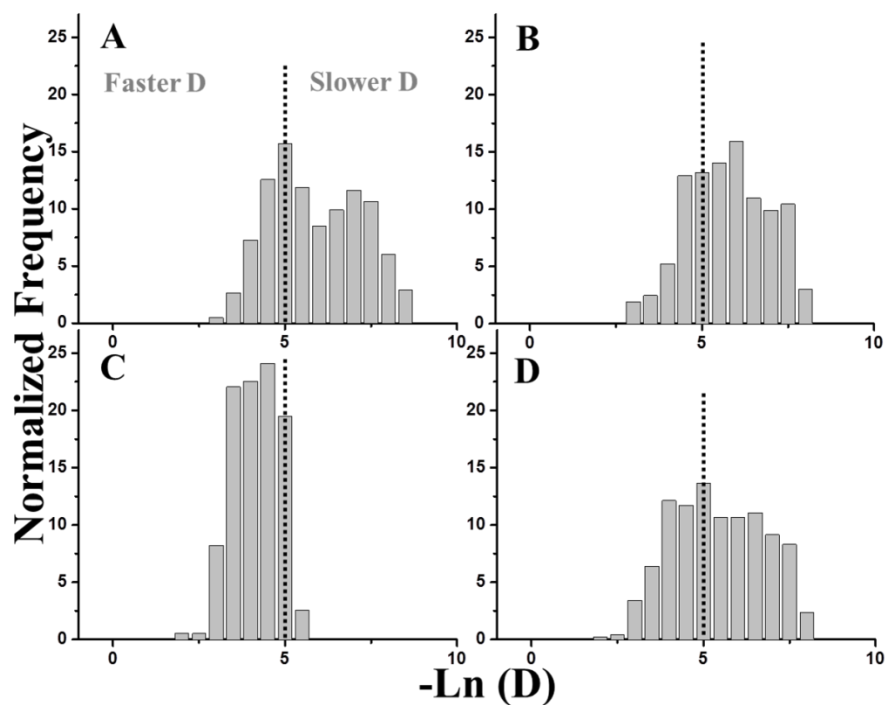


Figure S3.9. Histograms of diffusion coefficients for the **confined trajectories (inside domains of confined diffusion)** of HA-RAGE in the GM07373 cell membrane treated with: (A) No treatment; (B) 5 mM M β CD to extract cholesterol from the membrane; (C) 62% MGO-BSA and (D) 62% MGO-BSA and 5 mM M β CD. The diffusion coefficient is plotted as the negative natural logarithm. The dotted line is shown for clarity in comparing the changes in the distribution.

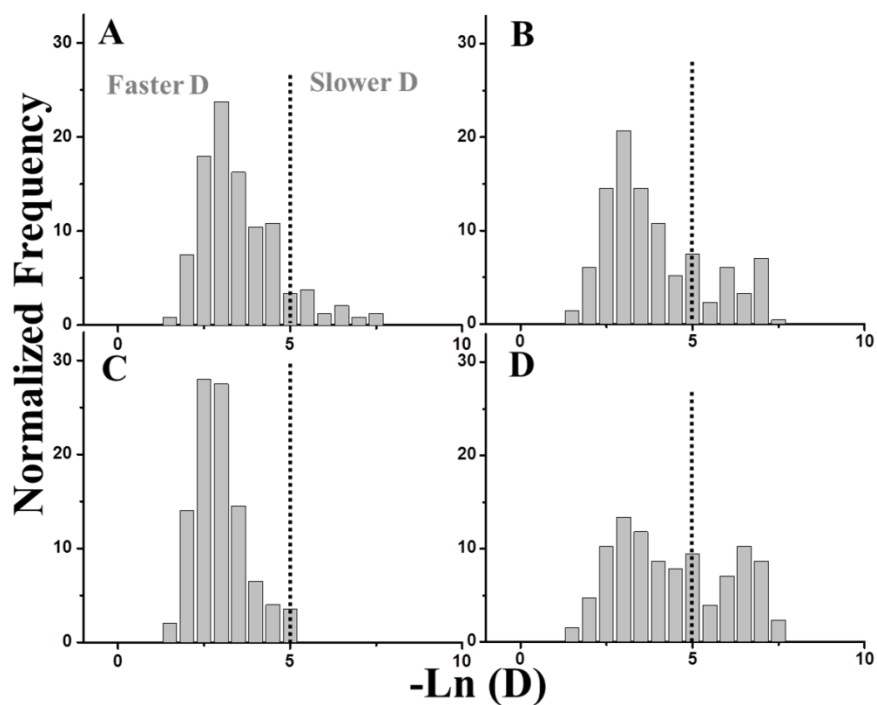


Figure S3.10. Histograms of diffusion coefficients for the **confined trajectories (outside domains of confined diffusion)** of HA-RAGE in the GM07373 cell membrane treated with: (A) No treatment; (B) 5 mM M β CD to extract cholesterol from the membrane; (C) 62% MGO-BSA and (D) 62% MGO-BSA and 5 mM M β CD. The diffusion coefficient is plotted as the negative natural logarithm. The dotted line is shown for clarity in comparing the changes in the distribution.

References for supporting information for Chapter 3

- [1] M. Neeper, A.M. Schmidt, J. Brett, S.D. Yan, F. Wang, Y.C. Pan, K. Elliston, D. Stern, A. Shaw, Cloning and expression of a cell surface receptor for advanced glycosylation end products of proteins, *J. Biol. Chem.*, 267 (1992) 14998-15004.
- [2] A. Syed, Q. Zhu, E. Smith, Lateral Diffusion and Signaling of Receptor for Advanced Glycation End-products (RAGE): A Receptor Involved in Chronic Inflammation, *Eur. Biophys. J.*, Submitted (2016).
- [3] H. Towbin, T. Staehelin, J. Gordon, Electrophoretic transfer of proteins from polyacrylamide gels to nitrocellulose sheets: procedure and some applications, *Proc. Natl. Acad. Sci. U.S.A.*, 76 (1979) 4350-4354.
- [4] P.T. Matsudaira, Strategies for obtaining partial amino acid sequence data. In a practical guide to protein and peptide purification for microsequencing, in, Academic Press, New York, 1989, pp. 29-30.
- [5] G. Vistoli, D. De Maddis, A. Cipak, N. Zarkovic, M. Carini, G. Aldini, Advanced glycoxidation and lipoxidation end products (AGEs and ALEs): an overview of their mechanisms of formation, *Free Radic. Res.*, 47 Suppl 1 (2013) 3-27.

CHAPTER 4

**THE ROLE OF A CONSERVED MEMBRANE PROXIMAL CYSTEINE IN ALTERING
 α PS2C β PS INTEGRIN DIFFUSION**

A paper submitted for publication as a research article

Aleem Syed, Neha Arora, Thomas A. Bunch^b, and Emily A. Smith

4.1. Abstract

Cysteine residues (Cys) in the membrane proximal region are common post-translational modification (PTM) sites in transmembrane proteins. Herein, the effects of a highly conserved membrane proximal α -subunit Cys¹³⁶⁸ on the diffusion properties of α PS2C β PS integrins are reported. Sequence alignment shows that this cysteine is palmitoylated in human α 3 and α 6 subunits. Replacing Cys¹³⁶⁸ with valine (Val¹³⁶⁸) putatively blocks a PTM site and alters integrins' ligand binding and diffusion characteristics. Both fluorescence recovery after photobleaching (FRAP) and single particle tracking (SPT) diffusion measurements show Val¹³⁶⁸ integrins are more mobile compared to Cys¹³⁶⁸ integrins. Approximately 33% and 8% more Val¹³⁶⁸ integrins are mobile as measured by FRAP and SPT, respectively. The mobile Val¹³⁶⁸ integrins also exhibit less time-dependent diffusion, as measured by FRAP. Tandem mass spectrometry data suggest that Cys¹³⁶⁸ contains a redox or palmitoylation PTM in α PS2C β PS integrins. This membrane proximal cysteine may play an important role in the diffusion of other alpha subunits that bear this conserved residue.

4.2. Introduction

The integrin family of cell surface receptors plays a critical role in many fundamental cellular processes like cell adhesion, progression, growth, and proliferation [1]. Integrins mediate bidirectional signaling across the cell membrane [2]. This signaling occurs via ligand binding to integrins (*outside-in signaling*) and via binding of several cytosolic proteins (*inside-out signaling*). In general, signaling depends on the concentration of the involved proteins and also their correct localization in the signaling region [3]. Recent studies highlighted the importance of post-translational modifications (PTM) in localizing a protein into membranes and membrane domains [4]. The goal of the current study is to identify the role of a highly conserved membrane proximal cysteine (Cys¹³⁶⁸) of the α PS2C β PS integrins on the receptor's lateral diffusion in the cell membrane.

Due to the nucleophilicity and redox sensitivity of non-disulfide cysteine amino acid residues, they are prone to various PTMs [5, 6]. Cysteine residues are modified through both spontaneous and enzyme-catalyzed reactions. Some of the common modifications include oxidation (*e.g.* sulfhydrylation, glutathionylation, sulfenylation, sulfonation, and nitrosation), prenylation, palmitoylation, and Michael addition with lipid-derived electrophiles [7-11]. In addition to these, there are rare modifications at cysteine such as methylation and phosphorylation that are reported for both eukaryotic and prokaryotic proteins [12]. There are diverse functional consequences on protein localization, interactions, and trafficking in the cell membrane as a result of cysteine PTMs [13]. Alterations in cysteine PTMs are reported to contribute to proliferative and degenerative diseases [14-16].

Figure 4.1 depicts the multiple sequence alignment of the transmembrane and cytoplasmic domains of selected integrin α subunits of *Caenorhabditis elegans*, *Drosophila melanogaster*, *Homo sapiens*, and *Mus musculus*. There is a cysteine in the membrane proximal region that is conserved among all the subunits. This specific cysteine is palmitoylated in human α 3 and α 6 integrin subunits [17]. Palmitoylation increases the affinity of proteins towards membranes nanodomains [18]. This leads

to the hypothesis that the highly conserved cysteine in the membrane proximal region of α PS2C β PS integrins and its putative PTMs play a role in governing the receptor's biophysical properties. Additionally, it has been reported that the highly conserved GFFXR domain adjacent to the cysteine regulates the adhesive and ligand binding properties of integrins. The deletion of the cytoplasmic tail after the GFFXR domain, deleting the GFFXR domain, or mutating the GFFXR sequence resulted in a two to twelve-fold *increase* in ligand binding affinity compared to wild-type human and *Drosophila* integrins in several cell types [19-22]. On the other hand, there was a two-fold *decrease* in ligand binding affinity when Cys¹³⁶⁸ is replaced with Val¹³⁶⁸ in the α subunit of α PS2C β PS integrins [23]. If Cys¹³⁶⁸ alters α PS2C β PS integrin diffusion properties, it is expected that a mutation to a different residue at this position will produce altered diffusion properties compared to the wild-type receptor. We test this hypothesis by generating a Val¹³⁶⁸ mutation through site directed mutagenesis. The consequences of this mutation on integrin diffusion are measured using fluorescence microscopy. Ensemble diffusion, that is an average across numerous receptors, is measured using fluorescence recovery after photobleaching (FRAP) and the diffusion of single receptors is measured using single particle tracking (SPT). Since receptor diffusion is primarily non-synchronous, measuring one receptor at a time accounts for diffusion heterogeneity. Finally, tandem mass spectrometry is used to identify potential PTMs at Cys¹³⁶⁸.

4.3. Materials and Methods

Cell culture

Drosophila S2 cells were grown in Shields and Sang M3 insect media (M3, Sigma) supplemented with 10% fetal bovine serum (Irvine Scientific), 12.5 mM streptomycin, 36.5 mM penicillin, and 0.2 μ M methotrexate (Fisher Scientific). Six stably transformed S2 cell lines were developed by expressing: (i) wild-type (α PS2C β PS) integrins, (ii) Val¹³⁶⁸ (α PS2C(C1368V) β PS) integrins, (iii) Venus yellow

fluorescent protein (YFP)-tagged wild-type integrins, (iv) YFP-tagged Val¹³⁶⁸ integrins, (v) HA (YPYDVPDYA)-tagged wild-type integrins, and (vi) HA-tagged Val¹³⁶⁸ integrins. YFP or HA tags were inserted in the serine rich loop of the α PS2C subunit as reported previously [20]. The heat shock inducible promoter was used to express all exogenous proteins. Cells were maintained in a 22°C incubator and were heat-shocked in a 36 °C water bath for 30 min to induce expression of integrins before conducting any further experiments.

Immunoprecipitation and LC-MS/MS analysis of wild-type and Val¹³⁶⁸ integrins

Both wild-type and Val¹³⁶⁸ integrin alpha subunits were purified using an HA (YPYDVPDYA) epitope tag. S2 cells expressing HA-tagged wild-type or Val¹³⁶⁸ integrins were heat-shocked for 30 minutes in a 36 °C water bath. Cells were kept in a 22 °C incubator for 3 hours before cell lysis. Cells were lysed using RIPA buffer (150 mM sodium chloride, 1.0% NP-40 detergent, 0.5% sodium deoxycholate, 0.1% sodium dodecyl sulfate, 50 mM Tris, pH8.0) as described previously [24]. Cell lysates were incubated with Pierce™ anti-HA magnetic beads using the manufacturer's instructions. Bound HA-tagged wild-type or Val¹³⁶⁸ integrin alpha subunit was eluted by incubating the beads at 95 °C for 10 minutes with sodium dodecyl sulfate sample buffer (5% SDS, 5% Glycerol, 125 mM Tris-HCl (pH=6.8) and 0.01% Bromophenol Blue). Supernatant from the elution step was directly added to a pre-cast protein gel for separation by electrophoresis. Coomassie stained protein bands corresponding to wild-type or Val¹³⁶⁸ integrin alpha subunit were excised from the gel and were digested with trypsin or chymotrypsin on an automated ProGest (Digilab, Marlborough, MA) protein digestion station. Digested fragments were loaded onto the Q-Exactive tandem mass spectrometer (Thermo Scientific) for LC-MS/MS analysis. The measured peptide fragments were searched for potential PTMs including sulfhydrylation (addition of -SH), nitrosation (addition of -NO), sulfonation (addition of -SO₃) and palmitoylation (addition of palmitic acid through acylation of thiol on cysteine).

Instrumentation

A Nikon Eclipse TE2000U microscope (Melville, NY, USA) equipped with an oil immersion objective (100× 1.49 NA) was used for all microscopy experiments. A mercury lamp was used for imaging, and fluorescence images were collected using a PhotonMAX 512 EMCCD camera (Princeton Instrument, Trenton, NJ, USA). For SPT, a filter set from Omega Optical (XF304-1, Brattleboro, VT, USA) was used for excitation (425/45-nm) and to collect the quantum dot emission (605/20-nm). FRAP images were collected using a 500/20-nm excitation and a 535/30-nm emission filter.

FRAP microscopy

FRAP data were collected and analyzed according to previously published protocols [24-26]. Briefly, cells expressing YFP-tagged wild-type or Val¹³⁶⁸ integrins were plated onto ligand-coated glass slides. A series of images were acquired before and after photobleaching using mercury-lamp excitation on a timeframe of 75 s. Photobleaching was accomplished with the 488-nm line of an argon ion laser. Data were analyzed using ImageJ version 1.38. FRAP curves were fit to extract diffusion parameters according to the method of Feder et al. by fitting the recovery curves to three different models - Brownian, constrained, and mixed diffusion [27]. A reduced χ^2 value closest to 1 was used to indicate the best-fit model, which was the mixed diffusion model for all presented data.

Single particle tracking

Amine-derivatized polyethylene glycol (PEG) quantum dots (Life Technologies) measuring 16 nm in diameter and with emission maxima at 605 nm were used for SPT measurements. Quantum dot probes for SPT were prepared as previously reported [25]. Briefly, quantum dots were conjugated with a recombinant version of the α PS2C β PS integrin ligand, RBB-tiggrin, by mixing a ratio of 1 quantum dot to 20 RBB-Tiggrin in 10 mM phosphate buffer, pH 8.5 for 2 h. The ligand-coated quantum dots were

sonicated for 2 h before diluting to the required concentration for cell incubation, and were then used within half an hour to limit the aggregation of quantum dots [25].

Quantum dot-labeled integrins were localized and tracked using the Particle Tracker Plugin of ImageJ. A total of 91 trajectories were generated for each cell line. Data analysis was performed using a graphical user interface (GUI) in MATLAB to distinguish trajectories with Brownian diffusion, confined diffusion, to calculate diffusion coefficients, and to identify immobile integrin fractions [28].

4.4. Results and Discussion

Cys¹³⁶⁸ to Val¹³⁶⁸ mutation increases α PS2C β PS integrins' mobile fraction

S2 cells expressing wild-type Cys¹³⁶⁸ integrins or Val¹³⁶⁸ integrins are used in this study to reveal the role of Cys¹³⁶⁸ in altering the receptor's diffusion properties. Table 4.1 lists the diffusion parameters for both cell lines obtained from the FRAP curves shown in Figure 4.2. The percentage of mobile wild-type integrins is $59.9 \pm 0.7\%$. In comparison, $93 \pm 1\%$ of the integrins are mobile in cells expressing Val¹³⁶⁸ integrins. Similar to the FRAP results, SPT also measured more mobile integrin trajectories in the Val¹³⁶⁸ cell line (80%) compared to the wild-type cell line (72%) as shown in Table 4.2. (The values measured by SPT are obtained from counting among all measured trajectories so no uncertainty is reported). Thus, the presence of Cys¹³⁶⁸ results in the immobilization of a fraction of integrins.

A difference between the FRAP and SPT experiments is the population of integrins that are measured. All integrins with a fluorescent tag, that is all the integrins in these FRAP studies, contribute to the FRAP signal. On the other hand, the integrins must be bound to ligand on the quantum dot in order to generate a signal in SPT. This may explain the difference in the percentage change of the mobile fraction as measured by the two techniques. In other words, there is a smaller increase in the mobile fraction of the ligand-bound population of integrins measured by SPT as compared with the total integrin population as measured by FRAP when Cys¹³⁶⁸ is replaced with Val¹³⁶⁸.

Cys¹³⁶⁸ to Val¹³⁶⁸ mutation generates more Brownian-like diffusion as measured by FRAP

The α value measured by FRAP is indicative of the time dependence of the diffusion coefficient. An α value of 1 represents Brownian diffusion; lower α values are indicative of more diffusion constraints and a time-dependent diffusion coefficient. For wild-type integrins, the measured α was 0.59 ± 0.01 and this increased to 0.74 ± 0.02 with Val¹³⁶⁸ mutation, indicating more Brownian-like diffusion for Val¹³⁶⁸ integrins. The local constraints to the diffusion of membrane protein arise from interaction with other intracellular, membrane or extracellular components. The Val¹³⁶⁸ mutation may alter one or a combination of interactions, resulting in less time-dependent diffusion.

As measured by SPT, confined domains are defined as regions in the cell membrane where a receptor is located for a time period that is longer than can be explained by Brownian diffusion. Diffusion is Brownian when no confined domains exist during the observed trajectory. A confinement index, L , was calculated at each time point of each trajectory. An L greater than 3.16 for a duration greater than 1.125 s had a likelihood of greater than 99% to reflect confined diffusion as determined from simulated data [24]. Figure 4.3 shows trajectories and plots of the confinement index and diffusion coefficient for a trajectory exhibiting only Brownian diffusion and a trajectory with one confined domain (blue circle). As expected, the confinement index and diffusion coefficient are inversely proportional.

There is no significant difference in the number of confined domains measured for wild-type and Val¹³⁶⁸ integrins (3 confined domains per 30 seconds). When a trajectory shows regions of confinement, the trajectory is further analyzed to determine the size of the confined domains, time in the confined domains and the diffusion coefficient inside the confined domains. These parameters are calculated and compared between wild-type and Val¹³⁶⁸ integrins (Table 4.2). Frequency histograms of confined domain size and duration of confinement are shown in Figures 4.4 and 4.5, respectively. For wild-type integrins, confined domains are 0.260 μm in diameter and the confinement lasted for an average of 2.36

s. There is no statistically significant change in either the time in (2.44 s) or diameter of (0.370 μm) confined domains measured for Val¹³⁶⁸ integrins. While there is no statistically significant change in the average domain size, it is worthy to note that the largest domain size measured for wild-type integrins is 896 nm, while the largest measured for Val¹³⁶⁸ integrins is 2.520 μm .

Alterations in the diffusion coefficient after Cys¹³⁶⁸ to Val¹³⁶⁸ mutation

The last diffusion property to consider is the diffusion coefficient. The average diffusion coefficient measured by FRAP at one second decreased 25% when Cys¹³⁶⁸ in wild-type integrins is replaced with Val¹³⁶⁸. As discussed above, the diffusion coefficient is time dependent as a result of α being less than one; the percent difference in the diffusion coefficient is also time dependent.

For SPT data, an average diffusion coefficient from all points in the trajectory is calculated for the Brownian trajectories. Furthermore, the diffusion coefficients inside confined domains are separately calculated. As shown in Table 4.2, the average diffusion coefficient of Val¹³⁶⁸ integrins was statistically similar to the average diffusion coefficient of wild-type integrins inside and outside confined domains (*i.e.*, when diffusion is Brownian). This indicates that Cys¹³⁶⁸ does not affect the average diffusion coefficient of the ligand-bound integrins as measured in SPT. There is a 4 order of magnitude spread (0.001 to 10 s) in diffusion coefficients measured by SPT, which is consistent with the high degree of diffusion coefficient heterogeneity for many receptors (Figure 4.6).

Post-translational modification of Cys¹³⁶⁸

Tandem mass spectrometry was used to identify modifications at Cys¹³⁶⁸ on the αPS2C subunit. Trypsin digestion of wild-type αPS2C unexpectedly did not result in detection of the peptide containing Cys¹³⁶⁸. Trypsin digests at lysine residues; in the case of the αPS2C subunit, there is a lysine adjacent to Cys¹³⁶⁸ at the C-terminus. Cleavage at this lysine should generate an easy to detect hydrophilic peptide. If trypsin does not cut at this adjacent lysine, however, the next nearest cut site is 36 amino acids away

into the extracellular domain. This would generate a hard to detect, large hydrophobic peptide. Interestingly, the expected fragment containing Val¹³⁶⁸ was detected after trypsin digestion (Table 4.3), indicating the specific presence of Cys¹³⁶⁸ prevents trypsin digestion. We hypothesize that a PTM at Cys¹³⁶⁸ inhibits trypsin digestion (possibly due to steric hindrance) at the adjacent lysine. Peptides containing palmitoylated cysteine (Cys¹⁰⁴ and Cys¹⁷⁰) were detected in the fragment mass spectrum, however, these were found in small hydrophilic peptides.

On the other hand, chymotrypsin digestion (primarily at tyrosine, phenylalanine, tryptophan, and to a lesser extent at leucine and methionine) of integrin α PS2C subunit does produce peptides containing Cys¹³⁶⁸. The mapped amino acids are shown in Figure S4.1 in red font. The Cys¹³⁶⁸ is observed to be modified with a sulfhydryl group or a sulfo group in four detected peptides as shown in Table 4.3. The peptides with sulfhydryl or sulfo-modified Cys¹³⁶⁸ are detected in four independent analyses, although the confidence match in the fragment mass spectrum was low. In two of the four analyses, peptides containing Cys¹³⁶⁸ are also observed to be nitrosylated (addition of -NO) as shown in Table 4.3. It is reported that cysteine modification occurs through nitrosation, as direct sulfhydration is not energetically favorable [29]. Palmitoylation at Cys¹³⁶⁸, however, is not excluded based on the collected data. Detected palmitoylation sites measured after trypsin digestion produce the same PTM detected at Cys¹³⁶⁸ after chymotrypsin digestion. It is possible that the PTM group added by palmitoylation may be labile in these chymotrypsin digests. In summary, redox PTMs were detected on Cys¹³⁶⁸. Given the sequence homology to other integrin alpha subunits that are known to be palmitoylated at this site, it is highly suspected that Cys¹³⁶⁸ is palmitoylated in α PS2C.

4.5. Conclusions

This study revealed a role of Cys¹³⁶⁸ in altering α PS2C β PS integrin diffusion. Both FRAP and SPT measured more mobile integrins when Cys¹³⁶⁸ is mutated, as well as less time-dependent diffusion and a slower average diffusion coefficient as measure by FRAP. Cys¹³⁶⁸ is proposed to be an important PTM

site that regulates the diffusion properties of α PS2C β PS integrins; this conserved cysteine may play a similar role in the biophysical properties of the other integrins listed in Figure 4.1.

Author information

^bCellular and Molecular Medicine, University of Arizona, Tucson, AZ 85721

Acknowledgements

Support for this work was provided by the National Science Foundation (CHE-0845236 and CHE-1412084). The cell lines used in this study were developed by TAB with financial support from National Institute of Health (R01GM42474). The authors thank Joel Nott of the protein facility at Iowa State University for help with mass spectrometry.

4.6. References

- [1] F.G. Giancotti, E. Ruoslahti, Integrin signaling, *Science*, 285 (1999) 1028-1032.
- [2] J. Qin, O. Vinogradova, E.F. Plow, Integrin bidirectional signaling: a molecular view, *PLoS Biol.*, 2 (2004) e169.
- [3] J. Goedhart, J. van Unen, M.J.W. Adjobo-Hermans, T.W.J. Gadella, Signaling efficiency of G alpha q through its effectors p63RhoGEF and GEFT depends on their subcellular location, *Sci. Rep.*, 3 (2013).
- [4] M.J. Nadolski, M.E. Linder, Protein lipidation, *The FEBS J.*, 274 (2007) 5202-5210.
- [5] R.K. Cannan, B.C. Knight, Dissociation Constants of Cystine, Cysteine, Thioglycollic Acid and alpha-Thiolactic Acid, *Biochem. J.*, 21 (1927) 1384-1390.
- [6] Z.R. Gan, W.W. Wells, Identification and reactivity of the catalytic site of pig liver thioltransferase, *J. Biol. Chem.*, 262 (1987) 6704-6707.
- [7] M. Lo Conte, K.S. Carroll, The redox biochemistry of protein sulfenylation and sulfinylation, *J. Biol. Chem.*, 288 (2013) 26480-26488.
- [8] N. Gould, P.T. Doulias, M. Tenopoulou, K. Raju, H. Ischiropoulos, Regulation of protein function and signaling by reversible cysteine S-nitrosylation, *J. Biol. Chem.*, 288 (2013) 26473-26479.
- [9] O. Kabil, N. Motl, R. Banerjee, H₂S and its role in redox signaling, *Biochim. Biophys. Acta*, 1844 (2014) 1355-1366.
- [10] F.L. Zhang, P.J. Casey, Protein prenylation: molecular mechanisms and functional consequences, *Annu. Rev. Biochem.*, 65 (1996) 241-269.
- [11] C.T. Tom, B.R. Martin, Fat chance! Getting a grip on a slippery modification, *ACS Chem. Biol.*, 8 (2013) 46-57.
- [12] S.M. Couvertier, Y. Zhou, E. Weerapana, Chemical-proteomic strategies to investigate cysteine posttranslational modifications, *Biochim. Biophys. Acta*, 1844 (2014) 2315-2330.
- [13] J. Charollais, F.G. Van Der Goot, Palmitoylation of membrane proteins (Review), *Mol. Membr. Biol.*, 26 (2009) 55-66.
- [14] A. Garcia-Garcia, L. Zavala-Flores, H. Rodriguez-Rocha, R. Franco, Thiol-Redox Signaling, Dopaminergic Cell Death, and Parkinson's Disease, *Antioxidants & Redox Signaling*, 17 (2012) 1764-1784.
- [15] Y.M. Go, D.P. Jones, Cysteine/cystine redox signaling in cardiovascular disease, *Free Radic. Biol. Med.*, 50 (2011) 495-509.
- [16] M.D. Resh, Targeting protein lipidation in disease, *Trends Mol. Med.*, 18 (2012) 206-214.
- [17] X. Yang, O.V. Kovalenko, W. Tang, C. Claas, C.S. Stipp, M.E. Hemler, Palmitoylation supports assembly and function of integrin-tetraspanin complexes, *J. Cell Biol.*, 167 (2004) 1231-1240.
- [18] I. Levental, D. Lingwood, M. Grzybek, U. Coskun, K. Simons, Palmitoylation regulates raft affinity for the majority of integral raft proteins, *Proc. Natl. Acad. Sci. U.S.A.*, 107 (2010) 22050-22054.
- [19] T.E. O'Toole, Y. Katagiri, R.J. Faull, K. Peter, R. Tamura, V. Quaranta, J.C. Loftus, S.J. Shattil, M.H. Ginsberg, Integrin cytoplasmic domains mediate inside-out signal transduction, *J. Cell Biol.*, 124 (1994) 1047-1059.
- [20] T.A. Bunch, T.L. Helsten, T.L. Kendall, N. Shirahatti, D. Mahadevan, S.J. Shattil, D.L. Brower, Amino acid changes in Drosophila alphaPS2betaPS integrins that affect ligand affinity, *J. Biol. Chem.*, 281 (2006) 5050-5057.
- [21] P.E. Hughes, F. Diaz-Gonzalez, L. Leong, C. Wu, J.A. McDonald, S.J. Shattil, M.H. Ginsberg, Breaking the integrin hinge. A defined structural constraint regulates integrin signaling, *J. Biol. Chem.*, 271 (1996) 6571-6574.
- [22] C.F. Lu, T.A. Springer, The alpha subunit cytoplasmic domain regulates the assembly and adhesiveness of integrin lymphocyte function-associated antigen-1, *J. Immunol.*, 159 (1997) 268-278.

- [23] T. Kendall, L. Mukai, A.L. Jannuzi, T.A. Bunch, Identification of integrin beta subunit mutations that alter affinity for extracellular matrix ligand, *J. Biol. Chem.*, 286 (2011) 30981-30993.
- [24] N. Arora, A. Syed, S. Sander, E.A. Smith, Single particle tracking with sterol modulation reveals the cholesterol-mediated diffusion properties of integrin receptors, *Phys. Biol.*, 11 (2014) 066001.
- [25] D. Mainali, E.A. Smith, The effect of ligand affinity on integrins' lateral diffusion in cultured cells, *European biophysics journal : Eur. Biophys. J.*, 42 (2013) 281-290.
- [26] S. Sander, N. Arora, E.A. Smith, Elucidating the role of select cytoplasmic proteins in altering diffusion of integrin receptors, *Anal. Bioanal. Chem.*, 403 (2012) 2327-2337.
- [27] T.J. Feder, I. Brust-Mascher, J.P. Slattery, B. Baird, W.W. Webb, Constrained diffusion or immobile fraction on cell surfaces: a new interpretation, *Biophys. J.*, 70 (1996) 2767-2773.
- [28] S.A. Menchon, M.G. Martin, C.G. Dotti, APM_GUI: analyzing particle movement on the cell membrane and determining confinement, *BMC Biophys.*, 5 (2012) 4.
- [29] M.R. Filipovic, Persulfidation (S-sulphydration) and H₂S, *Handb. Exp. Pharmacol.*, 230 (2015) 29-59.

4.7. Figures and Tables

	Transmembrane domain	Cytoplasmic domain
<i>Dm</i> alpha PS2C	ACAGALIFLLLVWLLYK	CGFFNRRNRP TDHSQERQPLRNGYHGDEHL
<i>Hs</i> alpha 8	IVILAILLGLLVLAITLALWK	CGFFDRARPPQ EDMTDREQLTNDKTPEA
<i>Hs</i> alpha 6	WIILVAILAGILMLALLVFIWK	CGFFKRSRYDD SVPRYHAVRIRKEEREIKDEKYIDNLEKKQWITKWNRNESYS
<i>Hs</i> alpha 3	LVLVAVGAGLLLLGLIILLWK	CGFFKRTRYQ IMPKYHAVRIRREEERYPPPGSTLPTKKHWVTSWQTRDQYY
<i>Hs</i> alpha E	LPIIIKGSVGGLLVLIVILVILFK	CGFFKRKYQQL NLESIRKAQLKSENLEEEN
<i>Ce</i> PAT2	WLYLLAILIGLAILLILLLWR	CGFFKRNRPP TEHAELRADROPNAQYADSQSRYTSQDQYNQGRHGQML
<i>Mm</i> alpha 3	LVLVAVGAGLLLLGLIILLWK	CGFFKRARTR ALYEAKRQKAEMKSPSETERLTDDY

Figure 4.1. Sequence alignment of integrin's α -cytoplasmic and transmembrane domains across different species. The single-letter amino acid code is used. Species are: *Ce*, *Caenorhabditis elegans*; *Dm*, *Drosophila melanogaster*; *Hs*, *Homo sapiens*; *Mm*, *Mus musculus*. The amino acid sequence of *Drosophila* α PS2C domain is shown in bold and the conserved cysteines are shown in red.

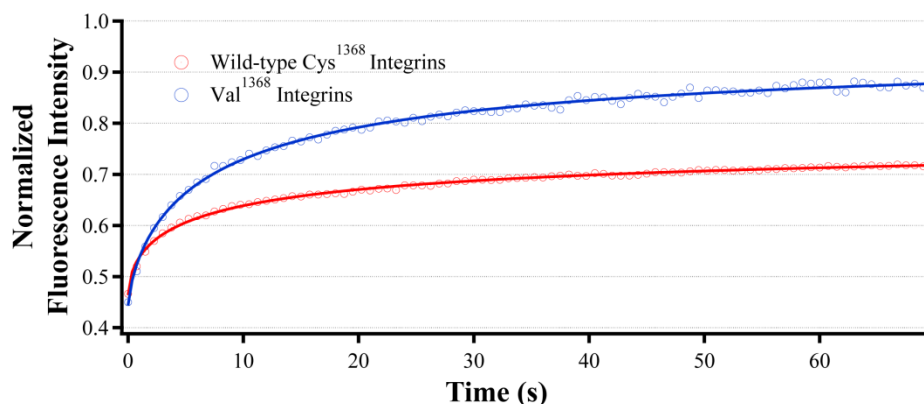


Figure 4.2. Average fluorescence recovery after photobleaching (FRAP) curves (open circles) and corresponding best fit (solid line) to the data. The diffusion parameters extracted from the fit are shown in Table 4.1.

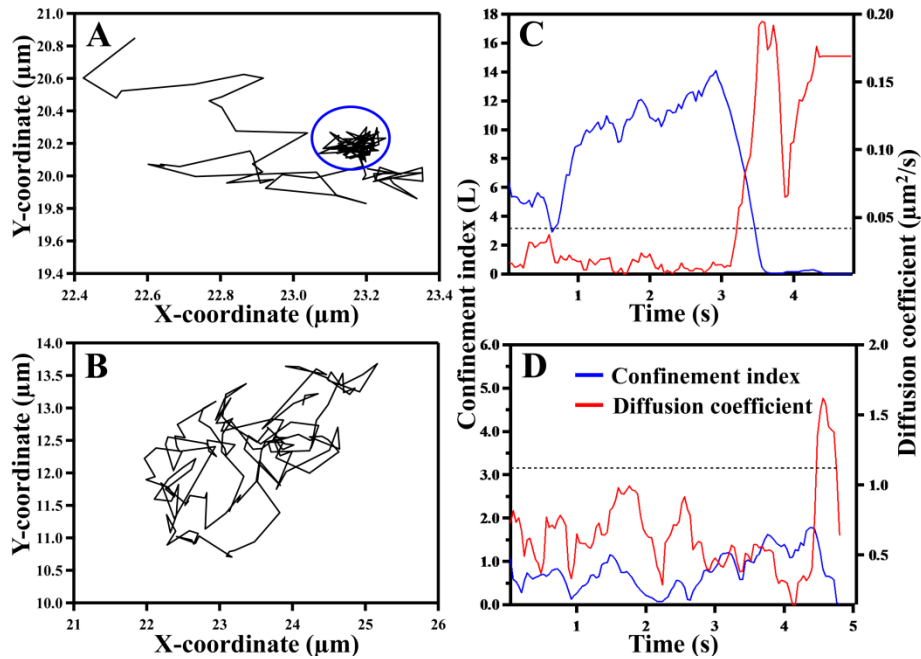


Figure 4.3. Plots showing (A) a trajectory with a single confined domain depicted by a blue circle; (B) a Brownian trajectory with no confined domains. Right panel C-D shows instantaneous diffusion coefficient and confinement index plots. Confined domains are identified from the calculated confinement index (L). An L greater than 3.16 (shown by the dotted line in C and D) for a duration greater than 1.125 s has a greater than 99% likelihood to reflect confined diffusion.

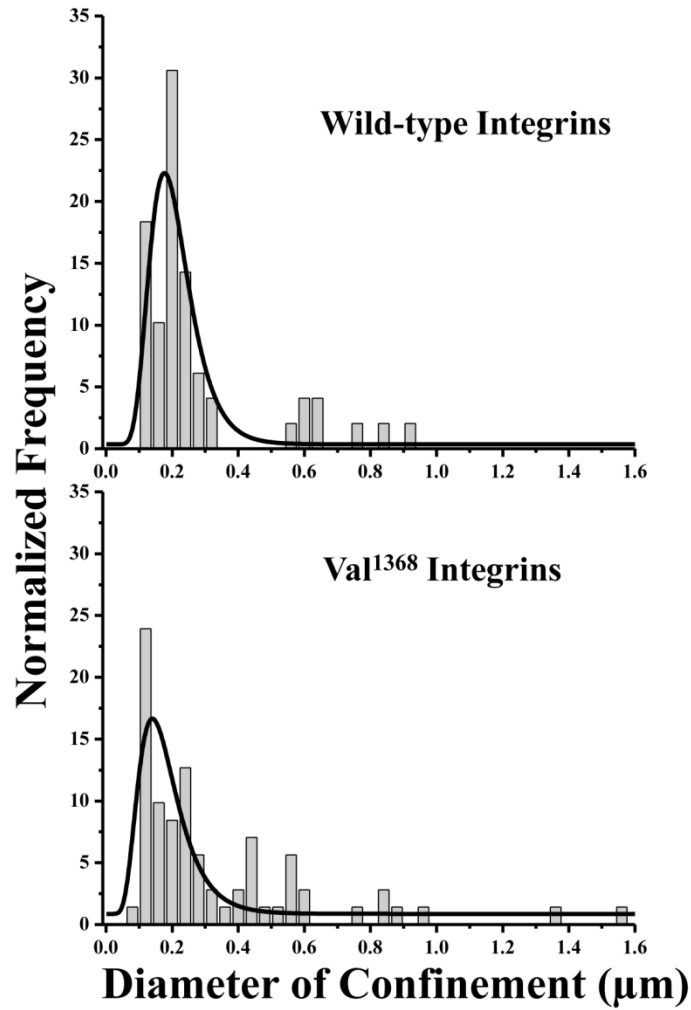


Figure 4.4. Frequency histograms of the size of confined domains. The results were normalized to the total number of measured confined domains (wild-type: 49 confined domains over 539 seconds, and Val¹³⁶⁸ mutant: 71 confined domains over 723 seconds). For clarity, two values are omitted from the Val¹³⁶⁸ graph: one at 2.52 μm and one at 2.08 μm.

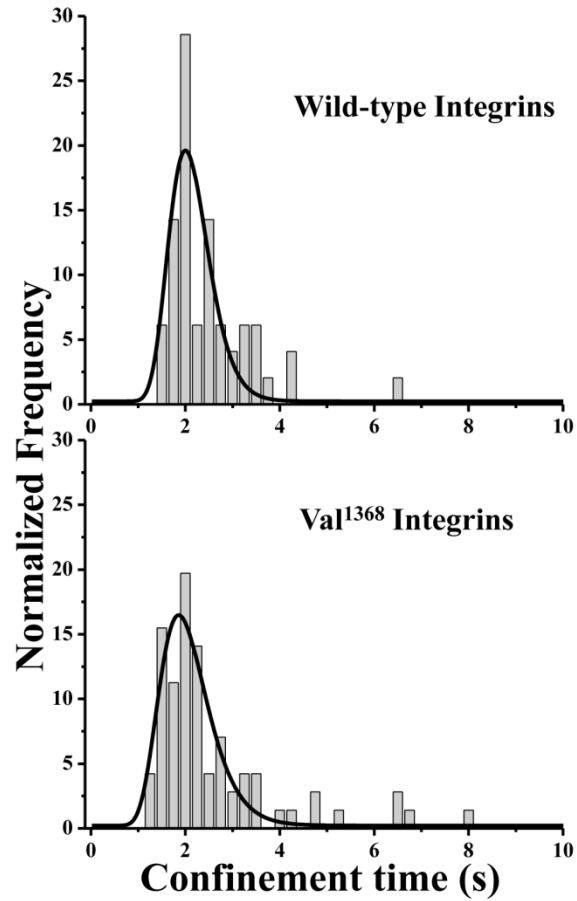


Figure 4.5. Frequency histograms of the duration of confined domains. The results were normalized to the total number of measured confined domains.

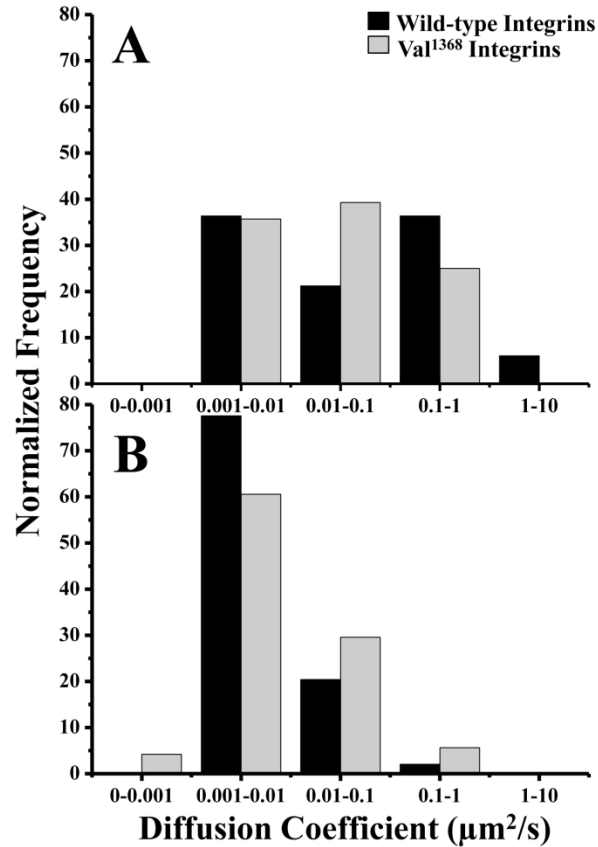


Figure 4.6. Histogram of diffusion coefficients of mobile wild-type and Val¹³⁶⁸ integrins exhibiting (A) Brownian diffusion and (B) for diffusion within confined domains. Histograms were normalized with respect to the total number of trajectories in each data set.

Table 4.1. Diffusion parameters obtained from FRAP experiments.

	D (1s) ($\mu\text{m}^2/\text{s}$)	α	Mobile fraction(%)
Wild-type integrins	0.69 ± 0.02	0.59 ± 0.01	59.9 ± 0.7
Val¹³⁶⁸ integrins	0.52 ± 0.02	0.74 ± 0.02	93 ± 1

Reported values \pm one standard deviation are obtained by fitting the average recovery curve from at least 10 replicate measurements.

Table 4.2. Diffusion parameters obtained from SPT experiments.

	Wild-type integrins	Val¹³⁶⁸ integrins
Total Mobile trajectories (%)	72	80
Average diffusion coefficient for Brownian trajectories ($\mu\text{m}^2/\text{s}$)	0.27	0.10 (p=0.22)
Number of confined domains in 30 seconds	3	3
Average diffusion coefficient inside the confined domains ($\mu\text{m}^2/\text{s}$)	0.013	0.031 (p=0.29)
Average time in confined domains (s)	2.36	2.44 (p=0.57)
Average diameter of the Confined domains (μm)	0.260	0.370 (p=0.16)

p values are obtained from comparing wild-type and Val¹³⁶⁸ data sets using the Kolmogorov–Smirnov (K-S) test.

Table 4.3. Identified peptide fragment containing **Cys¹³⁶⁸** or **Val¹³⁶⁸** and corresponding identified post-translational modification.

Detected Peptides	Detected Post Translational Modification	MH ⁺ (Da)	m/z (Da)
VGFFNR	none	739.39	370.20
KCGFFNRNRPTDHSQERQPL	C2(Sulfo); R17(Deamidated)	2511.13	1256.07
VWLLYKCGF	C7(Sulfo)	1208.54	604.78
LYKCGFFNRNRPTDHSQERQPLRNGYHGDEHL	C4(Sulfo); N10(Deamidated); N24(Deamidated)	3966.77	992.45
LLYKCGFFNRNRPTDHSQERQPL	C5(Sulfo)	2899.38	1450.19
LLYKCGF	C5(Sulhydration)	844.45	422.73
LYKCGFFNRNRPTDHSQERQPL	C4(Sulhydration); N8(Deamidated); N10(Deamidated)	2709.30	903.78
KCGFFNRNRPTDHSQERQPLRNGY	C2(Sulhydration); R9(Deamidated); R17(Deamidated); R21(Deamidated)	2924.37	975.46
LLYKCGFF	C5(Sulhydration)	991.52	496.26
YKCGFFNRNRPTDHSQERQPL	C3(Nitrosyl); R8(Deamidated); R10(Deamidated); R18(Deamidated)	2625.18	875.73
YKCGFFNRNRPTDHSQERQPLRNGY	C3(Nitrosyl)	3112.47	778.87

4.8. Supporting Information for Chapter 4

MSGDSIHRRRMALHCPIITSLILLIAMS GHGYNIDLPSYVFRFRQSSNSMFGFSIAMHKGR
 SGFYGNQNNVSLIVGAPKFDTSRYQQGVTEAGGVFKCSLNDDCKLVPFDSKGNRNRVNDK
 EVVDRKSYQWL GATVATGRDSDLVACAPRYVFHTMTPSRAFRIDPVGTCFTSHNFEEFY
 EVSPCRTNNGYHRQGSCQAGFSAAINGNRSRLFIGAPGSWYWQGQTYSI PPDAKFPFKP
 PLYQPFGTGGMASSHVDTRPENQVFSTSESASVNDDSYLGYSMVTGDFDGD RSEDVAIGM
 PRGGNLVGRIVVNRWNMANIFNITGRQIGEYFGYSLATSDVDGDGLD~~DL~~LIGAPMYTDPD
 NVEGKYDVGRVYILLQGGPTEEKRWTEHIRDGYH~~SKGR~~FGLALTTLGDVNGDGYGDFAV
 GAPYDGP EGRGVVYIFHGSPMGPLAKPSQIIKSEQLVEGAPYPRTFGFALSGGLDMDGNT
 YPDLAVGAYSSDQVFI FKS RPVA AVNAETS FASNSKLI SLDDRSCQLVRDHKKVPCMLLT
 TCWSYTGRYLPEQLDFDVSWLLDAKLLNPRMFFLRDEGKNIRNQTIRLNYGQKYCLNET
 VYLLDKVQDKLTPLEVEARYNLRSSRPLD~~PMVRHRRS~~ILEPVIDQNREIVLRDAINIQKN
 CGPDNICEPDLKLKVSTVDKYLFGSPEPLVIEVFI SNTNEDAFEAAFYMVTPPDLQF~~RKL~~
 QQLGEKKDTPITCSPPTPENNHTLKCDIGNPLESGKIAHFKISLVPEEKYGSSSSSYDFYW
 EANSTNLEKPGSEYDNKIRQSVGIWVDTDLDIKGTSLPDYQLY~~KADDYKELE~~NATKEDDI
 GPQVVHIYEIRNNRPSIIIEAAEVFIHLPYETIVGDPLMYLLNQPETGGKIQCDVAFNEY
 NLLLDEKLVKKSYLQAQGAIWNSAQVSGQSSSSSSSGGASVHIEKARGE~~GFVRGVLVSNS~~
 TDAGDKLSPKQVEQRRQEDTLEALGDASFVHRDRASQAVQEPQVNQTSFTTYSTSSSSSG
 SGAPSAQLRGHSTQGHIQMAGPVQHTSSSSSSSNYRSWPAQQQQHQQLLY~~PYDVPDYALA~~
 GSGGSLGSPVTFNDKSQFGGRNNNFHTGTLDLGTLN RGNVDNELY~~RSQGQYQNPSQSLG~~
 QSQGQFQANANQGHYQGQNAQFQARNPGFQGQTSYQGQTQYSGQPGGYQTHHVITYSSGS
 KPYYGRENE~~FYDEDNLQQATPGHWSSSSSSSSSSSGTRRLRRSNDKDGATEKPLQIDLNS~~
 PCQSARCKSIRCVVTNLGTEDGDAAFVAIRARMVAKTMEKLASNVPLNVSTLAVANVTLL
 PFIGAPKDAIVKTHEIFYKAEPEPLQVPDVVPLWVVVLAACAGALIFLLLVLLLYK~~CGFF~~
 NRRNRPTDHSQERQPLRNGYHGDEHL

Figure S4.1. Identified peptides (in red) for integrin α PS2C subunit in tandem mass spectrometry across two experiments. The data confirm that the separation and purification of the α PS2C subunit from the cell membrane was successful. The fragment in blue font represents the HA-tag. Underlined “C” residue represents Cys¹³⁶⁸.

CHAPTER 5**THE NUMBER OF ACCUMULATED PHOTONS AND THE QUALITY OF STIMULATED
EMISSION DEPLETION LIFETIME IMAGES**

A paper published in Photochemistry and Photobiology as a research article

(Photochem. Photobiol. 90,762-772 (2014). doi: 10.1111/php.12248)

Aleem Syed, Michael D. Lesoine, Ujjal Bhattacharjee, Jacob W. Petrich and Emily A. Smith

5.1. Abstract

Time binning is used to increase the number of photon counts in the peak channel of stimulated emission depletion (STED) fluorescence lifetime decay curves to determine how it affects the resulting lifetime image. The fluorescence lifetime of the fluorophore, Alexa Fluor 594 phalloidin, bound to F-actin is probed in cultured S2 cells at a spatial resolution of ~40 nm. This corresponds to a ten-fold smaller probe volume compared to confocal imaging, and a reduced number of photons contributing to the signal. Pixel-by-pixel fluorescence lifetime measurements and error analysis show that an average of 40 ± 30 photon counts in the peak channel with a signal-to-noise ratio of 20 is enough to calculate a reliable fluorescence lifetime from a single exponential fluorescence decay. No heterogeneity in the actin cytoskeleton in different regions of the cultured cells was measured in the 40- to 400-nm spatial regime.

5.2. Introduction

Fluorescence microscopy has been unparalleled for probing living processes and imaging biological structures in their native environment [1, 2]. Despite the ease of implementation, the inherent inability to resolve closely spaced objects due to the diffractive nature of light remained a major drawback of optical microscopy for decades. Light emitted from a point source in the object plane produces a three dimensional intensity distribution with finite width in the image plane, known as a point spread function (PSF). Hence, closely-spaced point objects are not necessarily separated in the image plane. The diffraction limit hinders the resolution of objects closer than 200 to 300 nm in the lateral and 500 to 700 nm in the axial direction using confocal optical microscopy. Sub-diffraction optical imaging techniques circumvent the diffraction limit, and many of these methodologies have a spatial resolution of 20 nm or better in the lateral and 30-50 nm in the axial directions [3-7]. Stimulated emission depletion (STED) imaging and STED fluorescence lifetime imaging are two sub-diffraction fluorescence techniques [3, 8-10]. In STED microscopy, an improved spatial resolution is achieved by depleting the fluorescence from the periphery of the PSF with a doughnut shaped secondary beam called the depletion beam. Stimulated emission generates an effective PSF with a full-width at half-maximum (FWHM) of a few tens of nanometers in the image plane. Resolution in STED microscopy mainly depends on the intensity of the depletion beam, beam alignment, beam quality, and proper gating of the signal [11-16]. Highly photostable and bright fluorophores, such as the ATTO dye series or quantum dots, are required to achieve the best resolution with STED.

Despite low photostabilities relative to many inorganic fluorophores, conventional organic dyes and fluorescent proteins are desirable in biological fluorescence microscopy due to their ease of implementation and biocompatibility. A major challenge of using these traditional fluorophores in STED fluorescence lifetime imaging, however, is collecting sufficient photons in the peak channel to extract meaningful lifetimes. Theoretical results have shown that one needs to have at least 185 photon

counts in a time window of 8 ns with 256 time channels to measure a 2.5 ns lifetime with 10% variance [17]. Single-molecule fluorescence detection of a dye in a mixture can, however, be performed with fewer photons by comparing the molecular lifetime with bulk lifetimes. Prummer *et al.*, have shown that a total of ~500 photons is required to distinguish four fluorescence lifetimes with 99.9% confidence [18]. On the other hand, exact fluorescence lifetime measurements required ~5000 photon counts to resolve two constrained and two free lifetimes of auto-fluorescent NADH for data acquired in 256 time channels [19]. In this case, fluorescence decay profiles with ~5000 photon counts were achieved only after performing a 3×3 binning of adjacent detector pixels. This strategy increases the signal-to-noise ratios (SNR) in the decay curves, but at the expense of reduced spatial resolution. This strategy is thus not suitable for use in STED lifetime imaging.

Herein, we quantitatively address how the number of photons in the peak channel affects STED fluorescence lifetime images. We discuss ways to increase the photon counts in the peak channel without spatially binning pixels, which compromises the spatial resolution that is the key advantage of using STED microscopy, or increasing acquisition times, which results in unwanted photobleaching that also degrades the spatial resolution [20]. Sub-diffraction lifetime imaging is implemented to study the actin cytoskeleton of cultured cells. Actin inside the cells exists in two forms, a globular monomeric G-actin and polymeric fibrous F-actin. G-actin reversibly polymerizes into a double helical structure and produces thin filaments of F-actin [21]. Sub-diffraction and conventional confocal images are generated. A histogram of lifetimes of 262,144 pixels from confocal and STED lifetime images are compared, and lifetime from different parts of the cell are analyzed.

5.3. Materials and Methods

Sample Preparation

Cultured S2 cells were used in all the experiments. Culture techniques were described previously [22]. The cells (50 μ L, 1.5×10^6 cells/mL) were spread on clean glass coverslips (474030-9000-000, Carl Zeiss Microscopy, Thornwood, NY) for one hour. Unspread cells were rinsed away with phosphate buffer saline (PBS). Paraformaldehyde (4%, in PBS) was used to fix the cells for ten minutes, followed by rinsing with PBS. Triton X-100 (0.1%, in PBS) was used to permeabilize the membrane for 2 minutes followed by the rinsing with PBS. Cells were incubated with bovine serum albumin (1%, in PBS) to avoid nonspecific binding of dye to the glass surface. The actin cytoskeleton was stained with Alexa Fluor 594 conjugated with phalloidin (Life Technology, Gran Island, NY). Phalloidin specifically binds with F-actin [23, 24]. The sample was rinsed with PBS and embedded with mounting medium (VECTASHIELD Hardest Mounting Medium, Burlingame, CA), sandwiched with another coverslip and left to dry for 30 minutes before imaging.

STED apparatus

Our home-built STED system was previously described [12]. Briefly, a super-continuum laser (SC-450-pp-he, Fianium, Southampton, UK) was split into a 570 (± 5)-nm excitation beam and a 695 (± 10)-nm STED beam using a polarizing beam splitter (DMLP605R, Thorlabs, Newton, New Jersey). The laser repetition rate was 2 MHz and the pulse widths for the excitation and STED pulses were approximately 120 and 160 ps with pulse energies 50 pJ and 2 nJ, respectively. An optical delay was used in the STED beam path to offset the STED beam arrival on to the sample by ~ 100 ps. The doughnut profile of the STED beam was generated using a vortex phase plate (RPC Photonics, Rochester, NY). Half-wave plates and quarter-wave plates (Thorlabs) were used in the beam paths as required to adjust the

polarization. Spatially expanded STED and excitation beams were recombined using a dichroic mirror (ZT594RDC, Chroma, Bellows Falls, VT) and sent to the sample through a microscope (Eclipse Ti, Nikon, Melville, NY) immersion oil objective (CFI Apo TIRF 100x, 1.49 NA, Nikon) with a second dichroic mirror (635-70BPDC, Chroma). The fluorescence signal was collected by the same objective and guided to a photo-multiplier tube (PMT) detector (HPM-100-40, Becker and Hickl, Berlin, Germany). A time-correlated, single-photon counting (TCSPC) card was linked to the PMT detector.

Imaging

Samples were raster-scanned over the excitation and STED beams using a sub-nanometer accurate piezo stage (Nano-PDQ375, Mad City Laboratories, Madison, WI). The STED and confocal images were acquired in consecutive scans. Photon counts at each pixel were recorded using single-photon counter v9.30 software (Becker and Hickl). An ~8 ns time window with 64 time channels was used for all measurements. All images were collected at room temperature with 7 ms per pixel dwell time with 512×512 pixels. For all data presented herein, the STED image was collected first followed by the confocal image. There is no measured difference in the mean lifetime measured by STED or confocal imaging modes when image order is switched.

Analysis

Intensity images were analyzed with SPCImage (Becker and Hickl) software. Due to the delay between excitation and depletion beam, suppression of excited molecules with the depletion beam was not efficient at early time points. The signal from the first ~500 ps was discarded by time gating to achieve the best spatial resolution. 64-time channel fluorescence decay curves for 262,144 pixels of the image were extracted using SPCImage. 32- and 16-time channel curves were obtained from 64-time channel

data by adding adjacent two or four channels, respectively. All decay curves were fit to a single exponential decay using IGOR Pro V 6.32A (WaveMetrics Inc., Lake Oswego, OR). Variance (var_N) in the fluorescence lifetime (τ) for N number of collected photons was calculated using the equation [17]:

$$var_N = \frac{1}{N} \tau^2 \frac{\kappa^2}{r^2} [1 - \exp(-r)] \left(\frac{\exp\left(\frac{r}{\kappa}\right) [1 - \exp(-r)]}{\left[\exp\left(\frac{r}{\kappa}\right) - 1\right]^2} - \frac{\kappa^2}{\exp(r) - 1} \right)^{-1}$$

where, κ represents the number of time channels and r is T/τ . T is the measurement window of fluorescence data collection (8.2 ns). The standard deviation is the square root of the variance. Error bars in the lifetime histograms represent an average standard deviation of all measured fluorescence lifetimes in a specific bin. SNRs are calculated from the time gated data as the average signal from the initial six time channels divided by the average signal from the last six time channels. Cross sections were measured using ImageJ 1.44p (National Institutes of Health, USA). All cross sections were fit to a Lorentzian profile. Uncertainties in the cross section are the standard error in the fit. MATLAB version R2013a (Mathworks, Natick, MA) and Origin (OriginLab, Northampton, MA) were used for subsequent analysis.

5.4. Results and Discussion

40-nm spatial resolution STED images of the actin cytoskeleton

F-actin in fixed cultured cells was stained with Alexa Fluor 594 conjugated with phalloidin. The actin cytoskeletal network was imaged with STED (Figure 5.1a and 5.1c) and conventional confocal microscopy (Figure 5.1b and 5.1d). Cross sections of selected actin projections were measured in both STED and confocal (Figure 5.1e) images. At cross section 1 in Figure 5.1a, the measured thickness of the actin fiber was 44 ± 4 nm, as determined by STED imaging, whereas the same fiber was observed to be 400 ± 80 nm with confocal imaging. A spatial resolution of 40 nm was reported previously for the

STED system used to collect similar data [12]. For the previous and current experiments, the microscope objective was underfilled to achieve the best spatial resolution in the STED imaging format. Optical artifact in the illumination profile due to defects in the optics can be minimized by underfilling the objective [25]. Underfilling the back aperture of the objective produces a nearly Gaussian illumination profile in the focal plane and reduces the effective numerical aperture of the objective. The expanded illumination in the focal plane degrades the spatial resolution in confocal images to ~ 400 nm, but provides the best spatial resolution in the STED imaging mode based on our experimental observation.

In STED image Figure 5.1a, the actin projections shown in cross section 2 were two separate filaments with cross sections 120 ± 10 and 72 ± 7 nm. The same actin projections in confocal mode were convoluted to produce an apparent single fiber with a FWHM of 510 ± 40 nm. Similarly, at cross section 3 in Figure 5.1c, STED could resolve actin fibers with thicknesses of 100 ± 20 nm and 44 ± 6 nm that appeared to be a single actin filament with a cross section of 800 ± 100 nm in the confocal image Figure 5.1d. Also, four adjacent actin fibers in cross section 4 (Figure 5.1c) were well resolved in the STED image with cross sections 70 ± 10 , 70 ± 20 , 250 ± 40 and 130 ± 20 nm. The same four actin fibers were poorly resolved into two fibers with thicknesses of 610 ± 90 and 800 ± 100 nm. Figure 5.1a and 5.1c show a STED imaging artifact. Intense features are surrounded by a shadow that slightly reduces signal to background ratios. This artifact is attributed to incomplete depletion from the depletion laser beam [12].

STED lifetime imaging and the required number of peak channel photon counts to measure lifetimes accurately

The smaller probe volume in the STED imaging mode correlates to probing a maximum of 60 Alexa Fluor 594 phalloidin molecules attached to F-actin. The confocal probe volume is ten-fold larger. An

average of 600 ± 400 and 2000 ± 2000 photons per pixel from 262,144 pixels was measured in the STED (Figure 5.1a) and confocal image (Figure 5.1b) with a time window of 8.2 ns and 64 channels. The standard deviation is large because background pixels (presumed to contain no Alexa Fluor 594 molecules) have been included in the analysis. The average number of photon counts in the peak channel of the STED image was 40 ± 30 and the SNR was 20 for data collected in 64 time channels. In regards to STED lifetime imaging, extracting accurate fluorescence lifetimes may be problematic from the data with few photons in the peak channels.

In order to compare the lifetime extracted from the single-exponential fits of decay curves at each pixel in the STED lifetime image (Figure 5.1a) as the number of photons collected in the peak channel increases, time binning the decay curves was employed. Either 64, 32, or 16 channels were considered at each pixel of a 512×512 pixel image. Representative decay curves are shown in Figure 5.2 for three pixels from the locations shown by the corresponding colored arrows in Figure 5.1a (a: 64 channels, b: 32 channels and c: 16 channels). As the number of time channels is reduced, the quality of the fit increased with the number of photon counts in the peak channel. The adjusted R squared value of the fit is improved from 0.7 (64 channels) to 0.98 (16 channels) for the pixel represented with red symbols in Figure 5.2. Considering all 262,144 pixels in the image, the average number of counts in the peak channel is 40 ± 30 , 70 ± 50 and 100 ± 100 for the 64, 32 and 16 time channel analyses, respectively. In all three cases, the time per channel (0.125 ns/channel to 0.5 ns/channel) is larger than the lifetime of Alexa Fluor 594 in the cell (approximately 2 ns).

The decay curves were fit to a single exponential function, and the average lifetimes were found to be statistically similar 2.0 ± 0.1 , 2.1 ± 0.1 and 2.3 ± 0.2 ns as the number of time channels decreased from 64 to 32 to 16 for the first pixel highlighted in Figure 5.2. A histogram of lifetimes is suitable to evaluate whether this trend holds for all 262,144 pixels in the image (Figure 5.3). Histograms of lifetimes show remarkable similarities with Gaussian fits that have means of 2.0 ± 0.1 , 1.9 ± 0.1 and 2.0

± 0.1 ns for 64, 32 and 16 time channel data, respectively, and statistically similar widths. This indicates that an average of 40 ± 30 photons in the peak channel with a SNR of 20 is sufficient to extract meaningful lifetime values when the decay curves are fit to a single exponential function. This also shows that time binning can be applied to increase the number of photons in the peak channel without affecting the lifetime values.

Comparison of diffraction limited and sub-diffraction fluorescence lifetime images

Depending on the size of the feature that generates the fluorescence signal, the distribution of fluorescence lifetimes may vary for a diffraction-limited and a sub-diffraction microscopy experiment. For example, if there are domains that form in the tens of nanometer regime, and the lifetime of fluorophores in these regimes are altered compared to the "bulk" lifetime, STED lifetime imaging will reveal these altered lifetimes; whereas confocal imaging will produce an average lifetime. To evaluate the fluorescence lifetime distribution in sub-diffraction and diffraction limited imaging modes, fluorescence lifetimes measured for data collected in 64 channels for all 262,144 pixels in STED and confocal imaging were compared. Figure 5.4 shows the histograms of fluorescence lifetimes for the STED and confocal images of the same cell. Gaussian fits to STED and confocal distributions resulted in a mean fluorescence lifetime of 2.0 ± 0.1 and 1.76 ± 0.05 ns for Alexa Fluor 594 phalloidin, respectively.

In order to evaluate the reason for the 0.2 ns shift to longer lifetimes in the mean value of the STED distribution, background contributions to the histogram should be considered. There are three sources of background in the STED images. These are lifetimes that are generated in regions with concentrations of Alexa Fluor 594 that are below the detection limit (i.e., primary regions where the cell is not located), background that is generated from the depletion laser, and background that is generated from incomplete depletion of Alexa Fluor 594 at the periphery of the excitation beam. Incomplete

depletion does not shift the mean fluorescence lifetime nor alter the shape of the histogram compared to that shown in Figure 5.4 for the STED images (Figure 5.5a), and thus can be largely ignored when interpreting the histogram. If the depletion is not complete, however, the pixel frequency for any lifetime in the histogram may be slightly increased. Background from the STED laser alone is shown in Figure 5.5b for a solution of Alexa Fluor 594. Compared to the histogram generated using both the excitation and depletion lasers, the histogram generated using only the depletion laser shifts the mean frequency to longer lifetimes by 0.2 ns. The data in Figure 5.5b were collected for a solution. The difference between a solution Alexa Fluor 594 lifetime of 3.9 ns and the fluorescence lifetime measured in the cell could be the result of quenching inside the cell, as reported for fluorescein-type dyes [26, 27]. The background generated in regions with low concentrations of Alexa Fluor 594 produces a broad histogram with a mean of 1.7 ns (confocal) and 1.1 ns (STED) as shown in Figure 5.5c. In the confocal images, this is the only source of background and represents approximately 15% of all the pixels for the image shown in Figure 5.1b. In theory this contribution to the background could be removed with an intensity threshold representing the maximum background value. However, a histogram of pixel frequency versus intensity is continuous and application of a threshold will produce either false positive or false negative pixels, depending on the value of the threshold. Considering all three sources of background, the depletion beam is expected to be the main difference in the background between confocal and STED images. This is most likely the reason the STED histogram exhibits a slight shift to longer lifetimes compared to the confocal histograms. The extent of this shift depends on the concentration of Alexa Fluor 594 in the probed region.

Since the local environment of actin and the lifetime of Alexa Fluor 594 phalloidin bound to actin might be altered in different parts of the cell, lifetime histograms were also generated for selected regions of interest (Figure 5.6). In all regions except f, the mean value of the STED histogram has a statistically significant shift to longer lifetimes compared to the confocal data. The magnitude of the

shift varies from one region to another (0.4, 0.4, 0.3, 0.4, 0.4, 0.2 ns for a to f, respectively), and correlates with the mean fluorescence intensity for each region of interest. This is expected for increased background signal from the STED beam. The Alexa Fluor 594 concentration in region f is relatively low compare to other regions. The background from the depletion beam does not result in a statistically significant shift of the mean fluorescence lifetime compared to regions with higher fluorophore concentrations. The similarities in the STED and confocal fluorescence lifetime distributions, when expected from background are considered, indicate no detectable heterogeneity in the Alexa Fluor 594 phalloidin environment is present in the 40- to 400-nm spatial regime.

5.5. Conclusions

Sub-diffraction images of the actin-cytoskeleton were generated with a spatial resolution of ~40 nm in cultured cells. The photon count in the peak channel was increased by time binning the 64 time channel data without compromising the spatial resolution. Detailed pixel-by-pixel analysis of fluorescence lifetime measurements with different photon counts in the peak channel has shown that an average of 40 ± 30 photons in the peak channel and approximately 600 photons collected in total with a SNR of 20 is enough to calculate reliable lifetimes. This is an important parameter since it governs the collection time required to obtain a meaningful fluorescence lifetime while reducing photodamage and photobleaching to biological samples and fluorophores. The current work used a 2 MHz laser. STED imaging with a 20 MHz laser has been demonstrated. Assuming a 20 MHz laser was used and a 40% detection efficiency, 600 photons could be recorded with a 75 microsecond dwell time per pixel. Under these experimental conditions, the state settling time (i.e., the time it takes after the translation stage moves to settle to a point where vibrations do not affect the data), which is one the order of a few milliseconds, represents the majority of the imaging time. Although the probe volume in the STED imaging mode is tenfold smaller compared to the confocal mode, similar fluorescence lifetime distributions of the fluorophore

attached to F-actin were obtained across the entire cultured cell when expected contributions from background are considered. However, the current study indicates STED fluorescence lifetime imaging can be used to probe heterogeneity in the 40-nm regime in biological samples in aqueous environments.

Acknowledgments

The STED microscope was built using funds from the National Science Foundation Chemical Research Instrumentation and Facilities program (CHE-1026028) and image analysis was supported by the National Science Foundation under Grant CHE-0845236. Image collection was supported by the U.S. Department of Energy, Office of Basic Energy Sciences, Division of Chemical Sciences, Geosciences, and Biosciences through the Ames Laboratory. The Ames Laboratory is operated for the U.S. Department of Energy by Iowa State University under Contract No. DE-AC02-07CH11358.

5.6. References

- [1] J.W. Lichtman, J.A. Conchello, Fluorescence microscopy, *Nat. Methods*, 2 (2005) 910-919.
- [2] B.N. Giepmans, S.R. Adams, M.H. Ellisman, R.Y. Tsien, The fluorescent toolbox for assessing protein location and function, *Science*, 312 (2006) 217-224.
- [3] S.W. Hell, J. Wichmann, Breaking the diffraction resolution limit by stimulated emission: stimulated-emission-depletion fluorescence microscopy, *Opt. Lett.*, 19 (1994) 780-782.
- [4] M. Hofmann, C. Eggeling, S. Jakobs, S.W. Hell, Breaking the diffraction barrier in fluorescence microscopy at low light intensities by using reversibly photoswitchable proteins, *Proc. Natl. Acad. Sci. U.S.A.*, 102 (2005) 17565-17569.
- [5] M.J. Rust, M. Bates, X. Zhuang, Sub-diffraction-limit imaging by stochastic optical reconstruction microscopy (STORM), *Nat. Methods*, 3 (2006) 793-795.
- [6] E. Betzig, G.H. Patterson, R. Sougrat, O.W. Lindwasser, S. Olenych, J.S. Bonifacino, M.W. Davidson, J. Lippincott-Schwartz, H.F. Hess, Imaging intracellular fluorescent proteins at nanometer resolution, *Science*, 313 (2006) 1642-1645.
- [7] D. Wildanger, R. Medda, L. Kastrup, S.W. Hell, A compact STED microscope providing 3D nanoscale resolution, *J. Microsc.*, 236 (2009) 35-43.
- [8] E. Auksoorius, B.R. Boruah, C. Dunsby, P.M. Lanigan, G. Kennedy, M.A. Neil, P.M. French, Stimulated emission depletion microscopy with a supercontinuum source and fluorescence lifetime imaging, *Opt. Lett.*, 33 (2008) 113-115.
- [9] J. Buckers, D. Wildanger, G. Vicidomini, L. Kastrup, S.W. Hell, Simultaneous multi-lifetime multi-color STED imaging for colocalization analyses, *Opt. Exp.*, 19 (2011) 3130-3143.
- [10] P.-Y. Lin, Y.-C. Lin, C.-S. Chang, F.-J. Kao, Fluorescence Lifetime Imaging Microscopy with Subdiffraction-Limited Resolution, *Jpn. J. Appl. Phys.*, 52 (2013) 028004.
- [11] M.D. Lesoine, U. Bhattacharjee, Y. Guo, J. Vela, J.W. Petrich, E.A. Smith, Subdiffraction, Luminescence-Depletion Imaging of Isolated, Giant, CdSe/CdS Nanocrystal Quantum Dots, *J. Phys. Chem. C*, 117 (2013) 3662-3667.
- [12] M.D. Lesoine, S. Bose, J.W. Petrich, E.A. Smith, Supercontinuum stimulated emission depletion fluorescence lifetime imaging, *J. Phys. Chem. B*, 116 (2012) 7821-7826.
- [13] M. Leutenegger, C. Eggeling, S.W. Hell, Analytical description of STED microscopy performance, *Opt. Exp.*, 18 (2010) 26417-26429.
- [14] J.R. Moffitt, C. Osseforth, J. Michaelis, Time-gating improves the spatial resolution of STED microscopy, *Opt. Exp.*, 19 (2011) 4242-4254.
- [15] G. Vicidomini, G. Moneron, K.Y. Han, V. Westphal, H. Ta, M. Reuss, J. Engelhardt, C. Eggeling, S.W. Hell, Sharper low-power STED nanoscopy by time gating, *Nat. Methods*, 8 (2011) 571-573.
- [16] G. Vicidomini, A. Schonle, H. Ta, K.Y. Han, G. Moneron, C. Eggeling, S.W. Hell, STED nanoscopy with time-gated detection: theoretical and experimental aspects, *PLoS One*, 8 (2013) e54421.
- [17] M. Köllner, J. Wolfrum, How many photons are necessary for fluorescence-lifetime measurements?, *Chem. Phys. Lett.*, 200 (1992) 199-204.
- [18] M. Prummer, C.G. Hubner, B. Sick, B. Hecht, A. Renn, U.P. Wild, Single-molecule identification by spectrally and time-resolved fluorescence detection, *Anal. Chem.*, 72 (2000) 443-447.
- [19] M.A. Yaseen, S. Sakadzic, W. Wu, W. Becker, K.A. Kasischke, D.A. Boas, In vivo imaging of cerebral energy metabolism with two-photon fluorescence lifetime microscopy of NADH, *Biomed. Opt. Exp.*, 4 (2013) 307-321.
- [20] J. Hotta, E. Fron, P. Dedecker, K.P. Janssen, C. Li, K. Mullen, B. Harke, J. Buckers, S.W. Hell, J. Hofkens, Spectroscopic rationale for efficient stimulated-emission depletion microscopy fluorophores, *J. Am. Chem. Soc.*, 132 (2010) 5021-5023.

- [21] K.C. Holmes, I. Angert, F.J. Kull, W. Jahn, R.R. Schroder, Electron cryo-microscopy shows how strong binding of myosin to actin releases nucleotide, *Nature*, 425 (2003) 423-427.
- [22] D. Dibya, N. Arora, E.A. Smith, Noninvasive measurements of integrin microclustering under altered membrane cholesterol levels, *Biophys. J.*, 99 (2010) 853-861.
- [23] J.E. Estes, L.A. Selden, L.C. Gershman, Mechanism of action of phalloidin on the polymerization of muscle actin, *Biochemistry*, 20 (1981) 708-712.
- [24] J. Vandekerckhove, A. Deboen, M. Nassal, T. Wieland, The phalloidin binding site of F-actin, *EMBO J.*, 4 (1985) 2815-2818.
- [25] S.T. Hess, W.W. Webb, Focal volume optics and experimental artifacts in confocal fluorescence correlation spectroscopy, *Biophys. J.*, 83 (2002) 2300-2317.
- [26] N. Marme, J.P. Knemeyer, M. Sauer, J. Wolfrum, Inter- and intramolecular fluorescence quenching of organic dyes by tryptophan, *Bioconjug. Chem.*, 14 (2003) 1133-1139.
- [27] H. Chen, S.S. Ahsan, M.B. Santiago-Berrios, H.D. Abruna, W.W. Webb, Mechanisms of quenching of Alexa fluorophores by natural amino acids, *J. Am. Chem. Soc.*, 132 (2010) 7244-7245.

5.7. Figures and Tables

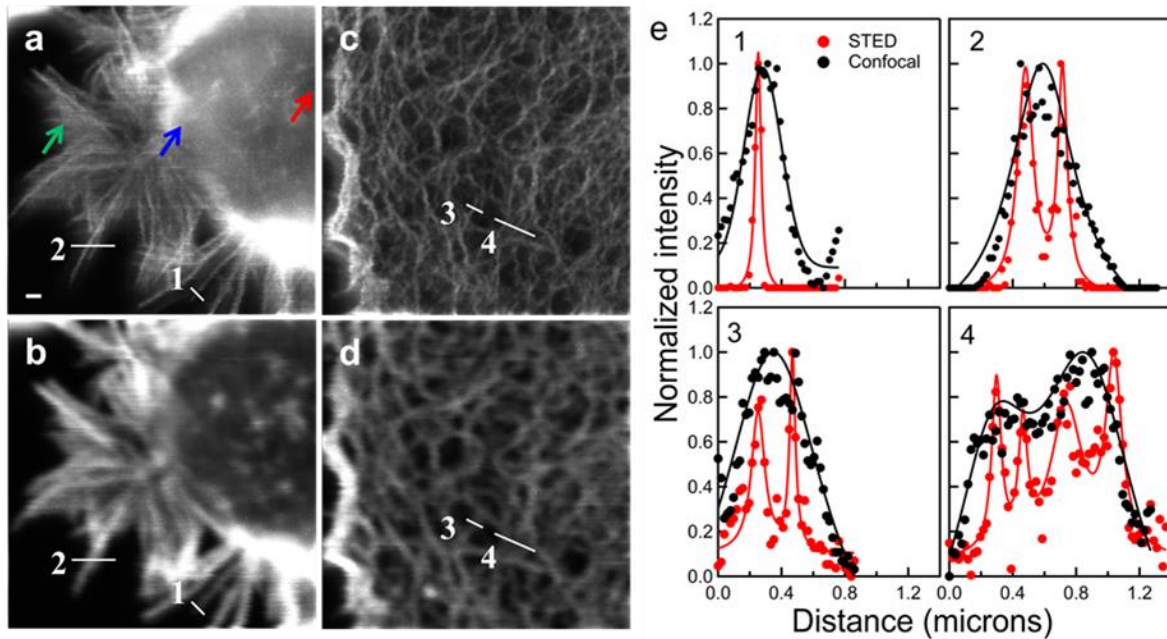


Figure 5.1. Intensity images of actin fibers labeled with Alexa Fluor 594 phalloidin: (a) and (c) STED; (b) and (d) confocal images. The scale bar in the lower left corner of image a is the same for all images: 500 nm. (e) Corresponding cross-sections (1, 2, 3 and 4) for STED (red solid circle) and confocal (black solid circle) imaging modes. The cross sections are fit to a Lorentzian function (solid line) to obtain the width of the fiber(s). Uncertainties in the cross section are the standard error in the fit. Three pixels highlighted with colored arrows in 1a represent locations where the fluorescence decay curves in Figure 5.2 were obtained.

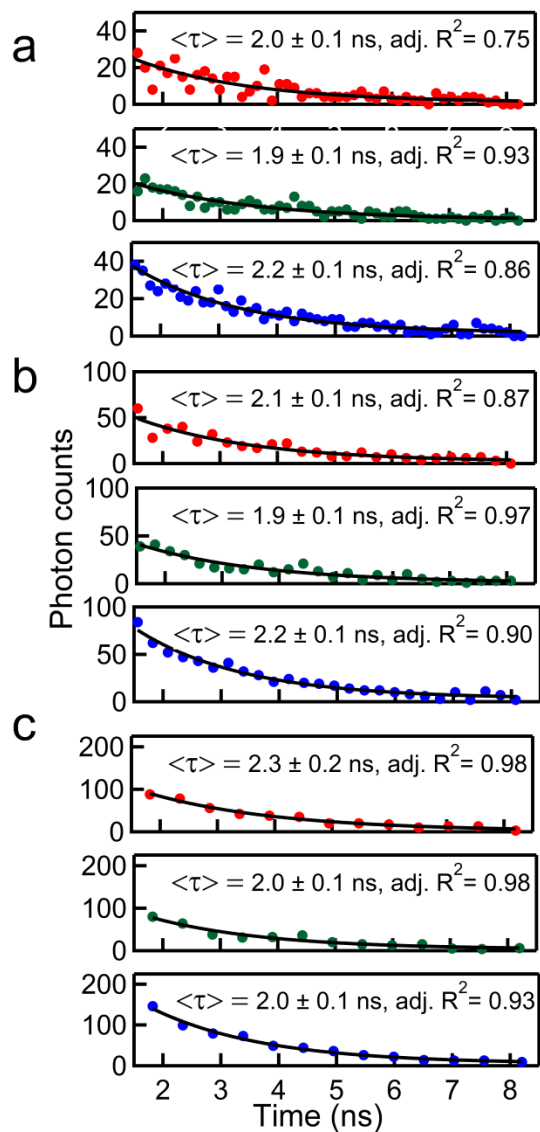


Figure 5.2. Representative fluorescence lifetime decay curves (circles) and corresponding exponential fits (solid lines) for three different pixels shown with corresponding color coded arrows in Figure 5.1a: (a) 64 channels; (b) 32 channels; (c) 16 channels. The average lifetime and adj. R^2 values from the exponential fit are shown in each panel.

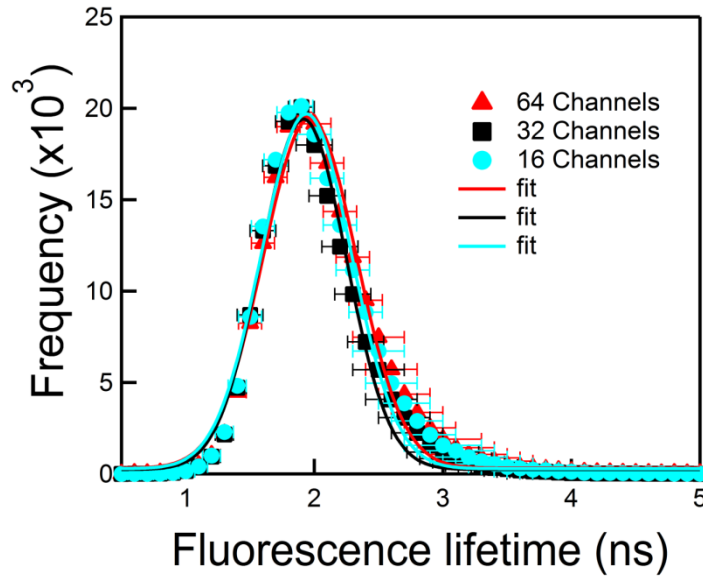


Figure 5.3. Fluorescence lifetime histograms with varying number of time channels for the image shown in Figure 5.1a (64 channels: red symbols, 32 channels: black symbols, 16 channels: light blue symbols). The fit (solid line) is Gaussian. Error bars in the lifetime histograms represent an average standard deviation of all measured fluorescence lifetimes in a specific bin.

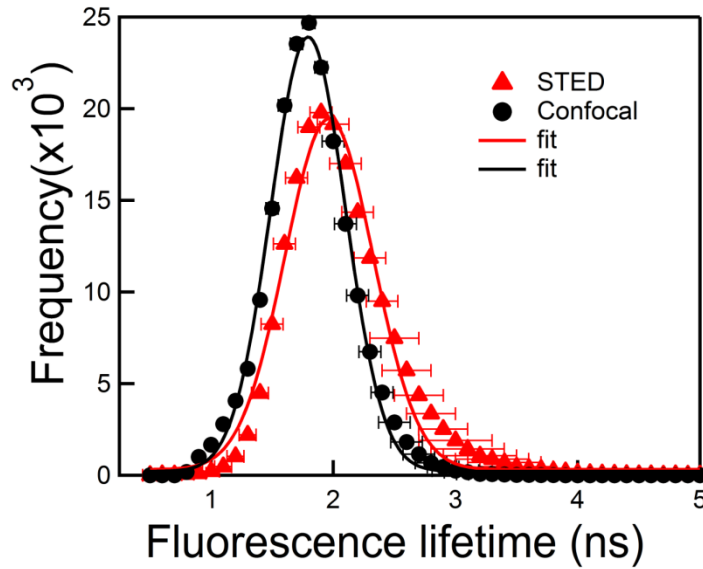


Figure 5.4. Fluorescence lifetime histograms constructed from all 262,144 pixels in the images shown in Figure 5.1a (STED, red symbols) and 5.1b (confocal, black symbols) for 64 time channel decay curves. The fit (solid line) is Gaussian. Error bars in the lifetime histograms represent an average standard deviation of all measured fluorescence lifetimes in a specific bin.

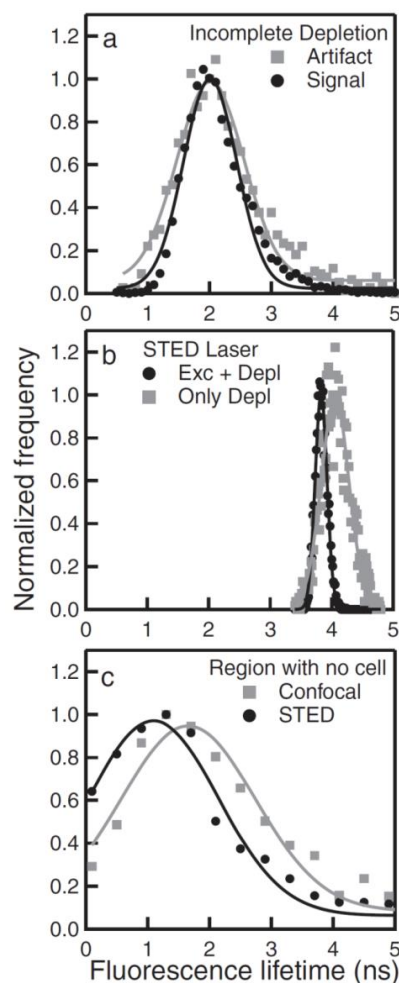


Figure 5.5. Characterization of the sources of background in the STED image. (a) The background that results from incomplete depletion of the Alexa Fluor 594 phalloidin fluorescence at the periphery of the excitation beam (gray symbols) compared to the signal (black symbols) for the image shown in Figure 5.1a. (b) Fluorescence lifetime histograms constructed for Alexa Fluor 594 phalloidin on a glass cover slip using the depletion and excitation laser (red symbol) or only the depletion laser (blue symbol). (c) The background from regions of the image shown in the Figure 5.1a (black symbols) or Figure 5.1b (gray symbols) where the cell is not located. All fits (solid line) are Gaussian.

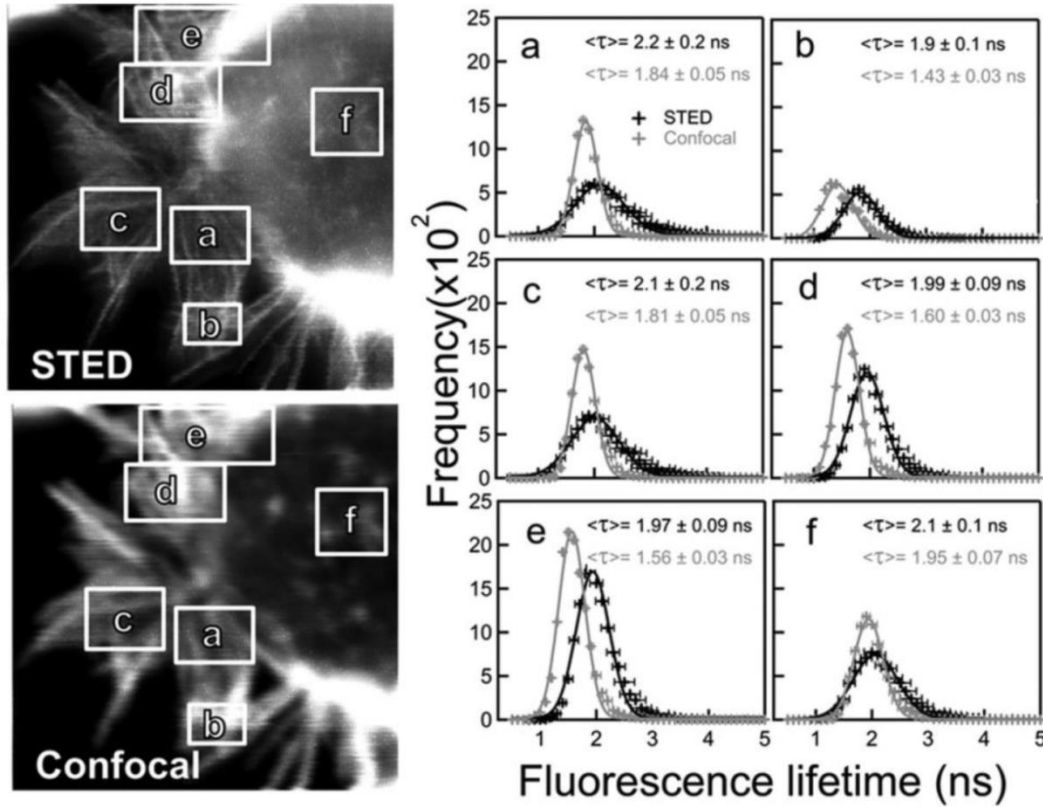


Figure 5.6. Rectangular regions a, b, c, d, e, and f in the images correspond to the labeled fluorescence lifetime histograms in the STED (black symbol) and confocal (gray symbol) image using 64 time channel decay curves. The fit (solid line) is Gaussian. Error bars in the lifetime histograms represent an average standard deviation of all measured fluorescence lifetimes in a specific bin.

CHAPTER 6

GENERAL CONCLUSIONS AND FUTURE WORK

The major goal of the work presented in this dissertation was to use fluorescence-based imaging techniques to study the lateral diffusion of the membrane proteins receptor for advanced glycation endproducts (RAGE) and integrins. The lateral diffusion of membrane protein is an important aspect that governs how protein functions in the cell membrane. Although RAGE signaling has been studied extensively, knowledge pertaining to RAGE lateral diffusion and the factors that affect RAGE diffusion in the cell membrane largely remain unknown. Fluorescence recovery after photobleaching (FRAP) was used to measure the diffusion of RAGE. FRAP experiments on red-fluorescent protein fused RAGE (RAGE-mRFP) indicated that the RAGE-mRFP follows Brownian motion in the cell membrane with a large mobile fraction at native GM07373 cellular conditions. The polymerization and depolymerization dynamics of the actin cytoskeleton play a role in increasing the RAGE mobile fraction, although only the depolymerizing cytochalasin-D treatment showed a RAGE-dependent change in p-ERK signaling.

In Chapter 3, it was shown that the ligand (methylglyoxal modified-bovine serum albumin (MGO-BSA)) binding affinity affects RAGE lateral diffusion as measured with single particle tracking (SPT). The MGO-BSA binding to sRAGE (a soluble variant of RAGE) was observed to be dependent on the percent primary amine modification and the net negative surface charge on the ligand. MGO-BSA incubation affected RAGE lateral diffusion, however, there was no direct correlation measured between ligand binding affinity, net negative surface charge on the ligand and RAGE diffusion properties. Ligand induced changes are not present when the cholesterol is depleted from the cell membrane, indicating a role for cholesterol in MGO-BSA-induced changes to RAGE diffusion.

Using similar fluorescence-based techniques, the effect of highly conserved membrane proximal alpha-subunit cysteine (Cys¹³⁶⁸) on the lateral diffusion properties of Drosophila integrins (α PS2C β PS) were measured. Replacing Cys¹³⁶⁸ with Val¹³⁶⁸ increased the mobile population of Val¹³⁶⁸ integrins

compared to Cys¹³⁶⁸ integrins as measured by FRAP and SPT. Tandem mass spectrometry and protein sequence analysis data suggested that Cys¹³⁶⁸ harbors a redox or palmitoylation post-translational modification in integrins. The Cys¹³⁶⁸ was proposed to be an important post-translational modification site that regulates the diffusion of α PS2C β PS integrins. This membrane proximal cysteine may play an important role in the diffusion of other alpha subunits that bear this conserved residue.

Finally, stimulated emission depletion microscopy was used to generate sub-diffraction images of the actin-cytoskeleton with a spatial resolution of ~40 nm in cultured cells. The quality of the fluorescence lifetime data obtained at sub-diffraction spatial resolution was evaluated. The photon count in the peak-channel was increased by time binning the 64 time channel data without compromising the spatial resolution. Detailed pixel-by-pixel analysis of fluorescence lifetime measurements with different photon counts in the peak channel showed that an average of 40 ± 30 photons in the peak channel and approximately 600 photons collected in total with a signal-to-noise ratio of 20 was enough to calculate reliable lifetimes. This is an important parameter since it governs the collection time required to obtain a meaningful fluorescence lifetime while reducing photodamage and photobleaching to biological samples and fluorophores. Although the probe volume in the STED imaging mode was tenfold smaller compared to the confocal mode, similar fluorescence lifetime distributions of the fluorophore attached to F-actin were obtained across the entire cultured cell when expected contributions from background were considered. The study indicates STED fluorescence lifetime imaging can be used to probe heterogeneity in the 40-nm regime in biological samples in aqueous environments.

Future work could aim at using the SPT to interrogate RAGE diffusion in altered cellular conditions. For example, RAGE is known to interact with cytoplasmic protein Diaphanous-1 (Dia-1) through specific amino acids in the RAGE sequence. A site specific mutagenesis can be used to alter the amino acid sequence in the wild-type RAGE and SPT can be used to study the effect of disrupted interaction between RAGE and Dia-1. Also, the discrepancy observed in the ligand binding affinity and

RAGE diffusion can be further studied by using ligands with well-defined valancy. Further, the sub-diffraction technique STED described in the Chapter 5 can be coupled with fluorescence correlation spectroscopy to study the diffusion of membrane protein labeled with an organic fluorophore molecule, at similar or better temporal resolution compared to SPT.

APPENDIX A

**SINGLE PARTICLE TRACKING WITH STEROL MODULATION REVEALS THE
CHOLESTEROL-MEDIATED DIFFUSION PROPERTIES OF INTEGRIN RECEPTORS**

A paper published in Physical Biology as a research article

(Phys. Biol., 11, 06001(2014). doi: 10.1088/1478-3975/11/6/066001)

Neha Arora, Aleem Syed, Suzanne Sander and Emily A. Smith

A.1. Abstract

A combination of sterol modulation with cyclodextrins plus fluorescence microscopy revealed a biophysical mechanism behind cholesterol's influence on the diffusion of a ubiquitous class of receptors called integrins. Single particle tracking (SPT) measured heterogeneous diffusion of integrins bound to ligand-coated quantum dots, and fluorescence recovery after photobleaching (FRAP) measured the ensemble changes in integrin diffusion. A $25 \pm 1\%$ reduction of membrane cholesterol resulted in three significant changes to the diffusion of ligand-bound α PS2C β PS integrins as measured by SPT. There was a 23% increase in ligand-bound mobile integrins; there was a statistically significant increase in the average diffusion coefficient inside zones of confined diffusion, and histograms of confined integrin trajectories showed an increased frequency in the range of 0.1-1 $\mu\text{m}^2/\text{s}$ and a decreased frequency in the 0.01-0.1 $\mu\text{m}^2/\text{s}$ range. No statistical change was measured in the duration of confinement or the size of confined zones. Restoring the cholesterol-depleted cells with exogenous cholesterol or exogenous epicholesterol resulted in similar diffusion properties as measured prior to cholesterol depletion. Epicholesterol differs from cholesterol in the orientation of a single hydroxyl group. The ability of epicholesterol to substitute for cholesterol suggests a biophysical mechanism for cholesterol's effect on integrin diffusion. Influences of bilayer thickness, viscosity and organization are discussed as possible explanations for the measured changes in integrin diffusion when the membrane cholesterol concentration is reduced.

A.2. Introduction

As a major lipid component of the cell membrane, cholesterol plays a crucial role in membrane organization, dynamics and function [1]. Over the past several years it has been revealed that cholesterol is involved in the organization of the cell membrane [2-7]. Lipid nanodomains contain heterogeneous concentrations of lipids, proteins, and small molecules such as cholesterol compared to the bulk membrane. These nanodomains have been implicated as platforms for the co-localization of many membrane proteins necessary for transmembrane signaling [2, 8].

Alterations in cell membrane cholesterol concentration are known to affect the function of a number of receptor proteins [9]. In this regard, the most extensively studied receptor family is G-protein coupled receptors (GPCRs) [10]. Depletion of cholesterol from the cell membrane reduces the ligand-binding affinity of several GPCRs including oxytocin, cholecystokinin, galanin and serotonin [10-13]. An increase in the amount of membrane cholesterol favors the inactive conformation of the photoreceptor rhodopsin [14, 15]. Cholesterol is also necessary for the proper functioning of the nicotinic acetylcholine receptors [16].

The present study explores the mechanism and heterogeneity of cholesterol-mediated diffusion of an important class of membrane protein receptors called integrins. Diffusion heterogeneity exists when all receptors are not diffusing at the same rate or exhibit different levels of confinement. Integrins are known to be involved in numerous fundamental cellular processes, including cell growth, survival, motility, adhesion and proliferation [17]. Integrins' biological function including ligand binding, cell adhesion and signaling are affected by the cholesterol concentration in the membrane. Depletion of cholesterol from Jurkat cells is reported to decrease integrin mediated cell adhesion to the extra cellular matrix via lowering the ligand affinity [18]. Cholesterol modulates integrin function and clustering [19, 20]. A recent study revealed the influence of cholesterol on adhesion and signaling properties of $\alpha_v\beta_3$ and $\alpha_5\beta_1$ integrins [21, 22]. Cholesterol has also been found to be essential for the formation of a

signaling protein complex comprising $\alpha_v\beta_3$ integrins [21]. Depleting cholesterol from the membrane led to the dissociation of this protein complex as revealed by the absence of co-immunoprecipitation of the proteins in the complex. In a study by Krauss et al., it was shown that integrin LFA-1 mediated cell adhesion was disrupted when the cholesterol content of the membrane was reduced [23]. Additionally, less integrin clustering was observed after 27% cholesterol depletion from the cell membrane [20]. Although it is evident that cholesterol plays an important role in modulating integrin function, details of the heterogeneous nature of and mechanism behind cholesterol-mediated integrin diffusion are not known. The diffusion of integrins is important to their function. Diffusion can affect the localization and clustering of integrins [24, 25]. An increase in cell adhesion is observed with an increase in integrin diffusion [12, 26]. Herein, cholesterol-dependent integrin diffusion properties are discussed and a mechanism of cholesterol-mediated changes in integrin function is proposed.

One strategy to study the influence of cholesterol-dependent properties is to perform measurements at native, reduced and restored cholesterol or epicholesterol concentrations, as has been demonstrated for exocytosis in platelets [27]. Epicholesterol differs from cholesterol only in the orientation of the hydroxyl group at position 3 (Figure A.1 (a) and (b)). Physical properties of the cell membrane, including membrane fluidity and lipid domain formation, are unaffected by the substitution of cholesterol with epicholesterol in the membrane [28]. However, the difference in the structure of the two isomers can result in remarkable differences in their specific biochemical roles [29, 30]. Thus, the specificity of cholesterol in altering integrin diffusion and the mechanism behind cholesterol-mediated regulation of integrin diffusion can be determined by modulating the membrane sterol composition. Heterogeneous diffusion of integrin receptors in the cell membrane was measured using single particle tracking (SPT) with ligand-coated quantum dots or fluorescence recovery after photobleaching (FRAP) for ensemble diffusion measurements. Cholesterol modulation was performed using methyl- β -cyclodextrin (M β CD). Cyclodextrins have been used extensively to modulate the cholesterol levels in cells due to their ability to act as efficient donors and acceptors of sterol [31]. Sterol and integrin

quantification were performed with liquid chromatography-mass spectrometry using atmospheric pressure chemical ionization (LC/APCI-MS) and Western blotting, respectively.

A.3. Materials Methods

Cell Culture

Drosophila S2 cells used in this study were transformed to express wild-type α PS2C β PS integrins under the regulation of the heat shock promoter. For FRAP experiments, α PS2C β PS integrins were tagged with a Venus fluorescent protein in the serine-rich loop, which has previously been used to insert epitope tags without any change to measurable function [32]. For Western blotting, the hemagglutinin epitope was added to the extracellular region of alpha subunit. The cells were cultured as previously published [33]. To induce integrin expression, cells were placed in a 36 °C water bath for 30 min and allowed to recover for 3 h at 22 °C before taking measurements.

Cholesterol depletion, restoration and substitution

After the heat shock and 3 h incubation, the cell suspension was centrifuged at approximately $600 \times g$ for 3 min and the pellet was resuspended in serum-free M3 medium containing 2.5 mM or 5mM M β CD (Sigma-Aldrich, St. Louis, MO) solution for 30 min at 22 °C to deplete cholesterol [20]. For cholesterol restoration, cholesterol-depleted cells were incubated with a M β CD solution saturated with cholesterol (M β CD:cholesterol, molar ratio of 8:1) that was prepared as described previously [27] for 30 min at 22 °C. Briefly, a small volume of cholesterol stock solution in chloroform was added to a glass vial and dried under a stream of nitrogen. The dried samples were then resuspended in 2.5 mM M β CD or 5mM M β CD, vortexed and sonicated to allow mixing, and incubated overnight with shaking at 200 rpm and 37 °C. The solution was filtered using a 0.2 μ m filter immediately prior to use.

To substitute cholesterol with epicholesterol, cholesterol-depleted cells were exposed to a saturated M β CD:epicholesterol solution for 30 min at 22 °C. M β CD:epicholesterol was prepared using a similar

protocol as used to prepare M β CD:cholesterol. Before lipid extraction, diffusion measurements or no measurable phenotype changes in the cells after any of the above-mentioned treatments.

Extraction of lipids and LC/APCI-MS quantification of cholesterol and epicholesterol

After the heat shock and 3 h recovery, membrane and total cellular lipids were extracted as described previously [20, 34] with the following change: the lipids were resuspended in methylene chloride for subsequent LC/APCI-MS measurements.

Cholesterol and epicholesterol were quantified using an Agilent 6540 Ultra-High-Definition (UHD) Accurate-Mass Quadrupole Time-of-Flight (Q-TOF) liquid chromatography mass spectrometry (LC-MS) system. Analyses were performed on Agilent XDB C18, 4.6 x 150 mm, 1.8 μ m column coupled with Agilent QTOF 6540 mass spectrometer equipped with APCI ion source. A mixture of methanol and water (100:0.5 v/v) at 1 ml/min flow rate was used as a mobile phase. The sample injection volume was 1 μ L. All data were acquired in the positive ion mode. Commercial standards of cholesterol (Sigma, St. Louis, MO) and epicholesterol (Stereloids, Newport, RI) were used to assign the peaks in the chromatograms and stigmasterol was used as an internal standard (Figure A.1 (c)). The measured resolution between the cholesterol and epicholesterol peaks was 1.2 for both the standard solutions and the lipid extract from the cells (Figure A.1 (c) and (d)). For quantification purposes, an external calibration curve was set up every day. Peaks were extracted and integrated using Agilent Masshunter software. The m/z values of 369.35 and 383.34 were used for quantification of both cholesterol and epicholesterol. All measurements were duplicated.

Preparation of ligand-coated quantum dots and labeling

Quantum dots (QDs) measuring 16 nm in diameter were obtained from Life Technologies (Carlsbad, CA, USA). The size of the ligand-coated quantum dots used in this study is comparable to that of integrin, therefore integrin clusters are not being formed as a result of multivalent binding to a ligand-

coated quantum dot. The conjugation of positively charged QDs with net-negatively charged RBB-Tiggrin ligand was achieved as described previously [35]. For labeling the integrins with ligand-coated quantum dots (hereafter QD-RBB-Tiggrin), cells that had been heat shocked and allowed to recover for 3 h were centrifuged at approximately $600 \times g$ for 3 min and the resulting pellet was resuspended in serum-free medium to adjust the final concentration to 5×10^5 cells/mL. Cells were then spread on RBB-Tiggrin coated glass slides for 1 h at room temperature [33]. Media was removed and cells were incubated with a 50 μ L suspension of 0.1 nM QD-RBB tiggrin for 5 min. Finally, the cells were rinsed with BES Tyrodes buffer for imaging. The binding specificity of QD-RBB-Tiggrin to integrins was examined using untransformed S2 cells that have no detectable endogenous integrin expression. Nonspecific binding was negligible, approximately 1 %.

Imaging

Imaging of the cells was performed by fluorescence microscopy at room temperature. A Nikon Eclipse TE2000U inverted microscope (Melville, NY, USA) was equipped with an oil-immersion objective (100 \times , NA=1.49) and specific filter sets were used for excitation and emission of QDs and YFP for SPT and FRAP experiments, respectively. A mercury lamp was used for illumination and all images were captured using a PhotonMAX 512 EMCCD camera (Princeton Instrument, Trenton, NJ, USA). Winview software (Photometrics, Tucson, AZ, USA) allowed the recording of images as a function of time. Data collection was completed within 1 h after adding BES buffer to the cells.

Single Particle Tracking (SPT)

Images were recorded at 25 frames/second for a total of 30 seconds. Images were processed using Image J version 1.45 s and the ImageJ plugin Particle Tracker version 1.2. At least 90 ligand-coated quantum dots from at least 15 cells were used to generate trajectories as described previously [35]. The number of trajectories collected generates reliable average diffusion coefficients as reported by Saxton

[36]. Single ligand-coated quantum dots were identified by their on-off blinking behavior and only trajectories generated from single ligand-coated quantum dots were analyzed. Trajectories consisting of less than 100 frames were excluded from the analysis.

Trajectory analysis was performed using a MATLAB-implemented application with graphical user interface that is based on the established algorithms of Simson et al. and Melihac et al [37-39]. Trajectories of single ligand-coated quantum dots were analyzed for the presence of confinement zones. Confinement zones are regions where a diffusing particle remains for a time duration considerably longer than a Brownian diffusant would stay in an equally sized region. A confinement index, L , was calculated for each trajectory as described previously [37]. Trajectories were categorized into two different modes of diffusion: Brownian diffusion with no confined zones, and confined diffusion with one or more confined zones. An $L > 3.16$ for a duration > 1.1 s had a likelihood of more than 99.9 % to reflect confined diffusion. For each trajectory, characteristic and instantaneous diffusion coefficients were calculated by analyzing the plot of mean square displacement (MSD) vs time according to Michalet et al. [40]. Trajectories with confined diffusion were further analyzed to determine the size of the confinement, the duration of the confinement and the diffusion coefficients inside the confined zones.

Fluorescence recovery after photobleaching (FRAP)

FRAP experiments were carried out on S2 cells transformed to express integrins attached with Venus fluorescent proteins. The 488-nm line of an argon ion laser was used for photobleaching, and the recovery of fluorescence was monitored using mercury lamp excitation. Images were collected using a 500/20-nm excitation and a 535/30-nm emission filter. The exposure time for each image was 0.35 s, and images were collected every 0.40 s. The bleaching time was 0.35 s and the bleached area was $41 \mu\text{m}^2$. Fluorescence images were analyzed as previously described [24] by fitting them to models based on Eq. 1 [25] with an in-house-developed Igor Pro macro (version 4.0).

$$F(t) = \frac{F_0 + F_\infty \left(\frac{t}{\tau}\right)^\alpha}{1 + \left(\frac{t}{\tau}\right)^\alpha} \quad (1)$$

The fluorescence at time t is $F(t)$, F_0 is the initial fluorescence intensity after photobleaching; F_{in} is the fluorescence intensity at an infinite recovery time; τ is the time for 50% of the fluorescence to recover, and α is the time exponent providing a measure of how much diffusion is confined. The most appropriate model was determined by comparing the reduced χ^2 values obtained for each model. Most FRAP curves (Figure SA.1) were best fit to a model for time-dependent diffusion ($\alpha < 1$) with an immobile fraction ($F_{in} < 1$). Values obtained from the fit of the fluorescence recovery curve were used to calculate the diffusion coefficient, $D(t)$ (Eq. 2).

$$D(t) = \frac{\omega^2}{4(\tau)^\alpha (t)^{(\alpha-1)}} \quad (2)$$

where ω is the radius of the focused Gaussian laser beam [41].

A.4. Results and Discussion

Modulation of cellular cholesterol concentration with methyl- β -cyclodextrin

M β CD was used to alter the sterol content in S2 cells transformed to express α PS2C β PS integrins. The total cellular and membrane cholesterol concentrations as measured by liquid chromatography-mass spectrometry in untreated, cholesterol-depleted and cholesterol-restored cells are summarized in Figure A.2. Membrane cholesterol is the most relevant fraction for this study since it can influence integrin diffusion in the cell membrane (Figure A.2 (a)). Total cellular (intracellular plus membrane) cholesterol concentration was also measured to provide information about the efficacy of the sterol depletion and restoration (Figure A.2 (b)). Total cellular cholesterol was depleted by 45 ± 5 % with 2.5 mM M β CD treatment. The percent decrease in membrane cholesterol (25 ± 1 %) was lower than the measured decrease for total cellular cholesterol. This is consistent with a previous study supporting the notion that

the distribution of cholesterol into intracellular and cell membrane pools is affected by cholesterol depletion [20]. Similar cholesterol depletion levels were achieved using 5 mM M β CD, indicating 2.5 mM M β CD is sufficient for subsequent experiments.

Exposing the previously cholesterol-depleted cells to 2.5 mM M β CD preloaded with cholesterol (M β CD:cholesterol) restores the total cellular and membrane cholesterol levels to $126 \pm 12 \%$ and $82 \pm 13 \%$ of the native levels, respectively. A complete restoration of membrane cholesterol was not achieved despite a higher total cellular cholesterol concentration. Similar to what was found with the depletion step, 5 mM M β CD:cholesterol produced statistically similar results as 2.5 mM M β CD:cholesterol, therefore, 2.5 mM M β CD:cholesterol was used for subsequent restoration experiments.

Classification of integrin diffusion by SPT: cholesterol depletion increases the integrin mobile fraction

Integrin diffusion was analyzed for 90 to 100 trajectories and categorized as immobile, or mobile with Brownian or confined diffusion in each cell population: untreated, cholesterol-depleted and cholesterol-restored. A ligand-coated quantum dot, and therefore a trajectory, was considered to be immobile in a given region if the median of its instantaneous diffusion coefficient was below $0.001 \mu\text{m}^2/\text{s}$. All mobile trajectories collected from the three cell populations are shown in Figure SA.2. The most obvious difference among the three cell populations is the varying number of mobile trajectories. In untreated cells with a native cholesterol concentration, 74% of ligand-bound integrins were mobile with 36 mobile trajectories exhibiting confined diffusion and 38 mobile trajectories exhibiting Brownian diffusion (Table A.1). Immobile and confined trajectories may represent the population of integrins in confined membrane regions and/or interacting with confined cytoskeletal proteins.

After cholesterol depletion, the ligand-bound integrin mobile fraction increased to 97% (Table A.1), which indicates cholesterol is directly or indirectly the main causes of ligand-bound integrin immobilization at native cholesterol concentrations. There is a small increase in the number of

trajectories exhibiting Brownian diffusion after cholesterol depletion; however, the increase in the mobile fraction is primarily associated with a larger number of integrins diffusing with confined zones. An increase in the size of confined zones or the time integrins spend in confined zones could explain this observation since both would increase the probability of a confined event being detected during the observation time. However, there isn't a statistically significant change in either of these parameters after cholesterol depletion (Table A.1 and Figure A.3). This suggests a higher fraction of diffusing integrins partitions into confined zones after cholesterol depletion.

After cholesterol restoration (Table A.1) the mobile ligand-bound integrin fraction decreased to 82% and the number of trajectories exhibiting confined diffusion decreased to 50. These values are higher than what was measured in the untreated cell population (i.e., 74% and 38). This may be the result of incomplete restoration of membrane cholesterol upon treatment with M β CD:cholesterol (Figure A.2), the result of other changes that may occur in the membrane, for example other lipids may be affected by M β CD, or there may be a time dependence to the restoration of some diffusion properties. The percentage of trajectories exhibiting Brownian diffusion decreased to 32.

In contrast to SPT, the ensemble FRAP measurements showed a 25% decrease in the mobile integrin fraction after cholesterol depletion and a 35% increase after cholesterol restoration (Table A.2). The main reason for the difference is understood by considering each pool of integrin measured in the experiment. In FRAP, all ligand-bound and ligand-unbound integrins are labeled with fluorescent protein, and all integrins within the probed membrane region of a few microns square contribute to the signal. Whereas in SPT only integrin bound to ligand-coated quantum dots is measured. Arnold et al. have shown that 300 ligand-bound integrins per μm^2 is the minimum density required for cells to spread [42]; whereas if only size constraints are considered, a maximum of several thousand integrins can pack in the same area. It could be argued that the quantum dot affects the diffusion measurements; yet the same diffusion properties have been previously measured by FRAP and SPT under some experimental conditions [35]. A more complete picture of how the integrins are moving in the cell membrane is

obtained with a combination of FRAP and SPT measurements. The integrins bound to ligand-coated quantum dots are more mobile after cholesterol depletion, but the bulk integrins are less mobile after cholesterol depletion.

Cholesterol depletion influences integrin diffusion coefficient in the confined zones

Plots of confinement index and instantaneous diffusion coefficient for a trajectory exhibiting only Brownian diffusion and a trajectory with one confined zone (red circle) are shown in Figure A.4. In general, the instantaneous diffusion coefficient varies significantly at different times in the trajectory and confinement zones are associated with lower instantaneous diffusion coefficients. For trajectories with confined zones, average diffusion coefficients were calculated inside and outside the confinement zones (Table A.1). After cholesterol depletion, the average diffusion coefficient in the confined zones showed a statistically significant increase and there was no significant change in the diffusion coefficient outside the confinement zones. The distribution of measured diffusion coefficients (Figure A.5) provides more information than the average values reported in Table A.1 due to the heterogeneity in the single receptor data. After cholesterol depletion, there are two significant changes observed in the distribution of diffusion coefficients inside the confined zones when considering differences of 5% or more. There is a 11% decrease in the integrin population with a diffusion coefficient in the range of 0.01-0.1 $\mu\text{m}^2/\text{s}$, and a 8% increase in the population in the range 0.1-1 $\mu\text{m}^2/\text{s}$ after cholesterol depletion.

To confirm the measured diffusion coefficient changes were attributable to cholesterol depletion, cholesterol was restored in a previously cholesterol-depleted cell population. After cholesterol restoration, the average diffusion coefficient within the confined zones returns to the value measured for untreated cells (Table A.1). Similarly, the histogram of diffusion coefficients within confined zones after cholesterol restoration has no changes greater than 5% compared to the histogram recorded for cells with a native cholesterol concentration (Figure A.5). This indicates that integrin diffusion in the

confined zones is cholesterol-dependent; whereas outside the zones the diffusion is cholesterol-independent as measured by SPT.

There is a statistically significant increase in the ensemble integrin diffusion coefficient measured by FRAP after cholesterol depletion (Table A.2). The diffusion coefficient measured by FRAP after cholesterol restoration decreases to a value near what was measured at native cholesterol concentrations, indicating the increase in the diffusion coefficient after cholesterol depletion is cholesterol-mediated and not the result of another change to the membrane composition.

Mechanism for cholesterol-mediated changes to integrin diffusion

The measured differences in integrin diffusion properties after cholesterol depletion could be due to: (i) cholesterol affecting the physical properties of the membrane such as its fluidity or (ii) cholesterol interacting with integrin or another membrane component that influences integrin diffusion. It is also possible that a combination of both occur simultaneously. Any direct interaction with cholesterol is likely to be stereoselective; whereas cholesterol's influence on the biophysical properties of the membrane is not. To elucidate the mechanism by which cholesterol affects integrin diffusion, cholesterol in the cell membrane was partially substituted with its stereoisomer epicholesterol. If similar diffusion properties are measured after cholesterol restoration or partial epicholesterol substitution, it can be concluded that cholesterol regulates integrin diffusion by changing the physical properties of the membrane, otherwise specific biochemical interactions may also be involved.

M β CD saturated with epicholesterol (M β CD:epicholesterol) was used to partially substitute cholesterol with epicholesterol in the cell membrane. The treatment resulted in a 47 ± 1 % substitution of cholesterol by epicholesterol in the cell membrane (Figure A.2), and a nearly ideal restoration of membrane sterol concentration. This is consistent with previous studies that showed ~50% substitution of epicholesterol in the cell membrane irrespective of the concentration of M β CD used [29, 43, 44]. The total cellular sterol concentration was not restored after M β CD:epicholesterol treatment (Figure A.2

(b)), which may be the result of altered membrane internalization. In order to measure whether sterol modulation affected integrin concentration, Western blot analyses were performed using cells with native, depleted, restored or substituted sterol content (Figure A.6). There was no statistically significant change in integrin concentration among any of the cell populations, indicating measured differences in diffusion properties are not the result of changes in integrin concentration.

Epicholesterol generated statistically similar integrin diffusion properties as were measured after cholesterol restoration. As measured by SPT there was no statistically significant difference in the average diffusion coefficient of mobile integrins inside or outside the confined zones after cholesterol restoration and partial epicholesterol substitution (Table A.1). The ensemble diffusion coefficient measured by FRAP was also statistically similar (Table A.2). Finally, the fraction of mobile integrins exhibiting confined diffusion is also similar after cholesterol restoration and partial epicholesterol substitution, and there is a 82% mobile fraction in both cell populations (Table A.1).

Since epicholesterol substitution restores changes in the diffusion coefficients measured after cholesterol depletion, there is a biophysical mechanism behind cholesterol's influence on integrin diffusion. The specific biophysical mechanism may be changes in one or more of the following: bilayer viscosity, thickness, or organization. Additional mechanisms, for example there may be an effect of cholesterol on integrin's rotational diffusion, can't be determined with these experiments. Reports vary on cholesterol's effect of on membrane thickness. When cholesterol is added to a synthetic bilayer in the absence of proteins there is a 4 Å increase in bilayer thickness [45-49]. According to the Saffman and Delbrück membrane diffusion model, this would change the diffusion coefficient by no more than 6%. This could not be the complete explanation for the 3-fold increase in the average diffusion coefficient inside confined zones. In an artificial bilayer or cell membrane, a 2-fold increase in membrane viscosity was measured after the addition of 30 mole percent cholesterol [50, 51]. According to the Saffman and Delbrück model this results in a 2-fold change in receptor diffusion [52]. Finally, modifications in the membrane organization along with changes in integrins' clustering and interaction

with other membrane proteins are likely to contribute to the measured changes in integrin diffusion upon cholesterol depletion. Cholesterol is necessary for the formation of $\alpha 4\beta 1$, $\alpha 5\beta 1$ and $\alpha PS2C\beta PS$ integrins clusters in the cell membrane of various cell types [18, 20, 22]. Association and signaling of $\alpha v\beta 3$ integrin, integrin associated protein and G protein complex is cholesterol dependent in C32 human melanoma cells [21].

A.5. Conclusions

Integrins in the cell membrane exhibit a biophysical-dependent change in integrin diffusion upon cholesterol-depletion. Partial substituting of cholesterol with epicholesterol restored the depletion-induced changes to integrin diffusion. Epicholesterol is known to mimic the effects of cholesterol on membrane physical properties. Hence, the changes to integrin diffusion that are measured after cholesterol depletion are likely due to the overall changes in the membrane and not a result of specific biochemical interactions of cholesterol involving the β -hydroxy group.

Acknowledgements

This work was supported by the National Science Foundation (CHE-0845236). The authors thank ISU Chemical Instrumentation Facility and Dr. Kamel Harrata for training and assistance using the Agilent QTOF6540 LC/APCI-MS.

A.6. References

- [1] P.L. Yeagle, Cholesterol and the cell membrane, *Biochimica et biophysica acta*, 822 (1985) 267-287.
- [2] D.A. Brown, E. London, Functions of lipid rafts in biological membranes, *Annu. Rev. Cell Biol.*, 14 (1998) 111-136.
- [3] K. Simons, R. Ehehalt, Cholesterol, lipid rafts, and disease, *J. Clin. Invest.*, 110 (2002) 597-603.
- [4] K. Simons, E. Ikonen, Functional rafts in cell membranes, *Nature*, 387 (1997) 569-572.
- [5] K. Simons, E. Ikonen, How cells handle cholesterol, *Science*, 290 (2000) 1721-1726.
- [6] K. Simons, D. Toomre, Lipid rafts and signal transduction, *Nat. Reviews. Mol. cell Biol.*, 1 (2000) 31-39.
- [7] J.M. Crane, L.K. Tamm, Role of cholesterol in the formation and nature of lipid rafts in planar and spherical model membranes, *Biophys. J.*, 86 (2004) 2965-2979.
- [8] L.J. Pike, Lipid rafts: bringing order to chaos, *J. Lipid Res.*, 44 (2003) 655-667.
- [9] A.G. Lee, How lipids affect the activities of integral membrane proteins, *BBA-Biomembranes*, 1666 (2004) 62-87.
- [10] T.J. Pucadyil, A. Chattopadhyay, Role of cholesterol in the function and organization of G-protein coupled receptors, *Prog. Lipid Res.*, 45 (2006) 295-333.
- [11] G. Gimpl, K. Burger, F. Fahrenholz, Cholesterol as modulator of receptor function, *Biochemistry-U.S.*, 36 (1997) 10959-10974.
- [12] B. Chini, M. Parenti, G-protein coupled receptors in lipid rafts and caveolae: how, when and why do they go there?, *J. Mol. Endocrinol.*, 32 (2004) 325-338.
- [13] G. Khelashvili, S. Mondal, O.S. Andersen, H. Weinstein, Cholesterol modulates the membrane effects and spatial organization of membrane-penetrating ligands for G-protein coupled receptors, *J. Phys. Chem. B.*, 114 (2010) 12046-12057.
- [14] D.C. Mitchell, M. Straume, J.L. Miller, B.J. Litman, Modulation of metarhodopsin formation by cholesterol-induced ordering of bilayer lipids, *Biochemistry*, 29 (1990) 9143-9149.
- [15] M. Straume, B.J. Litman, Equilibrium and dynamic bilayer structural properties of unsaturated acyl chain phosphatidylcholine-cholesterol-rhodopsin recombinant vesicles and rod outer segment disk membranes as determined from higher order analysis of fluorescence anisotropy decay, *Biochemistry*, 27 (1988) 7723-7733.
- [16] F.J. Barrantes, Structural basis for lipid modulation of nicotinic acetylcholine receptor function, *Brain Res. Rev.*, 47 (2004) 71-95.
- [17] F.G. Giancotti, E. Ruoslahti, Integrin signaling, *Science*, 285 (1999) 1028-1032.
- [18] B. Leitinger, N. Hogg, The involvement of lipid rafts in the regulation of integrin function, *J. Cell Sci.*, 115 (2002) 963-972.
- [19] G. Pande, The role of membrane lipids in regulation of integrin functions, *Curr. Opin. Cell Biol.*, 12 (2000) 569-574.
- [20] D. Dibya, N. Arora, E.A. Smith, Noninvasive Measurements of Integrin Microclustering under Altered Membrane Cholesterol Levels, *Biophys. J.*, 99 (2010) 853-861.
- [21] J.M. Green, A. Zhelesnyak, J. Chung, F.P. Lindberg, M. Sarfati, W.A. Frazier, E.J. Brown, Role of cholesterol in formation and function of a signaling complex involving $\alpha\text{v}\beta\text{3}$, integrin-associated protein (CD47), and heterotrimeric G proteins, *J. Cell Biol.*, 146 (1999) 673-682.
- [22] P. Gopalakrishna, S.K. Chaubey, P.S. Manogaran, G. Pande, Modulation of $\alpha\text{5}\beta\text{1}$ integrin functions by the phospholipid and cholesterol contents of cell membranes, *J. Cell. Biochem.*, 77 (2000) 517-528.
- [23] K. Krauss, P. Altevogt, Integrin leukocyte function-associated antigen-1-mediated cell binding can be activated by clustering of membrane rafts, *J. Biol. Chem.*, 274 (1999) 36921-36927.

- [24] S. Miyamoto, H. Teramoto, O.A. Coso, J.S. Gutkind, P.D. Burbelo, S.K. Akiyama, K.M. Yamada, Integrin function: molecular hierarchies of cytoskeletal and signaling molecules, *J. Cell Biol.*, 131 (1995) 791-805.
- [25] D. Lepzelter, M.H. Zaman, Clustered diffusion of integrins, *Biophys. J.*, 99 (2010) L106-108.
- [26] P.Y. Chan, M.B. Lawrence, M.L. Dustin, L.M. Ferguson, D.E. Golan, T.A. Springer, Influence of receptor lateral mobility on adhesion strengthening between membranes containing LFA-3 and CD2, *J. Cell Biol.*, 115 (1991) 245-255.
- [27] S.C. Ge, J.G. White, C.L. Haynes, Critical Role of Membrane Cholesterol in Exocytosis Revealed by Single Platelet Study, *ACS Chem. Biol.*, 5 (2010) 819-828.
- [28] X.L. Xu, E. London, The effect of sterol structure on membrane lipid domains reveals how cholesterol can induce lipid domain formation, *Biochemistry*, 39 (2000) 843-849.
- [29] V.G. Romanenko, K.S. Roser, J.E. Melvin, T. Begenisich, The role of cell cholesterol and the cytoskeleton in the interaction between IK1 and maxi-K channels, *Am. J. Physiol. Cell Physiol.*, 296 (2009) C878-888.
- [30] S. Taskinen, M. Hyvonen, P.T. Kovanen, S. Meri, M.O. Pentikainen, C-reactive protein binds to the 3beta-OH group of cholesterol in LDL particles, *Biochem. and Biophys. Res. Commun.*, 329 (2005) 1208-1216.
- [31] A.E. Christian, M.P. Haynes, M.C. Phillips, G.H. Rothblat, Use of cyclodextrins for manipulating cellular cholesterol content, *J. Lipid Res.*, 38 (1997) 2264-2272.
- [32] T.A. Bunch, T.L. Helsten, T.L. Kendall, N. Shirahatti, D. Mahadevan, S.J. Shattil, D.L. Brower, Amino acid changes in *Drosophila* alphaPS2betaPS integrins that affect ligand affinity, *J. Biol. Chem.*, 281 (2006) 5050-5057.
- [33] D. Dibya, S. Sander, E.A. Smith, Identifying cytoplasmic proteins that affect receptor clustering using fluorescence resonance energy transfer and RNA interference, *Anal. Bioanal. Chem.*, 395 (2009) 2303-2311.
- [34] L. Bezrukov, P.S. Blank, I.V. Polozov, J. Zimmerberg, An adhesion-based method for plasma membrane isolation: evaluating cholesterol extraction from cells and their membranes, *Anal. Biochem.*, 394 (2009) 171-176.
- [35] D. Mainali, E. Smith, The effect of ligand affinity on integrins' lateral diffusion in cultured cells, *Eur. Biophys. J.*, 42 (2013) 281-290.
- [36] M.J. Saxton, Single-particle tracking: the distribution of diffusion coefficients, *Biophys. J.*, 72 (1997) 1744-1753.
- [37] R. Simson, E.D. Sheets, K. Jacobson, Detection of temporary lateral confinement of membrane proteins using single-particle tracking analysis, *Biophys. J.*, 69 (1995) 989-993.
- [38] N. Meilhac, L. Le Guyader, L. Salome, N. Destainville, Detection of confinement and jumps in single-molecule membrane trajectories, *Phys. Rev. E Stat. Nonlin. Soft Matter Phys.*, 73 (2006) 011915.
- [39] S.A. Menchon, M.G. Martin, C.G. Dotti, APM_GUI: analyzing particle movement on the cell membrane and determining confinement, *BMC Biophys.*, 5 (2012) 4.
- [40] X. Michalet, Mean square displacement analysis of single-particle trajectories with localization error: Brownian motion in an isotropic medium, *Phys. Rev. E Stat. Nonlin. Soft Matter Phys.*, 82 (2010) 041914.
- [41] J. Yguerabide, J.A. Schmidt, E.E. Yguerabide, Lateral mobility in membranes as detected by fluorescence recovery after photobleaching, *Biophys. J.*, 40 (1982) 69-75.
- [42] M. Arnold, E.A. Cavalcanti-Adam, R. Glass, J. Blummel, W. Eck, M. Kantlehner, H. Kessler, J.P. Spatz, Activation of Integrin Function by Nanopatterned Adhesive Interfaces, *ChemPhysChem*, 5 (2004) 383-388.
- [43] V.G. Romanenko, G.H. Rothblat, I. Levitan, Modulation of endothelial inward-rectifier K⁺ current by optical isomers of cholesterol, *Biophys. J.*, 83 (2002) 3211-3222.

- [44] V.G. Romanenko, G.H. Rothblat, I. Levitan, Sensitivity of volume-regulated anion current to cholesterol structural analogues, *J. Gen. Physiol.*, 123 (2004) 77-87.
- [45] J. Gallova, D. Uhrikova, A. Islamov, A. Kuklin, P. Balgavy, Effect of cholesterol on the bilayer thickness in unilamellar extruded DLPC and DOPC liposomes: SANS contrast variation study, *Gen. Physiol. Biophys.*, 23 (2004) 113-128.
- [46] J. Gallova, D. Uhrikova, N. Kucerka, M. Svorcova, S.S. Funari, T.N. Murugova, L. Almasy, M. Mazur, P. Balgavy, Influence of cholesterol and beta-sitosterol on the structure of EYPC bilayers, *J. Membr. Biol.*, 243 (2011) 1-13.
- [47] L. Karami, S. Jalili, Effects of cholesterol concentration on the interaction of cytarabine with lipid membranes: a molecular dynamics simulation study, *J. Biomol. Struct. Dyn.*, (2014) 1-15.
- [48] K. Mitra, I. Ubarretxena-Belandia, T. Taguchi, G. Warren, D.M. Engelman, Modulation of the bilayer thickness of exocytic pathway membranes by membrane proteins rather than cholesterol, *Proc. Natl. Acad. Sci. U.S.A.*, 101 (2004) 4083-4088.
- [49] F.A. Nezil, M. Bloom, Combined influence of cholesterol and synthetic amphiphilic peptides upon bilayer thickness in model membranes, *Biophys. J.*, 61 (1992) 1176-1183.
- [50] A. Grammenos, M.A. Bahri, P.H. Guelluy, G. Piel, M. Hoebeke, Quantification of Randomly-methylated-beta-cyclodextrin effect on liposome: an ESR study, *Biochem. and Biophys. Res. Comm.*, 390 (2009) 5-9.
- [51] N. Khatibzadeh, S. Gupta, B. Farrell, W.E. Brownell, B. Anvari, Effects of cholesterol on nano-mechanical properties of the living cell plasma membrane, *Soft. Matter*, 8 (2012) 8350-8360.
- [52] P.G. Saffman, M. Delbruck, Brownian motion in biological membranes, *Proc. Natl. Acad. Sci. U.S. A.*, 72 (1975) 3111-3113.

A.7. Figures and Tables

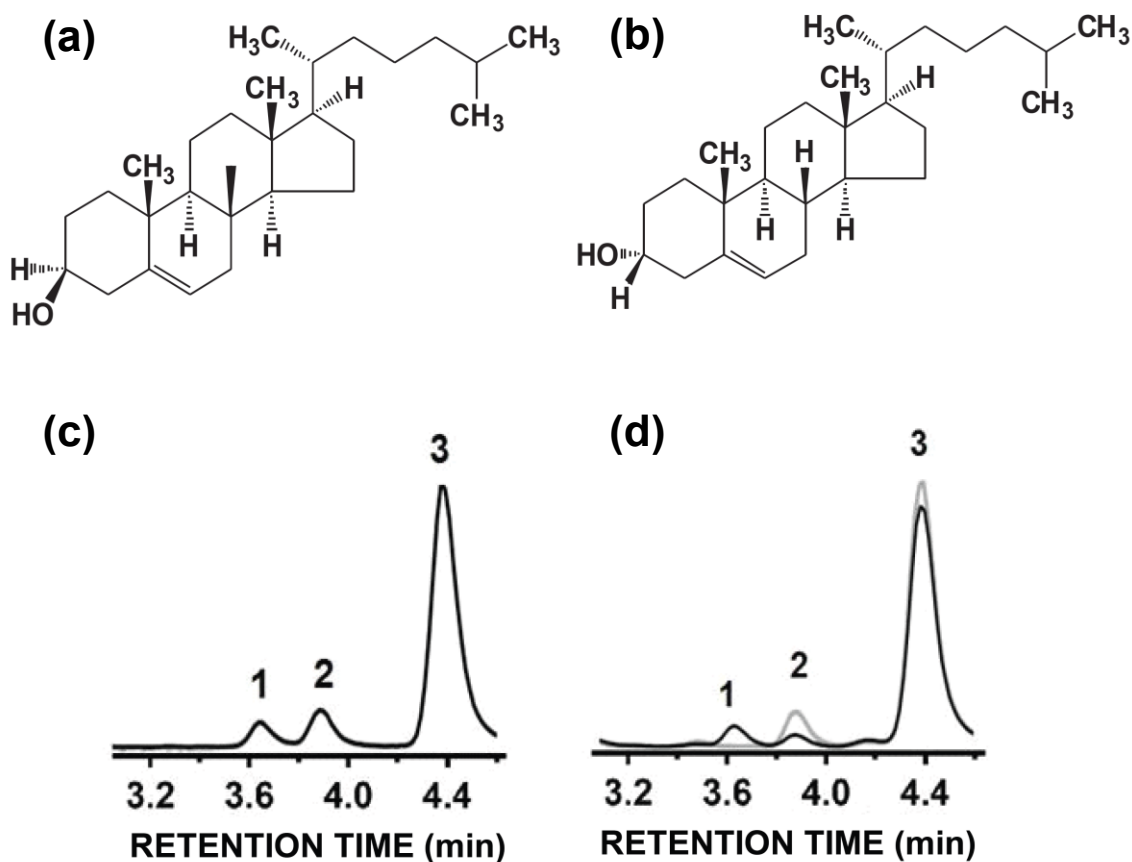


Figure A.1. Structure of (a) cholesterol and its stereoisomer (b) epicholesterol. (c) The chromatogram of a standard mixture of the two isomers and stigmasterol (internal standard) separated and detected by LC/APCI-MS. (d) The chromatogram of the lipids extracted from untreated cells (gray) and partial epicholesterol-substituted cells (black). Peak 1: epicholesterol, Peak 2: cholesterol, Peak 3: stigmasterol

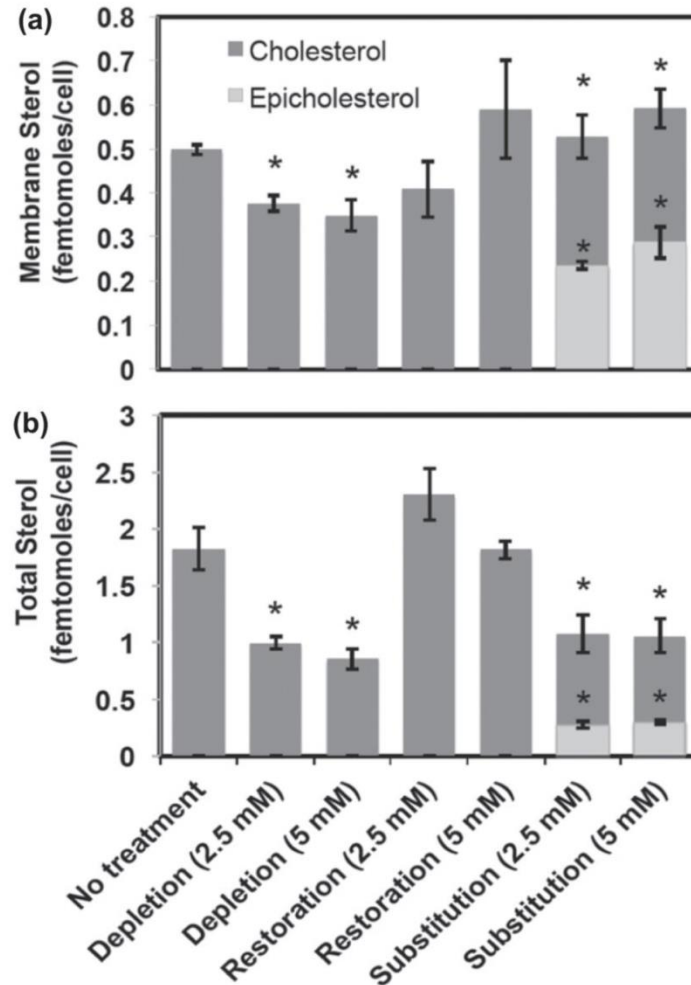


Figure A.2. (a) Membrane and (b) total cellular cholesterol concentration as measured by LC/APCI-MS in S2 cells expressing α PS2C β PS integrins in untreated cells, cells exposed to 2.5 or 5 mM M β CD to deplete cholesterol concentrations (*depletion*), in cells first depleted of cholesterol using empty 2.5 or 5 mM M β CD and then exposed to 2.5 or 5 mM M β CD:cholesterol (*restoration*) and in cells first depleted of cholesterol using empty 2.5 or 5 mM M β CD and then exposed to 2.5 or 5 mM M β CD:epicholesterol (*substitution*). The dark gray bars represent cholesterol and the light gray bars represent epicholesterol. Error bars represent one standard deviation from duplicate measurements. * p-value < 0.05 compared to the no treatment data.

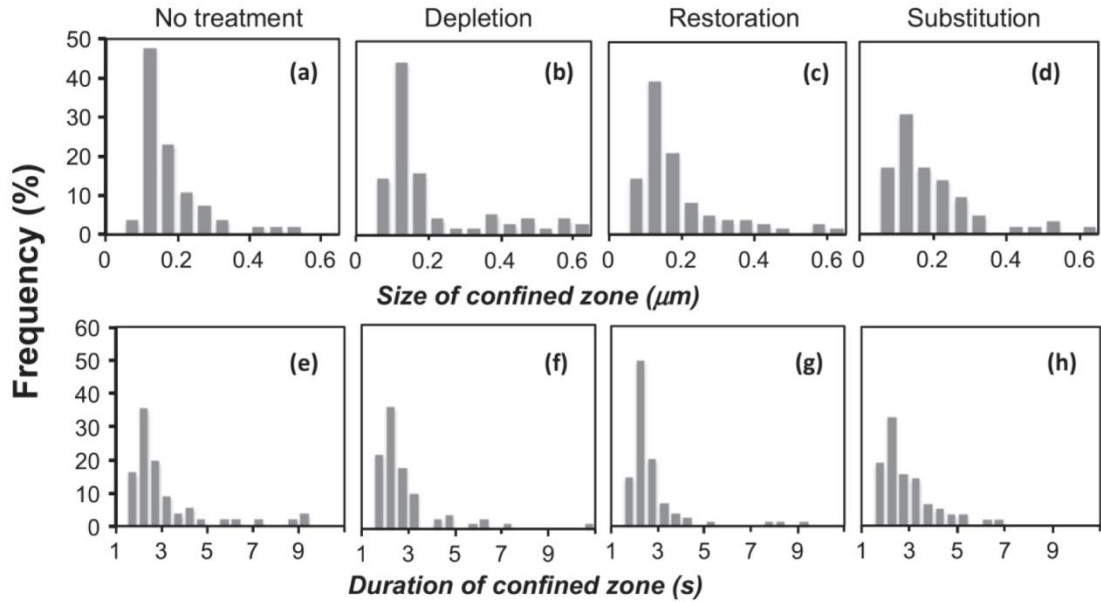


Figure A.3. Frequency histograms of (a-d) the size of confined zones and (e-h) duration in confined zones. The results were normalized to the total number of mobile trajectories exhibiting confined zones (Table A.1).

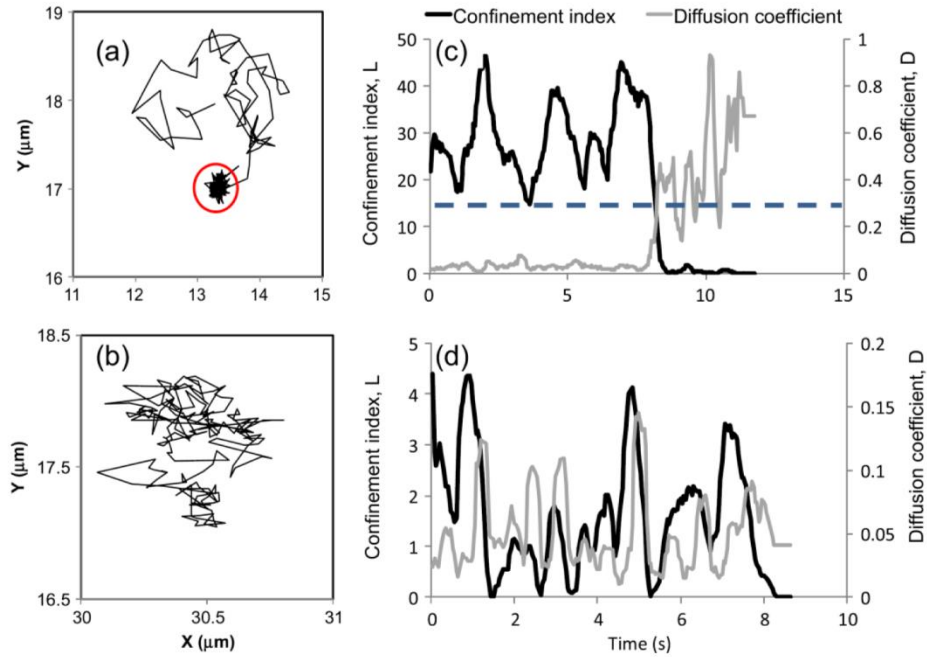


Figure A.4. Plots showing (a) a trajectory with a single confined zone depicted by a red circle (b) a Brownian trajectory with no confined zones. Panels (c-d) show instantaneous diffusion coefficient and confinement index plots. Dashed blue line indicates the critical threshold value of confinement index, L [37].

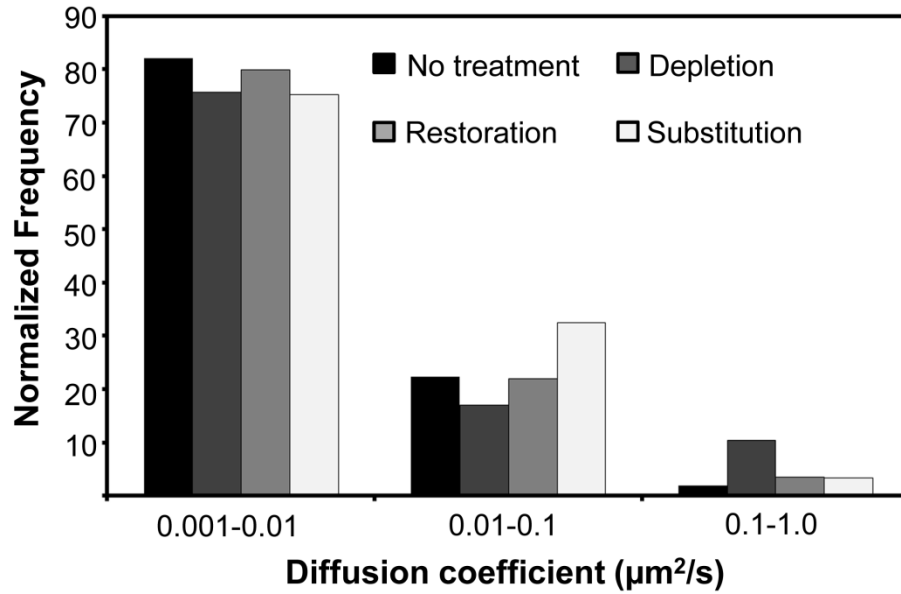


Figure A.5. Histograms of diffusion coefficients inside the confined zone measured for each confined integrin trajectory in: untreated cells, cholesterol-depleted cells, cholesterol-restored cells, and partial epicholesterol-substituted cells. Histograms were normalized with respect to the number of mobile trajectories and the total number of trajectories in each data set; the number of mobile trajectories in each data set is shown in Table A.1.

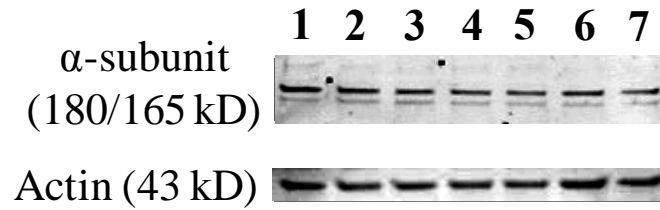


Figure A.6. Western blot of the HA-tagged α PS2 integrin subunit. The α PS2 subunit has been shown to produce two bands at 180 kD and 165 kD [53]. 1: no treatment, 2: 2.5 mM M β CD (*depletion*), 3: 5 mM M β CD (*depletion*), 4: 2.5 mM M β CD followed by 2.5 mM M β CD:cholesterol (*restoration*) and 5: 5 mM M β CD followed by 5 mM M β CD:cholesterol (*restoration*), 6: 2.5 mM M β CD followed by 2.5 mM M β CD:epicholesterol (*substitution*) and 7: 5 mM M β CD followed by 5 mM M β CD:epicholesterol (*substitution*). Actin (43 kD) was used as a loading control.

Table A.1. Diffusion parameters obtained from SPT analysis of 100 integrin trajectories.^a

	No treatment	Cholesterol depletion	Cholesterol restoration	Partial epicholesterol substitution
Mobile trajectories (%)	74	97	82	82
Brownian Trajectories				
Trajectories with Brownian diffusion (#)	36	40	32	32
Diffusion coefficient ($\mu\text{m}^2/\text{sec}$)	0.2 ± 0.3	0.2 ± 0.3 (p=0.9)	0.1 ± 0.1 (p=0.1)	0.1 ± 0.1 (p=0.3)
Confined trajectories				
Trajectories with confined diffusion (#)	38	57	50	51
Diffusion coefficient inside the confined zones ($\mu\text{m}^2/\text{sec}$)	0.01 ± 0.03	0.03 ± 0.06 (p=0.03*)	0.01 ± 0.03 (p=0.5)	0.02 ± 0.04 (p=0.3)
Diffusion coefficient outside the confined zones ($\mu\text{m}^2/\text{sec}$)	0.1 ± 0.3	0.1 ± 0.1 (p=0.6)	0.1 ± 0.1 (p=0.4)	0.1 ± 0.1 (p=0.3)
Diameter of confined zones (μm)	0.2 ± 0.2	0.4 ± 0.4 (p=0.09)	0.2 ± 0.2 (p=0.8)	0.2 ± 0.2 (p=0.5)
Duration of confined zones (s)	3 ± 2	3 ± 3 (p=0.9)	2 ± 1 (p=0.09)	2 ± 1 (p=0.3)

^a p-values were obtained from Welch's t-test. *statistically significant at the 95% confidence level.

Table A.2. Integrin mobile fractions and diffusion coefficients measured by FRAP.

Treatments	Mobile Fraction	Diffusion Coefficient at 1s ($\mu\text{m}^2/\text{s}$)	Diffusion Coefficient at 50s ($\mu\text{m}^2/\text{s}$)
No treatment	0.77 ± 0.02	0.84 ± 0.07	0.50 ± 0.05
Cholesterol depletion	0.58 ± 0.02	1.8 ± 0.1	2.5 ± 0.5
Cholesterol restoration	0.90 ± 0.05	0.8 ± 0.1	0.26 ± 0.04
Partial epicholesterol substitution	0.74 ± 0.03	0.9 ± 0.1	0.31 ± 0.04

A.8. Supporting Information for Appendix A

Western blot analysis

After the heat shock and 3 h recovery, integrin expressing cells were subjected to cholesterol depletion, restoration, or substitution as described above. Cells were washed twice with cold $1 \times$ PBS, pH 6.5 (0.13 M NaCl, 7 mM Na_2HPO_4 , 3 mM NaH_2PO_4) at 4 °C and lysed using RIPA buffer (150 mM sodium chloride, 1.0% NP-40 detergent, 0.5% sodium deoxycholate, 0.1% SDS, 50 mM Tris, pH 8.0) containing Halt™ Protease Inhibitor Cocktail (Thermo Scientific, Rockford, IL). Proteins were chloroform/methanol precipitated, redissolved in sodium dodecyl sulfate (SDS) buffer (4% SDS, 50 mM Tris, 5 mM EDTA, pH 7.4) and separated by SDS polyacrylamide gel electrophoresis (PAGE). After electrophoresis, the proteins were electro-transferred to Immun-Blot® LF PVDF membrane (Bio-Rad, Hercules, CA) according to standard protocols. Following protein transfer, the membrane was probed following the manufacturer's protocol (Bio-Rad). Antibodies used for blotting were: anti-HA rabbit polyclonal (primary, 1:1000, Invitrogen, Oregon) and Alexa Fluor 647-conjugated goat anti-rabbit IgG (secondary, 1:10,000, Invitrogen, Oregon). The antibody labeling was detected and analyzed by fluorescent scanning on a Typhoon 9410 (GE Healthcare, Waukesha, WI). As a loading control, the membrane was stripped and reprobed with an antibody against the cytoplasmic protein actin (Santa Cruz Biotechnology, Santa Cruz, CA). The normalized intensity of the 180 kD/43 kD bands was measured in Image J version 1.45 s.

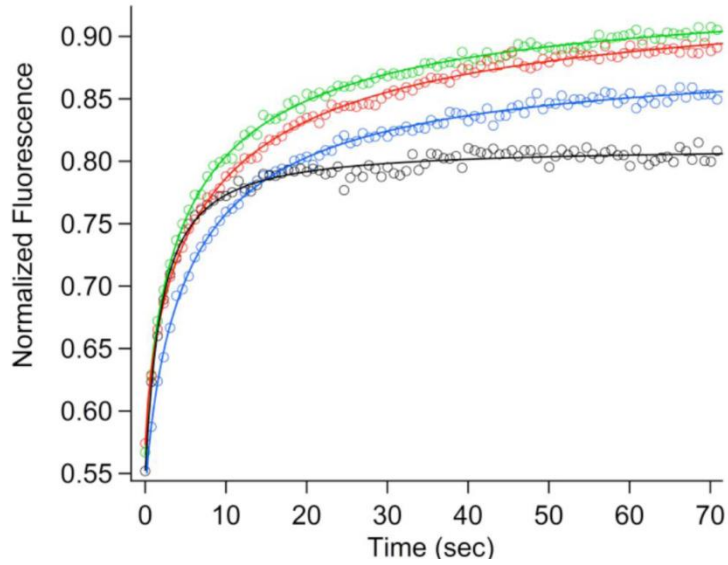


Figure SA.1. Average fluorescence recovery after photobleaching (FRAP) curves from 10 replicate measurements (circles) of S2 cells expressing α PS2C β PS-Venus integrins (blue) at native cholesterol concentration; (black) reduced cholesterol concentration; (green) restored cholesterol concentration; (red) restored epicholesterol concentration. The data are fit (solid lines following the same color scheme previously described) to a model for time-dependent diffusion with an immobile fraction. Curves have been normalized to the pre-photobleach intensity.

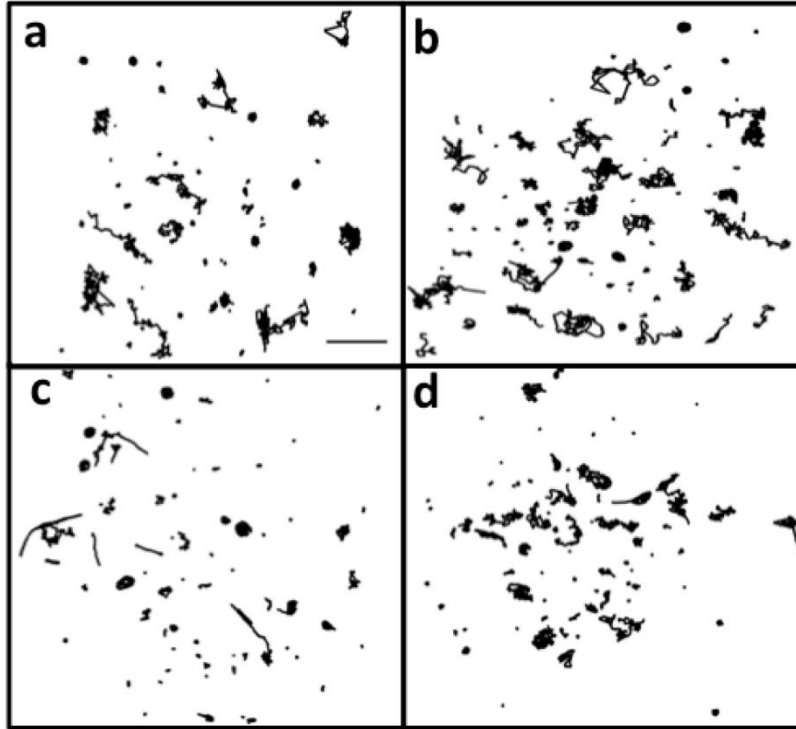


Figure S.A.2. Trajectories of all mobile integrins obtained from SPT measurements showing diffusion of α PS2 β PS integrins in: (a) untreated cells, (b) cholesterol-depleted cells, (c) cholesterol-restored cells, (d) partial epicholesterol-substituted cells. The absolute position of trajectories in the graph has no meaning since some trajectories were moved to prevent overlap, and the trajectories were collected from several cells with different shapes and locations on the microscope slide.

APPENDIX B**SELF-IMMOLATIVE PHTHALATE ESTERS SENSITIVE TO HYDROGEN PEROXIDE AND LIGHT**

“Reproduced with permission from [Mahoney, K. M.; Goswami, P. P.; Syed, A.; Kolker, P.; Shannan, B.; Smith, E. A.; Winter, A. H., *The Journal of Organic Chemistry*, **79**, 11740-11743 (2014).] Copyright [2014] American Chemical Society.”

*Kaitlyn M. Mahoney, Pratik P. Goswami, Aleem Syed, Patrick Kolker, Brian Shannan, Emily A. Smith
and Arthur H. Winter*

B.1. Abstract

Self-immolative aryl phthalate esters are conjugated with cleavable masking groups sensitive to light and hydrogen peroxide. The phthalate linker releases the fluorescent dye 7-hydroxycoumarin upon exposure to light or H₂O₂, respectively, leading to an increase in fluorescence. The light-sensitive aryl phthalate ester is demonstrated as a pro-fluorophore in cultured S2 cells.

B.2. Introduction

Self-immolative linkers have proven to be useful for connecting a cleavable masking molecule to an output cargo molecule [1-4]. Upon exposure to an input stimulus that cleaves the mask, self-immolative linkers release their cargo. Self-immolative linkers have found applications in enzyme activated prodrugs [5-12], chemical sensors [2], traceless linkers [13-15], biological probes [16-18], and degradable polymers [19-21]. Released chemical cargos are often biomolecules, drugs, or reporters such as fluorescent dyes. Ideally, self-immolative linkers should be simple in design, stable, compatible with water, and transformed into a benign byproduct upon release of the output cargo. Additionally, they should be easy to conjugate, readily adaptable to a variety of inputs and outputs, and quickly release the output cargo. A drawback to some self-immolative linkers is that cargo release rates can be slow

(minutes to hours), leading to loss of temporal resolution. Our group has recently reported aryl phthalate esters as self-immolative linkers [3]. In this previous work, we demonstrated that a fluoride-sensitive masking group could release cargo phenols and phenolic-based fluorescent dyes. Phthalate self-immolative linkers exploit the rapid hydrolysis of esters with adjacent catalytic carboxylate moieties, a classic case of neighboring group participation [22-24] (phenyl hydrogen phthalate releases phenol in <5 s in neutral water [3]). These intra-molecularly catalyzed reactions involve neighboring group attack by the free carboxylate upon the adjacent ester to generate a transient anhydride that undergoes spontaneous hydrolysis to yield the diacid. Here, we demonstrate that phthalate esters masked with light- and peroxide-sensitive groups can release a coumarin dye upon exposure to light or peroxide (Scheme B.1). Peroxide is an important biological signaling molecule, whereas light-releasable fluorescent dyes (pro-fluorophores) have found application in monitoring dynamic events in real time [25-29] as well as recording images with subdiffraction resolution at the nanometer level [30-33].

B.3. Results and Discussion

Both compound **1** and **2** were synthesized by the addition of the trigger molecule to phthalic anhydride followed by the addition of 7-hydroxycoumarin by either a DCC/DMAP or EDC/DMAP coupling. Compounds **1** and **2** were exposed to UV light and hydrogen peroxide, respectively. The reactions were monitored using fluorescence and ^1H NMR spectroscopy. The titration of **1** resulted in an 18-fold increase in fluorescence intensity and **2** showed an 8-fold increase as a result of releasing the free fluorescent dyes.

The titrations of **1** and **2** were followed by fluorescence spectroscopy (Figure B.1). To aid with solubility, experiments with **1** were carried out by first dissolving the compound in DMF and exposing the resulting solution to 350-nm light, a small aliquot (7 μL) of the solution was then injected into buffered water (3.0 mL, pH 7.0, 1 mM phosphate buffer) and fluorescence was followed as a function of time. Experiments for **2** were carried out by first dissolving the compound in DMF and titrating with

hydrogen peroxide. This procedure was followed by injection of a small aliquot of the DMF/H₂O₂ solutions into buffered water for the fluorescence analysis.

Compound **1** was stable in water/DMF mixtures in the absence of light for at least one day at room temperature (see the Supporting Information for details). Compound **2** did show some instability, as seen by a small increase in fluorescence after a 16-h period in a water/DMF mixture in the absence of hydrogen peroxide (see the Supporting Information for spectra). Additionally, it is noteworthy that this structure **2** is quite unstable under the seemingly mild conditions required to synthesize it (*e.g.* DCC/DMAP ester coupling), possibly the result of the boronate ester under the reaction conditions catalyzing a spontaneous ester hydrolysis (**2** is stable as a solid or dissolved in a solution lacking hydrogen peroxide, however). Additionally, NMR product studies of **1** after exposure to light indicate that the organic products are the expected free 7-hydroxycoumarin as well as phthalic acid. The toxicity of phthalic acid has been studied due to its industrial use in the synthesis of phthalate plastics and esters; it has not been found to be very toxic in mice (LD50 (mouse) is 2.53 g/kg).

Because **1** showed the largest increase in fluorescence intensity and the greatest stability during the titration studies, we chose to use it for cellular experiments. Compound **1** was incubated with *Drosophila* S2 cells, and dye release was monitored using fluorescence microscopy. See Figure B.2.

The *Drosophila* S2 cells were loaded with **1** and subjected to continuous irradiation with 335-nm light. Fluorescence images were collected every 500 ms for a total of 33 min (Figure B.2). Fluorescence emission was observed at 450 nm. Fluorescence intensity for Figure B.2 (i–iii) was taken from the periphery of the cell where the concentration of **1** was highest. As shown in Figure B.2E–H, at the beginning of the experiment there was minimal fluorescence; however, after exposure to light a gradual increase in fluorescence is seen for up to 33 min. The initial fluorescence seen at time zero can be attributed to cellular auto fluorescence, which undergoes initial bleaching prior to significant release of the free coumarin dye. Control studies were performed to make sure the fluorescence was due to the controlled release of 7-hydroxycoumarin by irradiation. Parts A–D of Figure B.2 show that there is a

minimal change in fluorescence of cells when they are irradiated without being loaded with **1**. Another control study (Figure B.2 (ii)) was performed with cells incubated with **1** but not exposed to irradiation. There was an initial fluorescence signal due to cellular auto fluorescence; however, a decrease in fluorescence signal is seen, eventually leveling off to intensity similar to that of the unloaded cells, indicating that the **1** does not release the dye in the absence of irradiation.

The cytotoxicity of **1** in the cells was determined by incubating the cells (1×10^6 cells/mL) with different dilutions (100, 50, 25, 12.5, 6.25, and 3.125 μM) of **1** in phosphate buffer saline (PBS, pH = 7.1) for 1 h. At a compound concentration of 50 μM , 83% of the cells remained viable after 1 h, and this concentration was used in all fluorescence imaging cell studies.

B.4. Conclusions

We have shown that aryl phthalate self-immolative linkers are easily conjugated with the light-sensitive 2-nitrobenzyl alcohol group and the hydrogen peroxide sensitive group 4-(hydroxymethyl) phenylboronic acid pinacol peroxide sensor. Compound **1** is of interest because it is able to deliver cargo in a temporally and spatially controlled manner using irradiation. Release of caged 7-hydroxycoumarin occurs upon irradiation within S2 cells. We note finally that the known fast rates of hydrolysis of phthalate self-immolative linkers may make these structures good candidates for domino self-immolative linkers [34-38], wherein a single input reaction results in the spontaneous release of numerous cargo molecules. Current domino self-immolative linkers tend to have slow kinetics of release. A recent method to synthesize aryl mellitic acid esters [39] may enable these structures to be used within fast releasing domino self-immolative systems.

B.5. Experimental Section

Synthesis of 2-(nitrobenzyl) hydrogen phthalate

Phthalic acid (0.100 g, 0.675 mmol) and 2-nitrobenzyl alcohol (0.103 g, 0.675 mmol) were refluxed in toluene under argon overnight. The crude product was collected by evaporation under reduced pressure. The resulting mixture was dissolved in ethyl acetate, and the product was extracted with aqueous sodium bicarbonate followed by acidification with 1 M aqueous hydrogen chloride. Final collection of a white solid was performed by vacuum filtration. The product was dried under vacuum and used without any further purification (0.203 g, 36%): ^1H NMR (400 MHz, DMSO- d_6) δ 13.35 (s, 1H), 8.15 (dd, J = 8.1, 1.2 Hz, 1H), 7.85–7.60 (m, 7H), 5.63 (s, 2H); ^{13}C (DMSO- d_6 , 100 MHz) δ 168.4, 167.6, 147.8, 134.6, 132.1, 131.9, 131.9, 131.5, 129.9, 129.8, 129.4, 128.8, 125.3, 64.1; mp 142–145 °C; HRMS (ESI) m/z $[\text{M} + \text{Na}]^+$ for $\text{C}_{15}\text{H}_{11}\text{NNaO}_6$ requires 324.0479, found 324.0480.

Synthesis of 7-hydroxycoumarinyl 2-(nitrobenzyl) hydrogen phthalate (1)

2-(Nitrobenzyl) hydrogen phthalate (0.200 g, 0.664 mmol), N-(3-(dimethylamino)propyl)-N'-ethylcarbodiimide hydrochloride (0.126 g, 0.657 mmol), and 4-(N,N-dimethylamino)-yridine (0.089 g, 0.728 mmol) were dissolved in dry DCM (10 mL), followed by continuous stirring of the solution. 7-Hydroxycoumarin potassium salt (0.132 g, 0.660 mmol) and 18-crown-6 (0.174 g, 0.660 mmol) were added next to the reaction mixture, and the reaction was stirred under an argon atmosphere for 12 h. The product was washed with an aqueous saturated sodium bicarbonate solution. The solvent was then removed under reduced pressure to yield the crude product as a white solid. Flash chromatography (Hex/EtOAc, 30:70 \rightarrow chloroform/MeOH 95:5) gave the pure final product (0.123 g, 42%): ^1H NMR (DMSO- d_6 , 400 MHz) δ 8.16–8.08 (m, 2H), 8.06–7.91 (m, 2H), 7.90–7.72 (m, 5H), 7.67–7.56 (m, 1H), 7.34 (d, J = 2.2 Hz, 1H), 7.23 (dd, J = 8.4, 2.2 Hz, 1H), 6.53 (d, J = 9.6 Hz, 1H), 5.74–5.69 (m, 2H), 1.24 (s, 1H), 0.84 (t, J = 6.8 Hz, 1H); ^{13}C NMR (DMSO- d_6 , 100 MHz) δ 166.3, 165.7, 160.0, 154.5, 153.0, 148.0, 144.2, 134.5, 132.8, 131.0, 130.3, 130.0, 129.9, 129.8, 125.3, 118.6, 117.4, 116.2, 110.2,

79.6, 79.4, 79.1, 64.4; mp >260 °C; HRMS (ESI) calcd. for $C_{24}H_{15}NO_8$ $[M + H]^+$ requires 446.0870, found 446.0872.

Synthesis of 4-(hydroxymethyl)benzeneboronic acid pinacol hydrogen phthalate

Phthalic anhydride (0.049 g, 0.294 mmol) and 4-(hydroxymethyl)benzeneboronic acid pinacol (0.077 g, 0.329 mmol) were refluxed in toluene overnight. The crude product was collected by evaporation under reduced pressure. The resulting mixture was dissolved in ethyl acetate, and the product was extracted with aqueous sodium bicarbonate followed by acidification with hydrogen chloride. Vacuum filtration was used to collect the white solid. The product was dried under vacuum and used without any further purification (0.045 g, 40%): 1H NMR (DMSO- d_6 , 400 MHz) δ 7.85 (s, 1H), 7.72 (m, 6H), 7.52 (d, 1H, $J = 0.8$ Hz), 1.36 (s, 12H); ^{13}C (DMSO- d_6 , 100 MHz) δ 168.4, 167.9, 139.4, 137.0, 135.0, 134.7, 132.6, 131.9, 129.4, 128.8, 127.8, 127.4, 84.2, 67.1, 25.1; mp 121–123 °C; HRMS (ESI) calcd. for $C_{21}H_{23}BO_6$ $(M - H^+)^-$ requires 380.1551, found 380.1550 (mass calculated using boron isotope ^{10}B).

Synthesis of 7-hydroxycoumarinyl 2-(4-hydroxymethyl)-benzeneboronic phthalate (2)

4-(Hydroxymethyl)benzeneboronic acid pinacol hydrogen phthalate (0.100 g, 0.262 mmol), N,N-dicyclohexylcarbodiimide (0.068 g, 0.314 mmol), 4-(N,N-dimethylamino) pyridine (0.011 g, 0.087 mmol), and 18-crown-6 ether (0.069 g, 0.262 mmol) were dissolved in dry DMF (3 mL) followed by continuous stirring of the solution. 7-Hydroxycoumarin potassium salt (0.052 g, 0.262 mmol) was next added to the reaction mixture, and the reaction was stirred under an argon atmosphere overnight. The dicyclohexylurea byproduct was filtered off as a white solid. The solvent was then removed under reduced pressure to yield the crude product as a white solid. Flash chromatography (Hex/EtOAc, 50:50) gave the pure final product (5.6 mg, 4.1%): 1H NMR (400 MHz, DMSO- d_6) δ 8.10 (d, $J = 9.6$ Hz, 1H), 8.02–7.90 (m, 2H), 7.87–7.75 (m, 3H), 7.62 (dd, $J = 7.0, 1.3$ Hz, 2H), 7.43 (d, $J = 7.6$ Hz, 2H), 7.32 (d, $J = 2.1$ Hz, 1H), 7.18 (ddd, $J = 8.5, 2.2, 0.8$ Hz, 1H), 6.52 (dd, $J = 9.6, 0.8$ Hz, 1H), 5.40 (s, 2H), 1.27 (d,

$J = 0.8$ Hz, 12H); ^{13}C NMR (DMSO- d_6 , 100 MHz) δ 166.6, 165.8, 160.3, 154.7, 153.3, 142.8, 138.2, 135.1, 131.8, 131.6, 131.5, 129.5, 129.2, 128.6, 127.5, 118.4, 116.8, 116.2, 110.4, 80.9, 67.6, 24.9; mp; HRMS (ESI) calcd. for $\text{C}_{30}\text{H}_{27}\text{BO}_8$ ($\text{M} + \text{H}$) $^+$ requires 526.1904, found 526.1908 (mass calculated using boron isotope ^{10}B).

Acknowledgements

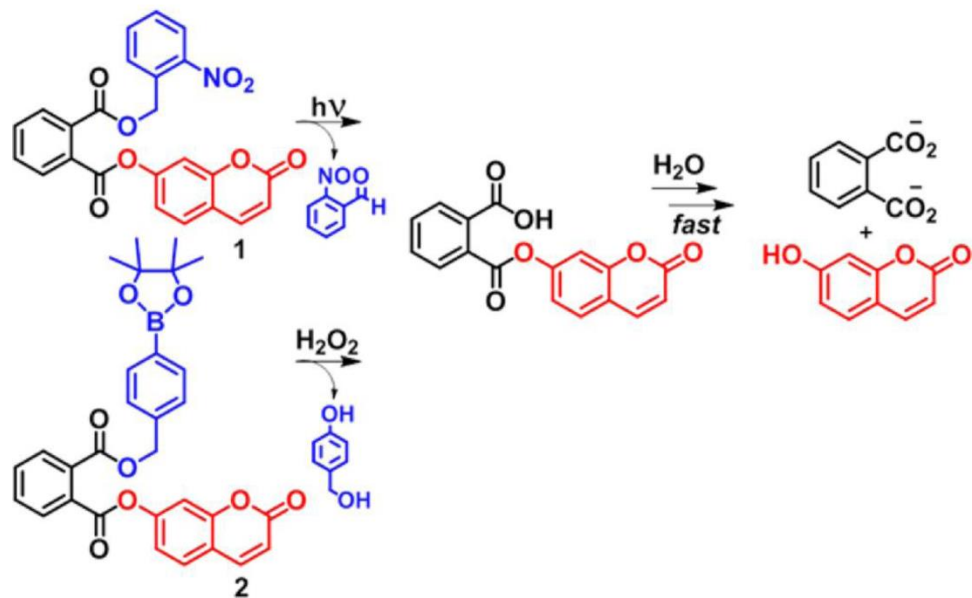
A.H.W acknowledges the Research Corporation for Scientific Advancement (Cottrell Scholar Award) and the Petroleum Research Fund for financial support. E.A.S acknowledges National Science Foundation (CHE-0845236) for financial support.

B.6. References

- [1] R.J. Amir, N. Pessah, M. Shamis, D. Shabat, Self-Immolative Dendrimers, *Angew. Chem. Int. Ed.*, 42 (2003) 4494-4499.
- [2] S.S. Chandran, K.A. Dickson, R.T. Raines, Latent Fluorophore Based on the Trimethyl Lock, *J. Am. Chem. Soc.*, 127 (2005) 1652-1653.
- [3] K.M. Mahoney, P.P. Goswami, A.H. Winter, Self-Immolative Aryl Phthalate Esters, *J. Org. Chem.*, 78 (2013) 702-705.
- [4] K.M. Schmid, L. Jensen, S.T. Phillips, A Self-Immolative Spacer That Enables Tunable Controlled Release of Phenols under Neutral Conditions, *J. Org. Chem.*, 77 (2012) 4363-4374.
- [5] R.J. Amir, M. Popkov, R.A. Lerner, C.F. Barbas, D. Shabat, Prodrug Activation Gated by a Molecular "OR" Logic Trigger, *Angew. Chem.*, 44 (2005) 4378-4381.
- [6] G.M. Dubowchik, R.A. Firestone, L. Padilla, D. Willner, S.J. Hofstead, K. Mosure, J.O. Knipe, S.J. Lasch, P.A. Trail, Cathepsin B-Labile Dipeptide Linkers for Lysosomal Release of Doxorubicin from Internalizing Immunoconjugates: Model Studies of Enzymatic Drug Release and Antigen-Specific In Vitro Anticancer Activity, *Bioconj. Chem.*, 13 (2002) 855-869.
- [7] A. Gopin, N. Pessah, M. Shamis, C. Rader, D. Shabat, A Chemical Adaptor System Designed To Link a Tumor-Targeting Device with a Prodrug and an Enzymatic Trigger, *Angew. Chem.*, 42 (2003) 327-332.
- [8] D. Niculescu-Duvaz, I. Niculescu-Duvaz, F. Friedlos, J. Martin, R. Spooner, L. Davies, R. Marais, C.J. Springer, Self-Immolative Nitrogen Mustard Prodrugs for Suicide Gene Therapy, *J. Med. Chem.*, 41 (1998) 5297-5309.
- [9] O. Redy, D. Shabat, Modular theranostic prodrug based on a FRET-activated self-immolative linker, *J. Con. Rel.*, 164 (2012) 276-282.
- [10] J.A. Sáez, B. Escuder, J.F. Miravet, Supramolecular hydrogels for enzymatically triggered self-immolative drug delivery, *Tetrahedron*, 66 (2010) 2614-2618.
- [11] R. Weinstain, P.S. Baran, D. Shabat, Activity-Linked Labeling of Enzymes by Self-Immolative Polymers, *Bioconj. Chem.*, 20 (2009) 1783-1791.
- [12] J.J. Yang, S.A. Kularatne, X. Chen, P.S. Low, E. Wang, Characterization of in Vivo Disulfide-Reduction Mediated Drug Release in Mouse Kidneys, *Mol. Pharmaceutics*, 9 (2012) 310-317.
- [13] S. Ding, N.S. Gray, Q. Ding, P.G. Schultz, A Concise and Traceless Linker Strategy toward Combinatorial Libraries of 2,6,9-Substituted Purines, *J. Org. Chem.*, 66 (2001) 8273-8276.
- [14] J.R. Horton, L.M. Stamp, A. Routledge, A photolabile 'traceless' linker for solid-phase organic synthesis, *Tetrahedron Lett.*, 41 (2000) 9181-9184.
- [15] F. Stieber, U. Grether, H. Waldmann, An oxidation-labile traceless linker for solid-phase synthesis, *Angew. Chem.*, 38 (1999) 1073-1077.
- [16] J.A. Duimstra, F.J. Femia, T.J. Meade, A Gadolinium Chelate for Detection of β -Glucuronidase: A Self-Immolative Approach, *J. Am. Chem. Soc.*, 127 (2005) 12847-12855.
- [17] S.C. Jeffrey, M.Y. Torgov, J.B. Andreyka, L. Boddington, C.G. Cerveny, W.A. Denny, K.A. Gordon, D. Gustin, J. Haugen, T. Kline, M.T. Nguyen, P.D. Senter, Design, Synthesis, and in Vitro Evaluation of Dipeptide-Based Antibody Minor Groove Binder Conjugates, *J. Med. Chem.*, 48 (2005) 1344-1358.
- [18] Y.-L. Leu, C.-S. Chen, Y.-J. Wu, J.-W. Chern, Benzyl Ether-Linked Glucuronide Derivative of 10-Hydroxycamptothecin Designed for Selective Camptothecin-Based Anticancer Therapy, *J. Med. Chem.*, 51 (2008) 1740-1746.
- [19] D. Shabat, Self-immolative dendrimers as novel drug delivery platforms, *J. Polym. Sci. Part A: Polym. Chem.*, 44 (2006) 1569-1578.
- [20] R. Weinstain, A. Sagi, N. Karton, D. Shabat, Self-Immolative Comb-Polymers: Multiple-Release of Side-Reporters by a Single Stimulus Event, *Chem. Eur. J.*, 14 (2008) 6857-6861.

- [21] C.A. Blencowe, A.T. Russell, F. Greco, W. Hayes, D.W. Thornthwaite, Self-immolative linkers in polymeric delivery systems, *Polym. Chem.*, 2 (2011) 773-790.
- [22] D.J. Pasto, M.P. Serve, Neighboring Group Participation by Carbonyl Oxygen, *J. Am. Chem. Soc.*, 87 (1965) 1515-1521.
- [23] G.O. Andrés, A.M. Granados, R.H. de Rossi, Kinetic Study of the Hydrolysis of Phthalic Anhydride and Aryl Hydrogen Phthalates, *J. Org. Chem.*, 66 (2001) 7653-7657.
- [24] J.W. Thanassi, T.C. Bruice, Neighboring Carboxyl Group Participation in the Hydrolysis of Monoesters of Phthalic Acid. The Dependence of Mechanisms on Leaving Group Tendencies, *J. Am. Chem. Soc.*, 88 (1966) 747-752.
- [25] R.W. Dirks, C. Molenaar, H.J. Tanke, Methods for visualizing RNA processing and transport pathways in living cells, *Histochem. Cell Biol.*, 115 (2001) 3-11.
- [26] Y. Xu, T.J. Melia, D.K. Toomre, Using light to see and control membrane traffic, *Curr. Opin. Chem. Biol.*, 15 (2011) 822-830.
- [27] S.S. Agasti, R.H. Kohler, M. Liong, V.M. Peterson, H. Lee, R. Weissleder, Dual Imaging and Photoactivated Nanoprobe for Controlled Cell Tracking, *Small*, 9 (2013) 222-227.
- [28] S.R. Adams, R.Y. Tsien, Controlling Cell Chemistry with Caged Compounds, *Annu. Rev. Physiol.*, 55 (1993) 755-784.
- [29] J.C. Politz, Use of caged fluorochromes to track macromolecular movement in living cells, *Trends in Cell Biol.*, 9 (1999) 284-287.
- [30] M. Fernandez-Suarez, A.Y. Ting, Fluorescent probes for super-resolution imaging in living cells, *Nat. Rev. Mol. Cell Biol.*, 9 (2008) 929-943.
- [31] B. Huang, M. Bates, X. Zhuang, Super-Resolution Fluorescence Microscopy, *Annu. Rev. Biochem.*, 78 (2009) 993-1016.
- [32] D. Toomre, J. Bewersdorf, A New Wave of Cellular Imaging, *Annu. Rev. Cell Biol.*, 26 (2010) 285-314.
- [33] S. van de Linde, M. Heilemann, M. Sauer, Live-Cell Super-Resolution Imaging with Synthetic Fluorophores, *Annu. Rev. Phys. Chem.*, 63 (2012) 519-540.
- [34] I.S. Turan, E.U. Akkaya, Chemiluminescence Sensing of Fluoride Ions Using a Self-Immolative Amplifier, *Org. Lett.*, 16 (2014) 1680-1683.
- [35] M. Shamis, D. Shabat, Single-Triggered AB₆ Self-Immolative Dendritic Amplifiers, *Chem. Eur. J.*, 13 (2007) 4523-4528.
- [36] R.J. Amir, E. Danieli, D. Shabat, Receiver–Amplifier, Self-Immolative Dendritic Device, *Chem. Eur. J.*, 13 (2007) 812-821.
- [37] A. Sagi, E. Segal, R. Satchi-Fainaro, D. Shabat, Remarkable drug-release enhancement with an elimination-based AB₃ self-immolative dendritic amplifier, *Bioorg. Med. Chem.*, 15 (2007) 3720-3727.
- [38] N. Karton-Lifshin, D. Shabat, Exponential diagnostic signal amplification via dendritic chain reaction: the dendritic effect of a self-immolative amplifier component, *New J. Chem.*, 36 (2012) 386-393.
- [39] M.R. Geraskina, M.J. Juetten, A.H. Winter, Access to Aryl Mellitic Acid Esters through a Surprising Oxidative Esterification Reaction, *J. Org. Chem.*, 79 (2014) 5334-5337.

B.7. Schemes and Figures



Scheme B.1. General unmasking scheme for compound 1 and 2.

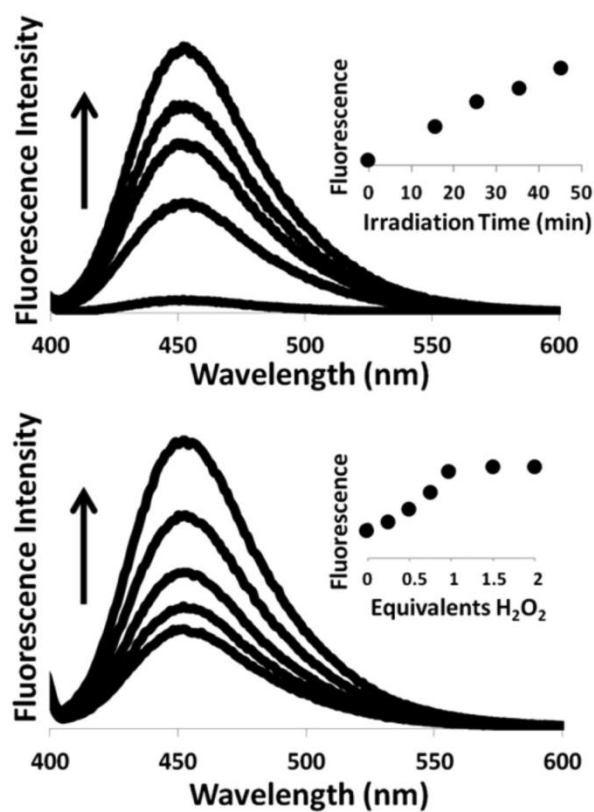


Figure B.1. Fluorescence of compound **1** (6.27×10^{-6} M) as a function of irradiation time (top); fluorescence of **2** (6.27×10^{-6} M) as a function of peroxide (bottom) in pH 7.0 buffer. Plot inserts depict fluorescence at the emission maxima (453 nm) vs time of irradiation or equivalents of hydrogen peroxide.

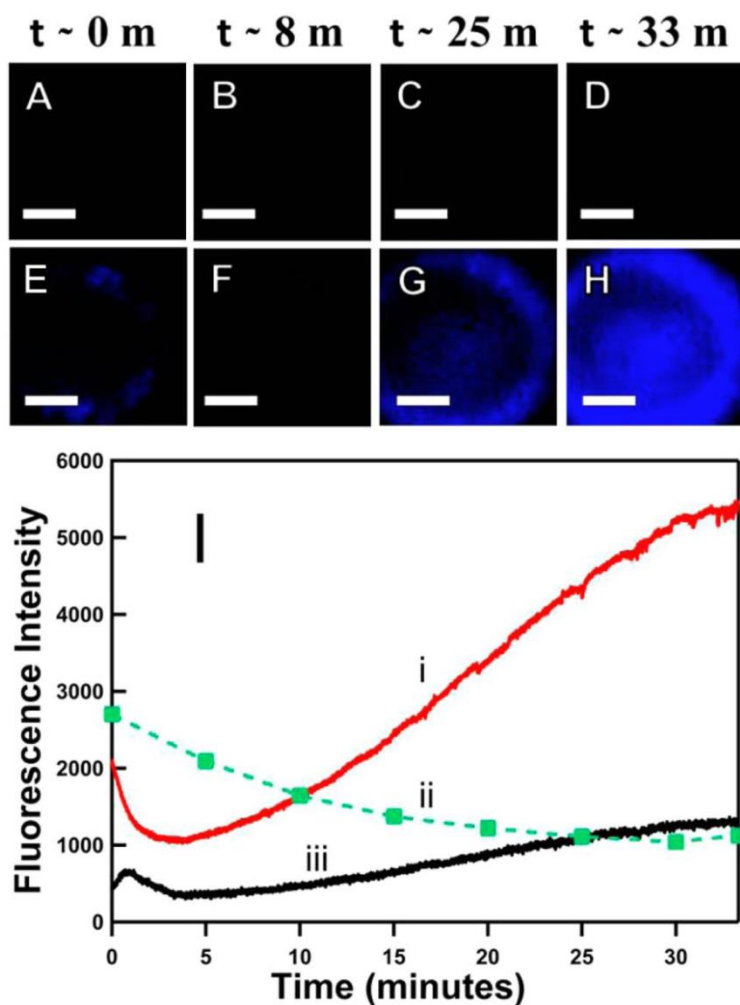


Figure B.2. Fluorescence images of a cell with no compound **1** (A–D) and cell incubated with compound **1** ($50 \mu\text{M}$) (E–H) as a function of irradiation time. (I) Average fluorescence intensity as a function of time for (i) four cells incubated with compound **1** and exposed to continuous irradiation for 35 min, (ii) four cells incubated with compound **1** and only exposed to irradiation briefly every 5 min to obtain an image, and (iii) a cell without compound **1** and exposed to continuous irradiation for 35 min. Scale bar represents $5 \mu\text{m}$ in all images.

B.8. Supporting Information for Appendix B

Complete electronic supporting information is available on ACS website (<http://pubs.acs.org/doi/suppl/10.1021/jo501900h>)

Cell Preparation and Imaging

Cell culture

Drosophila S2 cells were used in all live cell experiments. Cells were cultured according to the culture techniques described previously [1-3]. Briefly, cells were cultured in Shields and Sang M3 insect medium with heat-inactivated 10% fetal bovine serum 12.5 mM streptomycin and 36.5 mM penicillin in a 22 °C incubator.

Cytotoxicity assay

Cells (1×10^6 cells/mL) were incubated with different dilutions (100 μ M, 50 μ M, 25 μ M, 12.5 μ M, 6.25 μ M and 3.125 μ M) of the 7-hydroxycoumarinyl 2-(nitrobenzyl)ethyl hydrogen phthalate in phosphate buffer saline (PBS, pH=7.1) for an hour. Cytotoxicity of the compound was measured using trypan blue exclusion assay [4]. One volume of the cell suspension from each dilution and one volume of the trypan blue stain were incubated for 3 minutes at room temperature. The number of viable cells was counted using a hemacytometer .

Cell sample preparation for fluorescence imaging

Cells (50×10^5 cells/mL) were incubated with 50 μ M of the compound (in PBS, pH=7.1) for an hour. The RBB-Tiggrin ligand-coated microscope cover glasses were prepared as described previously [5]. Incubated cells were allowed to spread on ligand coated cover glass for half an hour at room temperature. Cells were rinsed with PBS (pH=7.1) to remove unspread cells before imaging experiments.

Fluorescence imaging and analysis

All fluorescence imaging experiments were performed on a Nikon TE-2000 microscope in wide-field, epi-fluorescence mode with a 100× Apo, 1.49 numerical aperture oil-immersion objective. Samples were illuminated with mercury lamp (X-Cite 120 PC, EXFO Photonic Solutions Inc., Mississauga, Ontario, Canada) through excitation filter (365/35 nm, XF1409, Omega optical, Brattleboro, VT, USA) and reflected via dichoric mirror (400DCLP, Omega optical, Brattleboro, VT, USA). Resultant fluorescence signal was collected through emission filter (450/65 nm, XF3002, Omega optical, Brattleboro, VT, USA). Fluorescence images were collected every 500 ms for a total of 33.3 minutes using PhotonMAX 512 EMCCD camera. All experiments were performed at room temperature.

Cell sample preparation for fluorescence imaging

Cells (50×10^5 cells/mL) were incubated with 50 μ M of the compound (in PBS, pH=7.1) for an hour. The RBB-Tiggrin ligand-coated microscope cover glasses were prepared as described previously [5]. Incubated cells were allowed to spread on ligand coated cover glass for half an hour at room temperature. Cells were rinsed with PBS (pH=7.1) to remove unspread cells before imaging experiments.

Fluorescence imaging and analysis

All fluorescence imaging experiments were performed on a Nikon TE-2000 microscope in wide-field, epi-fluorescence mode with a 100× Apo, 1.49 numerical aperture oil-immersion objective. Samples were illuminated with mercury lamp (X-Cite 120 PC, EXFO Photonic Solutions Inc., Mississauga, Ontario, Canada) through excitation filter (365/35 nm, XF1409, Omega optical, Brattleboro, VT, USA) and reflected via dichoric mirror (400DCLP, Omega optical, Brattleboro, VT, USA). Resultant fluorescence signal was collected through emission filter (450/65 nm, XF3002, Omega optical, Brattleboro, VT,

USA). Fluorescence images were collected every 500 ms for a total of 33.3 minutes using PhotonMAX 512 EMCCD camera. All experiments were performed at room temperature.

pH and concentration sensitivity assays

Effect of the surrounding media pH on the cleavage of the 7-hydroxycoumarin from the Compound 1 was monitored with the same imaging conditions used for live cell imaging experiments. 25 μM of compound was prepared in PBS (pH=2.5, pH=5.0, pH=7.1, pH=9.0 and pH=11.5). 50 μL of the diluted compound were dropped on microscope glass coverslip and fluorescence signal was monitored with time. Similarly, the relationship between initial concentration and the fluorescence intensity was monitored for 100 μM , 50 μM , 25 μM and 12.5 μM of the compound in PBS (pH=7.1) over time.

Figures and Tables

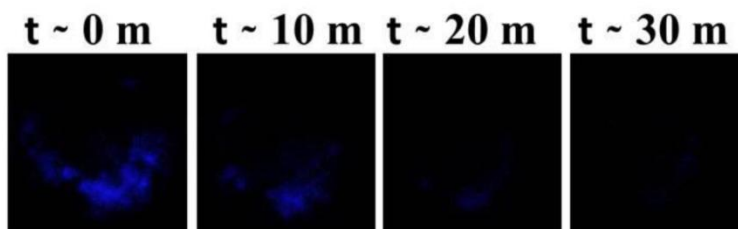


Figure SB.1. Images of cells incubated with compound but no illumination except brief (i.e., a few seconds) illumination to collect the images). Initial fluorescence at time zero is due to cellular auto fluorescence. Some bleaching is seen and no significant increase in fluorescence is observed.

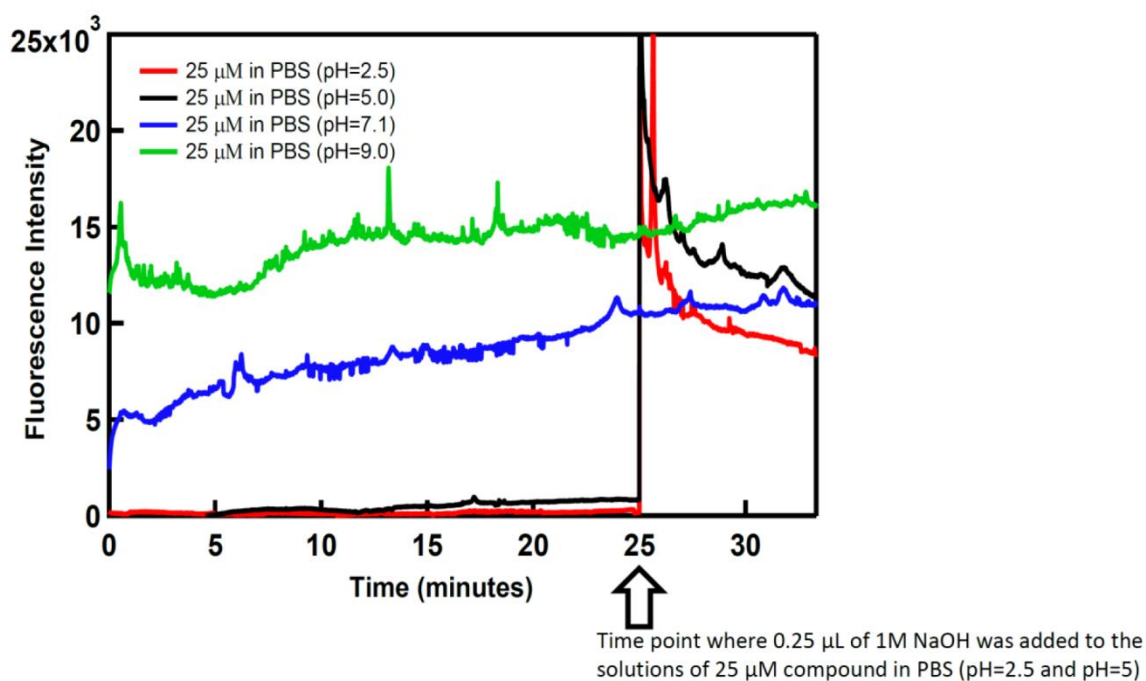


Figure SB.2. Fluorescence intensity with illumination time for 25 μM compound in (red) PBS, pH=2.5; (black) PBS, pH=5.0; (blue) PBS, pH=7.1; (green) PBS, pH=9.5. At 25 minutes 0.25 μL of 1 M NaOH is added to (red) and (black).

Table SB.1. Cytotoxicity of compounds as measured with trypan blue exclusion assay.

Concentration of the compound in PBS (pH=7.1)	% of viable cells (Trypan blue assay)
100 μ M	78
<u>50 μM*</u>	<u>83</u>
25 μ M	94
12.5 μ M	100
6.25 μ M	100
3.125 μ M	100

*Fluorescence imaging performed with 50 μ M compound

References for Supporting Information for Appendix B

- [1] T.A. Bunch, D.L. Brower, *Drosophila* PS2 integrin mediates RGD-dependent cell-matrix interactions, *Development*, 116 (1992) 239-247.
- [2] T.A. Bunch, Y. Grinblat, L.S. Goldstein, Characterization and use of the *Drosophila* metallothionein promoter in cultured *Drosophila melanogaster* cells, *Nucleic. Acids Res.*, 16 (1988) 1043-1061.
- [3] M. Zavortink, T.A. Bunch, D.L. Brower, Functional properties of alternatively spliced forms of the *Drosophila* PS2 integrin alpha subunit, *Cell Adhes. Commun.*, 1 (1993) 251-264.
- [4] W. Strober, *Trypan Blue Exclusion Test of Cell Viability*, (2001).
- [5] E.A. Smith, T.A. Bunch, D.L. Brower, General in vivo assay for the study of integrin cell membrane receptor microclustering, *Anal. Chem.*, 79 (2007) 3142-3147.

APPENDIX C

BODIPY-DERIVED PHOTOREMOVABLE PROTECTING GROUPS UNMASKED WITH GREEN LIGHT

“Reproduced with permission from [Goswami, P. P.; Syed, A.; Beck, C. L.; Albright, T. R.; Mahoney, K. M.; Unash, R.; Smith, E. A.; Winter, A. H., *Journal of American Chemical Society*, **137**, 3783-3786 (2015).] Copyright [2015] American Chemical Society.”

Pratik P. Goswami, Aleem Syed, Christie L. Beck, Toshia R. Albright, Kaitlyn M. Mahoney, Ryan

Unash, Emily A. Smith and Arthur H. Winter

C.1. Abstract

Photoremovable protecting groups derived from *meso*-substituted BODIPY dyes release acetic acid with green wavelengths > 500 nm. Photorelease is demonstrated in cultured S2 cells. The photocaging structures were identified by our previously proposed strategy of computationally searching for carbocations with low-energy diradical states as a possible indicator of a nearby productive conical intersection. The superior optical properties of these photocages make them promising alternatives to the popular *o*-nitrobenzyl photocage systems.

C.2. Introduction

Photoremovable protecting groups, sometimes called photocages or phototriggers, are popular light-sensitive chemical moieties that mask substrates through covalent linkages that render the substrates inert. Upon irradiation, the masked substrates are released, restoring their reactivity or function. While photocages have important applications in areas such as organic synthesis [1-3], photolithography [4, 5], and light-responsive organic materials [6-8], these structures are particularly prized for their ability to trigger biological activity with high spatial and temporal resolution [9-13]. Examples of such chemical tools include photocaged proteins [14-16], nucleotides [17, 18], ions [19-23], neurotransmitters [24, 25],

pharmaceuticals [26, 27], fluorescent dyes [28-30] and small molecules [31, 32] (*e.g.* caged ATP). These biologically relevant caged molecules and ions can be released from the caging structure within particular biological microenvironments using pulses of focused light. The most popular photocages used in biological studies are the *o*-nitrobenzyl systems [31-33] and their derivatives, but other photocages that see significant use include those based on the phenacyl [34], acridinyl [35], benzoinyl [36, 37], coumarinyl [38], xanthenyl [39] and *o*-hydroxynaphthyl structures [40]. Unfortunately, with few exceptions [41, 42], a serious limitation of most popular photocages is that they absorb mostly in the ultraviolet where the limited penetration of UV light into tissues largely restricts these studies to fixed cells and tissue slices. Furthermore, prolonged exposure of cells or tissues to intense UV light can lead to cellular damage or death.

Consequently, new photocaging structures that absorb visible light are urgently needed. Advantages of visible light irradiation include diminished phototoxicity compared to UV light and deeper optical penetration into tissue. Additionally, visible light photolysis can be performed with cheap lamps and Pyrex glassware, while UV photolysis requires expensive UV sources. Unfortunately, the major problem that has hindered the development of new photocages that absorb visible light is the lack of a structure-reactivity relationship for excited state heterolysis. That is, it is difficult to predict *a priori* which structures, when irradiated with light, will undergo an efficient photoheterolysis reaction. Thus, attempts to prepare visible light absorbing photocages have mostly bypassed this problem by using metal-ligand photoreleasing systems [42-44] or by using creative indirect schemes. Examples of such creative schemes include upconverting nanoparticles with surface-attached UV-absorbing photocages [45-47], using multiphoton absorption uncaging processes [48-50] or release mediated by photoinduced electron transfer with a sacrificial electron donor [51].

However, visible light absorbing organic structures that offer simple photorelease schemes and structures would potentially make a more compelling case for widespread use in biologically oriented labs [52]. A recent computational study performed in our lab suggested the hypothesis that

photoheterolysis reactions may be under conical intersection control [53]. That is, photoheterolysis of C-LG (carbon—leaving group) bonds to generate ion pairs [54] may be favored if the ion pair has access to a nearby productive conical intersection that provides an efficient channel for the excited state of the photoprecursor to decay to the ground-state ion pair. Because conical intersections are challenging to compute, we further suggested the idea of using the vertical energy gap of the carbocation to its first excited state as a simple predictor of a nearby conical intersection (CI). A low S_0 - S_1 energy gap of the cation would suggest the possibility of a nearby CI between the S_0 and S_1 surfaces and the potential for a productive mechanistic channel for the photochemistry to proceed from the excited state of the photocaged precursor to the ion pair.

C.3. Results and Discussion

Computational studies

Thus, to find visible light absorbing photocages we searched for potential photocaging structures that would generate carbocations with low-lying diradical states. A time-dependent density functional theory (TD-DFT) computational investigation of carbocations attached to the BODIPY scaffold at the *meso* position indicated that these ions have low-lying excited states. For example, the TD-DFT computed S_0 - S_1 vertical energy gap of the carbocation derived from C-O scission of **2** is 8 kcal/mol (TD-B3LYP/6-311+G (2d,p), suggesting a near-degenerate diradical configuration. Indeed, all of the cations derived from C-O scission of **1-6** have vertical gaps <13 kcal/mol (see supporting information for computational details), and have singlet states with considerable diradical character. Large singlet stabilizations upon switching from restricted \rightarrow spin-purified unrestricted singlet computations indicate that the singlet states can be described as diradicals or possessing considerable diradical character (see supporting information for details). Thus, the exact vertical energies from the TD-DFT computations are to be viewed with suspicion, but it is clear that there are low-energy diradical forms for these ions, suggesting a nearby CI between the closed-shell singlet and singlet diradical forms of the carbocations in the

vicinity of the ion pair geometry. Further, the singlet-triplet gaps of all the carbocations derived from **1-6** are ~ 5 kcal/mol in favor of the triplet state, suggesting that the “carbocations” produced by heterolysis of **1-6** may in fact be better described as ion diradicals than by traditional closed-shell carbocation structures [55].

Encouraged by these computational studies, we synthesized structures **1-6** as photocages for acetic acid (Figure C.1). Advantages of the BODIPY scaffold include simple syntheses, a compact structure, known biological compatibility [56] and high extinction coefficients in the visible [57]. Other recent studies have shown BODIPY can be used as laser dyes [58] and have photochemical heterolysis reactivity at boron [59]. Photorelease studies, described below, indicate that these structures release acetic acid upon photolysis with wavelengths > 500 nm.

Photorelease studies and quantum efficiencies

The observed substrate release rate as a function of photolysis time is quantified by the quantum efficiency parameter ($\epsilon\Phi$), which is the product of the extinction coefficient at the irradiation wavelength (ϵ) and the quantum yield (Φ). Extinction coefficients for **1-6** were determined by UV-Vis spectroscopy (see Table C.1). To compute the quantum yields of photorelease (Φ), the flux of a 532-nm laser excitation beam (ND:YAG, 1st harmonic) was determined using potassium ferrioxalate actinometry. Release of acetic acid as a function of laser irradiation time in MeOH was followed by quantitative LC/UV (see supporting information for details). Each quantum yield reported is the average of 3 separate runs. Essentially identical actinometry measurements performed after photolysis demonstrated high flux stability of the laser. Additionally, repeating the quantum yield measurement for **2** on a different day with a different laser power setting (in triplicate) gave essentially the same value for the quantum yield, indicating reproducibility. A preparative photolysis of **2** in MeOH gave a *meso*-substituted methyl ether adduct as a stable photoproduct of the photocaging moiety, suggestive of solvent trapping of an intermediate carbocation. Mass spec studies of the photoproduct also indicate

trace amount of deborylated BODIPY photoproduct as well as BODIPY dimers, possibly arising from the diradical nature of the “carbocations” formed from heterolysis leading to coupling processes. Additionally, lamp photolysis of **2** showed no major difference in release of acetic acid under argon or air atmosphere. Curiously, unlike **1-4** and **6**, the brominated compound **5** was found to be unstable. It decomposes after one day stored on the shelf in the dark, and photolysis of freshly prepared and purified **5** led to secondary products in addition to acetic acid release, and photolysis was accompanied by rapid solution bleaching. Consequently, we were not confident in our quantum yield measurements for **5** and excluded it from Table C.1. Probably, **5** also has access to alternative photochemical pathways (*e.g.* C-Br homolysis) and thermal degradation channels similar to benzyl-based photocages, which include bromine [60]. In contrast, photocaged compound **1-4** and **6** are thermally stable in the dark. Boiling these compounds in MeOH for 1h in a foil wrapped vessel led to no change in the ^1H NMR spectrum (see supporting information for spectra).

In general, the quantum efficiencies for **1-4** and **6** are slightly lower or comparable with the popular caged *o*-nitrobenzyl systems [61]. Quantum yields for **1-4** are lower than those for typical *o*-nitrobenzyl photocaged structures, but this lower quantum yield is compensated by the much higher extinction coefficients of the BODIPY chromophores compared to the *o*-nitrobenzyl chromophore, leading to reasonable quantum efficiencies. The iodinated derivative **6** has the largest quantum efficiency, comparable to that of some caged *o*-nitrobenzyl systems, but with a λ_{max} at ~550 nm rather than in the UV (the parent *o*-nitrobenzyl system has a λ_{max} of ~280 nm while a popular dimethoxy analog has a λ_{max} of ~350 nm), although still much lower than the best known photocaging system. A plausible explanation for the higher quantum yield of **6** is that the iodine atoms promote intersystem crossing (ISC) to a triplet state, which are usually longer lived than singlet excited states, giving more time for release. For example, the phenacyl photocage derivatives described by Givens undergo photorelease in the triplet state [62]. The plausibility of a rapid ISC event is supported by the very weak fluorescence of solutions of **5** and **6**, compared to solutions of **1-4**.

Optical properties of 1-6

The UV-Vis spectra and fluorescence spectra of **1-6** are shown in Figure C.2. These structures absorb between 515 and 553 nm (and emit between 520 and 580 nm), typical of simple BODIPY dyes, and feature large extinction coefficients ($\sim 50,000\text{-}70,000\text{ M}^{-1}\text{cm}^{-1}$ at λ_{max} in MeOH).

Cell Studies

To test the viability and usefulness of the BODIPY derived photocages in biological systems, compound **7** was synthesized. 2,4-dinitrobenzoic acid is a known [63] fluorescence quencher for BODIPY dyes. This quencher was coupled with our BODIPY moiety using a simple DCC/DMAP ester coupling reaction. We anticipated that **7** would be weakly fluorescent, but upon photorelease of the quencher the fluorescence would increase. Indeed, when **7** was irradiated with a mercury lamp (excitation = 500 nm, see supporting information) and its fluorescence was plotted over time (Figure C.3N). There was a steady growth in fluorescence attributed to release of the quencher. Photorelease of the quencher was also confirmed by ^1H NMR. As a control, similar steady state fluorescence measurements were performed over time for compound **7** in the dark without light exposure, leading to essentially no change in fluorescence.

Compound **2** and **7** were incubated with Drosophila S2 cells and monitored using fluorescence microscopy (Figure C.3A-L). The Drosophila S2 cells loaded with **2** and **7** were irradiated continuously with 500-nm light. Fluorescence images were collected every 36 ms for a total of 10.8 seconds. The fluorescence intensity for compound **7** inside cell as shown in Figure C.3I-L increases rapidly. This increase in fluorescence can be attributed to the release of the quencher. The same fluorescence study with **2** as a control in Figure C.3E-H shows no such increase in fluorescence. For **2**, the leaving group is acetate, which is not a quencher. Thus, little change in the fluorescence would be anticipated upon photorelease of acetic acid from this moiety. The background decay in fluorescence for both **2** and **7** can be attributed to photobleaching under intense focused light. Parts A-D of Figure C.3 show that there is a

minimal change in fluorescence of cells when they are irradiated without being loaded with compound **2** or **7**. Figure C.3M shows the fluorescence intensity change over time for cells incubated with compound **2** and **7**, and the control experiments without any compound.

Cytotoxicity of compounds was measured with trypan blue exclusion assay. All values are normalized with the control cells which were not incubated with any compound. At a compound concentration of 25 μM , 97% for compound **2** and 92% for compound **7** remained viable after 1h.

C.4. Conclusions

BODIPY-derived photocages unmask carboxylic acid with green light excitation > 500 nm and photocleavage can be carried out in living cells. These photocages are promising alternatives for the popular *o*-nitrobenzyl photocaging systems, being easy to synthesize, utilizing a biocompatible chromophore, and having superior optical properties to the most popular photocages in current use. More generally, our strategy of identifying new photocages by searching for carbocations with low-energy diradical states seems to be a promising one. BODIPY derivatives that release functional groups other than carboxylic acids and that have red-shifted absorptions into the biological window (600-1000 nm) are currently under investigation.

Acknowledgments

We thank the Petroleum Research Fund and the Cottrell Scholar Award from the Research Corporation for Scientific Advancement for financial support. We are grateful to the lab of Mark E. Thompson for providing us with an initial sample of **2** for preliminary testing. The fluorescence microscopy cellular studies (EAS) were supported by National Science Foundation grant CHE-1412084.

C.5. References

- [1] P.G.M. Wuts, T.W. Greene, *Greene's Protective Groups in Organic Synthesis*, Wiley, Hoboken, NJ, USA., 2006.
- [2] J.A. Barltrop, P. Schofield, Photosensitive Protecting Groups, *Tetrahedron Lett.*, 3 (1962) 697-699.
- [3] A. Patchornik, B. Amit, R.B. Woodward, Photosensitive protecting groups, *J. Am. Chem. Soc.*, 92 (1970) 6333-6335.
- [4] D. Wöll, S. Laimgruber, M. Gaetskaya, J. Smirnova, W. Pfeleiderer, B. Heinz, P. Gilch, U.E. Steiner, On the Mechanism of Intramolecular Sensitization of Photocleavage of the 2-(2-Nitrophenyl)propoxycarbonyl (NPPOC) Protecting Group, *J. Am. Chem. Soc.*, 129 (2007) 12148-12158.
- [5] D. Woll, N. Lukzen, U.E. Steiner, Diffusion-controlled sensitization of photocleavage reactions on surfaces, *Photochem. Photobiol. Sci.*, 11 (2012) 533-538.
- [6] R.H. Pawle, V. Eastman, S.W. Thomas, UV-induced fluorescence recovery and solubility modulation of photocaged conjugated oligomers, *J. Mater. Chem.*, 21 (2011) 14041-14047.
- [7] B.S. Park, H.M. Lee, New photosensitive polymer containing o-methylphenacyl photocage, *Bull. Korean Chem. Soc.*, 29 (2008) 2054-2056.
- [8] R.M. Hensarling, E.A. Hoff, A.P. LeBlanc, W. Guo, S.B. Rahane, D.L. Patton, Photocaged pendent thiol polymer brush surfaces for postpolymerization modifications via thiol-click chemistry, *J. Polym. Sci., Part A: Polym. Chem.*, 51 (2013) 1079-1090.
- [9] P. Klán, T. Šolomek, C.G. Bochet, A. Blanc, R. Givens, M. Rubina, V. Popik, A. Kostikov, J. Wirz, Photoremovable Protecting Groups in Chemistry and Biology: Reaction Mechanisms and Efficacy, *Chem. Rev.*, 113 (2012) 119-191.
- [10] G.C.R. Ellis-Davies, Caged compounds: photorelease technology for control of cellular chemistry and physiology, *Nat. Methods*, 4 (2007) 619-628.
- [11] A. Specht, F.d.r. Bolze, Z. Omran, J.Ä.o. Nicoud, M. Goeldner, Photochemical tools to study dynamic biological processes, *HFSP J.*, 3 (2009) 255-264.
- [12] H. Yu, J. Li, D. Wu, Z. Qiu, Y. Zhang, Chemistry and biological applications of photo-labile organic molecules, *Chem. Soc. Rev.*, 39 (2010) 464-473.
- [13] G. Mayer, A. Heckel, Biologically Active Molecules with a "Light Switch", *Angew. Chem. Int. Ed.*, 45 (2006) 4900-4921.
- [14] J. Zhao, S. Lin, Y. Huang, J. Zhao, P.R. Chen, Mechanism-Based Design of a Photoactivatable Firefly Luciferase, *J. Am. Chem. Soc.*, 135 (2013) 7410-7413.
- [15] D.S. Lawrence, The preparation and in vivo applications of caged peptides and proteins, *Curr. Opin. Chem. Biol.*, 9 (2005) 570-575.
- [16] C.W. Riggsbee, A. Deiters, Recent advances in the photochemical control of protein function, *Trends Biotechnol.*, 28 (2010) 468-475.
- [17] M.C. Pirrung, Spatially Addressable Combinatorial Libraries, *Chem. Rev.*, 97 (1997) 473-488.
- [18] M. Chee, R. Yang, E. Hubbell, A. Berno, X.C. Huang, D. Stern, J. Winkler, D.J. Lockhart, M.S. Morris, S.P. Fodor, Accessing genetic information with high-density DNA arrays, *Science (New York, N.Y.)*, 274 (1996) 610-614.
- [19] M.A. Priestman, D.S. Lawrence, Light-mediated remote control of signaling pathways, *Biochim. Biophys. Acta*, 1804 (2010) 547-558.
- [20] T.M. Gomez, N.C. Spitzer, In vivo regulation of axon extension and pathfinding by growth-cone calcium transients, *Nature*, 397 (1999) 350-355.
- [21] R. Zucker, Chapter 2 Photorelease Techniques for Raising or Lowering Intracellular Ca²⁺, in: N. Richard (Ed.) *Methods in Cell Biology*, vol. Volume 40, Academic Press, 1994, pp. 31-63.

- [22] H.W. Mbatia, H.M. Dhammika Bandara, S.C. Burdette, CuproCleave-1, a first generation photocage for Cu⁺, *Chem. Commun.*, 48 (2012) 5331-5333.
- [23] H.M.D. Bandara, T.P. Walsh, S.C. Burdette, A Second-Generation Photocage for Zn²⁺ Inspired by TPEN: Characterization and Insight into the Uncaging Quantum Yields of ZinCleave Chelators, *Chem. Eur. J.*, 17 (2011) 3932-3941.
- [24] L. Sjulson, G. Miesenböck, Photocontrol of Neural Activity: Biophysical Mechanisms and Performance in Vivo, *Chem. Rev.*, 108 (2008) 1588-1602.
- [25] R.H. Kramer, J.J. Chambers, D. Trauner, Photochemical tools for remote control of ion channels in excitable cells, *Nat. Chem. Biol.*, 1 (2005) 360-365.
- [26] J.S. Katz, J.A. Burdick, Light-Responsive Biomaterials: Development and Applications, *Macromol. Biosci.*, 10 (2010) 339-348.
- [27] C.-C. Lin, K. Anseth, PEG Hydrogels for the Controlled Release of Biomolecules in Regenerative Medicine, *Pharm. Res.*, 26 (2009) 631-643.
- [28] D. Puliti, D. Warther, C. Orange, A. Specht, M. Goeldner, Small photoactivatable molecules for controlled fluorescence activation in living cells, *Biorg. Med. Chem.*, 19 (2011) 1023-1029.
- [29] W.-h. Li, G. Zheng, Photoactivatable fluorophores and techniques for biological imaging applications, *Photochem. Photobiol. Sci.*, 11 (2012) 460-471.
- [30] T. Fukaminato, Single-molecule fluorescence photoswitching: Design and synthesis of photoswitchable fluorescent molecules, *J. Photochem. Photobiol. C: Photochem. Rev.*, 12 (2011) 177-208.
- [31] J.H. Kaplan, B. Forbush, J.F. Hoffman, Rapid Photolytic Release Of Adenosine 5'-Triphosphate From A Protected Analog - Utilization By Na-K Pump Of Human Red Blood-Cell Ghosts, *Biochemistry*, 17 (1978) 1929-1935.
- [32] J. Engels, E.J. Schlaeger, Synthesis, structure, and reactivity of adenosine cyclic 3',5'-phosphate-benzyltriesters, *J. Med. Chem.*, 20 (1977) 907-911.
- [33] G. Ciamician, P. Silbert, Chemische Lichtwirkungen, *Chem. Ber.*, 34 (1901) 2040-2046.
- [34] J.C. Anderson, C.B. Reese, A photo-induced rearrangement involving aryl participation, *Tetrahedron Lett.*, 3 (1962) 1-4.
- [35] A.J. Ackmann, J.M.J. Frechet, The generation of hydroxide and methoxide ions by photo-irradiation: use of aromatization to stabilize ionic photo-products from acridine derivatives, *Chem. Commun.*, (1996) 605-606.
- [36] J.C. Sheehan, R.M. Wilson, Photolysis of Desyl Compounds. A New Photolytic Cyclization, *J. Am. Chem. Soc.*, 86 (1964) 5277-5281.
- [37] J.C. Sheehan, R.M. Wilson, A.W. Oxford, Photolysis of methoxy-substituted benzoin esters. Photosensitive protecting group for carboxylic acids, *J. Am. Chem. Soc.*, 93 (1971) 7222-7228.
- [38] R.S. Givens, B. Matuszewski, Photochemistry of phosphate esters: an efficient method for the generation of electrophiles, *J. Am. Chem. Soc.*, 106 (1984) 6860-6861.
- [39] P. Šebej, J. Wintner, P. Müller, T. Slanina, J. Al Anshori, L.A.P. Antony, P. Klán, J. Wirz, Fluorescein Analogues as Photoremovable Protecting Groups Absorbing at ~520 nm, *J. Org. Chem.*, 78 (2013) 1833-1843.
- [40] S. Arumugam, V.V. Popik, Photochemical Generation and the Reactivity of o-Naphthoquinone Methides in Aqueous Solutions, *J. Am. Chem. Soc.*, 131 (2009) 11892-11899.
- [41] T. Pastierik, P. Šebej, J. Medalová, P. Štacko, P. Klán, Near-Infrared Fluorescent 9-Phenylethynylpyronin Analogues for Bioimaging, *J. Org. Chem.*, 79 (2014) 3374-3382.
- [42] A.K. Pal, S. Nag, J.G. Ferreira, V. Brochery, G. La Ganga, A. Santoro, S. Serroni, S. Campagna, G.S. Hanan, Red-Emitting [Ru(bpy)₂(N-N)]²⁺ Photosensitizers: Emission from a Ruthenium(II) to 2,2'-Bipyridine 3MLCT State in the Presence of Neutral Ancillary "Super Donor" Ligands, *Inorg. Chem.*, 53 (2014) 1679-1689.

- [43] W.J. Smith, N.P. Oien, R.M. Hughes, C.M. Marvin, Z.L. Rodgers, J. Lee, D.S. Lawrence, Cell-mediated assembly of phototherapeutics, *Angew. Chem. Int. Ed.*, 53 (2014) 10945-10948.
- [44] T.A. Shell, J.R. Shell, Z.L. Rodgers, D.S. Lawrence, Tunable Visible and Near-IR Photoactivation of Light-Responsive Compounds by Using Fluorophores as Light-Capturing Antennas, *Angew. Chem., Int. Ed.*, 53 (2014) 875-878.
- [45] W. Li, J. Wang, J. Ren, X. Qu, Near-Infrared Upconversion Controls Photocaged Cell Adhesion, *J. Am. Chem. Soc.*, 136 (2014) 2248-2251.
- [46] F.o. Auzel, Upconversion and Anti-Stokes Processes with f and d Ions in Solids, *Chem. Rev.*, 104 (2003) 139-174.
- [47] Y. Yang, Q. Shao, R. Deng, C. Wang, X. Teng, K. Cheng, Z. Cheng, L. Huang, Z. Liu, X. Liu, B. Xing, In Vitro and In Vivo Uncaging and Bioluminescence Imaging by Using Photocaged Upconversion Nanoparticles, *Angew. Chem. Int. Ed.*, 51 (2012) 3125-3129.
- [48] C. Tran, T. Gallavardin, M. Petit, R. Slimi, H. Dhimane, M. Blanchard-Desce, F.C. Acher, D. Ogden, P.I. Dalko, Two-photon caging groups: effect of position isomery on the photorelease properties of aminoquinoline-derived photolabile protecting groups, *Org. Lett.*, 17 (2015) 402-405.
- [49] E.B. Brown, J.B. Shear, S.R. Adams, R.Y. Tsien, W.W. Webb, Photolysis of caged calcium in femtoliter volumes using two-photon excitation, *Biophys. J.*, 76 (1999) 489-499.
- [50] R. Weissleder, A clearer vision for in vivo imaging, *Nat. Biotechnol.*, 19 (2001) 316-317.
- [51] D.E. Falvey, C. Sundararajan, Photoremovable protecting groups based on electron transfer chemistry, *Photochem. Photobiol. Sci.*, 3 (2004) 831-838.
- [52] S.L. Jacques, Optical properties of biological tissues: a review, *Phys. Med. Biol.*, 58 (2013) R37.
- [53] A.T. Buck, C.L. Beck, A.H. Winter, Inverted Substrate Preferences for Photochemical Heterolysis Arise from Conical Intersection Control, *J. Am. Chem. Soc.*, 136 (2014) 8933-8940.
- [54] D.P. DeCosta, J.A. Pincock, Control of product distribution by Marcus type electron-transfer rates for the radical pair generated in benzylic ester photochemistry, *J. Am. Chem. Soc.*, 111 (1989) 8948-8950.
- [55] R.D. Little, L.M. Brown, M.R. Masjedizadeh, Expression of dipolar character in diyl trapping chemistry, *J. Am. Chem. Soc.*, 114 (1992) 3071-3075.
- [56] R.A. Peter L. Choyke, Haley M. Simpson, Josh Duberman, G. Craig Hill, Mikako Ogawa, Celeste Regino, Hisataka Kobayashi, Toxicity of Organic Fluorophores Used in Molecular Imaging: Literature Review, *Mol. Imaging*, 8 (2009) 1536-0121.
- [57] K. Umezawa, A. Matsui, Y. Nakamura, D. Citterio, K. Suzuki, Bright, Color-Tunable Fluorescent Dyes in the Vis/NIR Region: Establishment of New "Tailor-Made" Multicolor Fluorophores Based on Borondipyromethene, *Chem. Eur. J.*, 15 (2009) 1096-1106.
- [58] F. Amat-Guerri, M. Liras, M.L. Carrascoso, R. Sastre, Methacrylate-tethered analogs of the laser dye PM567--synthesis, copolymerization with methyl methacrylate and photostability of the copolymers, *Photochem. Photobiol.*, 77 (2003) 577-584.
- [59] N. Umeda, H. Takahashi, M. Kamiya, T. Ueno, T. Komatsu, T. Terai, K. Hanaoka, T. Nagano, Y. Urano, Boron Dipyromethene As a Fluorescent Caging Group for Single-Photon Uncaging with Long-Wavelength Visible Light, *ACS Chem. Biol.*, 9 (2014) 2242-2246.
- [60] J. Ma, A.C. Rea, H. An, C. Ma, X. Guan, M.-D. Li, T. Su, C.S. Yeung, K.T. Harris, Y. Zhu, J.L. Nganga, O.D. Fedoryak, T.M. Dore, D.L. Phillips, Unraveling the Mechanism of the Photodeprotection Reaction of 8-Bromo- and 8-Chloro-7-hydroxyquinoline Caged Acetates, *Chem. Eur. J.*, 18 (2012) 6854-6865.
- [61] P. Klan, T. Solomek, C.G. Bochet, A. Blanc, R. Givens, M. Rubina, V. Popik, A. Kostikov, J. Wirz, Photoremovable Protecting Groups in Chemistry and Biology: Reaction Mechanisms and Efficacy, *Chem. Rev.*, 113 (2013) 119-191.
- [62] R.S. Givens, B. Matuszewski, Photochemistry of Phosphate Esters: an Efficient Method for the Generation of Electrophiles, *J. Am. Chem. Soc.*, 106 (1984) 6860-6861.

[63] T. Kobayashi, T. Komatsu, M. Kamiya, C. Campos, M. González-Gaitán, T. Terai, K. Hanaoka, T. Nagano, Y. Urano, Highly Activatable and Environment-Insensitive Optical Highlighters for Selective Spatiotemporal Imaging of Target Proteins, *J. Am. Chem. Soc.*, 134 (2012) 11153-11160.

C.6. Figures and Tables

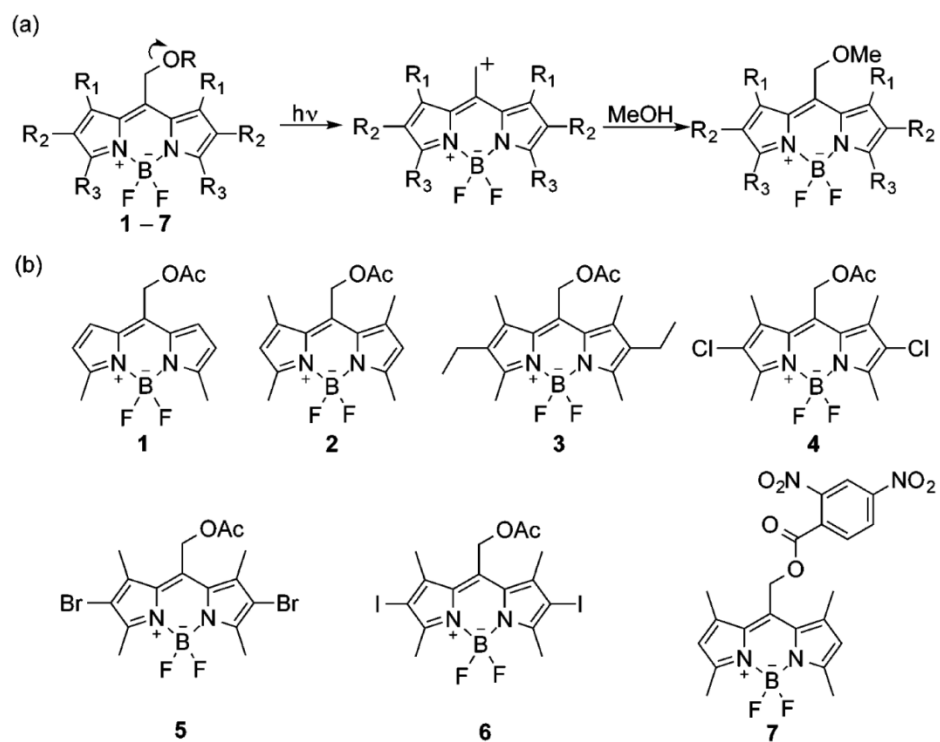


Figure C.1. (a) Possible pathway for the photolysis of photocaged acetic acid; (b) substrates describes in this study.

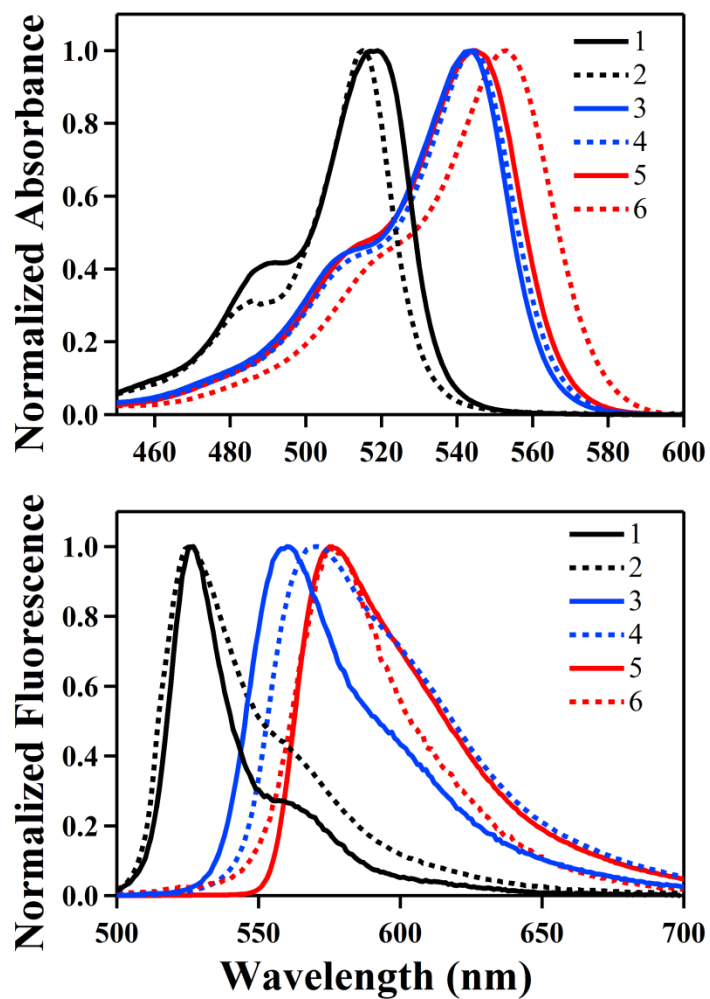


Figure C.2. Normalized absorbance and fluorescence spectra of **1-6**.

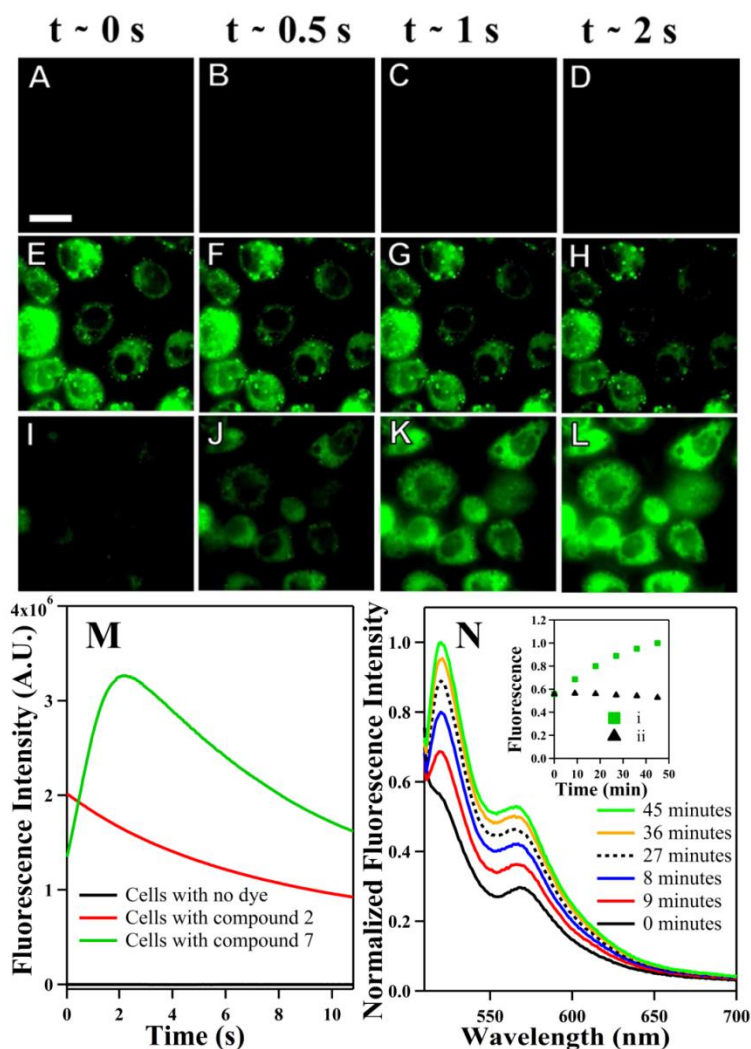


Figure C.3. Fluorescence image of S2 cells with no BODIPY compound (A-D), cells incubated with compound 2 (E-H) and cells incubated with compound 7 (I-L) as a function of irradiation time (top). Scale bar is 20 μm (shown in panel A) and is the same for all the images. Images were adjusted to same contrast in each row. Average fluorescence intensity profile versus irradiation time using 100% lamp power for excitation in cells (bottom left). Increase in free BODIPY fluorescence signal over time with quencher release from compound 7 in BES buffer (bottom right). Plot insert (bottom right) depicts the difference in growth of fluorescence vs time for compound 7 with (i) and without (ii) light irradiation.

Table C.1. Optical properties and quantum efficiencies of **1-6**^a

	λ_{\max} (nm)	λ_{em} (nm)	ϵ ($\times 10^4 \text{ M}^{-1} \text{ cm}^{-1}$)	Φ ($\times 10^{-4}$)	$\epsilon \Phi$ ($\text{M}^{-1} \text{ cm}^{-1}$)
1	519	527	5.7	6.4	37
2	515	526	7.1	9.9	70
3	544	560	6.2	9.5	59
4	544	570	4.8	4.0	19
5	545	575	--	--	--
6	553	576	4.9	23.8	117

^a Quantum yields of acetic acid release (Φ) determined by ferrioxalate actinometry in MeOH with a 532 nm ND:YAG laser source and release followed using quantitative LC-UV (Φ values are the average of 3 runs).

C.7. Supporting Information for Appendix C

Complete electronic supporting information is available on ACS website (<http://pubs.acs.org/doi/suppl/10.1021/jacs.5b01297>)

Fluorescence studies of compound 7

Steady-state absorption spectra of compound **2** and **7** in methanol were measured using a Hewlett-Packard 8453 UV-Visible spectrometer (Agilent technologies Inc., Santa Carla, CA). Compound **7** contains a fluorescence quencher 2, 4-Dinitrobenzene attached to BODIPY through a photo sensitive ester linkage. A 100 μ M solution of compound **7** in N,N-bis(2-hydroxyethyl) taurine (BES) buffer (pH=7.0) was excited with a mercury lamp (100% power, X-Cite 120 PC, EXFO Photonic Solutions Inc., Mississauga, Ontario, Canada) through excitation filter (HQ500/20 nm, Chroma Technology Crop. Bellows Falls, VT) and reflected by dichoric mirror (Q515LP, Chroma Technology Crop.) and directed to the cuvette. Quencher release from the compound **7** was monitored by measuring an increase in steady-state fluorescence from released BODIPY using a SPEX Fluoromax (ISA Jobin-Yvon/SPEX, Edison, NJ) with a 5-nm band pass and corrected for lamp spectral intensity and detector response. As a control, similar steady state fluorescence measurements were performed for compound **7** in the dark without any light exposure. For all fluorescence measurements samples were excited at 500 nm.

Cell Studies

Cell sample preparation for fluorescence imaging

All live cell experiments are performed with Drosophila S2 cells expressing α PS2 β PS integrins. S2 cells were cultured according to the culture techniques described previously [1-3]. Briefly, cells were cultured in Shields and Sang M3 insect medium (Sigma-Aldrich, St. Louis, MO) with heat-inactivated 10 % fetal bovine serum (Irvine Scientific, Santa Ana, CA), 12.5 mM streptomycin and 36.5 mM penicillin in a 22 °C incubator (Fisher Scientific, Pittsburgh, PA). Cells (50×10^5 cells/mL) were

incubated with 25 μ M of the compound **2** or **7** in M3 media for an hour. Cells were washed twice with serum free M3 media. The RBB-Tiggrin ligand coated microscope cover glasses were prepared as described previously [4]. Incubated cells were allowed to spread on ligand-coated cover glass for half an hour at room temperature. Cells were rinsed with BES buffer (pH=7.0) multiple times before imaging experiments.

Live cell fluorescence imaging

All fluorescence imaging experiments were performed on a Nikon Eclipse TE2000U microscope (Melville, NY) operating in wide-field, epi-fluorescence mode and equipped with a 100 \times Apo, 1.49 numerical aperture oil-immersion objective. Samples were illuminated with a mercury lamp (X-Cite 120 PC, EXFO Photonic Solutions Inc., Mississauga, Ontario, Canada) operating at 100% or 25 % lamp power with a ND4 neutral density filter in the optical path. The excitation filter (HQ500/20x) dichoric mirror (Q515LP) and emission filter (HQ535/30m) were from Chroma Technology Crop. Bellows Falls, VT. Fluorescence images were collected every 36 ms for a total of 10.8 seconds over 512 \times 512 pixels using a PhotonMAX 512 EMCCD camera (Princeton Instruments, Trenton, NJ) and WinView 2.6 imaging software (Princeton Instruments, Trenton, NJ). Images were further analyzed with imageJ (National institutes of Health, USA) and IGOR Pro V 6.32A (WaveMetrics Inc., Lake Oswego, OR). All imaging experiments were performed at room temperature.

pH and concentration sensitivity assays

Surrounding media pH was changed to see the effect of media pH on the photocleavage of the BODIPY from compound **7**. Released BODIPY was monitored with a similar imaging setup used for live cell imaging experiments. 50 μ M compound **7** was made in PBS (pH=2.7, pH=5.2, pH=7.2 and pH=9.7). 50 μ L of the diluted compound was dropped on microscope glass coverslip and the fluorescence signal was

monitored with irradiation time. The resultant fluorescence signal was background subtracted and averaged over three measurements.

Cytotoxicity assay

Cells (1×10^6 cells/mL) were incubated with 25 μ M of the compound **2** or **7** in serum free M3 media for an hour. Cells were rinsed thrice with phosphate buffered saline (pH=7.2). Cytotoxicity of the compound was measured using trypan blue exclusion assays [5]. Equal volumes of the cell suspension and 0.4% trypan blue stain (Thermo ScientificTM HycloneTM Trypan Blue, Waltham, MA) were incubated for 3 minutes at room temperature. The number of viable cells that excluded the dye was counted using the hemacytometer (Hausser Bright-Line, Hausser scientific, Horsham, PA). All values are normalized with the control cells which are not incubated with any compound. Error represents standard deviation in two independent measurements.

Additional studies to investigate the stability of the compound at physiological temperature

A 100 μ M solution of compound **7** in Ringer's live cell imaging buffer (pH=7.2, 155 mM NaCl, 5 mM KCl, 2 mM CaCl₂, 1 mM MgCl₂, 2 mM NaH₂PO₄, 10 mM HEPES, 10 mM Glucose) was incubated at 37 °C. Fluorescence from the compound was observed at different time intervals on SPEX Fluoromax (ISA Jobin-Yvon/SPEX, Edison, NJ). At each time interval, sample was excited at 500 nm with a 5 nm band pass and corrected for lamp spectral intensity and detector response to collect the fluorescence. After 13 hours of incubation at 37 °C, quencher release studies were performed as described. The natural logarithm of fluorescence intensity for compound **7** at 570 nm was plotted against time (min). Using the first order kinetic decay, the linear curve obtained was used to calculate the half-life ($t_{1/2}$) of compound **7** in the given conditions:

$$t_{1/2} = \frac{\ln 2}{-k} = \frac{0.6931}{0.0024} \text{ min} = 288.8 \text{ min} = 4.813 \text{ h}$$

Figures and Tables

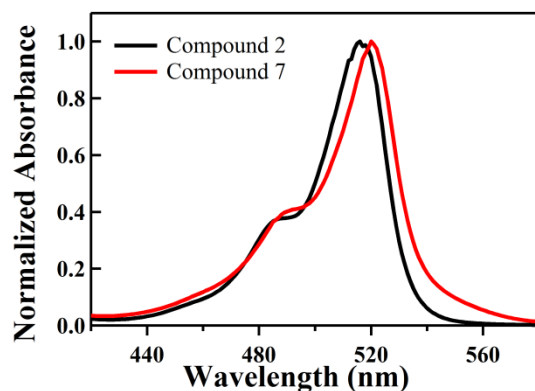


Figure SC.1. Normalized absorption spectra for compound 2 (black) and 7 (red) in methanol.

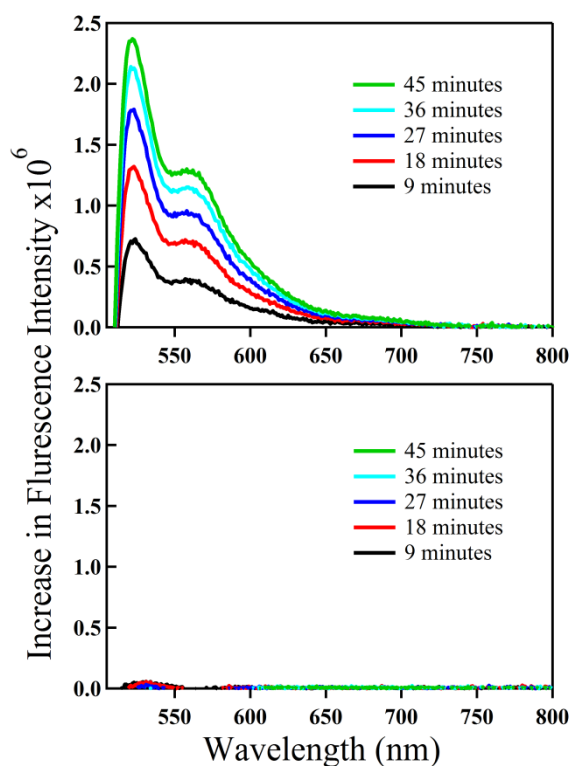


Figure SC.2. Increase in free BODIPY fluorescence signal over time with quencher release from compound 7 in BES buffer. (Upper panel) Sample was continuously irradiated with light, (Lower panel) Sample was kept in dark without any light irradiation before each measurement.

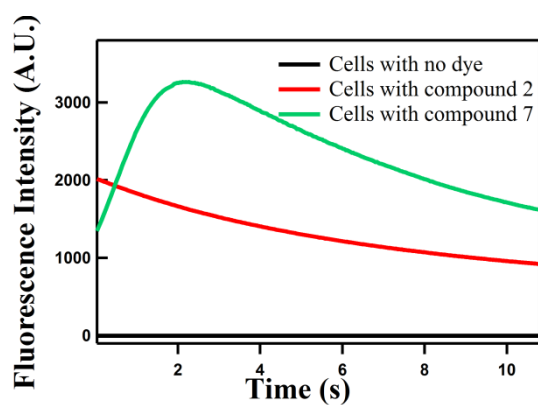


Figure SC.3. Average fluorescence intensity profile versus irradiation time using 100% lamp power for excitation. All intensity values are background subtracted and averaged over 30 to 42 cells.

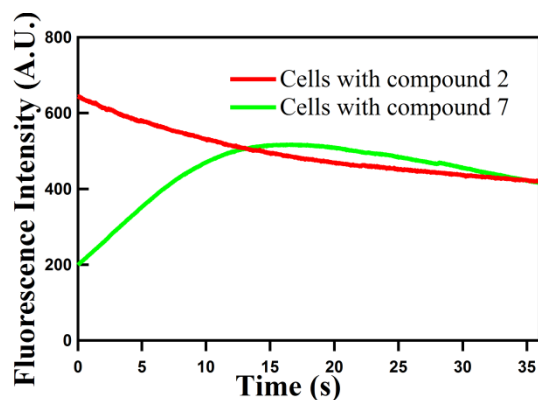


Figure SC.4. Average fluorescence intensity profile versus irradiation time using 25% lamp power for excitation. All intensity values are background subtracted and averaged from at least 15 cells.

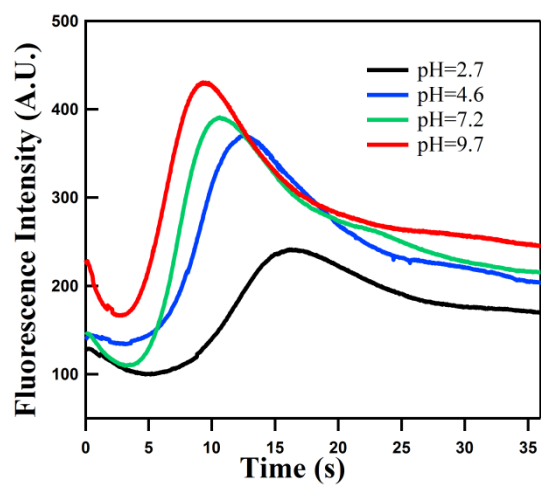


Figure SC.5. Increase in free BODIPY fluorescence signal over time with quencher release from compound **7** in PBS buffer with different pH.

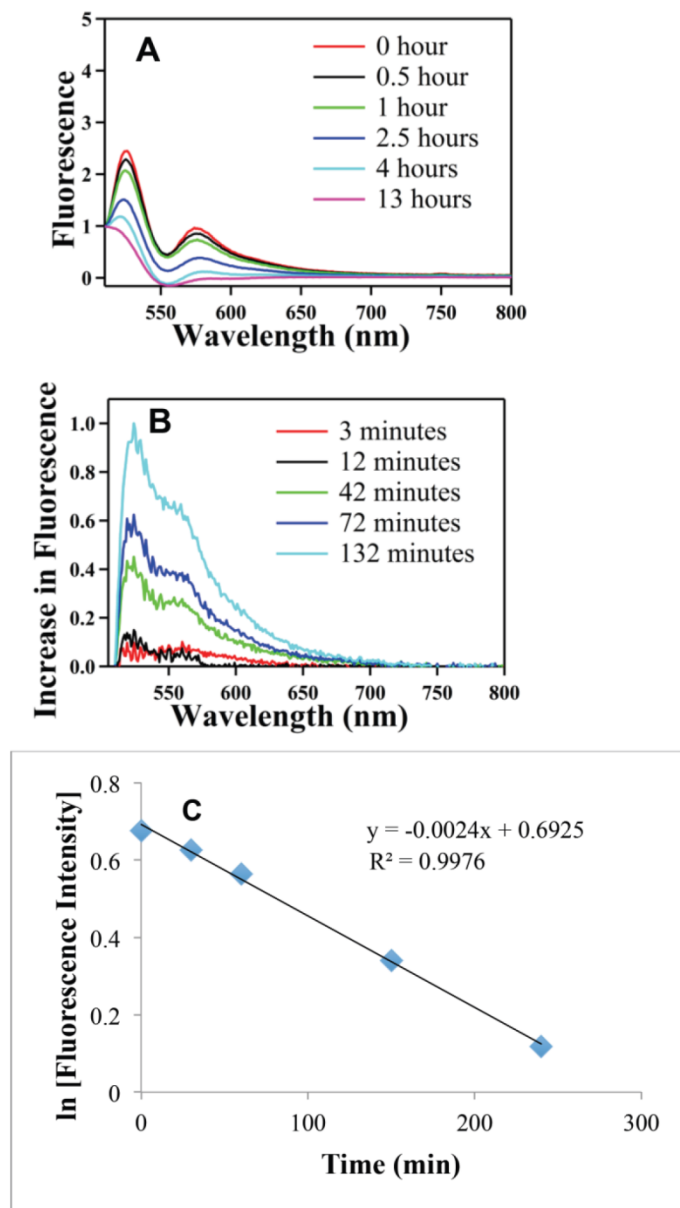


Figure SC.6. Observed fluorescence from the compound **7** incubated at 37 °C for 13 hours. B) Increase in the fluorescence due to quencher release upon irradiation after 13 hours of incubation period. Spectra were normalized with fluorescence intensity at 510 nm. C) Fluorescence intensity vs time (min) of compound **7** at 570 nm.

Table SC.1. Cytotoxicity of compounds as measured with trypan blue exclusion assay.

Compound (25μM)	% of Viable cells
Compound 2	97 \pm 2
Compound 7	92 \pm 2

References for Supporting Information for Appendix C

- [1] T.A. Bunch, D.L. Brower, *Drosophila* PS2 integrin mediates RGD-dependent cell-matrix interactions, *Development*, 116 (1992) 239-247.
- [2] T.A. Bunch, Y. Grinblat, L.S. Goldstein, Characterization and use of the *Drosophila* metallothionein promoter in cultured *Drosophila melanogaster* cells, *Nuc. Acids Res.*, 16 (1988) 1043-1061.
- [3] M. Zavortink, T.A. Bunch, D.L. Brower, Functional properties of alternatively spliced forms of the *Drosophila* PS2 integrin alpha subunit, *Cell Adhes Commun*, 1 (1993) 251-264.
- [4] E.A. Smith, T.A. Bunch, D.L. Brower, General in vivo assay for the study of integrin cell membrane receptor microclustering, *Anal. Chem.*, 79 (2007) 3142-3147.
- [5] W. Strober, Trypan Blue Exclusion Test of Cell Viability, in: *Current Protocols in Immunology*, John Wiley & Sons, Inc., 2001.

APPENDIX D**BODIPY-DERIVED PHOTOCAGES CLEAVED WITH RED LIGHT**

Julie A. Peterson, Aleem Syed, Kaitlyn M. Mahoney, Pratik P. Goswami, Toshia R. Albright, Chamari

Wijesooriya, Andrew S. Dutton, Emily A. Smith and Arthur H. Winter

D.1. Abstract

A family of BODIPY-derived photocages was synthesized that release carboxylic acids upon irradiation with wavelengths spanning the visible and entering the biological window (> 600 nm). These photocages feature potent chromophores ($\epsilon = 50,000$ - $120,000$ $M^{-1}cm^{-1}$), stability to heating in the dark, cell viability, and the ability to monitor the photorelease process using fluorescence spectroscopy via a fluorescence shift of the photocage byproduct. Photorelease with red light is demonstrated in live HeLa cells, *Drosophila* S2 cells, and bovine GM07373 cells using fluorescence microscopy. These photocages provide orthogonal external control over when, where, and how much of a substrate is activated using irradiation with essentially any visible wavelength.

D.2. Introduction

Photocages are light-sensitive moieties that are prized for giving investigators spatial and temporal control over the release of covalently-linked substrates [1-4]. When a photocage blocks a critical functional group on the substrate (*e.g.* a carboxylic acid), the substrate is rendered biologically inert. Light-induced cleavage of the photocage-substrate bond restores the reactivity or function of the substrate. Photocages have been used to activate proteins [5, 6], nucleotides [7, 8], ions [9-11], neurotransmitters [12, 13], pharmaceuticals [14, 15], and fluorescent dyes using light [16-18]. The vast majority of photocaging studies used in biological studies exploit the *o*-nitrobenzyl photocages [19, 20] and their derivatives, but others include those based on the phenacyl [21, 22], acridinyl [23], benzoinyl [24, 25], coumarinyl [26] and *o*-hydroxynaphthyl [27] structures.

A major limitation of these popular photocages is that their chromophores absorb mostly in the ultraviolet region of the optical spectrum. Ultraviolet light has limited tissue penetration, and thus restricts photocaging studies to fixed cells and thin tissue slices. In addition, exposure of cells or tissues to intense UV light eventually results in phototoxic cell damage or death. The ideal wavelength range to be used in animal tissues, known as the biological window, is ~600-1000 nm, where tissues have minimal absorbance. At these far red/near-IR wavelengths, light achieves maximal tissue penetration while minimizing phototoxicity [28]. Another problem with UV-absorbing photocages is that it is difficult to monitor the photorelease process in cells. It would be exceedingly useful to have a way to directly monitor the extent of photorelease via some reporting mechanism (*e.g.* a diagnostic increase in fluorescence), providing investigators proof of photorelease.

The drawbacks of using UV light as a biological initiator has led to a number of different approaches to permit photorelease of biologically-active substrates using visible light. The *de facto* method for releasing target molecules with visible light is to exploit multiphoton absorption methods, wherein a UV-absorbing photocage is excited with two or more visible light photons [29-31]. Other methods to achieve photorelease using visible light include photorelease initiated via photoinduced electron transfer [32-34], via metal-ligand photocleavage [35] or by using photosensitizers that generate reactive singlet oxygen that initiates a reaction cascade leading to substrate release [36-38].

However, for most cellular/tissue studies it would be desirable to achieve photorelease with simple organic structures that directly release substrates with single photons of visible light. Recently, a new class of photoremovable protecting groups derived from *meso*-substituted BODIPY dyes was reported by us and Weinstain [39, 40]. For these photocages (**1** and **2** in Figure D.1), cleavage occurs using green wavelengths ~520 nm. In related recent work, Klan and coworkers have also demonstrated the photorelease of carbon monoxide from irradiation of BODIPY-[41] and xanthene-[42]substituted carboxylic acids.

D.3. Results and Discussion

Building upon our prior work, we synthesized compounds **3-6** that have extended conjugation and a red-shifted λ_{max} values between 580 to 670 nm (λ_{em} between 600 to 690 nm) (See Figure D.2). Compounds **3-6** are thermally stable, showing no change by NMR when refluxed in the dark for 1 hour, yet release acetic acid when irradiated with visible light. The quantum yields of the release of acetic acid (ϕ) of **3-6** were determined by ferrioxalate actinometry and are reported as the average value of three separate trials. The extinction coefficient (ϵ) at the λ_{max} was determined by UV-vis spectroscopy (Table D.1). These photocages feature high extinction coefficients typical of BODIPY dyes ($\sim 50,000$ - $120,000 \text{ M}^{-1} \text{ cm}^{-1}$ at λ_{max}). In general, the quantum yields (ϕ) for photorelease of acetic acid for the longest wavelength absorbing photocages **3-6** are lower than those of the unconjugated substrates (**1** or **2**) but show release inside cells within a few minutes (Figure D.3I), making them highly practical for most biological studies given that red light irradiation has negligible phototoxicity.

Compound **7** was synthesized to test the usefulness of these photocages in live cell imaging. 4-nitrobenzoic acid was used as the leaving group, since nitrobenzoic acids are known fluorescence quenchers of BODIPY dyes. A short ethylene glycol chain (3 units) was appended to the styryl groups to aid with water solubility.

Compound **7** does not exhibit detectable fluorescence when kept in the dark at room temperature. We anticipated that upon irradiation a fluorescent peak would grow in at ~ 685 nm, similar to the fluorescence of compound **6**, as a result of release of the quencher leading to an increase in the fluorescence of the photocage byproduct. Interestingly, when **6** or **7** are irradiated either in MeOH or cell culture buffer we observe growth in fluorescence at 610 nm (See Figure D.3). This new blue-shifted fluorescent peak is similar to the emission wavelength of **3**, a BODIPY photocage containing only one of the styryl groups. Thus, the BODIPY byproduct is not simply the expected solvent trapping product of a postulated intermediate carbocation at the *meso* position (A small amount of this *meso*-methyl

alcohol photoproduct of **6** was isolated as a photoproduct, but this is not the major photoproduct and is not responsible for the blue-shifted fluorescence). ^1H NMR studies of the photolysis of **7** confirm that the quencher is released upon irradiation. Several blue-shifted photoproducts of the BODIPY have proven difficult to isolate due to their poor solubility. Photoproduct studies of **6** and **7** under air show that in addition to acetic acid, *p*-anisaldehyde is a minor photoproduct for **6** and the tri(ethylene) glycol-substituted anisaldehyde for **7**. Formation of the benzaldehyde and a λ_{em} at a similar wavelength to the *mono*-styryl derivative indicates that the major photocage byproducts have either cleaved or broken the conjugation of a styryl group.

The simplest release mechanism to consider is a photoheterolysis mechanism, either from the singlet or triplet excited state. Because the iodinated derivative **2** exhibits the highest quantum yield of release (Table D.1), it seems likely that the triplet excited state is a reactive state, since iodine atoms are well known to promote intersystem crossing via the heavy atom effect. It should be noted that the putative carbocation formed by heterolysis of **6** is computed to be a triplet ground state carbocation by ca. 5 kcal/mol using density functional theory (UB3LYP/6-31G(d), including correction for singlet spin contamination). Indeed, we selected *meso*-substituted BODIPY dyes as potential photocages based on these ions having low-lying diradical states, which we had previously suggested might be critical for providing a surface crossing between the excited state surface and the ground state ion pair surface [43]. Inspection of the computed singly occupied molecular orbitals (SOMOs) of the triplet carbocation indicates that the radicals are located on the styryl groups. Little is known about triplet carbocation reactivity [44], but triplet diradicals are known to react with oxygen, which could lead to a pathway involving oxidative cleavage at one of the styryl groups. A similar styryl BODIPY compound has been demonstrated to be reactive to radicals in the ground state, breaking the conjugation of the olefin and causing a similar wavelength shift to what we observe [45].

To corroborate that this fluorescence blue shift was correlated with release of the carboxylic acid and not just a competitive side photoreaction, compound **8** was synthesized as a control without a

leaving group and showed no fluorescence blue-shift upon photolysis. Irradiation of this compound simply led to a slow fluorescence bleaching at long irradiation times. This experiment correlates the blue-shifted fluorescence to the photorelease process. While unanticipated, this blue-shifted fluorescence fortuitously provides a convenient assay by which to follow the photorelease process using fluorescence spectroscopy, since the photocaged acid **6** does not absorb at 605 nm, the wavelength the blue-shifted byproduct absorbs.

To test whether photorelease could be performed in cells, compound **7** was incubated with HeLa cells at 36 ± 2 °C. The cells were irradiated with 635 ± 15 nm light. Fluorescence emission was measured at 605 nm. Control experiments were performed without irradiation. An increase in fluorescence was observed at 605 nm when irradiated (Figure D.3 A-D). In control studies, no increase in fluorescence was observed in the dark (Fig. D.3 E-H). Similar imaging studies were performed in bovine GM07373 cells and Drosophila S2 cells (see supporting information), yielding similar results. Cytotoxicity studies showed no decrease in cell viability (trypan blue exclusion assay) with treatment of **7** ($90\pm 3\%$ for HeLa cells with no treatment, $92\pm 5\%$ for HeLa cells with **7**, $95\pm 2\%$ for S2 cells without treatment, $93\pm 2\%$ for S2 cells with **7**, $90\pm 1\%$ for GM07373 cells without treatment, and $92\pm 5\%$ for GM07373 cells with **7**).

D.4. Conclusions

BODIPY-derived photocages release carboxylic acids at a range of wavelengths in the visible (absorptions range from ~450 to 700 nm (Figure D.2). The wide range of wavelengths of absorbance allows photorelease to be achieved using essentially any color of visible light. The unexpected blue-shift of the fluorescence of **6** and **7** upon photorelease provides a convenient assay to monitor the photorelease of substrates using fluorescence since the photocages have no emission at this wavelength prior to irradiation. In future work, the possibility of the targeted and controlled release of pharmaceuticals or other biomolecules using irradiation with red light in the biological window is an intriguing one, especially when coupled with a diagnostic change in fluorescence to follow and quantify

the release process. Additionally, it will be interesting to test the maximum wavelengths of photorelease possible, as increasing wavelengths correspond to decreased photon energies.

Acknowledgements

AHW thanks NSF 1464956 and DE-SC0014038 for financial support. The fluorescence microscopy cellular studies (EAS) were supported by National Science Foundation grant CHE-1412084.

D.5. References

- [1] P. Klan, T. Solomek, C.G. Bochet, A. Blanc, R. Givens, M. Rubina, V. Popik, A. Kostikov, J. Wirz, Photoremovable Protecting Groups in Chemistry and Biology: Reaction Mechanisms and Efficacy, *Chem. Rev.*, 113 (2013) 119-191.
- [2] G.C.R. Ellis-Davies, Caged compounds: photorelease technology for control of cellular chemistry and physiology, *Nat. Methods*, 4 (2007) 619-628.
- [3] S.R. Adams, R.Y. Tsien, Controlling cell chemistry with caged compounds, *Annu. Rev. Physiol.*, 55 (1993) 755-784.
- [4] A. Specht, F. Bolze, Z. Omran, J.-F. Nicoud, M. Goeldner, Photochemical tools to study dynamic biological processes, *HFSP J.*, 3 (2009) 255-264.
- [5] J. Zhao, S. Lin, Y. Huang, J. Zhao, P.R. Chen, Mechanism-Based Design of a Photoactivatable Firefly Luciferase, *J. Am. Chem. Soc.*, 135 (2013) 7410-7413.
- [6] D.S. Lawrence, The preparation and *in vivo* applications of caged peptides and proteins, *Curr. Opin. Chem. Biol.*, 9 (2005) 570-575.
- [7] N. Kretschy, A.-K. Holik, V. Somoza, G.-P. Stengele, M.M. Somoza, Next-Generation o-Nitrobenzyl Photolabile Groups for Light-Directed Chemistry and Microarray Synthesis, *Angew. Chem. Int. Ed.*, 54 (2015) 8555-8559.
- [8] M.C. Pirrung, Spatially Addressable Combinatorial Libraries, *Chem. Rev.*, 97 (1997) 473-488.
- [9] M.A. Priestman, D.S. Lawrence, Light-Mediated Remote Control of Signaling Pathways, *Biochim. Biophys. Acta.*, 1804 (2010) 547.
- [10] H.W. Mbatia, H.M.D. Bandara, S.C. Burdette, CuproCeav-1, a first generation photocage for Cu⁺, *Chem. Commun.*, 48 (20012) 5331-5333.
- [11] T.M. Gomez, N.C. Spitzer, *In vivo* regulation of axon extension and pathfinding by growth-cone calcium transients, *Nature*, 397 (1999) 350-355.
- [12] L. Sjulson, G. Miesenbock, Photocontrol of neural activity: biophysical mechanisms and performance *in Vivo*, *Chem. Rev.*, 108 (2008) 1588-1602.
- [13] R.H. Kramer, J.J. Chambers, D. Trauner, Photochemical tools for remote control of ion channels in excitable cells, *Nat. Chem. Biol.*, 1 (2005) 360-365.
- [14] J.S. Katz, J.A. Burdick, Light-Responsive Biomaterials: Development and Applications, *Macromol. Biosci.*, 10 (2010) 339-348.
- [15] J.A. Blake, B. Bareiss, L. Jimenez, M. Griffith, J.C. Scaiano, Design of xanthone propionate photolabile protecting group releasing acyclovir for the treatment of ocular herpes simplex virus, *Photochem. Photobiol. Sci.*, 11 (2012) 539-547.
- [16] D. Puliti, D. Warther, C. Orange, A. Specht, M. Goeldner, Small photoactivatable molecules for controlled fluorescence activation in living cells, *Bioorg. Med. Chem.*, 19 (2011) 1023-1029.
- [17] W.-h. Li, G. Zheng, Photoactivatable fluorophores and techniques for biological imaging applications, *Photochem. Photobiol. Sci.*, 11 (2012) 460.
- [18] H. Yu, J. Li, D. Wu, Z. Qiu, Y. Zhang, Chemistry and biological applications of photo-labile organic molecules, *Chem. Soc. Rev.*, 39 (2010) 464-473.
- [19] J.H. Kaplan, G.C.R. Ellis-Davies, Photolabile chelators for the rapid photorelease of divalent cations, *Photophysiol. Sci.*, 85 (1988) 6571-6575.
- [20] J. Engels, E.J. Schlaeger, Synthesis, structure, and reactivity of adenosine cyclic 3',5'-phosphate benzyl triesters, *J. Med. Chem.*, 20 (1997) 907-911.
- [21] J.C. Anderson, C.B. Reese, A Photo-induced rearrangement involving aryl participation, *Tetrahedron Lett.*, 1 (1962) 1-4.
- [22] C.-H. Park, R.S. Givens, New Photoactivated Protecting Groups. 6. *p*-Hydroxyphenacyl: A Phototrigger for Chemical and Biochemical Probes, *J. Am. Chem. Soc.*, 119 (1997) 2453-2463.

- [23] A.J. Ackmann, M.J. Frechet, The generation of hydroxide and methoxide ions by photo-irradiation: use of aromatization to stabilize ionic photo-products from acridine derivatives, *Chem. Commun.*, 5 (1996) 605-606.
- [24] J.C. Sheehan, R.M. Wilson, Photolysis of Desyl Compounds. A New Photolytic Cyclization, *J. Am. Chem. Soc.*, 86 (1964) 5277-5281.
- [25] J.C. Sheehan, R.M. Wilson, A.W. Oxford, Photolysis of Methoxy-substituted Benzoine Esters. Photosensitive Protecting Group for Carboxylic Acids, *J. Am. Chem. Soc.*, 93 (1971) 7222-7228.
- [26] R.S. Givens, B. Matuszewski, Photochemistry of Phosphate Esters: an Efficient Method for the Generation of Electrophiles, *J. Am. Chem. Soc.*, 106 (1984) 6860-6861.
- [27] S. Arumugam, V.V. Popik, Photochemical generation and the reactivity of *o*-naphthoquinone methides in aqueous solutions, *J. Am. Chem. Soc.*, 131 (2009) 11892-11899.
- [28] A.M. Smith, M.C. Mancini, S. Nie, Second window for *in vivo* imaging, *Nat. Nanotech.*, 4 (2009) 710-711.
- [29] C. Tran, T. Gallavardin, M. Petit, R. Slimi, H. Dhimane, M. Blanchard-Desce, F.C. Acher, D. Ogden, P.I. Dalko, Two-photon caging groups: effect of position isomery on the photorelease properties of aminoquinoline-derived photolabile protecting groups, *Org. Lett.*, 17 (2015) 402-405.
- [30] E.B. Brown, J.B. Shear, S.R. Adams, R.Y. Tsien, W.W. Webb, Photolysis of caged calcium in femtoliter volumes using two-photon excitation, *Biophys. J.*, 76 (1999) 199.
- [31] Q. Lin, Q. Huang, C. Li, C. Bao, Z. Liu, F. Li, L. Zhu, Anticancer Drug Release from a Mesoporous Silica Based Nanophotocage Regulated by either a one- or two-photon process, *J. Am. Chem. Soc.*, 132 (2010) 10645-10647.
- [32] D.M. Denning, N.J. Pedowitz, M.D. Thum, D.E. Falvey, Uncaging alcohols using uv or visible light photoinduced electron transfer to 9-phenyl-9-tritylone ethers, *Org. Lett.*, 17 (2015) 5986-5989.
- [33] D.E.F. Chitra Sundararajan, Alkylpicolinium Esters using photosensitization by high wavelength laser dyes, *J. Am. Chem. Soc.*, 127 (2005) 8000-8001.
- [34] D.E. Falvey, C. Sundararajan, Photoremovable protecting groups based on electron transfer chemistry, *Photochem. Photobiol. Sci.*, 3 (2004) 831-838.
- [35] T.A. Shell, J.R. Shell, Z.L. Rodgers, D.S. Lawrence, Tunable visible and near-ir photoactivation of light-responsive compounds by using fluorophores as light-capturing antennas, *Angew. Chem. Int. Ed.*, 53 (2013) 875-878.
- [36] G. Saravanakumar, J. Lee, J. Kim, W.J. Kim, Visible light-induced singlet oxygen-mediated intracellular disassembly of polymeric micelles co-loaded with a photosensitizer and an anticancer drug for enhanced photodynamic therapy, *Chem. Commun.*, 51 (2015).
- [37] A. Atilgan, E.T. Eaik, R. Guliyev, T.B. Uyar, S. Erbas-Cakmak, E.U. Akkaya, Near-IR-Triggered, Remote-Controlled Release of Metal Ions: A Novel Strategy for Caged Ions, *Angew. Chem. Int. Ed.*, 53 (2014) 10678-10681.
- [38] R.R. Nani, A.P. Gorke, T. Nagaya, H. Kobayashi, M.J. Schnermann, Near-IR Light-Mediated Cleavage of Antibody-Drug Conjugates Using Cyanine Photocages, *Angew. Chem.*, 127 (2015) 13839-13842.
- [39] N. Rubinstein, P. Liu, E.W. Miller, R. Weinstain, *meso*-Methylhydroxy BODIPY: a scaffold for photo-labile protecting groups, *Chem. Commun.*, 51 (2015) 6369-6372.
- [40] P. Goswami, A. Syed, C.L. Beck, T.R. Albright, K.M. Mahoney, R. Unash, E.A. Smith, A.H. Winter, BODIPY-Derived Photoremovable Protecting Groups Unmasked with Green Light, *J. Am. Chem. Soc.*, 137 (2015) 3783-3786.
- [41] E. Palao, T. Salanina, L. Muchova, T. Solomek, L. Vitek, P. Klan, Transition-Metal-Free CO-Releasing BODIPY Derivatives Activatable by Visible to NIR Light as Promising Bioactive Molecules, *J. Am. Chem. Soc.*, (2015).

- [42] L.A.P. Antony, T. Slanina, P. Sebej, T. Solomek, P. Klan, Fluorescein Analogue Xanthene-9-Carboxylic Acid: A Transition-Metal-Free CO Releasing Molecule Activated by Green Light, *Org. Lett.*, 15 (2013) 4552-4555.
- [43] A.T. Buck, C.L. Beck, A.H. Winter, Inverted Substrate Preferences for Photochemical Heterolysis Arises from Conical Intersection Control, *J. Am. Chem. Soc.*, 136 (2014) 8933-8940.
- [44] T.R. Albright, A.H. Winter, A Fine Line Separates Carbocations from Diradical Ions in Donor-Unconjugated Cations, *J. Am. Chem. Soc.*, 127 (2015) 3402-3410.
- [45] E.A. Haidasz, A.T.M.V. Kessel, D.A. Pratt, A Continuous Visible Light Spectrophotometric Approach To Accurately Determine the Reactivity of Radical-Trapping Antioxidants, *J. Org. Chem.*, (2015).

D.6. Figures and Tables

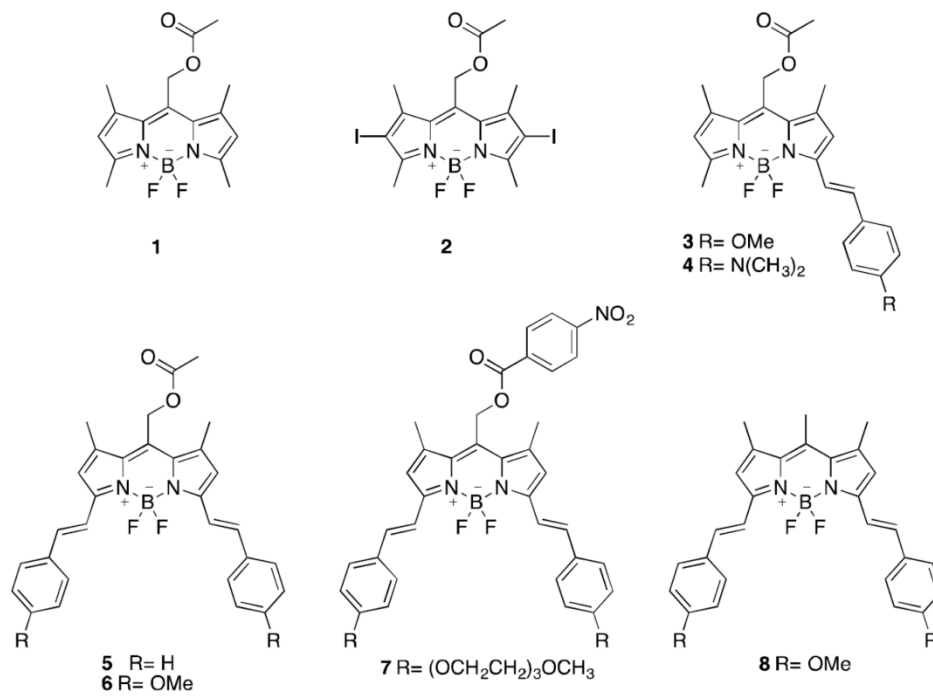


Figure D.1. Substrates described in this study. Substrates **1** and **2** are from our prior work [40], while **3-8** are described here.

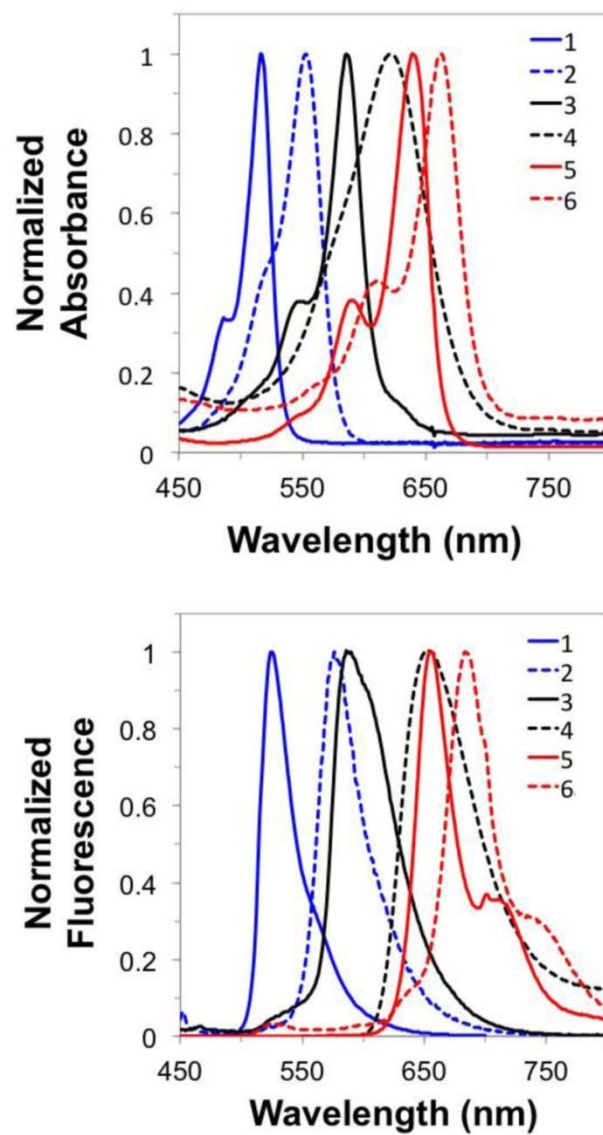


Figure D.2. Normalized absorption and fluorescence spectra of **1-6**.

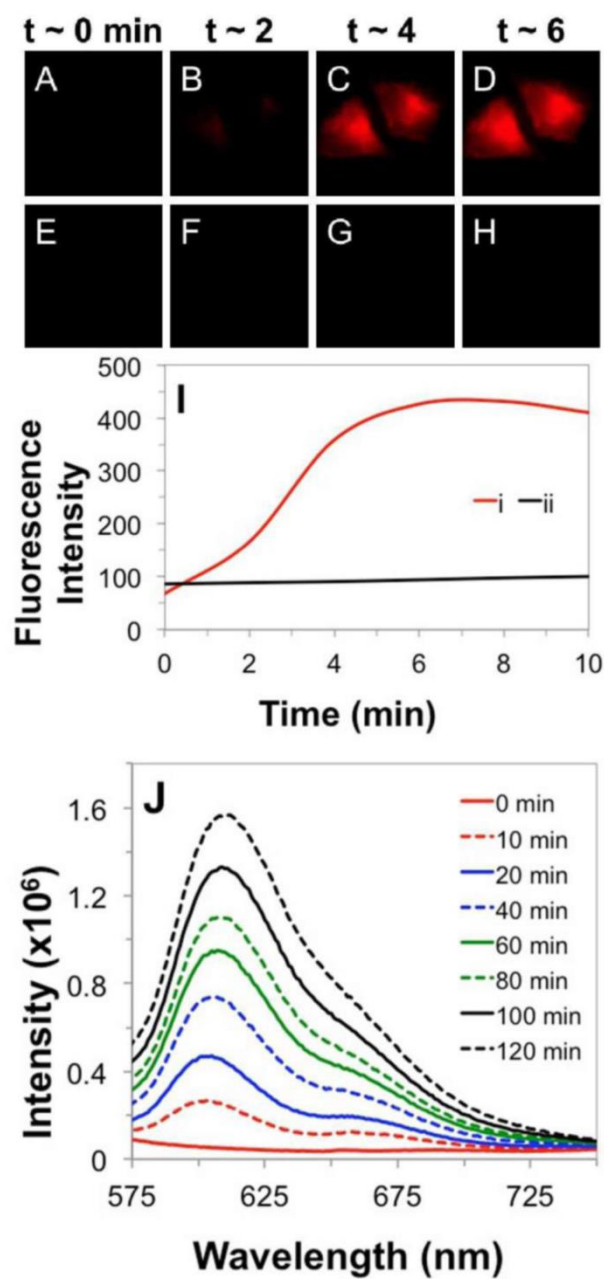


Figure D.3. Fluorescence images of HeLa cells incubated with compound **7** irradiated with 635-nm light (A-D) and cells incubated with compound **7** with no irradiation (E-H) as a function of irradiation time. Average fluorescence intensity v. time of **7** incubated in HeLa cells (n = 10) with (i) and without (ii) 635-nm irradiation (I). Increase in fluorescence of compound **7** in H₂O with 5% BSA when irradiated with a Xenon arc lamp (J).

Table D.1. Optical Properties and Quantum Efficiencies of **1-7**^a

	λ_{max} (nm)	λ_{em} (nm)	ϵ ($\times 10^4 \text{ M}^{-1} \text{ cm}^{-1}$)	Φ ($\times 10^{-4}$)	$\epsilon \Phi$ ($\text{M}^{-1} \text{ cm}^{-1}$)
1 ^b	515	526	7.1	9.9	70
2 ^b	553	576	4.9	23.8	117
3	586	607	6.1	9.8	6.0
4	633	650	6.0	6.9	4.1
5	640	656	6.5	4.5	2.9
6	661	684	6.5	4.1	2.7
7	667	N.D. ^c	12	--	--

^a Quantum yields of acetic acid release (Φ) determined by ferrioxalate actinometry in MeOH with a 532-nm ND:YAG laser source and release followed using quantitative LC-UV (Φ values are the average of 3 runs). ^b Values are taken from reference [40]. ^c N.D. = not detectable.

D.7. Supporting Information for Appendix D

Cell studies

Cell sample preparation for fluorescence imaging

In vivo cell experiments were performed with HeLa (human), GM07373 (bovine) or S2 (*Drosophila*) cells. HeLa and GM07373 cells were cultured in DMEM medium supplemented with 10% fetal bovine serum, 12.5 mM streptomycin, and 36.5 mM penicillin (Fisher Scientific, Pittsburgh, PA) in a 37 °C water jacketed CO₂ incubator (Thermo Scientific, Waltham, MA). HeLa and GM07373 cells were sub-cultured using 0.25% (w/v) trypsin-EDTA (Life Technology, Carlsbad, CA) solution every two days. Cells were sub-cultured onto custom-made glass bottom culture dishes two days before the microscopy experiment. On the day of the microscopy experiment, the growth media was replaced with 20 μM compound **7** in serum-free DMEM for one hour. Cells were rinsed with the imaging medium (pH = 7.2, 155 mM NaCl, 5 mM KCl, 2 mM CaCl₂, 1 mM MgCl₂, 2 mM NaH₂PO₄, 10 mM HEPES and 10 mM Glucose) prior to collecting microscopy images. S2 cells were cultured in Shields and Sang M3 insect medium (Sigma-Aldrich, St. Louis, MO) with heat-inactivated 12.5% fetal bovine serum (Irvine Scientific, Santa Ana, CA), 12.5 mM streptomycin, and 36.5 mM penicillin in a 22 °C incubator (Fisher Scientific, Pittsburgh, PA) [1, 2]. S2 cells were incubated with 20 μM of the compound **7** in M3 media for one hour and then washed twice with serum free M3 medium. Incubated S2 cells were allowed to spread on cover glass for half an hour at room temperature, and were then rinsed with BES buffer (pH = 7.0) multiple times prior to collecting microscopy images.

Live cell fluorescence imaging

All microscopy experiments were performed on a Nikon Eclipse TE2000U microscope (Melville, NY) operating in wide-field, epi-fluorescence mode and equipped with a 100× Apo, 1.49 numerical aperture oil-immersion objective. HeLa or GM07373 cells were imaged at 36±2 °C in a home-built housing

around the microscope. S2 cells were imaged at room temperature. For photolysis, the cells were illuminated with 635 ± 15 nm wavelength light from a mercury lamp (X-Cite 120 PC, EXFO Photonic Solutions Inc., Mississauga, Ontario, Canada) operating at 100% lamp power. Increased fluorescence due to quencher release during the photolysis reaction was collected through excitation (425 ± 45 -nm) and emission (605 ± 20 -nm) filters from Omega Optical (XF304-1, Brattleboro, VT). Fluorescence images were collected every 2 minutes using a PhotonMAX 512 EMCCD camera (Princeton Instruments, Trenton, NJ) and WinView 2.6 imaging software (Princeton Instruments, Trenton, NJ). The control experiments were performed without the 635 ± 15 -nm light illumination. Images were further analyzed with ImageJ (National Institutes of Health) and IGOR Pro V 6.32A (WaveMetrics Inc., Lake Oswego, OR).

Cytotoxicity assay

HeLa, GM07373 and S2 cells were each incubated with $20\ \mu\text{M}$ of the compound **7** for an hour. Cytotoxicity of the compound was measured using trypan blue exclusion assays [3]. Equal volumes of the cell suspension and 0.4% trypan blue stain (Thermo ScientificTM HycloneTM Trypan Blue, Waltham, MA) were incubated for 3 minutes at room temperature. The number of viable cells that excluded the dye was counted using a hemacytometer (Hausser Bright-Line, Hausser scientific, Horsham, PA) and an optical microscope.

Figures and Tables

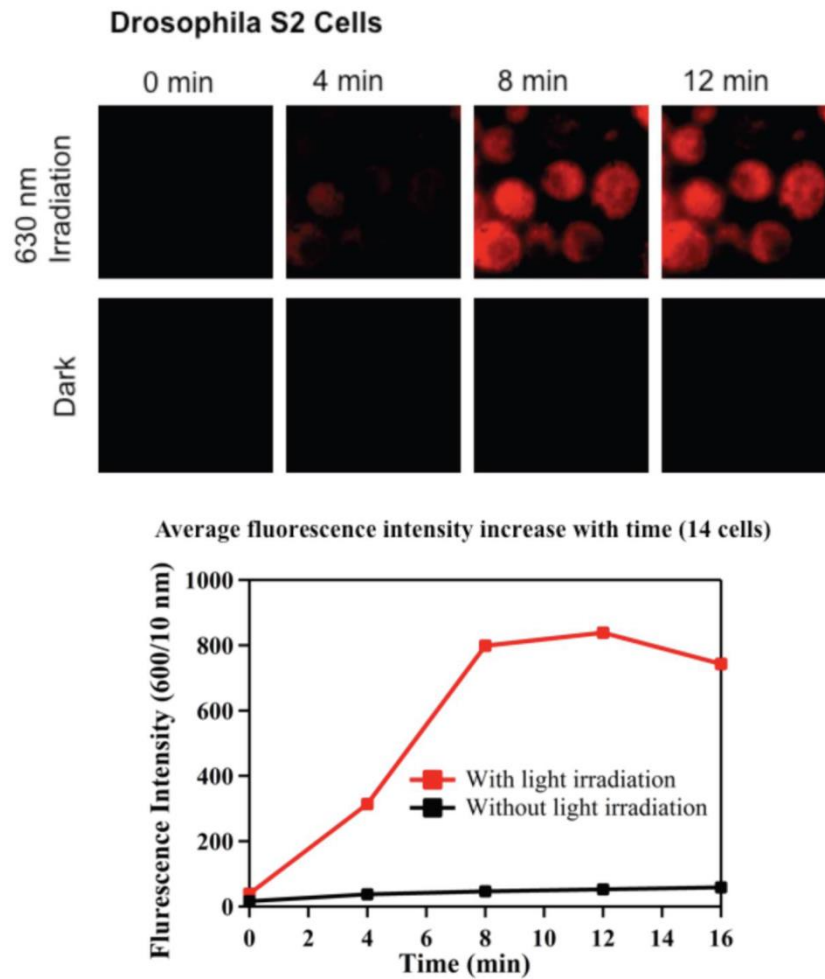


Figure SD.1. Photocage release in *Drosophila* S2 cells.

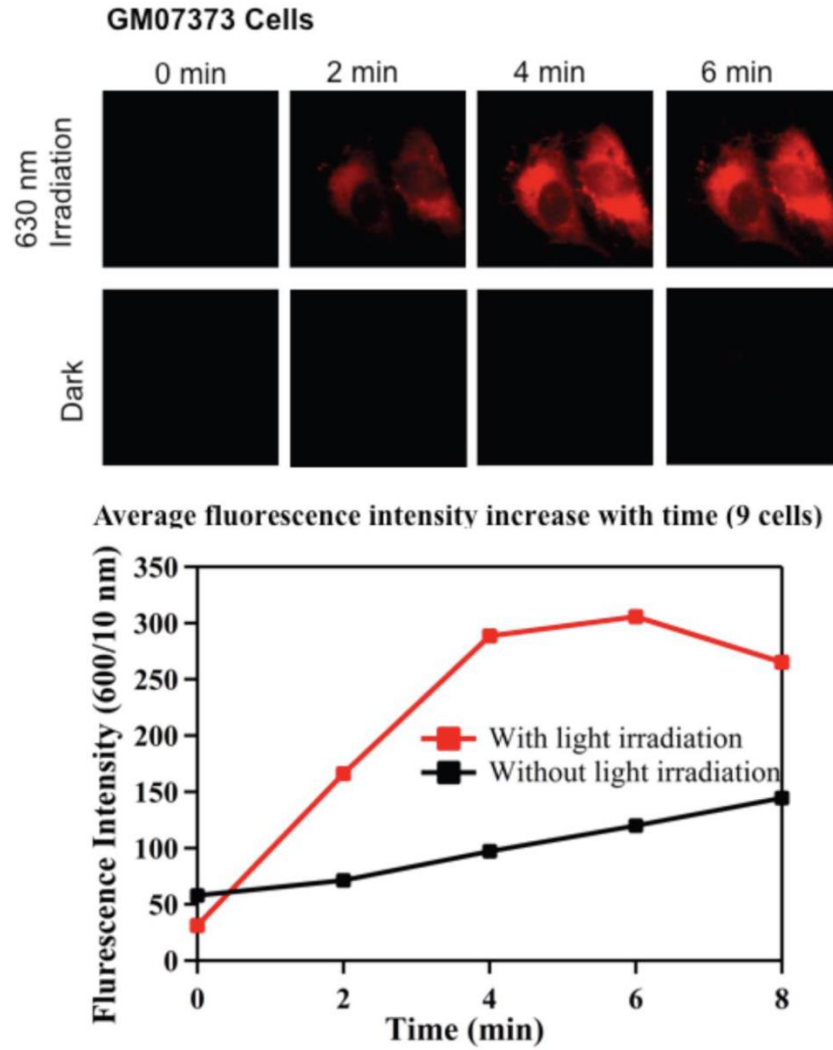


Figure SD.2. Photocage release in bovine GM07373 cells.

Table SD.1. Cytotoxicity of compounds as measured with trypan blue exclusion assay.

	% of Viable cells
HeLa cells	
No treatment	90±3
Cells incubated with 20 µM compound 7	92±5
S2 cells	
No treatment	95±2
Cells incubated with 20 µM compound 7	93±2
GM07373 cells	
No treatment	90±1
Cells incubated with 20 µM compound 7	92±5

Uncertainty represents standard deviation from two measurements

References for Supporting Information for Appendix D

- [1] T.A. Bunch, D.L. Brower, *Drosophila* PS2 integrin mediates RGD-dependent cell-matrix interactions, *Development*, 116 (1992) 239-247.
- [2] T.A. Bunch, Y. Grinblat, L.S. Goldstein, Characterization and use of the *Drosophila* metallothionein promoter in cultured *Drosophila melanogaster* cells, *Nuc. Acids Res.*, 16 (1988) 1043-1061.
- [3] W. Strober, Trypan Blue Exclusion Test of Cell Viability, (2001).